PRELIMINARY DESIGN AND ANALYSIS OF AN ENERGY STORAGE FLYWHEEL

A Dissertation Presented to the
Faculty of the School of Engineering and Applied Science
University of Virginia

In Partial Fulfillment
of the requirements for the Degree
Doctor of Philosophy

by

Arunvel Kailasan
May 2013

APPROVAL SHEET

This dissertation is submitted in partial fulfillment of
the requirements for the degree of
Doctor of Philosophy in Mechanical and Aerospace Engineering

_____

Arunvel Kailasan

This dissertation has been read and approved by the Examining Committee:

_____

Timothy Dimond, Advisor

_____

Houston Wood, Chairman

_____

George Gillies

_____

Andres Clarens

_____

Wei Jiang

Accepted for the School of Engineering and Applied Science:

_____

James H. Aylor, Dean

May 2013

Abstract

Energy storage is becoming increasingly important with the rising need to accommodate a greater population. Flywheel energy storage systems store kinetic energy by constantly spinning a compact rotor in a low-friction environment. When short-term back-up power is required as a result of utility power loss or fluctuations, the rotor's inertia allows it to continue spinning and the resulting kinetic energy is converted to electricity. Unlike the fossil-fuel power plants and batteries, the Flywheel based energy storage systems does not emit any harmful byproducts during their operation and have gained a lot of interest recently. A typical flywheel system is comprised of an energy storage rotor, a motor-generator system, bearings, power electronics, controls and housing. Conventional flywheel designs have a large diameter energy storage rotor attached to a smaller diameter section which is used as a motor/generator. The cost to build and maintain such a system can be substantial.

The goal of this thesis is to successfully design a 1KW-hr inside-out integrated ROMAC flywheel energy storage system using a single uniform composite rotor to perform the functions of energy storage, motor and generator. Active Magnetic bearings (2 radial and thrust) will be designed to support the flywheel. The weight savings from this type of design can be substantial, and additional advantages include lower component count, reduced material costs, lower mechanical complexity, and reduced manufacturing costs. The first part of the thesis deals with preliminary calculations, design and finite element analysis of the flywheel components. The subsequent parts of the thesis involve system level analyses to ensure the structural and functional integrity of the ROMAC flywheel.

Acknowledgement

I am sincerely and ever grateful to Prof. Paul Allaire for accepting me into the Rotating Machinery and Controls Laboratory (ROMAC). The technical and social experiences that I have gained under his guidance will last a lifetime. I am thankful to Dr. Timothy Dimond for his full-fledged support and guidance throughout my time in ROMAC. I am especially thankful for his advising and mentoring at a very difficult time. This thesis would have not been made possible without both Prof. Allaire and Dr. Dimond.

I would also like to mention my thesis committee Prof. Houston Wood, Prof. George Gillies, Prof. Andre Clarens and Dr. Wei Jiang for providing me with their valuable insights to shape up this thesis.

I would like to thank all my colleagues who helped me shape up this thesis. I would like to specially mention Mr. Jason Kaplan for his time in helping me with the ROMAC codes and Mr. Parinya Ananthachaisilp for his enthusiasm and patience in helping me understand the controller design.

I shall always be indebted to my family for their constant support and encouragement during this time period. I would like to thank my wife, Subhashini Vel, for being there for me whenever I needed help or a shoulder. I am thankful to my parents, Muthaiyan Kailasan and Thangamani Kailasan, for showing me the right path when in doubt. I would also like to thank my sister, Dr. Kruthikaveni Kailasan, and my brother in law, Dr. Vinodh kumar, for being a pillar of strength and support. Special thanks to my nephew, Vishaal Vinodhkumar, for helping me balance work and play.

I would like to end my note by mentioning that my graduate life at ROMAC and UVA has provided me with the necessary tools to succeed in my career and more importantly, to succeed as a human being.

Table of Contents

APPENDIX

Table of Figures

Table of Tables

Nomenclature

β	:	Thermal expansion coefficient
ϵ	:	Strain
ε	:	Emissivity of surface
κ	:	Thermal Conductivity
η_{eff}	:	Efficiency
ρ	:	Material density
ΔT	:	Temperature change
μ_0	:	Permeability of air
$\upsilon_{12}, \upsilon_{23}$	:	Major In-plane Poisson's ratio
ω	:	Nominal rotational Speed (angular velocity)
$\omega_{max}, \omega_{min}$	:	Maximum and minimum operating speeds
λ	:	Flux linkage
σ	:	Stress at rotational speed (General term)
σ_B	:	Stephan-Boltzmann constant
σ_{mat}	:	Conductivity of lamination
σ_t	:	Tensile stress
$\sigma_{max,tensile}$	:	Maximum tensile stress
σ_r	:	Radial Stress
σ_θ	:	Circumferential stress
θ_r	:	Rotor position angle
φ_1	:	Arbitrary flux linkage
A	:	Pole cross sectional area
A_{fp}	:	Area of flow path
A_{gi}	:	Area of air gap
$A_{i,shroud}$	:	Area of shroud
AM_{KW}	:	Manufacturing and assembly costs per kW
B	:	Magnetic Flux density
B_m	:	Amplitude of flux density
B_{mx}	:	X-component of flux density
B_{my}	:	Y-component of flux density
C_f	:	Coefficient of Fluctuation
$D_{in,cy}$	:	Inside diameter of object/cylinder
D_o, D_i	:	Outer and Inner Diameter of the flywheel
d_{cond}	:	Diameter of conductor
$E_{in,charge}$	:	Energy in during charge
E_{max}	:	Maximum energy stored in the flywheel
$E_{out,discharge}$	:	Energy out during discharge
E_1	:	Longitudinal In-plane Young's modulus
E_2	:	Transverse In-plane Young's modulus
e_{qs}, e_{ds}	:	Back-emf of q and d axes

F_{12}	:	View factor
f_f	:	Frequency of conductor
f_m	:	Damping coefficient
f_{rm}	:	Magnetic field reversal frequency
G_{12}	:	In-plane shear modulus
g	:	Acceleration due to gravity
g	:	Air gap (In magnetic bearing terminology, air gap is commonly denoted by g).
g_{tot}	:	Gyration coefficient
h	:	Height of the flywheel rotor
h_c	:	Height of containment
h_{con}	:	Heat transfer coefficient
I	:	Polar moment of Inertia
I(s)	:	Coil current
I_b	:	Bias Current
I_{DC}	:	DC link current
I_{max}	:	Peak current (Perturbation + Bias current)
i_{dc}	:	DC bus current
J_{max}	:	Maximum current density
K_i	:	Current gain
K_x	:	Open loop stiffness
k_{hys}	:	Hysteresis loss constant
L_A	:	Magnetizing inductance
L_c	:	Coil Inductance
L_{ls}	:	Stator phase leakeage
l_{fly}	:	Length of the flywheel
M	:	Ratio of input voltage to output voltage
M_r	:	Mass of rotor segment
m_{cond}	:	Mass of the conductor
me_u	:	Unbalance level
N	:	Number of turns
N_m	:	Number of turns on main pole of radial magnetic bearing
N_{oper}	:	Annual operating days per storage unit
N_s	:	Number of turns on side pole of radial magnetic bearing
N_u	:	Nusselt number
$n_{c/d}$	:	Number of charge/discharge cycles
OM_{KW}	:	Operational and Maintenance costs per kW
$P_{bc,i}$	:	Pressure exerted on burst liner wall
P_{Cu}	:	Copper losses
P_{eddy}	:	Eddy current losses
P_{ex}	:	Excess losses
P_{hyst}	:	Hysteresis losses
P_{int} , P_{out}	:	Internal and External Pressures
P_{Iron}	:	Iron losses
P_{rated}	:	Rated power output capacity of the energy storage system

P_{inv}^{out}	:	Output real power
PE_{KW}	:	Cost of power electronics per kW
PF	:	Power Factor
Q	:	Stiffness Matrix
Q_{cond}	:	Rate of heat conduction
Q_{inv}^{out}	:	Reactive power
$\mathcal{R}_i$	:	Dynamic reluctance
$\mathcal{R}_r$	:	Static reluctance
R_{KW}	:	Replacement cost per kW
R_{sw}	:	Stator winding resistance
R_{20}	:	Resistance at 20° C
r_c	:	Inner radius of magnet
$r_{c,h}$	:	Radius of housing containment
$r_{c,I}$	:	Radius of the burst liners inner wall
r_o, r_i	:	Outer and inner radii of the object
r_{out}	:	Outer radius of the flywheel
$r_{o,max}$	:	Maximum rotor radius
SF	:	Safety Factor
S_Θ	:	Strength of material in circumferential direction
T_e	:	Electromagnetic torque
T_{win}	:	Temperature at which winding resistance is measured
T_{work}	:	Working temperature of laminations
TS_{cost}	:	Total cost of storage unit
$TS_{cost,KW}$	:	Total cost of the storage unit per kW
$t_{c/d}$	:	Length of each charge/discharge cycle
t_i	:	Impact duration
t_r	:	Time period of replacement
t_{th}	:	Thickness of lamination
U_m	:	Mean fluid velocity
u_r	:	Radial direction displacement
V_{dc}	:	DC bus voltage
V_{iron}	:	Volume of iron
V_{rim}	:	Rim volume
$V_{t.l}$	:	Translated linear velocity of the rotor segment

1 Introduction

One of the largest means of energy generation and distribution is via electricity. The rise in global population and increased consumer use of electricity has increased the rate of per capita fossil energy consumption [1]. Climatic changes and limited fossil fuels have triggered a need to create a sustainable form of energy storage [2]. The challenge is to generate, store and distribute that energy in ways which will not negatively impact the environment and yet be sustainable.

Sustainable and renewable energy sources have vast potential to reduce dependence on fossil fuels and lower greenhouse gas emissions [3]. One of the main drawbacks to renewable sources is that they are subject to random environmental factors such as sunlight being blocked or intermittent wind conditions. Energy storage helps to alleviate this problem by providing a mechanism by which surplus energy can be stored during periods of low demand or high generation and supplied back to the grid when needed[4]. When energy storage is implemented with renewable resources it reduces supply disruptions and adds value to the overall system.

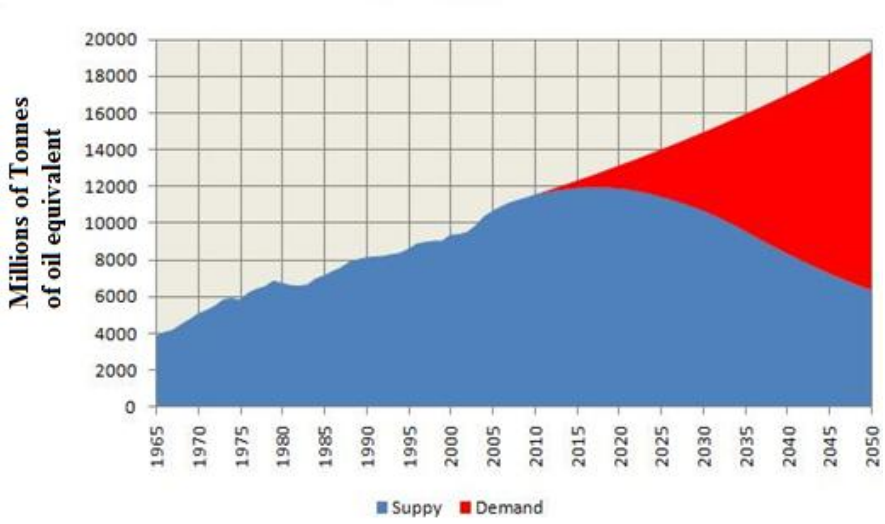

Figure 1-1. Predicted energy supply vs. demand (DOE)[5]

The recognized need for electrical energy storage is not new. Over the years, energy production methods have developed that strive to match the user demand in the most economical way

possible. While significant energy storage technology advances have been made in many areas, none have been successfully engineered to meet this challenge [6]. People have devised many methods of storing energy over the years; however, no method of energy storage has shown to be cost-effective, efficient and flexible enough to inspire widespread use. The problem of storing accessible energy in a cost effective and efficient manner has remained one of the most difficult science and engineering problems [7].

Many advances in electrical energy storage technologies and methods have been made in recent times. These advances have come in the areas of batteries, large scale pumped hydroelectric storage plants, compressed air energy storage, flywheels, superconducting magnetic energy storage, and super-capacitors. Chemical energy storage, most commonly applied in batteries, is the world's most common form of electric energy storage [8]. However, there are several drawbacks to batteries for large systems, including cost, short lifetime, and disposal concerns.

Figure 1-2 NASA's G2 Flywheel[9]

Flywheels are becoming a promising solution in a number of energy storage applications due to their high efficiency, long cycle life, wide operating temperature range and high power and energy densities. They are best suited for routinely storing small amounts of energy delivered at high power for short times (1-2 hours), or to smooth out peaks in power demand into and out of a much larger battery storage system[10]. Dubbed "electromechanical batteries, " early flywheel

designs stored kinetic energy in a cylindrical or ringed mass, spinning at very high speeds (~10,000-200,000 rpm), for a high energy density of 0.1-1 kW-h/L [11, 12]. Flywheels have the technical strengths of high efficiency (~95%), high power density, and long service life. There are also no chemical reactions to reverse and very little friction involved since flywheels are typically levitated by magnets in a vacuum chamber.

1.1 Problem Statement

Several advantages are associated with the use of flywheel energy storage (FES) systems compared to electrochemical battery storage. A detailed description of FES is given in Chapter 3 and Appendix A. The most commonly cited advantages are the superior power and excellent energy capacity per system mass of FES units. The specific power of many FES systems ranges between 5 and 10 kW/kg whereas values for electrochemical batteries are typically smaller by one order of magnitude [13]. The specific energy of advanced FES systems may exceed 200 W-h/kg and values of 100 W-h/kg are commonly achieved. Specific energies of electrochemical systems are usually around 30 W-h/kg for lead-acid batteries and in excess of 100 W-h/kg for lithium-ion batteries [14]. Other advantages of FES technology include faster response to changes in load, a smaller environmental impact due to the absence of harmful chemicals that are usually part of electrochemical batteries, and the ability of FES units to operate effectively over a wide temperature range. Electrochemical batteries perform effectively only within a relatively narrow temperature band.

In spite of these advantages, flywheels are not as commercially successful and widely used as batteries [15]. This is primarily due to high initial costs and safety concerns. Even with the technological advancements in composites, magnetic bearings and power electronics, flywheels are limited to use in large scale applications (10 MW-h or more). Flywheels today find applications primarily in large scale energy distribution, frequency regulation, power quality, large uninterrupted power supply (UPS) systems and outer space applications. Such FES systems tend to be bulky and expensive.

There is a growing need to develop clean energy storage solutions for small scale applications. While flywheels are ideal candidates for this, the associated initial costs and bulky designs tend

to discourage their use. Hence there is a need to develop a cost-efficient, compact flywheel design for use in small scale applications.

Flywheels designed for small scale applications usually operate at a speed less than 20,000 rpm, and use steel for the rotor material. This thesis presents a design for a high speed flywheel with an energy storage capacity of 1 kW-hr with a maximum continuous operating speed of 40,000 rpm. Composites are used for the rotor material. By utilizing a high speed rotor, more energy can be stored per unit volume of a material. This is because the energy stored in a rotor is proportional to the square of the operational speed.

Designing such a flywheel poses many challenges. The most important issue to be addressed from a safety perspective in a high speed flywheel design is the stresses associated with the composite material. Composites tend to have low tensile strength in the radial direction. Also high variability in composite material properties makes their performance more difficult to predict. This can be mitigated with higher factors of safety. Improper design characteristics result in the rotor parts separating from the composite hub due to centrifugal forces. Safety concerns at high rotational speeds (generally greater than 50,000 rpm) are another major issue to be addressed. Reliability issues due to power conversion capability, delamination of composites and bearing failures add to the problem. This thesis attempts to address these issues.

1.2 Thesis Objective

Flywheel energy storage systems comprise of an energy storage rotor, motor/generator system, bearings, power electronics, controls and housing [16]. Current designs of commercial flywheels comprise of 2 rotors: one for energy storage and one for the motor/generator system. This kind of design tends to be very bulky, complex and expensive. Minimizing the weight of the overall FES system is very important since lower weight systems would save on installation and material costs – which tend to be very high. A low weight flywheel system can also prove beneficial in space applications

The work presented in this thesis is the design and analysis of a 1 kW-hr integrated FES system. The flywheel is designed such that a single, uniform composite rotor will perform the functions of energy conversion and energy storage. This design is simpler mechanically than the traditional two-rotor systems. Further, the flywheel is designed to operate at a nominal speed of 40,000 rpm.

The flywheel rotor design employs magnetic levitation, using 2 thrust and 2 active radial magnetic bearings (AMBs). The main advantage of such a system is that it costs significantly less and avoids complex issues in coupling two rotors. The weight savings from this type of design can be substantial, and additional advantages include lower component count, reduced material costs, lower mechanical complexity, and reduced manufacturing costs.

Preliminary flywheel sizing calculations are performed to determine the dimensions of each component. The different components of the FES system including a permanent magnet (PM) alternator, power electronics, composite rotor, magnetic bearings and housing are designed and analyzed. Three dimensional finite element analyses are conducted on each component individually and on the system as a whole. These include electromagnetic, thermal, stress and rotordynamic analyses in order to fully characterize the system. A drop analysis is also conducted to anticipate the behavior of the system during and AMB failure. Novel contributions and specific thesis objectives are outlined in the next section.

1.3 Scope and novel contributions:

The main aim for this thesis is to design a 1 kW-hr cost efficient flywheel for potential use in small scale applications. This can be achieved by spinning the rotor at a high speed (40,000rpm). Successful design of a cost-effective and lighter flywheel can pave the future for residential and commercial small scale energy storage solutions. UPS storage and renewable energy solutions can be made more practical [17]. A smaller footprint can be created. By replacing batteries with flywheels we can reduce the impact of harmful chemicals on the environment. Regenerative braking solutions can make a huge advance with use of flywheels in hybrid cars and trains. It is projected that with a successful short term energy storage solution, about 60% of the energy lost as heat today can be put into use [18]. Further, power quality management can be improved at a smaller scale providing solutions to power disruptions and electrification problems. Electricity can be stored at the residential level and used during times of peak demand and limited supply. A practical solution can be provided for densely populated areas and developing countries by using a cost –efficient flywheel to store “wasted” energy.

The novel contributions of this thesis include:

1. Combining state of the art technologies in developing a novel cost efficient flywheel design

The uniqueness of the work lies in the combining various technologies like PM alternator, magnetic bearings, composite rotor , barrel type integrated system into designing the ROMAC flywheel. Such technologies, by themselves, have been used before but integrating them together in one compact system is a novel contribution by this thesis.

2. Developing a compact flywheel energy storage solution for small scale consumer level applications.

This thesis provides a possible solution to consumer level power applications by utilizing flywheel energy storage systems. Flywheel applications generally target large scale power systems (e.g.: Grid or a distributed energy facility) and could provide significant savings. Low cost flywheels could also be used at the consumer level to provide savings in terms of power and cost. (e.g.: utilizing a flywheel to power a home during peak demand).

3. Using a high speed rotor to design a 1kW-hr energy storage flywheel

Another novel approach taken in this thesis is to use a high speed rotor operating at 40,000 rpm to achieve a targeted energy storage of 1 kW-hr. Similar sized flywheels typically operate at much lower speeds (6,000-20,000 rpm) to achieve this energy capacity. A major advantage of such a high speed rotor is that more energy can be stored per volume of material used. The weight savings can be substantial which in turn translates into a cost efficient flywheel system.

4. The use of spline rings between the composite rotor and the system rotor components

Spline rings are a proven standard solution used in jet engine design to prevent withdrawal of the rotor components during high speed operation. Even though flywheels have the same driving concept as jet engines, such a solution has never been used in developing a flywheel energy storage system. The use of a double spline ring layer is unique in the ROMAC flywheel design.

5. Using efficient design techniques for individual components

This thesis acts as a means of providing a cost efficient design technique for individual components. The use of standard software such as ANSYS, Matlab and Autodesk to create a good first cut design approximation saves a lot of time and cost in testing each component. The simulation techniques such as thermal analysis, rotordynamic analysis and drop analysis

employed in this thesis at the design phase provide a good understanding of the overall design and hold a significant advantage over usual trial and error techniques.

1.4 Thesis Outline

The specific thesis outline is discussed in this section. In Chapter 2, the overall structure and orientation of the flywheel components is presented. An extensive literature review is performed to study the different orientations of commercial flywheel energy storage systems. Three different orientations (standard, barrel type and integrated flywheel) are analyzed and their advantages/disadvantages are compared. The different components of a flywheel energy storage system are also presented in this chapter. Chapter 3 covers the ROMAC prototype design concept and characteristics. A preliminary sizing of the flywheel is done to determine flywheel component dimensions and operating speed. An initial 3D stress analysis is performed analysis on the flywheel energy rotor to verify safe rotor operation at the determined dimensions. The design characteristics of the individual components including bearing support, power electronics and mechanical components are discussed in this chapter. Chapter 4 covers the design of the composite rotor and the housing. A simple analysis was done to better understand the rotor material choice (i.e. Steel vs. composite). A detailed stress analysis was carried out to test the structural integrity of flywheel rotor. Finally the design of the housing was done to ensure that the flywheel components would be contained safely in the event of a rotor failure. Chapter 5 presents the design and analysis of the bearing support system. Initial calculations and a 2-D analysis are done to determine the dimensions of the magnetic thrust and radial bearing. A 3-D non-linear finite element model is created to calculate axial force, stiffness, magnetic flux and other control parameters for the thrust and radial magnetic bearings. Finally, the back-up bearing design choice and parameters for the ROMAC flywheel energy storage system is presented. Chapter 6 extensively covers the design and analysis of the power electronic components. An analytical approach is taken to design the DC bus, pulse width modulator and the permanent magnet synchronous machine model. The different parameters such as input current voltage, power and efficiency were deduced from the mathematical model. Finally, the individual power electronic components are integrated to show the complete model. In Chapter 7, the system level analysis of the flywheel components are presented. A rotordynamic model of the flywheel is created to determine critical speeds, mode shapes and identify the gyroscopic effects on the

flywheel rotor model. This is followed by adopting techniques to design an effective PID controller. In Chapter 8, a thermal analysis is conducted to identify the heat sources and temperature rise during nominal flywheel operation. The different rotor and stator losses including eddy current losses, copper losses and hysteresis losses are also studied. Chapter 9 concludes this thesis by summarizing the thesis and providing future directions for research.

2 Flywheels- State of the Art and Literature Review

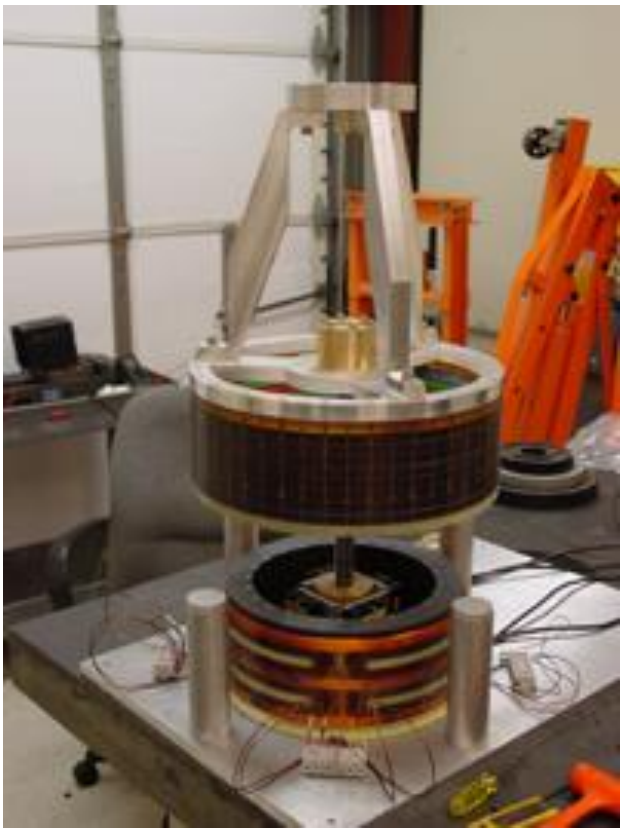

Figure 2-1 Launch point flywheel test rig.[19, 20]

2.1 Introduction

A flywheel energy storage system comprises of a rotating mass. This rotating mass is made of metal or composite, and it is accelerated by an electrical motor. To charge the flywheel with energy, pulses of electrical current are fed sequentially to fixed coils called the stator, and the magnetic fields from these currents exert torques on the rotor to accelerate it. Whether the modern flywheel is being accelerated, and thus storing energy, or whether it is decelerated, and thus providing energy, is determined by the control system and the voltage of the system to which it is connected. [10, 21]

When the flywheel's rotational speed is not changing, it idles. It can maintain a very-nearly constant speed for a long time, because the electrical drag losses in the bearings are very small. For power applications, when the voltage supplied to the flywheel drops below a preset value, the flywheel discharges energy to maintain that voltage [22, 23]. When the voltage rises above another set value, the flywheel can absorb that energy to maintain the bus voltage in the desired range.

The main parts of the modern flywheel are a power converter, a controller, a stator, bearings, and a rotor. The rotor includes the rotating part of the motor generator, and the rotating part of the bearings. The stator is also a part of the motor generator. A typical flywheel storage system component is depicted below.

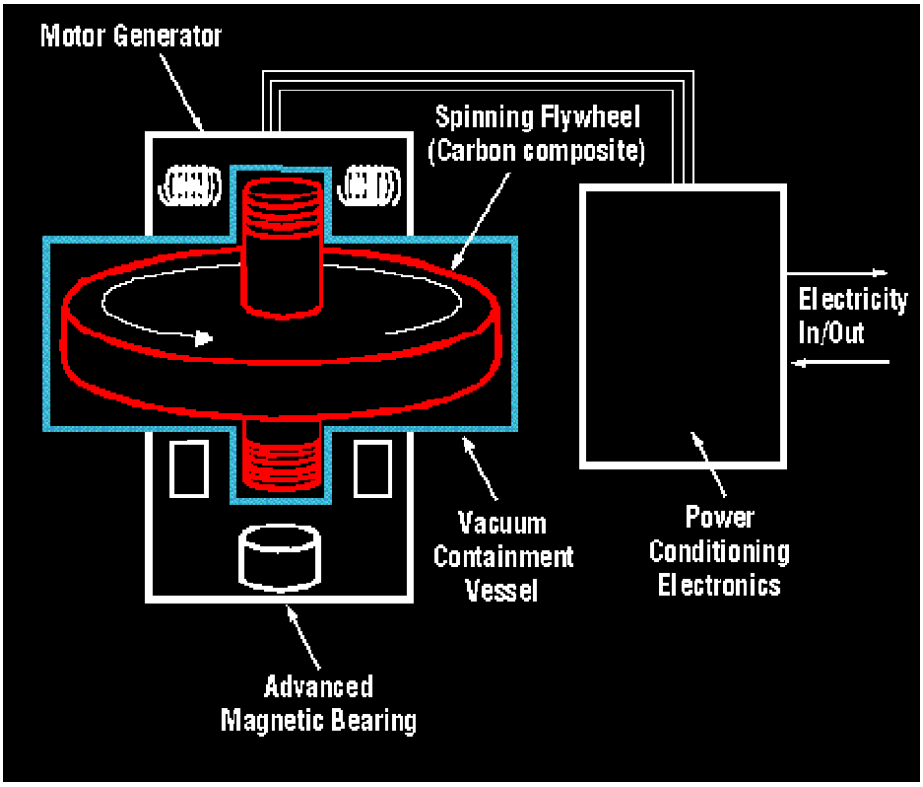

Figure 2-2 Schematic of flywheel system components [24]

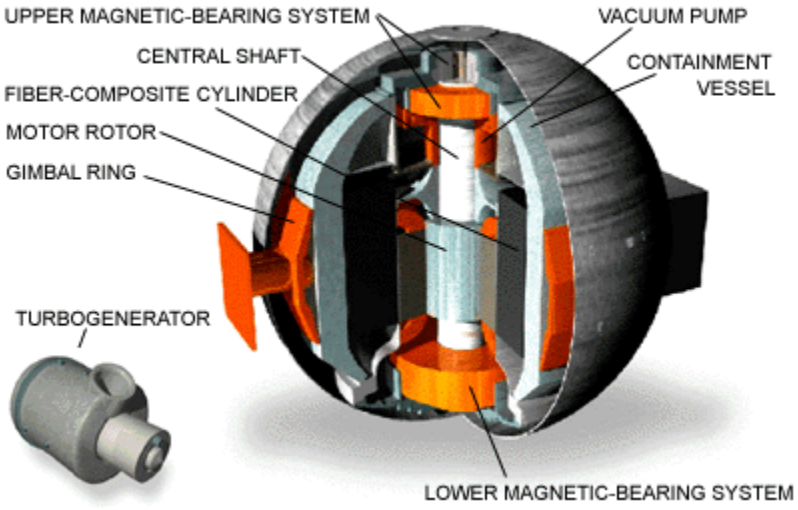

Figure 2-3 A NASA flywheel system to be used for space applications.[25]

2.2 Components of a flywheel energy storage system

Figure 2-4 Typical Components of a Flywheel System.[26]

A flywheel has several critical components as described below in this section. A general description of each component is also given.

2.2.1 Rotor

The rotor, as the energy storage mechanism, is the most important component of the flywheel energy storage system. The design of the rotor is the most significant contributor to the effectiveness and efficiency of the system. Rotors are designed to maximize energy density at a given rotational speed, while maintaining structural integrity in the face of rotational and thermal stresses [27]. Rotor designs can be divided into two broad categories: low-speed, and high speed rotors [28]. Low speed rotors can have either horizontal or vertical shafts. High speed rotors are usually vertical.

2.2.2 Bearings

The bearings support the flywheel rotor and keep it in position to freely rotate. The bearings must constrain five of the six degrees of freedom for rigid bodies, allowing only rotation around the axis of the rotor. The construction of the bearings is important in flywheel performance. In addition to the centrifugal stresses, the speed of the flywheel is limited in a large part by the friction on the bearings, and the resulting wear on the bearings often defines the maintenance schedule for the system.

There are several types of bearings used in flywheel construction. Mechanical bearings are the simplest form of flywheel bearings. These might be ball, sleeve, roller, or other type of mechanical bearing. These bearings are well understood, reliable, and inexpensive, but also suffer the most wear and tear, and produce the largest frictional forces, inhibiting high rates of rotation.

Magnetic bearings are required for high-speed flywheel systems [12, 23]. These bearings reduce or eliminate the frictional force between the rotor and its supports, significantly reducing the parasitic losses. There are several types of magnetic bearings. Passive magnetic bearings are simply permanent magnets, which support all, or part of the loads on the flywheel. Active

magnetic bearings, on the other hand, use controlled magnetic fields, where field strength on the bearing axes is varied to account for the effect of external forces on the rotor. Superconducting bearings are passive magnetic bearings, which use superconducting materials to produce the magnetic repulsive force to support the rotor assembly. These materials operate at very low temperatures, and also require cryogenic cooling systems. As they cannot be controlled, super conducting bearings are not an ideal solution for flywheel design.

2.2.3 Motor-Generator

Motors convert electrical energy into rotational mechanical energy stored in the flywheel rotor during charge, and generators reverse the process during discharge. In many modern flywheels the same rotating machine serves both functions. The machine is called a motor alternator or motor generator and consists of a wound- or permanent magnet rotor, usually revolving within a stator containing electrical winding through which current flows [29, 30]. Note that this machine, along with any power electronics, limits the power rating of the flywheel system. And in some practical systems the generator for discharging the wheel is higher power than the recharging motor. Thus at full power charging the wheel will require more time than discharging. The starter motor and alternator or generator are connected to the flywheel via the same steel shaft and may be either a single machine or two different machines. In both cases the rotor becomes part of the flywheel mass. When separate, the starter motor is typically a simple induction motor that is able to produce starting torque.

2.2.4 Power Electronics

Most flywheel energy systems have some form of power electronics that convert and regulate the power output from the flywheel. As the motor-generator or alternator draws on mechanical energy in the rotor, the rotor slows, changing the frequency of the AC electrical output.

The main function of these devices is to allow energy to be taken from the wheel before its frequency and power output drop below usable levels. In fact the low-end (i.e., end-of-discharge) cutout speed at which the flywheel is considered discharged is primarily dependent on the current carrying capability of the electronics (or electromechanical coupling) and the size of the

load [27]. For example, most flywheels have output current proportional to load and inversely proportional to speed. This means a lighter load can go to a lower speed before the system cuts out on maximum current.

2.2.5 Controls and Instrumentation

Flywheel systems require some controls and instrumentation to operate properly. Instrumentation is used to monitor critical variables such as rotor speed, temperature, and alignment [31] . Rotor speed and alignment are also often controlled variables, through active feedback loops. The latter is especially important for systems with magnetic bearings, and most magnetic systems have complex controls to reduce precession and other potentially negative effects on the rotor. In many systems, other instrumentation is used to monitor performance or design parameters related to failure modes. In some composite flywheel systems, for example, instrumentation is used to measure deformation of the rotor over time, alerting operators when the rotor shape indicates possible failure in the future.

2.2.6 Housing

The housing is the containment around the flywheel system, used to protect against hazardous failure modes. It is sometimes also used to maintain a vacuum around the rotor to reduce atmospheric friction.

2.3 Description of commercial flywheel systems

This section describes the various commercial flywheel systems available today. A detailed review of the flywheel system along with their specifications and major short comings are discussed.

The main manufacturers include Active Power, Acumentrics Corporation, AFS Trinity Power Corporation, Beacon Power, Kinetic Traction, Power-thru (Pentadyne), Piller (Caterpillar), TSI (Tribology Systems Inc.), Ricardo Kinergy Flywheel systems and Urenco Power Technologies.

While most companies offer standard products targeted at a range of applications, a few companies aim to design customized solutions in response to customer-specific requirements. Steel flywheel manufacturers are in the minority. Active Power and Caterpillar are actively marketing UPS systems using a steel flywheel. Piller has a well-established dynamic UPS product using inertial storage, and incorporating a unique electrical machine, designed to provide support from loss of power until a diesel generating set can be started and brought on-line. This is a high-security system solution designed specifically for UPS applications.

Many other organizations and research centers with various technical specialties have flywheel R&D programs. These include Boeing, Lawrence Livermore National Laboratory (LLNL), Argonne National Laboratory, Oak Ridge National Laboratory, Pennsylvania State University, Launch Point Technologies, Artemis Project, Philip Medlicott Ltd., Michigan State University, The Center for Electro Mechanics at The University of Texas, NASA Glenn Research Center, The Office of Transportation Technologies (OTT) of the US Department of Energy (DOE), and certain European universities.

2.3.1 Beacon Power

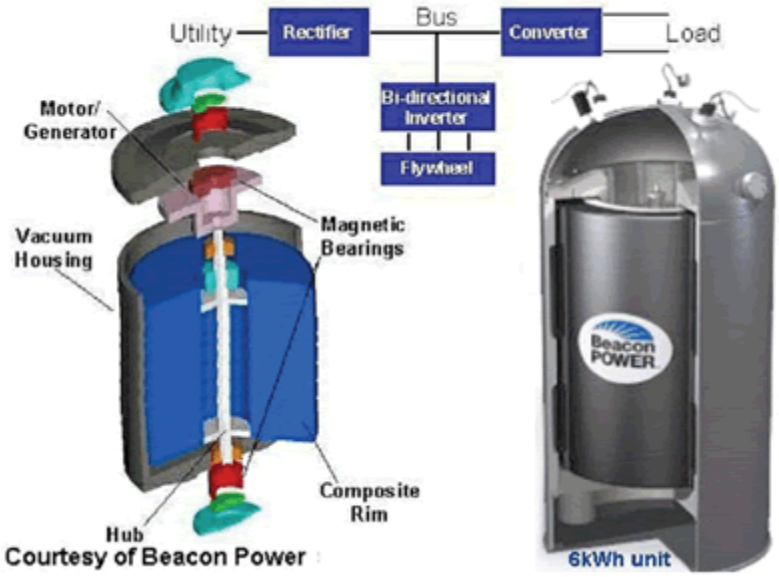

Figure 2-5 Beacon's Flywheel Energy System [32]

Beacon Energy is one of the key players in the flywheel energy storage market. Their flywheels are designed to last for about 20 years and require very little maintenance for their mechanical components. The main applications for Beacon energy flywheels include power quality and distributed energy. Hence their cyclic life capability is critical to ensure frequency regulation. Beacons Smart Energy 25 flywheel can perform over 150,000 full charge/discharge cycles at constant full power rate. This can be achieved with zero or little degradation in their energy storage capacity over time.

The schematic of the Beacon flywheel system is shown in figure 2-5. It consists of a carbon fiber rotor powered by a PM alternator. The rotor is sealed in a vacuum chamber to reduce aerodynamic drag and frictional losses. Further, the system uses a combination of permanent magnets and active magnetic bearings to levitate the composite rotor. The operational speed of the rotor is between 8,000 rpm and 16,000 rpm with an extractable energy of 25kW-hr. Several flywheels are connected in parallel to provide any desired megawatt-level power capacity. A 20

MW energy storage plant consists of 200 such flywheels. It is reported that the flywheel mechanical efficiency is over 97% while the total system round trip efficiency is about 85% [32].

The specifications and costs associated with the Beacon's Smart energy 25 (20MW frequency regulation plant) is shown below.

Specification	Value
Capital Cost	$1630/KW
Operational/Maintenance cost (Annual)	$11600/MW per year
Electricity cost / hour	$ 1.25/MW per hour
Output Power	20 MW max. continuous for 15 minutes
Power Range	40 MW (20 MW up or down)
Rated output energy	5MWh @ 20 MW
Response time	< 4 seconds (to rated power)
Input/output voltage	480 VAC, 3 phase, 50/60 Hz
Flywheel operating speed	8000-16000 rpm
Design life	20 years
Plant foot print	3.5 acre (14,165 sq.m)

Table 2-1 Beacon's Smart energy 25 specifications

The main shortcoming of the Beacon power flywheel is demagnetization issues due to the use of PM. Even though a composite rotor is used, the maximum operating speed is only about 16,000 rpm. Hence a maximum amount of energy is not stored in each module. Further their high initial cost, high weight to energy ratio and relatively larger footprint discourages use with commercial small scale applications. In addition, two major accidents have been reported due to improper electronics design and abnormal heat issues [33]. This reduces the overall reliability of the Beacon flywheel.

2.3.2 Powerthru (Formerly Pentadyne)

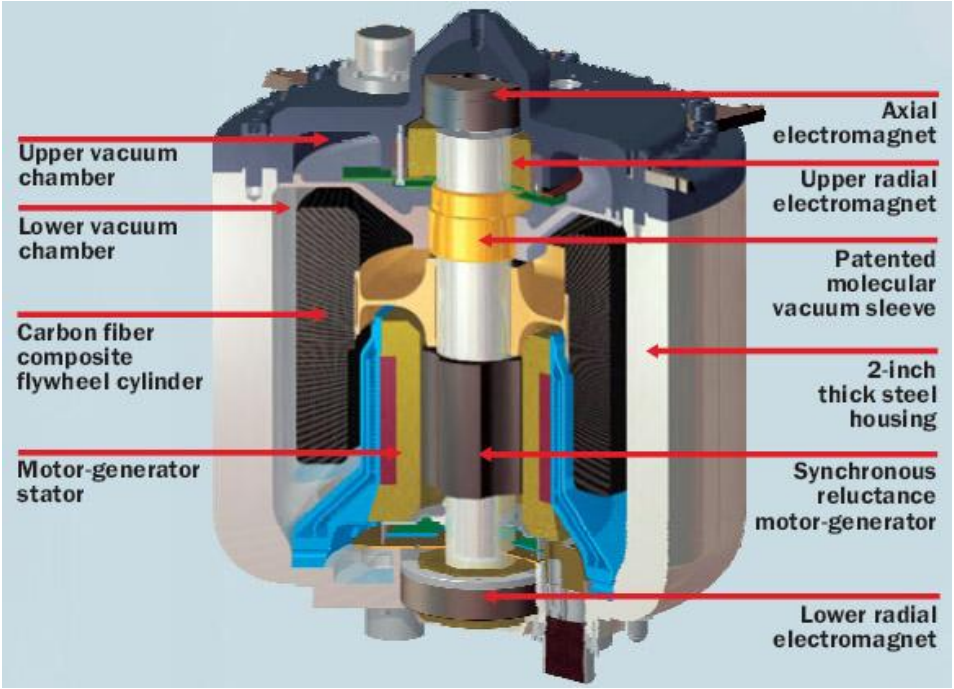

Figure 2-6 Pentadyne's Flywheel Energy System [34]

The Pentadyne GTX flywheel comprises of a carbon fiber composite rotor which rotates over a titanium hub. Similar to Beacon's smartgrid energy storage system, the GTX flywheel also uses magnetic bearings to support the rotor. One of the attractive features of the flywheel is that the flywheel takes full advantage of the composite rotor by operating at a speed of 52,000 rpm. The use of magnetic bearings also reduces the maintenance cost of replacing traditional mechanical bearings. A vacuum pump is used to reduce aerodynamic drag which functions without the use of a mechanical pump. This is done by the use of a molecular vacuum sleeve on the shaft. The shaft speed along with the sleeve's helical grooves crates a theoretical vacuum of 0.0001 Pa [34].

The Pentadyne GTX comprises of a synchronous reluctance motor generator design. The flywheel rotor weighs about 55 lbs and requires 300W to operate. The targeted power storage of the GTX is about 200KW per unit. As with Beacon's flywheel, multiple units can be used in

parallel to store more energy. [34]. The specifications of the Pentadyne flywheel are given below.

Specification	Value
Capital Cost	$1200/KW (estimated)
Operational/Maintenance cost (Annual)	$17-$20/KW per year
Electricity cost / hour	$ 1.25/MW per hour
Output Power	200 KW per unit
Power Range	1 MW to 4MW (max upto 8MW)
Response time	< 6 seconds (to rated power)
Voltage	570V-900V DC , <2VDC ripple
Flywheel operating speed	52000 rpm
Design life	15-20 years

Table 2-2 Power-thru's flywheel specifications

A major problem with the Pentadyne flywheel is that high acoustic noise, intense local saturation and high windage losses have been reported due to the use of the synchronous reluctance motor generator [35]. Even though the theoretical value of vacuum was estimated at 0.0001 Pa, the lower vacuum chamber was unable to maintain 97% of the vacuum. This results in high aerodynamic drag. The use of a titanium hub, while advantageous from an energy standpoint, increases the overall initial cost of the flywheel. Further, poor power controls contributed to decreased motor/generator efficiency.

2.3.3 Kinetic traction

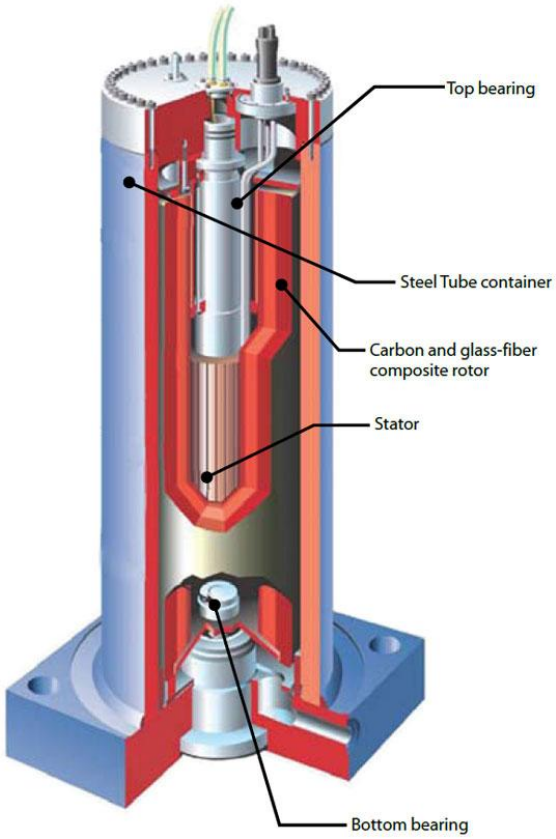

Figure 2-7 Kinetic Traction's Flywheel Energy system.[36]

Kinetic traction flywheel rotors are made up carbon fiber composites and are supported by a combination of magnetic bearings and hydrodynamic bearings. Each module is capable of a power capacity of 200 kW, a useable energy of 1.7 kW-hr and a maximum operating speed of 36,000 rpm. These flywheels have been designed to handle over 1000 charge-discharge cycles per day for about 20 years. Kinetic traction flywheels are operated by a permanent magnet DC alternator and have been used in major railway and subway systems in New York, London and Lyon to provide clean energy capture with significantly lower costs than traditional energy substations[36].

The technology behind Kinetic traction's high speed flywheel was coined in the 1990's to absorb and deliver power more effectively and reliably. It should be noted that the power consumption of their systems is less than 400 W [36].The specifications of the flywheel are given below.

Specification	Value
Capital Cost	$600/KW
Operational/Maintenance cost (Annual)	$10-$20/KW per year
Electricity cost / hour	$ 1.25/MW per hour
Output Power	200 KW per unit
Power Range	1 MW to 4MW (max upto 8MW)
Response time	< 5seconds (to rated power)
Voltage	570-900V DC , DC Ripple <1%
Flywheel operating speed	25800-37800 rpm
Design life	15-20 years
Average Standby power consumption	<400 W

Table 2-3 Kinetic traction flywheel specifications

One of the major disadvantages of Kinetic Traction's flywheel is the use of hydrodynamic bearings. These bearings undergo severe wear during start up and have to be replaced very quickly. The rotor performance was severely affected due to the design of these hydrodynamic bearings. Hence the cost of maintaining the flywheel is high (in addition to the high set up cost) Another major issue with these flywheels is that the composite rotor experienced heat issues and could not be operated for longer periods of time. This affects the performance and reliability of the flywheel. Finally the use of older power electronics technology implies that the energy storage per module is not optimum.

2.3.4 Active Power Systems

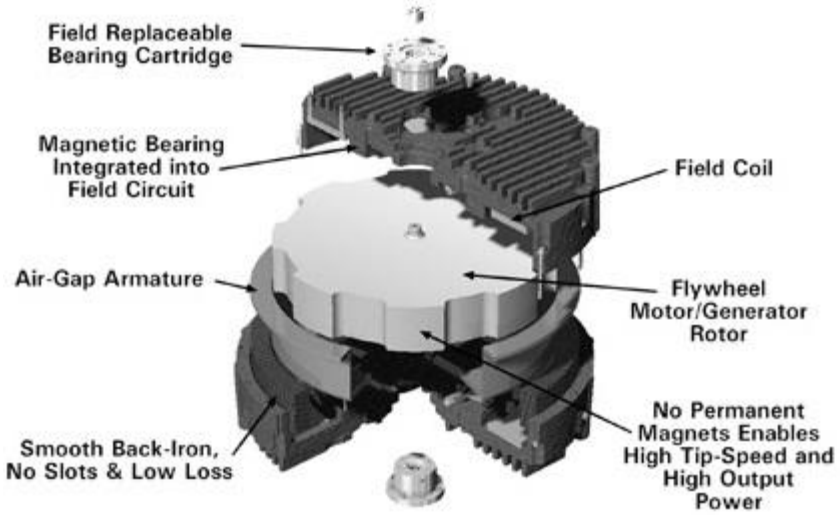

Figure 2-8 CleanSource DC flywheel [37]

Active power systems are one of the oldest commercial flywheel energy storage systems in the market. This flywheel uses an integrated 4340 steel rotor rotating at 7,700 rpm which performs the function of both the alternator and energy storage [37]. The CleanSource DC is capable of delivering up to 250kW of power and is primarily targeted to use as a UPS system. Like the above discussed flywheel systems, the CleanSource DC also uses a magnetic bearing which is integrated into the motor-generator field coil structure. It should be noted that the motoring commutation is controlled by optical sensors and that there are no permanent magnets or brushes on the rotor. The flywheel has been designed for an operating life of 15 to 20 years [37]. Table 2-4 summarizes the technical specifications of the CleanSource DC flywheel.

Specification	**Value**
Capital Cost	$700/KW (Estimated-high end)
Operational/Maintenance cost (Annual)	$5-$7/KW per year
Electricity cost / hour	$ 1.25/MW per hour
Output Power	100 -250 KW per unit

Power Range	750 KW to 2MW
Charging current	15-100 A per flywheel
Charging time	<2.5 minutes from discharge
Output discharge Voltage	360-550V DC , DC Ripple <2%
Flywheel operating speed	7700 rpm
Design life	15-20 years
Average Standby current consumption	2-3A DC
Weight	1724 Kg (3800 lbs.) – single unit

Table 2-4 CleanSource(Active Power) flywheel specifications

Due to the use of a steel rotor, low energy to power density ratio is obtained. The lower speed of the rotor results in a need of a bulky system to generate an equal power output as its competitor. This discourages use of the flywheel in small scale applications as it adds on to the initial set up cost along with higher maintenance costs. The main issue with the flywheel was that very high losses were obtained due to aerodynamic noise and drag. Heat issues with the alternator have also been noted. Several issues of poor motor commutation control and tuning were also reported [38].

2.3.5 Vycon

VYCON has developed highly efficient flywheel systems which provide consistent, dependable energy for a variety of important applications. VYCON's flywheel-based energy storage systems hold kinetic energy in a spinning mass, and convert this energy to electric power through the use of a high speed electric motor/generator.

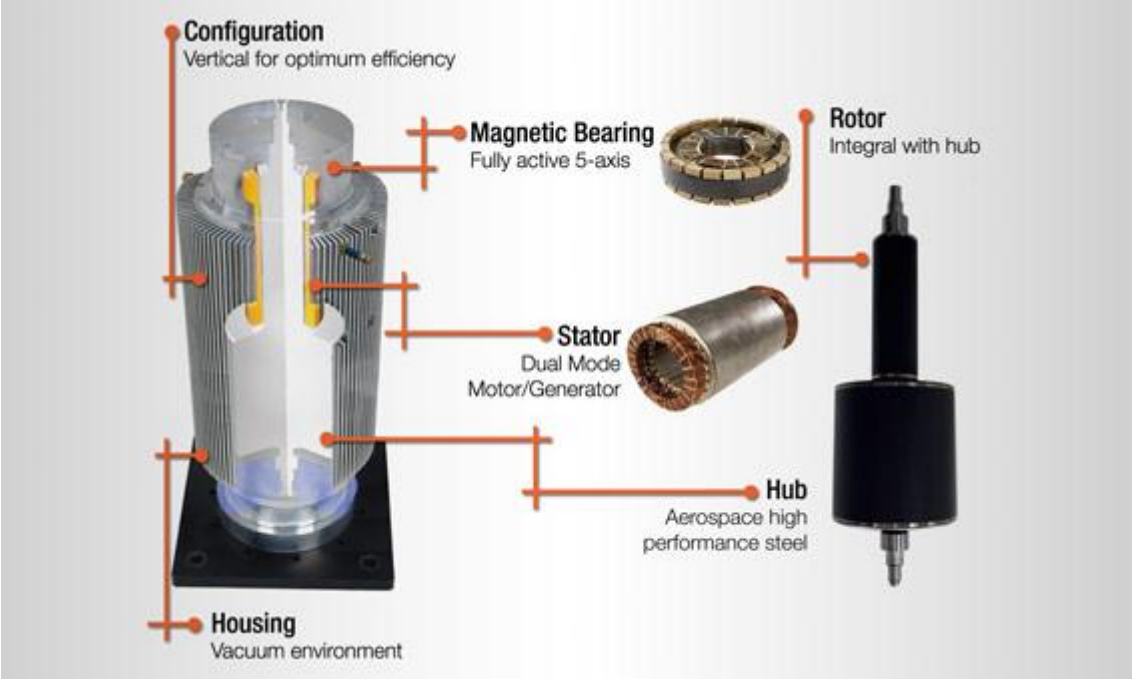

Figure 2-9 Vycon energy storage flywheel [26]

The Vycon flywheel energy storage system employs a steel rotor operating at a maximum speed of 36,750 rpm. It uses a combination of permanent magnets and active magnetic bearings to support the rotor. The Vycon flywheel is shown in figure 2-9. The rotor assembly of the flywheel operates in vacuum which is achieved by the help of an external pump. The power output of the flywheel is about 215 kW per unit and they are designed to operate for about 20 years with periodic maintenance. [26, 39, 40]. The specifications of the flywheel are presented in table 2-5.

Specification	**Value**
Capital Cost	$1280/KW (in 2008)
Operational/Maintenance cost (Annual)	$12-$15/KW per year
Electricity cost / hour	$ 1.25/MW per hour
Output Power	215 KW per unit
Max. energy storage	3000 KW-sec @ 100 KW

Charging current	15-50 A
Charging time	<2.5 minutes from discharge
Output discharge Voltage	400-520V DC , DC Ripple <2%
Flywheel operating speed	36750 rpm max.
Design life	20 years
Average Standby current consumption	1-3A DC
Weight	680 Kg (1500 lbs.) – single unit

Table 2-5 Vycon flywheel specification

Some of the major shortcomings of the Vycon flywheel energy storage flywheel system are due to the steel rotor. The use of a steel rotor results in a low energy to power density ratio and are much heavier than comparable flywheels. Hence, this design can be adopted by large scale applications only. Further it was observed that the rotor generated a lot of heat during nominal operation and also resulted in high windage losses.

2.3.6 Piller- Powerbridge

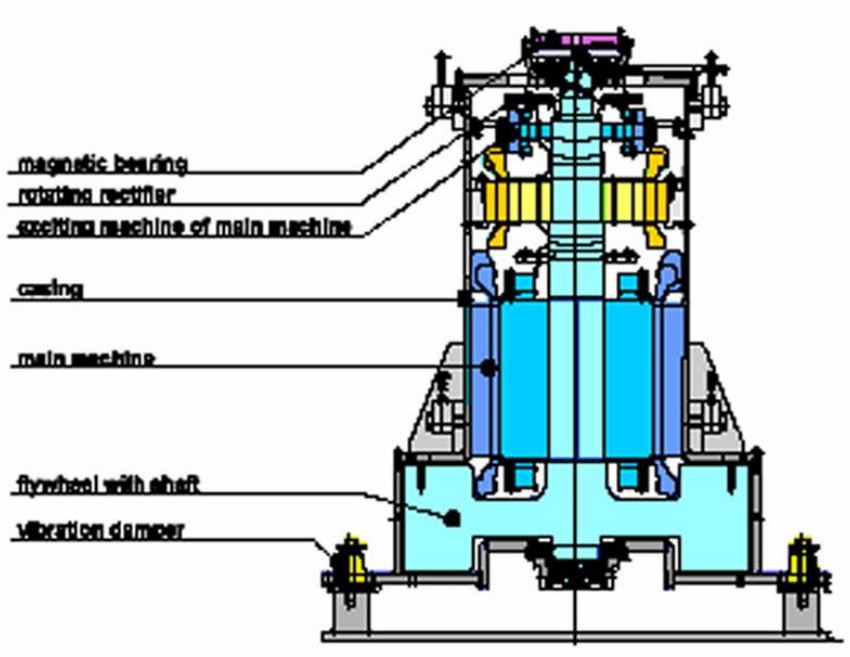

Figure 2-10 Piller-Powerbridge flywheel concept [41]

The Piller Powerbridge flywheel comprises of a steel rotor supported by magnetic bearings which operates between 1,500 rpm and 3,600 rpm. This flywheel uses a traditional design approach in which the rotor is coupled with a synchronous reluctance motor/generator system [41]. The concept of the Piller-Powerbridge flywheel is shown in figure 2-10. A single unit is capable of delivering power up to 2.4 MW. Many modules can be combined to achieve higher power. These flywheels are primarily used in load leveling and frequency regulation applications. The technical specifications of the flywheel are shown in table 2-6.

The Piller Powerbridge flywheel systems were not able to deliver efficient load regulation and suffered from severe vibration issues during operation. In addition, severe coupling issues between the rotor and the alternator were identified. A low speed of 3,600 rpm discourages use of this flywheel in high power applications.

Specification	Value
Capital Cost	$620/KW
Operational/Maintenance cost (Annual)	$7-$12/KW per year
Electricity cost / hour	$ 1.25/MW per hour
Output Power	Upto 21 MW (total with all units)
Charging time	<8 seconds from discharge
Output discharge Voltage	420-540V DC , DC Ripple <2%
Flywheel operating speed	3600 rpm
Design life	15 years

Table 2-6 Piller-Power bridge flywheel specifications

2.3.7 TSI Tribology systems

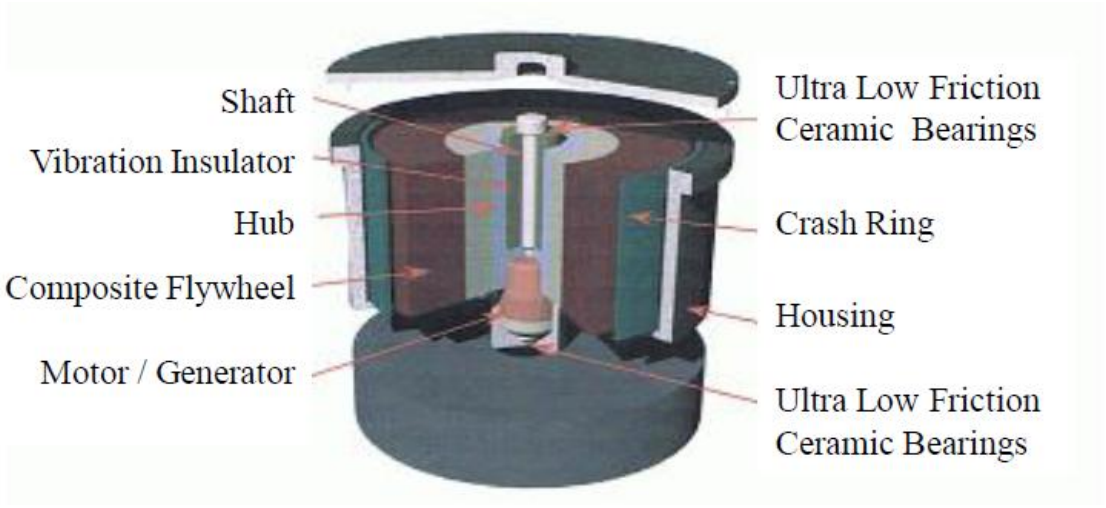

Figure 2-11 TSI Tribology flywheel concept [42]

The TSI tribology system comprises of a composite flywheel operating at 3,500 rpm which is supported by ceramic ball bearings. The ceramic ball bearings operate in vacuum. A crash ring has been designed around the rotor as a safety measure to withstand rotor failure. This is in addition to the housing system [42]. A schematic of the flywheel system is depicted in figure 2-11. The various technical specifications of the TSI tribology system is tabulated in table 2-7.

The use of ceramic ball bearings contributes to high losses, unreliability along with constant maintenance and replacement. Severe vibration issues were observed as the rotor operation was in the critical speed range. Even though a composite rotor is used, the operating speed of 3,500 is relatively low which discourages the uses of this flywheel in high power applications.

Specification	**Value**
Capital Cost	$960/KW
Operational/Maintenance cost (Annual)	$2-$3/KW per year (claims no maintenance needed for 10 years)
Electricity cost / hour	$ 1.25/MW per hour
Max. energy storage	1-5 KWhr
Charging current	10-50 A
Charging time	<10 minutes from discharge
Flywheel operating speed	3500 rpm max.
Design life	10-20 years

Table 2-7 TSI tribology flywheel specifications

2.3.8 AFS Trinity Systems

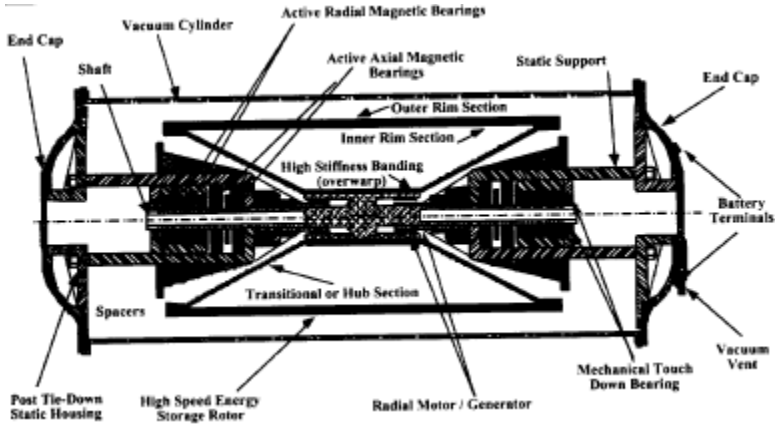

Figure 2-12 AFS trinity flywheel concept [43]

AFS Trinity Power Corporation had been working with flywheel technology but it is not on active business today. Although several kinds of flywheel designs have been developed by them, they have now moved into Ultra-capacitor technology as can be seen in their recent Extreme Hybrid^{TM} car. The most popular AFS design is depicted in the picture above (early 1990's). It comprises of an inner high speed energy storage rotor which is coupled to a radial motor/generator. Active radial and axial magnetic bearings are used to levitate the rotor. Much of their design cost is not known , so cost information in table 2-8 is estimated. The technical specifications can be summarized as below [43].

Specification	**Value**
Capital Cost	$420/KW (Projected in 1998)
Operational/Maintenance cost (Annual)	Unknown
Electricity cost / hour	$ 1.25/MW per hour
Max. energy storage	250-500 Whr

Charging current	Unknown
Charging time	<12 minutes from discharge (estimated)
Flywheel operating speed	7000 rpm max.
Design life	8-12 years

Table 2-8 AFS trinity flywheel specifications

As indicated previously, not much literature is accessible on the flywheel. They have moved into ultra-capacitor applications which indicate failure to implement their flywheel technology.

2.3.9 Critique of commercial flywheel systems

A summary of the critique of the commercial flywheel system is shown below.

Flywheel System	Critique
Beacon Power	1. Demagnetization issues due to the use of PM. 2. High weight to energy ratio. Heavier weight and larger footprint discourages small scale applications. 3. Even though it uses a composite rotor, the operating speed is only about 16,000 rpm. Hence, an optimal amount of energy is not stored in each module. 4. High initial cost discourages use with commercial small scale applications. 5. Poor Reliability and Unsafe design: two major accidents have been reported due to improper electronics design and abnormal heat issues.
Powerthru (formerly Pentadyne)	1. High acoustic noise, intense local saturation and high windage losses due to use of the synchronous reluctance motor-generator 2. The lower vacuum chamber was unable to maintain 0.0001 Pa vacuum which resulted in high aerodynamic drag. 3. The use of a titanium hub increases the cost of the overall flywheel 4. Poor power controls contributed to decreased motor/generator efficiency.
Kinetic Traction	1. The hydrodynamic bearings undergo severe wear during start up and hence had to be replaced quickly. 2. Poor rotor performance due to design of hydrodynamic bearings. 3. Composite rotor experienced heat issues and cannot be operated for long periods of time. 4. Uses relatively older power electronics technology and hence the energy storage / module is not optimum. High initial set up cost.
Active Power Systems	1. The use of a steel rotor at 7700 rpm results in low energy to power density ratio.

	2. The main issue with the flywheel was the inability to reduce the high aerodynamic noise and drag. 3. Poor motor commutation control and tuning. Heat issues have been documented along 4. High set up cost discourages use in small scale applications.
Vycon	1. Inability to maintain a 0.001 Pa vacuum resulted in high windage losses. 2.The use of a steel rotor results in low energy to power density ratio. 3. The design is most optimal for large scale applications only.
Piller Powerbridge system	1. The design is based on conventional flywheel design which results in severe coupling issues 2. Very low speed rotor (3600 rpm) discourages use in high power applications. 3. Inability to maintain efficient load regulation.
TSI Tribology systems	1. The use of ceramic ball bearings contributes to high losses, unreliability and constant maintenance and replacement. 2. Vibration issues observed during tests lead to the need of a vibration insulator. 3. Very low speed (3500 rpm) discourages use in high power applications.
AFS trinity systems	1. Not much literature is accessible on the flywheel. 2. They have moved into ultra-capacitor applications which indicate failure to implement their flywheel technology.

2.4 Past flywheel research

In addition to the commercial flywheel systems presented in Section 2.3, there were a good number of small scale flywheel research programs. In 1970, the investigations on flywheel based energy storage increased due to rising gasoline prices. Dr. Andrew Frank from the University of Wisconsin investigated the idea of using a very large flywheel to store substantial amounts of energy and allow engine off operation of buses [44]. Results showed up to 33% improvement in fuel economy by using the large flywheel as an energy buffer. Still, there were several other drawbacks that prevented the potential application of flywheel energy storage system in actual buses, for instance the need of a very heavy containment for the flywheel, the efficiency of the CVT system and the elevated bearing and windage losses.

In 1990, the potential of a Band Variable-Inertia Flywheel (BVIF) as an energy storage device for a diesel engine city bus was evaluated by Seattle University [45]. The results are compared with that of conventionally-powered bus. Based on their model, a fuel saving of up to 30 % is shown with the BVIF-integrated system. The regenerative braking system reduces brake wear by a factor of five in comparison with the conventional vehicle.

In research carried out by the collaboration of Jilin University of Technology and American Filtrono Co., a dynamic model of a high speed flywheel energy storage system is analyzed to study the characteristics of the system using time series. In order to retrieve this amount of energy, various feasible and efficient energy storage systems have been suggested by researchers to reuse the energy to improve the efficiency of the city buses. Finally, a comparison between simulation and experiment is given [46]. It was found that the simulations gave a good initial approximation of the design which was then fine-tuned by experimentation.

National University of Taiwan's research consists of conceptual vehicle hybrid power driving system consisting of an internal combustion engine, a motor, two continuously variable transmissions, a generator, a pulse width modulation electric controller, a planetary gear, and an energy storage flywheel. The flywheel drives a generator that generates electric power for the motor to drive the vehicle [47].

Dr. Barr and a team of researchers at the University of Warwick worked on mechanical hybrid project that included modeling, design and cost analysis [48]. The aim of the project is to assess alternative hybrid powertrains, in particular pneumatic, hydraulic and flywheel systems. They have documented a description of a simulation tool to investigate and evaluate the mechanical alternatives to electric hybrid vehicles and the results from two fuel economy case studies using the simulation tool: 2.6 ton SUV and 17 ton bus applications. They also outline a feasibility study of the mechanical hybrid options, including a cost benefit analysis of the different systems [48].

The University of Virginia had partnered with AFS Trinity Power System to develop a high speed flywheel; for potential use in space applications [49].The flywheel spun at a speed of 15000 rpm with a flexible rotor. A real time control and monitoring computer system was developed [50] and tested that achieved sufficient reliability and throughput to implement advanced state space controllers.

Ahrens and Larsonneur from ETH institute studied the performance of magnetically suspended flywheel energy storage [51]. They concluded that gyroscopic effects can drastically decrease system performance and can cause instability when a decentralized control system is used. Hall from the Air Force Institute of Technology presented results on attitude control of spacecraft using flywheels [52]. He deduced that 4 or more high speed flywheels can be used simultaneously to provide attitude control and energy storage. He concluded that a natural decoupling is possible using the singular value decomposition which allows the internal axial torques driving the rotors to perform attitude control and energy storage operations.

Rebeiro and Johnson described a flywheel energy storage system for advanced power applications in their work for the National Science Foundation and BWX technologies [53]. They show that flywheels can be integrated to power electronics converters to provide system stability, enhanced transmission capability and improved power quality. Jiancheng et al. discussed the potential use of a flywheel energy storage system in achieving high power quality [54]. He provides a design concept for a steel rotor based flywheel system and concludes that high efficiency can be made possible with choosing an effective control method.

Barton and Infield describe the potential use of flywheels with renewable energy [55]. They developed a simple probabilistic method to predict the ability of energy storage using a flywheel system in parallel to a wind turbine. They concluded that the addition of flywheels increases the capacity by 10% for every 10 minutes of use. Acarnley and Dickinson at the Newcastle University provides design principles of a flywheel energy storage for use in hybrid road vehicles [56] . They were able to design flywheel energy storage with 240 KJ of useable energy using magnetic bearings, brushless motor/generator system and a steel rotor. Similar work was done by Bangjie, Huang and Burtt who aimed at modeling a flywheel energy storage system for use in powertrain components [46, 47, 57-63]. Although they were able to design such a system, it was attributed with low efficiency and unresponsiveness.

2.5 Current flywheel research

The main research activity on flywheels is in the United States, where most manufacturers are located. The main activities are aimed at reducing the overall cost of flywheel systems, and reducing the losses and extending the life of bearings.

Lawrence Livermore Laboratory, where pioneering work was begun by Post in 1973, continues the development of passive magnetic bearings. Passive magnetic bearings have a long lifetime, do not require maintenance or lubrication, and have reduced frictional losses. Passive bearings are favored by Lawrence Livermore Laboratory because they are self-contained, unlike active magnetic bearings that require external electronics and electric power. However recent active magnetic bearing systems can also be self-contained [64].

Current research in the Composite Manufacturing Technology Center at Pennsylvania State University is aimed at developing a cost-effective manufacturing and fabrication process for advanced composite rotors. This includes the development of a rapid filament winding process for graphite fiber reinforced plastic (GRP) and carbon fiber reinforced plastic (CRP), the measurement of strain in high-speed rotors using opto-electronics devices, and the determination of fatigue behavior of composite rotor material using coupon tests [65, 66].

The NASA Glenn Research Center has an Aerospace Flywheel Development Program that aims to achieve a 5-fold increase in the specific energy of existing spacecraft batteries, and to achieve a 2-fold increase in battery life in low-earth orbit applications. A flywheel has been developed

and has achieved full-speed operation at 60000 rpm. Although this is targeted at spacecraft, it is possible that there will be technology transfer for other applications [67, 68].

The US DOE HEV program is considering flywheels for hybrid electric vehicle (HEV) applications. Flywheels could be used in HEVs in ways that exploit the ability to deliver very high power pulses. One concept combines a flywheel with a standard engine, providing assistance during acceleration, and absorbing braking energy. Another concept uses flywheels to replace chemical batteries, although the energy density of a flywheel system is generally considered to be too low [69, 70].

The Center for Electromechanics (CEM), University of Texas are involved in flywheel and alternator development for the Advanced Locomotive Propulsion System (ALPS), and leads the US Flywheel Safety and Containment Program, a consortium of several leading flywheel developers. Advances in high strength materials, rotor dynamics, containment, non-destructive evaluation, and thermal management, provides a technology base for much of the commercial development that is underway [71-73].

In addition, the CEM believe that compact flywheels are feasible with megawatt power and about 500 MJ (~140 kWh) stored energy, levels which are of interest for electric utility line stabilization.

A brief comparison between the various ongoing projects is shown in Table 2-9:

	University of Texas- Austin	Launch Point Technologies	Artemis Project	Michigan State University	Philip Medlicott, Ltd
Energy Storage Capacity	1 KW-hr	2KW-hr	500 W-hr	1 KW-hr	2KW-hr
Inner steel rotor present?	YES	NO	YES	YES	YES
Bearings	HTS superconducting bearings	Passive and Active Magnetic bearings	HTS superconduct-ing bearings	Active Magnetic bearings	Passive and Active Magnetic Bearings
Motor/Generator Type	Synchronous Reluctance type	Brushless, PM type	Brushless, PM type	Synchronous Reluctance type	Synchronous Reluctance type
Operating speed	10,000 rpm	12,000 rpm	30,000 rpm	25,000 rpm	15,000 rpm
Proposed Overall Weight	~200 Kg	~280 Kg	200-250 Kg	Not Specified	~230 Kg
Comments	The test rig failed because of bearing failure.	Failed due to detachment of the rotor components from the flywheel	Has not been built	Requires starter for the motor, excitation issues.	Demagnetization issues and cost due to PM material.

Table 2-9 Comparison between ongoing research projects

2.5.1 Non-contact bearings research

Bearings play an important part in the successful flywheel design. It has been established that non-contact bearings have a lot of advantages over mechanical bearings. There are different types of noncontact bearings, but the most widely accepted non-contact bearing solutions are high temperature superconductor bearings (HTS), passive magnetic bearings (PMBs), and active magnetic bearings (AMBs). The following paragraphs briefly explain the research work of each non-contact-type bearings.

2.5.1.1 HTS bearings

High temperature superconductor bearings (HTS) use the Meissner effect to stably levitate an object under magnetostatic equilibrium, similar to the way other diamagnetic materials are suspended. HTS bearings generate their own current and magnetic field in response to an externally applied magnetic field, in turn levitating the superconductive material above the externally applied magnetic field [74]. However, according to Mulcahy et al., "Although improvements in HTS processing continues, mass-levitation capabilities of HTS bearings are limited" [75]. This means that most HTS bearings can generate only a weak amount of force to support an object. Besides the insufficient force generated by HTS bearings for mass-levitation, they must be maintained at cryogenic temperatures, and the power that the cooling equipment consumes is a form of power loss. These two factors alone make HTS bearings less attractive bearing solutions compared to other widely accepted non-contact type bearing solutions.

Nexans Corporation is the first company that successfully tested an industrial sized superconductor bearing. Although HTS bearings are capable of operating in a vacuum environment, they usually require the bearing to be kept at or below 70 K. Because of this requirement, a constant supply of liquid nitrogen for cooling the bearing system is required. As a result, the system is difficult to be implemented for mobile applications or applications that require a small form-factor device. Although a flywheel rotor with a mass of 13.8 kg spinning at a rim speed of 420 m/s has been successfully levitated by a combination of PMB and HTS bearings [75, 76] , HTS bearings have proven to be difficult to maintain due to the requirements of a high uniform placement of the HTS bearing and a low temperature environment.

2.5.1.2 Passive magnetic bearings

Conceptually, passive magnetic bearings (PMB) may be the most optimum noncontact-type bearing solution that can provide near frictionless support to a body in motion without any power consumption. However, PMBs are inherently unstable as a consequence of the constraint imposed by Earnshaw's theorem [77]. This constraint combined with the intrinsically weak damping possessed by PMBs enforces a very stringent operational requirement, which often

leads to an impractical bearing support system. So far only a handful of studies have been conducted in regard to the use of PMBs, but one research project in particular (by Post and Smith) shows immense potential with the use of a PMB to support a flywheel energy storage system [77-79]. Despite the promise that PMBs show, as of this moment, there are currently no commercially available PMBs. To design as well as manufacture such bearings for commercial use will require great research and experimental efforts. The bearings are also anticipated to be responsive due to the raw material costs associated with rare earth elements. Therefore, the idea of using PMBs has not received as much attention compared to AMBs.

2.5.1.3 AMB research

Some of the existing flywheel energy storage systems that utilize AMBs to support the flywheel rotor are presented below; these flywheel energy storage systems are developed under either an industrial or an academic setting.

Active Power uses a combination of an AMB and mechanical bearings to support the flywheel rotor, and this rotor also serves as the rotor for the motor/generator. The AMB coils can also be integrated with the field coil of the homopolar inductor motor; this not only eliminates an extra set of coils, but also provides axial support to the flywheel rotor. The rest of the axial and radial supports are provided by the mechanical bearings [37].

VYCON proposes to use a combination of passive and active magnetic elements integrated into a single bearing unit to support a steel flywheel rotor. One design of this hybrid magnetic bearing structure possesses permanent-magnet-biasing to provide a constant bias-flux that linearizes the magnetic-force-current relationship in both the radial and axial directions. It has two sets of coils for generating restoring forces to support the load [26]. One coil is responsible for the radial control and the other coil is responsible for the axial control. In this design, the magnetic flux path taken by the control-flux differs from the magnetic flux path taken by the bias flux; because of this, the control-current efficiency is improved compared to configurations that have the control flux and the bias flux sharing the same path.

Launchpoint Technologies proposes the concept of "Power Ring", which can be designed and optimized to either provide a momentary, short duration of high electrical power, up to 153 MW RMS with 25 kWh of electrical energy storage capacity, or provide a long duration of electrical power up to 100 kW with 200 kWh of electrical energy storage capacity. This "Power Ring" is supported by a combination of permanent magnets and electromagnets [19, 80]. However, the presence of permanent magnets leads to possible demagnetization due to the temperature rise or the opposing magnetic field from the electromagnet [81]. Additionally, the cost and manufacturability of permanent magnets become more expensive and difficult as the size increases. So, having permanent magnets may not be the most optimal solution, especially for large scale flywheel energy storage systems [82].

Other academic projects have also demonstrated the effectiveness of AMBs used in the flywheel energy storage application. One example is a flywheel energy storage device that was designed to provide pulsed power for weapon systems and load leveling power for drive-train components used in hybrid electric combat vehicles. This flywheel employed AMBs to support a rotor having a mass of 595 kg (1310 lb) spinning at a rate of 20,000 rpm [83]. Another example is a miniature flywheel energy storage system that had an AMB supporting a 1.01 kg rotor. A flywheel energy storage device that had a 200 kg rotor spinning at a maximum rotation speed of 9000 rpm was also supported by an active magnetic radial bearing (AMRB); the analysis showed that the sum of the core loss and copper loss was less than 200 W [84]. Finally, a flywheel energy storage system that had an axial flux permanent magnet synchronous motor/generator integrated with an active magnetic thrust bearing (AMTB) was also proposed [85]; the goals of this design were to reduce the part counts and the system complexity. The results showed that the integration of a motor/generator with an AMTB is a viable design solution.

As can be seen from these examples, AMBs are crucial to the development and the continual advancement in flywheel energy storage systems. They have in fact become an integral part of the system. Furthermore, without AMBs, most of the flywheel energy storage systems would not exist.

2.5.2 Control Scheme Research

There are currently many control schemes that are being applied to control AMBs. Some of the more popular ones include the Fuzzy Logic based control scheme [86, 87], the Sliding Mode control scheme [88, 89] ,and the H-∞ control scheme[90, 91]. Despite numerous research efforts being put in the development of these innovative control schemes, ultimately, the proportional-integral-derivative (PID) control scheme has become an industry standard. The main reasons that contribute to the popularity of the PID control scheme include the effectiveness, the ease of implementation, as well as the proven history of successful and reliable utilization. Just as Zhang [92]and Chen [93] have stated, the PID control method is a simple yet effective control method that offers a maintainable and reliable means to control many existing systems.

A few of the research projects are given here to demonstrate the wide application range of the PID controller involving flywheel applications. Ritonja et al. [94] proposed using the decentralized PID control method to control four radial bearings and one axial active magnetic bearing to stably suspend a rotating shaft; the results showed that the use of a simple PID control algorithm can provide an adequate response to disturbances introduced by measurement devices. Zhang [92] proposed using a conventional PID control method to control three AMBs that were used to stabilize a flywheel rotor against translational and rotational motions; the results showed that the use of a PID control method can stabilize the flywheel rotor 0.9 s after it was disturbed from its equilibrium position. Pichot et al. [20] proposed using a PD compensator with the addition of a lead compensator and fixed frequency notch filters to control an AMRB that was used to stabilize a 595 kg flywheel rotor spinning at 20,000 rpm. The results showed that even with disturbances contributed by the sensor run out, sensor noise, mass imbalance, and inertial loading, the flywheel rotor operated stably over the entire nominal speed range (0 to 20,000 rpm). Zhang et al. [95] proposed using a PD compensator to control an axial flux permanent magnet synchronous motor/generator and an AMTB. The results showed promising potential for future implementations of this design in various flywheel energy storage systems. Chen [93] proposed using the Adaptive Genetic Algorithm (AGA) to fine tune the proportional, integral, and derivative gains of a PID controller to control a permanent-magnet-biased one-degree-of-freedom AMTB. These are just a few of the research projects that utilized the simplicity and

effectiveness of the PID control method. As can be seen from these research projects, the PID control method spans a wide range of applications.

2.5.3 Composites Research:

A primary area of flywheel research is in the use of composites as the rotor material. Lekhnitskii derived closed form solutions for radial and circumferential stresses in rotating, single and multi-ring composite rotors [96-98]. Huang et al. developed a similar Equation to Lekhnitskii's in order to determine the radial stresses of a polar woven rotor [47, 99-101]. Arnold et al. developed a set of unified solutions by incorporating several analytical methods to compute stresses and displacements under rotation, internal and external pressure, temperature variation and misfit for isotropic and anisotropic disks [14, 102]. These analytical solutions were used to identify the important parameters in the design of composite flywheel rotors. Advancements in Miner's rule and its modified versions resulted in a more complex and accurate fatigue analysis capability [103, 104]. Fisher and Lesieutre proposed health monitoring by detecting small changes in the balance state due to various types of flaws that can occur in composite flywheels [105]. Shiue, Lesieutre, and Bakis proposed a similar health monitoring scheme in which the balance state is monitored for changes due to small flaws in the flywheel [106].

Most of the groundwork for study of composite rotors was proposed by Giancarlo Genta in the 1980's. Some examples include bare filament rotors, cylindrical rings and profiled discs [107-111]. The cylinder rotor model proposed by Danfelt is credited as an interesting rotor concept [112]. It included thin layers of rubber in-between concentric layers of fiber composites in order to manipulate the radial stress distribution in the rotor. The topic had been carried forward by Portnov , although this approach does not seem to have found practical application in industry yet [113]. In another recent work, Fabien studied cylindrical rotors with some of the fibers oriented in the radial direction [114]. These rotors have also not been widely applied in industry, probably due to the difficulty of manufacturing them. Notable research in this field included that done by Sung Kyu Ha, who developed an analytical model for analysing the stress distribution inside a cylindrically wound composite rotor [115]. He showed how this model could be used when searching for an optimal distribution of material layers inside a rotor and also highlighted the importance of considering residual stresses from curing in such an analysis [115].

An important contribution by Andrew Arvin was made by noting that it can be advantageous to arrange materials in a cylindrical rotor in such a way that the specific stiffness increases with radius [107, 116, 117]. In fact, this is routinely found in practice and, in line with the methods of other authors such as [118, 119], Arvin's study disregards material sequences that do not result in increasing specific stiffness with radius. However, there does not seem not be any rigorous proof that this approach is always advantageous, and further research may therefore be warranted. Ha made another important contribution by showing that an optimal design, when scaled geometrically, remains optimal [120]. This is of great use, as it implies that a design problem can be solved to find a whole family of optimal rotors, from which a designer can choose one that suits the scale of the particular application.

Most recently, Pérez-Aparicio has proposed another analytical model for evaluating stress in composite cylinders [121].This model aims to take into account the effect of a hub while also providing for the effect of non-uniform curing and moisture absorption during the lifetime of the composite part.

2.5.4 Applications research

Although flywheels are not yet widespread in the power industry, they are slowly penetrating the market. They are used mostly for uninterruptible power supplies, power conditioning and pulse power, and are starting to be used with VRES. For example, a 5 kW-hr, 200 kW, flywheel is used to stabilize the 10 household grids in Utsira, Norway, in a wind-hydrogen system [122]. In addition, Urenco Power Technologies has also installed some flywheels for smoothing wind turbine output and stabilizing of a small-scale island wind supply [123]. Beacon Power claims that flywheels can be used for cloud cover effects mitigation for solar photovoltaic by preventing voltage disturbances, and as an energy buffer for mitigating wind power ramping [124]. Strategies have been suggested to combine the characteristics of flywheels, i.e., fast ramping and low energy, with another device, such as PHS, hydrogen, or diesel to remove the weaknesses of both devices for better VRES integration [122, 123, 125]. A unique strategy only applicable to wind is to use the rotating wind turbines as flywheels to remove the frequency variations to which the grid is susceptible [126].

Another major area of flywheel research is in the development of hybrid cars. Some of the most mature uses of flywheel technology in light-duty vehicles have occurred in European racing (Formula 1, Nurburgring Long Distance, and LeMans). Williams Hybrid Power Limited (WHP), Flybrid Systems LLP, and Ricardo UK Ltd (Ricardo) all in the United Kingdom, have developed Kinetic Energy Recovery System (KERS) flywheel units for racing that are currently being evaluated for mass produced road vehicles [127-129]. The WHP system makes use of a motor/generator incorporating its novel, patented Magnetically Loaded Composite (MLC) technology which was originally developed by Urenco engineers working on the design of uranium centrifuge machines [130] . The Flybrid and Ricardo flywheel systems use a mechanical powertrain [131]. The Flybrid flywheel is connected to the transmission of the vehicle via either a Continuously Variable Transmission (CVT) or a Clutched Flywheel Transmission (CFT), and manipulation of the transmission ratio achieves control of energy storage and recovery [131]. The Ricardo Kinergy flywheel concept features a flywheel in a hermetically-sealed vacuum/containment vessel, and the flywheel is magnetically coupled to a CVT [132].

In summary, flywheel research has been moving at a steady pace over the last few decades. There is a recognized need for the use of a clean and efficient energy storage method with flywheels being considered as a strong potential candidate. Researchers have focused on developing different modules of the flywheel like alternator, magnetic bearings, composites and power electronics. However, there has not been any major work attributed to the preliminary design phase of the entire flywheel energy storage system. Choosing and putting together all the different components and designing the entire system is a challenge due to the multi-disciplinary nature of the problem. The work done in this thesis is to design individual components of the flywheel system and understand the system behavior in its entirety.

3 ROMAC Flywheel Design Characteristics

An overview of the flywheel design developed for this thesis is presented in this chapter. The different components of the ROMAC flywheel along with their potential applications are discussed. Preliminary sizing calculations and various limitations to the design and are shown in this chapter.

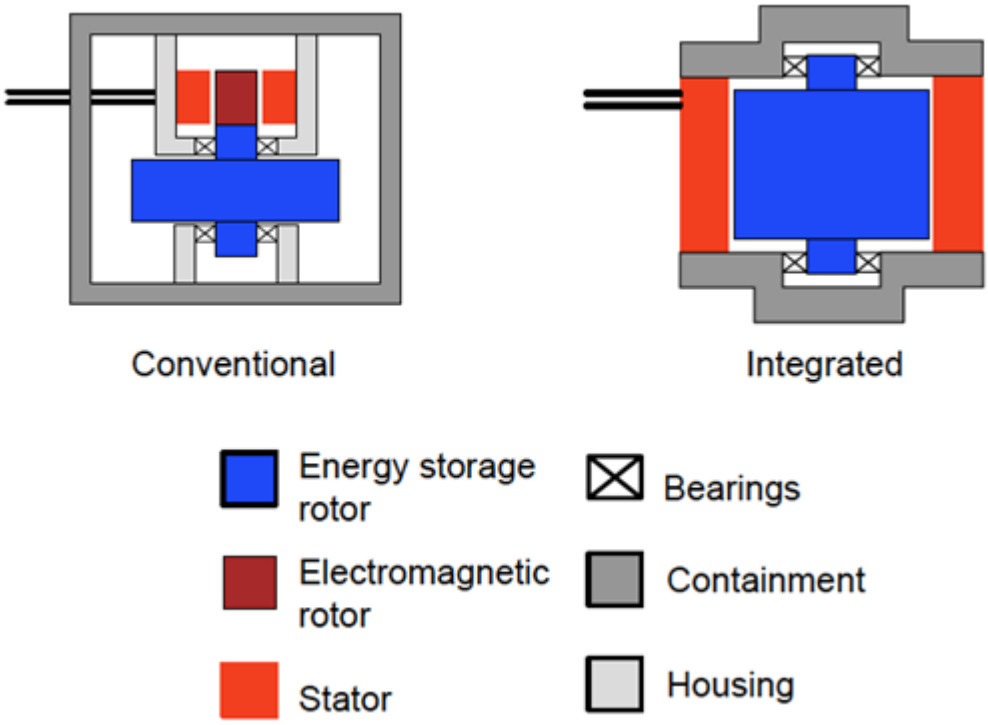

Figure 3-1 Basic Design configurations of FES systems.

Commercially, there are two basic design configurations of FES systems: a conventional design and an integrated design. In the "conventional design," the rotor has a large diameter section, where most of the kinetic energy is stored, attached to a smaller diameter section, which is used by the motor to spin the flywheel. This is the most common design. However, this configuration tends to have a larger housing and containment structure because of the additional rotor length. This results in a very heavy flywheel configuration which can be expensive to manufacture. The

second configuration is an “integrated design” in which the electromagnetic and energy storage portions of the rotor are combined. This type of design is found in newer generation flywheels but is not well suited for composite rotor flywheels because of the need for electromagnetic material for torque production. However, in the integrated configuration, the housing and stator of the motor comprise a large portion of the vacuum and burst containment for the flywheel. A typical 1kW-hr integrated flywheel weighs about 200 -250 Kg.

The ROMAC flywheel design is a hybrid design combining the integrated design into an inside-out barrel type system. It comprises of a permanent magnet synchronous machine and a composite rotor supported by 4 magnetic bearings – 2 thrust and 2 radial. Tapered rolling element bearings are used as the back-up bearings. A detailed description of the ROMAC flywheel design and the various components are presented below.

3.1 Proposed Flywheel Design

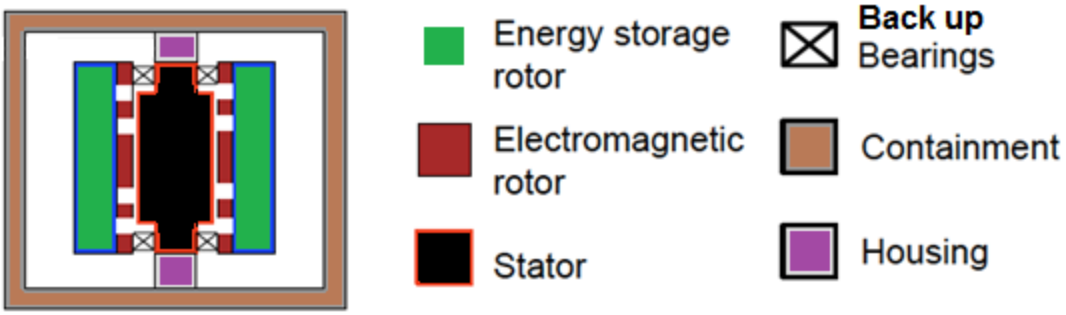

Figure 3-2 Schematic of the ROMAC flywheel energy storage system.

Figure 3-1 depicts a schematic of the ROMAC flywheel design. The flywheel is designed to have an energy storage capacity of about 1 kW-hr. This is an inside-out barrel type design in which the stator (shown in black) lies at the center. At the heart of the flywheel energy storage system is an integrated composite rotor (shown in blue). This rotor performs the function of the energy storing flywheel as well as the motor/generator system. The rotor is supported with two radial bearings and a double-acting thrust bearing. The design is conceived in such a way that all of the stator components have the same inner diameter. This ensures that they can be attached easily to a single back iron. Similarly, the rotor components are designed to have the same outer diameter. The rotor part of the bearings and the motor-generator system are attached to the composite

flywheel with two steel spline rings. The main purpose of this spline ring is to account for high tangential stresses on the composite and to prevent withdrawal of the rotor components when the flywheel rotates at high speed. Four-row tapered rolling element bearings will be used as back up bearings. The entire flywheel energy storage system will be operated in vacuum. This is done to reduce parasitic losses which results in an increase of overall electromechanical efficiency. The weight savings from this type of design could drive the overall flywheel cost down by about 15%~20%, and additional advantages include lower component count, reduced material costs, lower mechanical complexity, and reduced manufacturing costs. Furthermore, the use of a smaller clearance vacuum housing over the flywheel can help maintain a more effective vacuum containment.

3.1.1 Different components of ROMAC flywheel design

The different components of the ROMAC flywheel design is discussed in the following sections:

3.1.1.1 Alternator:

The key function of the alternator is during charging and discharging of the flywheel. When the flywheel is being charged, the alternator should function as a motor to accelerate the flywheel and store energy kinetically. During discharge – the alternator should behave as a generator , producing electricity using the stored kinetic energy. Traditional FES systems use a separate motor and generator system while modern ones use a single machine. The proposed flywheel design will use the same rotor to be the motor, generator and the flywheel energy storage. Designing such an alternator must include high efficiency, high power density, low idling speed and minimal rotor losses. Low rotor losses are critical due to limited heat dissipation. This is particularly important since most FES systems operate in vacuum. A flywheel cycle switches between charging and discharging modes over short durations of time. Hence low stand-by losses are desirable for energy storage over longer idling times. High efficiency is an obvious important requirement for an effective energy storage system.

The three most common electrical machines that have been used in FES systems are : permanent magnet synchronous machine (PMSM), induction machine (IM) and switched reluctance machine (SR). The pros and cons associated with these machines are presented in Table 3-1

Machine Type	Advantages	Disadvantages
Induction Machine (IM)	• Can be built using high strength-low cost materials. • No Demagnetization issues. • Ability to control excitation field with no electromagnetic spinning losses	• The starting current may be five to eight times the full load current • The speed is not easily controlled • Low power factor and high maintenance
Switched reluctance (SR)	• Very robust because rotor has no windings or slip rings • More power per unit weight and volume • Can run at high speed in hazardous atmosphere	• Noisy • Relatively unproven • High eddy current losses • Low power factor
Permanent magnet synchronous machine (PMSM)	• Low noise and vibration SR's and IMs • Operates at a higher power factor compared to induction motor (IM) due to the absence of magnetizing current. • Doesn't require regular brush maintenance like conventional wound synchronous machines • Lower rotor inertia and hence fast response • Larger energy density and compact structure • No need of excitation and high overall efficiency	• High cost of Permanent magnets • Demagnetization issues and temperature sensitivity

Table 3-1 Comparison between different motor types

Due to the advantages of the PMSM over their counterparts, they have been a good choice for high speed variable torque machines. The ROMAC flywheel alternator design is also a PMSM type. The design is done in such a way that the alternator is integrated with the flywheel energy storage rotor.

3.1.1.2 Bearings

One of the critical design aspects for optimum flywheel operation is the design of the bearings. Bearings should be designed to have low frictional and electromagnetic losses to maintain flywheel efficiency. The ROMAC flywheel consists of 2 radial and 2 thrust magnetic bearings in addition to a standard PID controller. Four-row tapered rolling element bearings will be used as back up bearings.

Magnetic bearings are the ideal choice when it comes to flywheel design. These bearings allow the rotor assembly to rotate at very high speeds with no physical contact with stationary components during normal operation, thereby taking advantage of the high efficiencies obtainable with flywheels, typically around 95%. This is achieved by levitating the rotating assembly through the force of a magnetic field. Further, the controller for the bearings can be designed to take in sudden speed changes. In addition to these advantages, magnetic bearings do not require lubrication, can operate in vacuum and have very long life periods. All these factors make magnetic bearings one of the crucial components in a high speed high efficiency flywheel energy storage system design.

Traditional slow speed FES systems use mechanical bearings to support the rotor. This is because of their low initial cost and relatively simple installation procedure. However, such bearings provide relatively high friction in addition to their easy wear and tear and cannot be used with high speed rotors. Further, maintenance and periodic lubrication requirements discourage use of these bearings with newer FES systems. High speed flywheels operate in a low pressure environment under vacuum, therefore mechanical bearings are very hard to implement.

There is a lot of interest in the potential use of passive high temperature superconducting (HTS) bearings for high speed rotors. The main attractive features of HTS bearings are low losses and the convenience of not having to have a separate control system. However, it should be noted

that implementation of HTS bearings requires an additional cryogenic cooling system to maintain bearing temperature in the superconducting region. Such a system is impractical to operate in a vacuum low pressure environment with limited heat dissipation. However, there is a lot of research in this field to potentially use them in FES and other high speed systems.

A summary of the three types of bearings is discussed in Table 3-2:

Bearing type	Power loss	Advantages	Disadvantages
Mechanical	10-250 W	Low cost, simple and compact design	High friction, requires periodic replacement and high maintenance
HTS	10-60 W	Low losses, ability to withstand high forces, no controller required	Requires cryogenic cooling, relatively unreliable for flywheel applications
Magnetic	10-100 W	No friction and contact , no maintenance, ability to withstand high forces, proven reliability, very long life	Requires additional controller and back up bearings, high initial cost

Table 3-2 Comparison between mechanical , HTS and magnetic bearings.

3.1.1.3 Choice of Rotor material

The proposed flywheel energy system will comprise of a light weight carbon- epoxy composite rotor. The faster we can spin a flywheel the more kinetic energy we can store in it ($E= ½ J\omega^2$). However, at extreme speeds, metal flywheels can literally tear themselves apart from the centrifugal forces that are generated. Further, the energy storage characteristics of the flywheel are influenced more strongly by its maximal rotational velocity than by its mass. A stronger, lighter flywheel may be able to store as much or more energy than its metallic counterpart. It is for this reason that newer flywheels are made out of composite materials. Furthermore, composite flywheels have higher efficiencies and higher energy densities and can be designed for benign failure modes.

3.1.1.4 Power Electronics

Power electronics helps to provide a control interface between the alternator and the power transfer interface. There are two main components which make up the power electronic interface: the bidirectional inverter/converter and a variable speed drive. Power is transferred to and from the flywheel via a DC link. When power is needed to transfer to an AC grid, another bi-directional converter is used. Depending upon the application, the converter may be single staged (AC-DC) or double staged (AC-DC-AC). Another important function of the power electronics is to act as means to convert AC current to a constant frequency. This is particularly useful when the flywheel operates in the generator mode - producing AC current with decreasing frequencies. Depending on the application the controls of the power electronic interface may vary. The proposed FES system is designed to be interconnected with an AC grid. Hence both active and reactive power control is needed.

Design goals for such an interface will require the power electronic system to be of a high power capability with high efficiency, low electrical losses and high switching frequencies. The converter for the proposed FES design will be based on insulated-gate bipolar transistors (IGBT's). This would make the entire system very compact and efficient.

3.1.1.5 Housing

One of the most important design parameters of a FES system is the overall flywheel efficiency. In order to keep the overall efficiency up, the rotor and stator losses have to be minimized. The main contributor to total system losses is the aerodynamic drag loss. As will be shown in section 8, the aerodynamic drag losses are directly proportional to the cube of the rotational speed. For a high speed flywheel, reduction of these losses is the most effective way to keeping the total system losses at a minimum. The most common solution to this is to mount the flywheel in a vacuum chamber. As a result, the air drag is eliminated and hence the losses are reduced. Another approach to reduce aerodynamic drag would be to operate the flywheel in low pressure using a gas mixture of helium and air. Mounting a flywheel in a vacuum chamber also reduces

the risk of damage and destruction to the people or the surroundings during rotor failure. If the rotor breaks apart, the housing chamber should be able to stop the free flying projectiles.

The housing of the ROMAC FES system will be made up of high strength steel. In order to enhance safety during rotor failure, there will be two layers of housing. The FES system will be installed underground and hence the thick steel casing can provide a first layer of protection while the underground installation will act as the second barrier. Even though this may drive up the installation costs – it is a necessity from a safety perspective.

3.1.2 Proposed Applications of ROMAC flywheel

The successful design of a low cost compact flywheel will find many applications in a variety of fields. The 1 KW-hr storage capacity can be scaled to higher energy ratings or multiple units can be put together for higher demand applications. A few proposed applications include:

Electric energy time shift: Energy is purchased during off-peak hours when prices are low and sold at a time when price is high. The stored energy can be used by the storage owner to avoid expensive energy purchase during hours of high demand. In addition, flywheels can be used in conjunction with renewable energy sources to save even more.

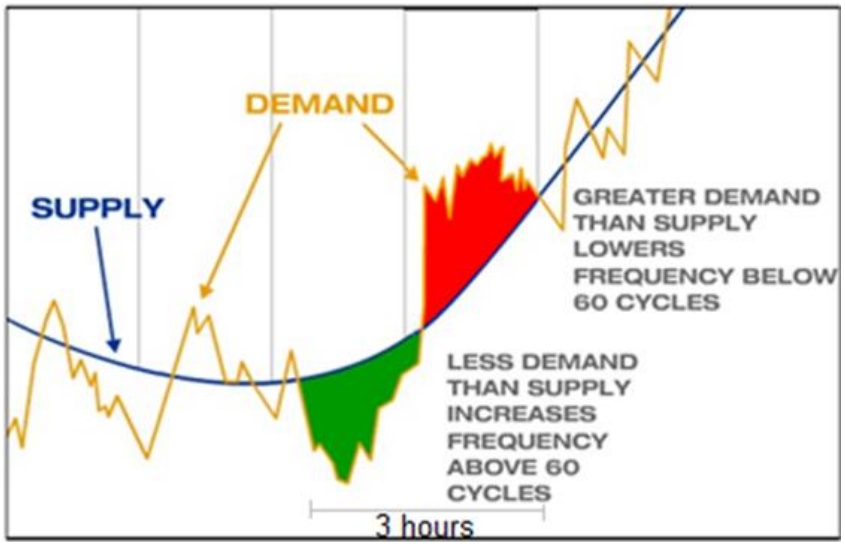

Figure 3-3 Energy supply vs demand within a 3 hour duration

Power Quality : The proposed FES system can be used to improve the quality of power to loads during short duration (in the order of second or minutes) faults in the electrical system. Examples of poor power quality that can be improved include voltage sags, harmonics and angular instability.

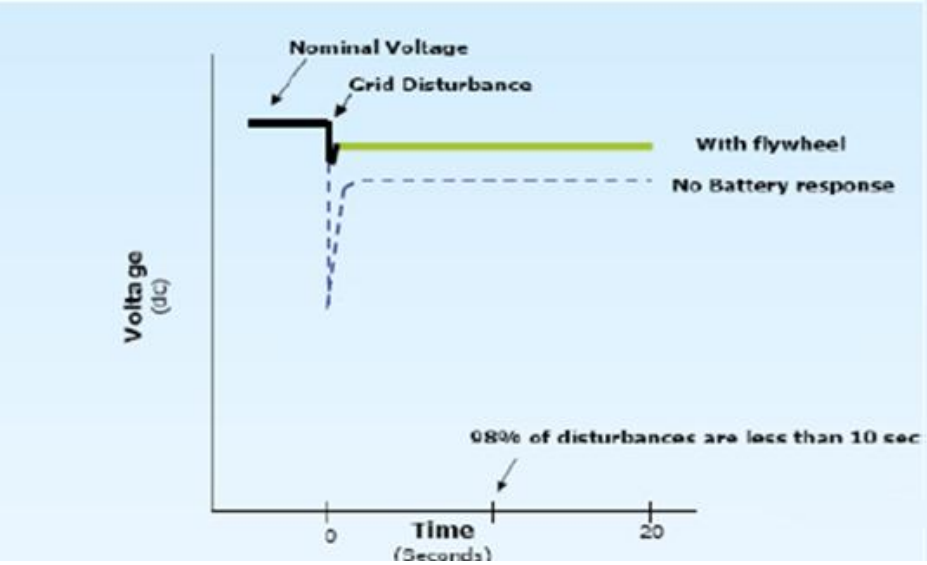

Figure 3-4 Flywheel vs Battery response

UPS systems : A related application that is in high demand today is UPS systems. The proposed flywheel system can be used as a UPS system due to its high responsiveness and much faster charge/discharge cycle. A comparison between flywheel and battery response is depicted in Figure 3-4

Brake Regeneration and Hybrid cars: A compact low weight flywheel has potential for use in hybrid cars and trains. Energy, during braking, can be transferred to the FES system which can be returned to the drive system during peak demand. Such a system would improve fuel efficiency of cars and would make use of the energy currently lost as heat.

3.2 Major limiting factors of flywheel design

Flywheels typically operate at very high speeds ranging from 3,000 to 40,000 rpm depending on the specific application. Hence designing a safe flywheel is an integral part for efficient energy storage. The energy-storage capacity of a flywheel is determined from its polar moment of inertia and its maximum safe running speed.

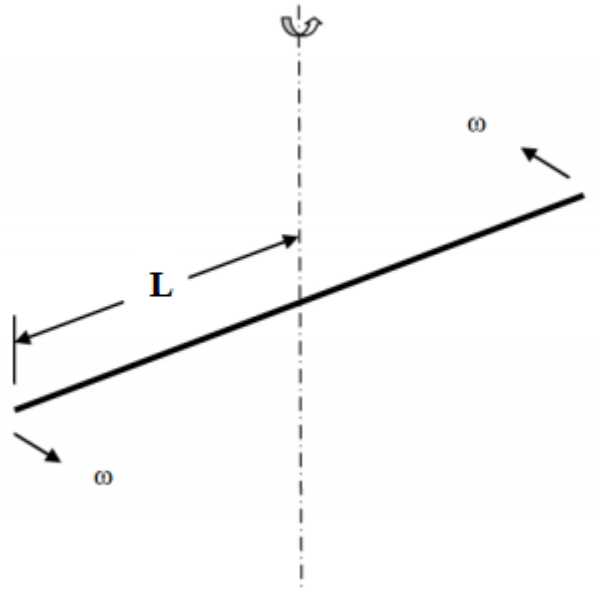

Figure 3-5. A schematic of a straight filament rotating around a vertical axis.

Consider an energy storage capability of a straight filament of length 2L rotating around a vertical axis at a rotational speed ω. This is shown in Figure 3-5. This is a simplified model of the composite rotor, in which many filaments are wound. The model gives us a quick and effective 1st cut approximation of the parameters involved. The kinetic energy of such a system can be given in terms of the moment of inertia, I and the rotational speed ω as:

$$E_K = \frac{1}{2} I \omega^2 \qquad \textbf{(3-1)}$$

Assuming a thin rod with weight W, the polar moment of inertia about the spin axis can be given as

$$I = \frac{L^2 W}{3g} \qquad \textbf{(3-2)}$$

From Equation ((3-2) we can deduce that the energy storage capability of a rotating thin filament depends on its weight, length and rotational speed. In a flywheel, the specific energy storage capacity is of utmost importance and can be written for Figure 3-5 as

$$\frac{E}{W} = \frac{1}{2}\frac{I\omega^2}{W} = \frac{R^2\omega^2}{6g} \qquad \textbf{(3-3)}$$

In terms of material properties, Equation ((3-3) can be expressed as

$$\frac{E}{W} = \frac{\sigma^2}{3\rho} \qquad \textbf{(3-4)}$$

Deducing from Equation (3-4) the two major limiting factors of a flywheel design are

(a) Strength of the flywheel material

(b) Density of the flywheel material

Another important limiting factor in flywheel design is the coefficient of speed fluctuation, C_f which is defined as

$$C_f = \frac{\omega_{max} - \omega_{min}}{\omega} \qquad \textbf{(3-5)}$$

For a high speed energy storage application, this value is taken between 0.3 and 0.6. The flywheel limiting speeds are calculated based on this coefficient.

The most important limitation in a flywheel design is the centrifugal stresses which acts upon its distributed mass and acts to pull it apart. This effect is analogous to that observed in an internally pressurized cylinder. The Equations for the tensile and radial stresses are given as

$$\sigma_t = \frac{\rho}{g}\omega^2\left(\frac{3+\vartheta}{8}\right)\left(r_i^2 + r_o^2 - \frac{1+3\vartheta}{3+\vartheta}r^2\right) \qquad \textbf{(3-6)}$$

$$\sigma_r = \frac{\rho}{g}\omega^2\left(\frac{3+\vartheta}{8}\right)\left(r_i^2 + r_o^2 - \frac{r_i^2 r_o^2}{r^2} - r^2\right) \qquad \textit{(3-7)}$$

As it can be seen from Equations (3-6) and ((3-7), both the tangential and radial component of stresses are directly proportional to the square of the rotational speed. This limits the maximum rotational speed of the flywheel. However, it can also be seen from Equation (3-3) that the faster the flywheel rotates, the more energy can be stored in it.

The point of utmost interest is the inner radius where the stress is maximum. The radial component of stress are quite often well within the material properties. The typical reason for flywheel failure is the tangential stress overload which when reached results in fracture. Since the forces causing the stress are a function of the rotational speed, rather than checking the stresses, the maximum speed at which the stresses reach the critical value is computed and safe operating speed is specified based on a safety factor. The safety factor typically employed in flywheel stress calculations is 3 to 5 (2 for rotor burst testing).

$$Safety\ Factor = \frac{\omega}{\omega_{yield}} \cong 3 \sim 5 \qquad \textit{(3-8)}$$

Table 3-3 shows the typical flywheel materials employed today along with their typical properties.

Material	**Density [g/cm^3]**	**Maximum peripheral speed [m/s]**	**Tensile Strength [N/mm^2]**	**Tensile strength to density ratio**
Carbon fiber composite	1.7	> 800	2000	1176.47
Glass fiber composite	2.0	600	700	350
Maraging steel, superhard alloy	8.0	525	2250	281.25

High strength steel	8.0	455	1700	212.50
Titanium	4.6	440	920	200
High strength aluminum alloy	2.8	425	520	185.71

Table 3-3. Suitable flywheel material candidates

Another common flywheel design practice is to use a "ID/OD ratio"(λ) for computations. The maximum energy stored in a flywheel in terms of λ can be given as

$$E_{max} = \lambda \times V_{rim} \times \sigma_t \quad \textbf{(3-9)}$$

Where V_{rim} = rim volume and σ_t = tensile stress. The ratio λ is defined as

$$\lambda = \frac{1}{4}\frac{\left[1-\left(\frac{ID}{OD}\right)^4\right]}{\left[1-\left(\frac{ID}{OD}\right)^2\right]} \quad \textbf{(3-10)}$$

Two useful concepts that can be developed from this are Max energy/weight and max. energy/ volume.

$$\frac{E_{max}}{W} = \frac{\lambda \sigma_{t.max}}{\rho_{rim}} \quad \textbf{(3-11)}$$

$$\frac{E_{max}}{V} = \frac{1}{4}\left[1-\left(\frac{ID}{OD}\right)^4\right]\sigma_{t.max} \quad \textbf{(3-12)}$$

Normalized maximum energy to weight and energy to volume ratios vs ID/OD ratio are plotted in Figure 3-6. It can be observed that as the energy to weight ratio increases with increasing ID/OD ratio while the energy to volume ratio decreases. A good compromise typically used in industry is ID/OD = 0.5 to 0.75 when the space inside the rim is used for the motor/generator. High energy-to-weight ratio is a more important factor than energy-to-volume, particularly for a thin-wall (lightweight) vacuum enclosure.

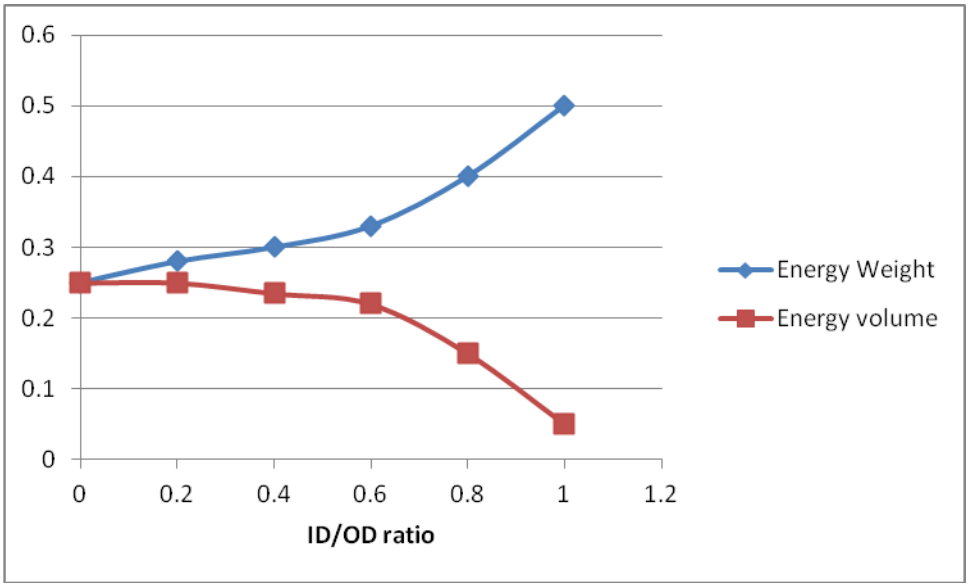

Figure 3-6. Plot of Energy/weight and energy/volume against ID/OD ratio

Two significant observations can be made from these Equations: Flywheel weight/energy ratio is proportional to its density (specific gravity). And energy storage is proportional to the product of tensile strength and volume of material at full tensile stress. So, to achieve high energy storage with light weight, rim material should be high-strength and low-density. The ROMAC flywheel is designed with an ID/OD ratio of 0.54 as a safe compromise between energy weight and volume.

3.3 Preliminary sizing of the flywheel

This section describes the most important parameters needed for a preliminary sizing of the flywheel.

3.3.1 Energy density and specific energy

The first step in the design process was to perform an initial sizing of the flywheel. This step is crucial as it can give us an initial estimate of the flywheel dimensions. Using the estimate, the different components of the FES system could be designed.

Considering a cylindrical rotor made from a material of density ρ and having an outer and inner radius of r_o and r_i respectively with a height h the energy stored in a flywheel is written as:

$$E_{kin} = \frac{1}{4}\rho\pi h(r_o^4 - r_i^4)\omega^2 \qquad \textbf{(3-13)}$$

From Equation (3-13), it is evident that the stored energy scales with the square of the angular velocity, and hence high rotational speeds are desired. The Equation also shows that the rotor diameter has an even greater influence on kinetic energy. However, the amount of stored energy is limited by the tensile strength of the material. A good design of the flywheel will ensure that the stresses produced in the flywheel will be below the ultimate tensile strength of the material using a safety factor of 2 to 3. Considering a thin rim flywheel design, the tangential stress can be given as

$$\sigma_{max,tensile} = \rho r^2 \omega^2 \qquad \textbf{(3-14)}$$

It can be shown that the product of maximum rotor radius and angular velocity is dependent on the square root of the specific strength of the rotor material.

$$r_{o,max}\,\omega = \sqrt{\frac{S_\varphi}{\rho}} \qquad \textbf{(3-15)}$$

Using Equations (3-13) and (3-14) the maximum energy density and specific energy for a given material can be deduced. For the case of a thin rim flywheel, the specific energy ($E_{s,e}$) and energy density ($E_{s,\rho}$) can be written as

$$E_{s,e} = \frac{1}{2}\frac{\sigma_{max,tensile}}{\rho} \qquad \textbf{(3-16)}$$

$$E_{s,\rho} = \frac{1}{2}\sigma_{max,tensile} \qquad \textbf{(3-17)}$$

From Equation (3-17), it is evident that in order to obtain high energy density, a material with high tensile strength has to be chosen. However, for most applications the total mass of the system must also be taken into account. This is shown in Equation (3-16). For a thin rim flywheel, it can be deduced that the specific energy is proportional to the maximum tensile stress of the material and inversely proportional to the mass density of the flywheel material. Fiber

composites far exceed metal counterparts in this regard. This can be deduced from Figure 3-7 which shows a comparison between the specific energy of various materials.

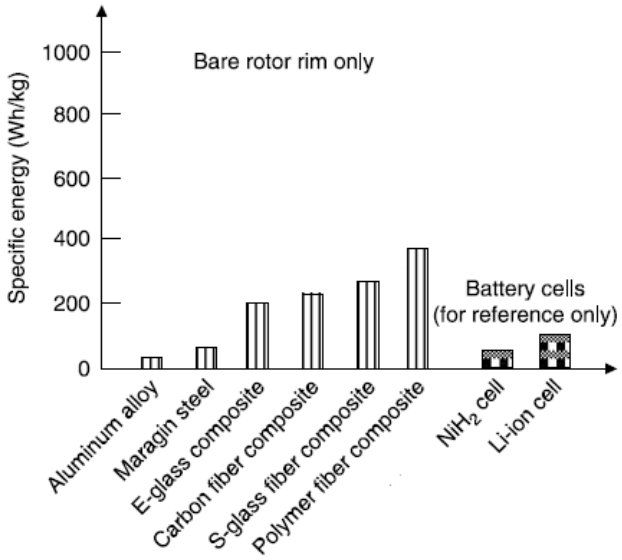

Figure 3-7 Theoretical maximum specific energy for various materials

Hence a high strength material with low density fiber-reinforced polymer composite filament wound in the circumferential direction would be optimal for flywheel rotors.

For the 1KWhr flywheel energy storage design, Equations (3-1) to (3-17) were used for the preliminary sizing. A carbon fiber epoxy composite was chosen as the flywheel material. The maximum hoop stress was kept at $2/3^{rd}$ of the ultimate tensile stress. The first objective was to compute an initial estimate of the flywheel rotor dimensions. The input parameters are shown in Table 3-4:

Input Parameters	**Value**
Targeted Energy storage (E_{max})	1 kW-hr
Material density (ρ) : Carbon Epoxy	1605 kg/m^3
Youngs modulus (E_{young})	160 GPa
Poisson's ratio	0.8
Angular velocity	40,000 rpm
Ultimate tensile stress (σ_{ult})	3.2 GPa

Table 3-4 Input Parameters in determining initial flywheel size

Based on the work done by Covao et al. the initial relationships between inner diameter (D_i), outer diameter (D_o) and height (h) for the 1KWhr case can be taken as [133]

$$D_o = 0.9h \quad \textbf{(3-18)}$$

$$D_o - D_i \geq 100\ mm \quad \textbf{(3-19)}$$

Based on the above Equations, the initial dimensions of the composite flywheel were calculated and are tabulated in Table 3-5

Parameter	Value
Outer diameter of the flywheel (D_o)	420 mm
Inner diameter of the flywheel (D_i)	230 mm
Height of the flywheel (h)	400 mm

Table 3-5 Initial flywheel parameters.

Different values of composite material strengths and properties were used to study the relationship between specific energy, mass and ultimate strength by mass density ratio. Figure 3-8 captures this relationship.

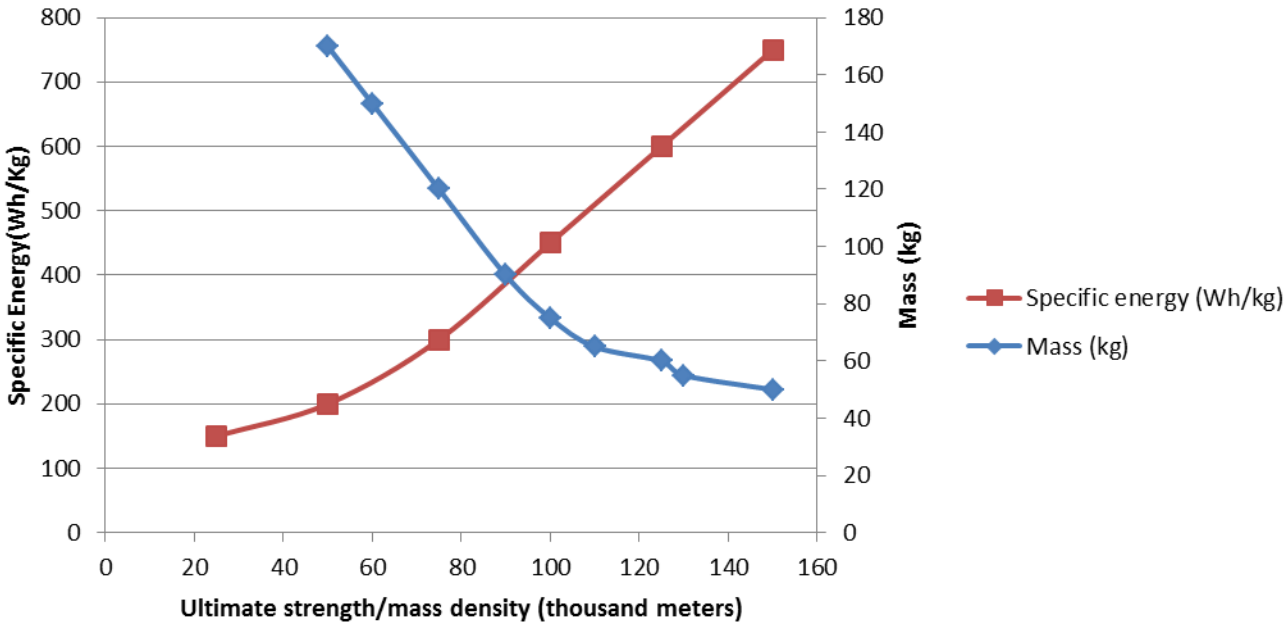

Figure 3-8 Specific energy and mass of 1Kw-hr flywheel vs Ultimate strength/mass density.

A specific energy of 60-120 Wh/Kg has been demonstrated at the rotor level for a 1KWhr flywheel rotating at 40,000 rpm.

3.4 Preliminary check

Having obtained the initial flywheel size, a simple stress analysis was conducted to ensure that it does not fail at the current dimensions. The simple stress analysis was done using ANSYS and assuming a generic carbon fiber epoxy as the rotor material.The stress analysis showed that at an operating speed of 40,000 rpm, the maximum stress obtained was about 2.61×10^{8} Pa which is well within the ultimate tensile stress of the composite material . Figure 3-9 shows a section of the 3D model created in ANSYS to run the simulation.

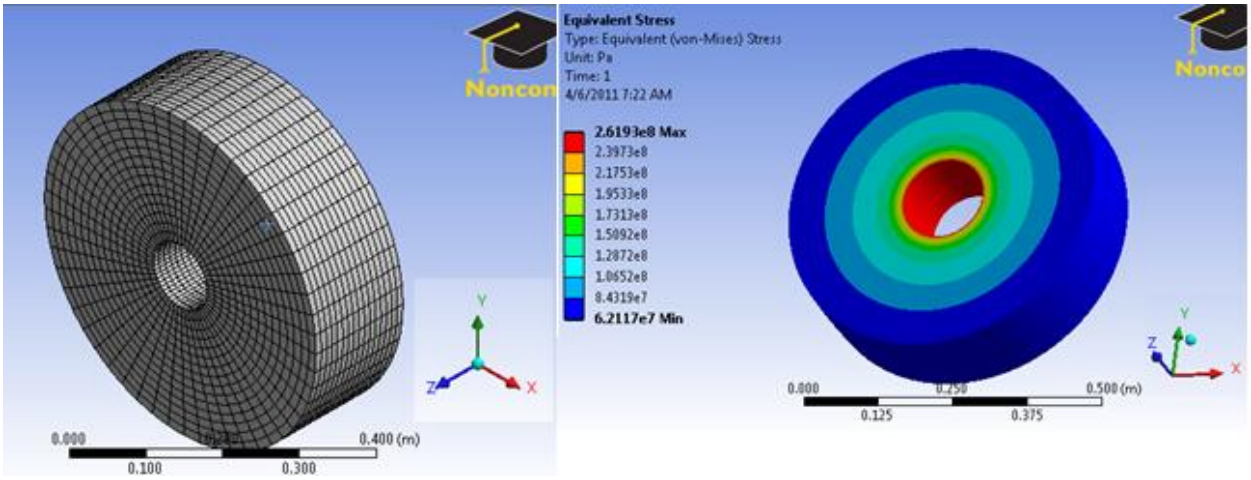

Figure 3-9 Preliminary model to verify initial calculations

It should be noted that the above analysis is done as a preliminary initial check to the calculated flywheel dimensions. A more complex stress analysis is carried out to strictly analyze rotor behavior during operation and is presented in Chapter 4

4 Flywheel Mechanical System Components

This chapter describes the major components of the flywheel mechanical system. This includes the rotor and housing design

4.1 Rotor

A study was done to understand the advantages of a composite rotor against its steel counterpart. The following section describes the analysis performed.

4.1.1 Steel vs. composite rotor analysis

4.1.1.1 Overview

In order to understand the differences between steel and composite rotors, we should take a look at the different applications of flywheels. Flywheels, in general, can be classified into two broad categories based on their rotational speed: Low speed flywheels and high speed flywheels. Low speed flywheels operate at a nominal speed between 1000-6,000 rpm while the latter operates at speeds ranging from 6,000 rpm to even 100,000 rpm in certain applications [134]. Low speed flywheels are generally used in applications such as UPS, power quality and load leveling while high speed flywheels find applications where there are very sudden fluctuations in power such as in transportation, aerospace and distributed generation [135].

Steel rotors are the typical choice for low speed applications while composite materials are often selected for higher speeds [136, 137]. The use of composites for high speeds is mainly because of the fact that steel rotors cannot withstand very high centrifugal forces. The primary reasons for selecting steel as the rotor material is due to its low cost and isotropic nature [138]. Composite materials are generally chosen due to their higher strength to weight ratios. However, the final choice of material cannot be based on just these factors. This thesis discusses the pros and cons associated with each choice.

4.1.1.2 Common misconceptions

There have been some misconceptions in trying to choose the rotor material for an application based flywheel design. It is necessary to understand the overcoming these misconceptions would give the flywheel designer a better insight into choosing an appropriate rotor material. The most common misconceptions are discussed below.

1. **Steel is a significantly cheaper than composite which means the overall flywheel product will be cheaper**

One of the common reasons for choosing a steel rotor is due to low cost. It should be noted that while the material cost of steel is low as compared to composites –the normalized cost of the energy storage capacity of the flywheel is not [139]. Steel costs $1/kg raw and approximately $3/kg fabricated. Several flywheels operate at about 2 W-hr/kg (0.56 kW-h/300 kg), resulting in a materials cost of about $1500/kW-hr. Compare this with a composite flywheel which costs about $100/kg fabricated and has an energy density of approximately 140 W-h/kg, resulting in a total energy storage capacity cost of about $700/kW-h. There are additional costs for containment, vacuum systems, support, bearing systems, etc., but these additional costs are similar for outer steel and composite rotors. It should be noted that steel flywheels are more than 10 to 20 times heavier per unit of stored energy than the composite flywheel. This additional weight increases mounting and installation costs.

2. **Composite rotor failures cause more damage than steel rotor failures due to their unpredicted anisotropic nature.**

Despite the concern, a composite flywheel is less likely to fail than its steel counterpart. With higher specific strengths, the burst modes of composite rotors are significantly higher than steel rotors. Spin to failure tests conducted by Texas A& M University prove that composite rotor failure modes can withstand higher rotational speeds compared to steel rotors and can be well controlled [140]. The primary difference between the two failure modes (steel and composite) is that steel rotors tend to rupture catastrophically from the inner rim while composite rotors tend to delaminate and disintegrate gradually from the outer circumference against the direction of fiber

orientation. However, it should be noted that composites tend to have a higher de-rating factor (the disintegration rate of the material due to temperature) due to high speed operation and there have been fatal accidents (including the famous BMW research center accident in destruction tests of composites [141]. One of the disadvantages of composite rotors is that they have to be in complete vacuum during operation as opposed to partial vacuum for steel rotors. This is because composite fibers are thought to be more susceptible to heat induced rupture than steel. However, this actually serves as an advantage during failure as it is enclosed by both the vacuum chamber and the housing (2 thick layers).

3. **All flywheels with composite rotors tend to have much lower weight than flywheels with steel rotors**

Composite rotors weigh significantly less than steel rotors for the same storage capacity due to higher power/energy densities. While this is true, it should be noted that the type of design plays a crucial role in determining overall system weight. For example, a composite rotor flywheel system with a barrel inside out configuration would have a comparable weight to an integrated steel flywheel system for the same energy capacity. This is because the rotor weight is only a small contribution to the overall system weight. The weight of the stator, containment and electronics are practically the same for both these rotors. Bender et al. designed a flywheel system with a composite rotor (420 W-hr energy capacity) which weighed 545 kg (the rotor weight was 40 kg). Steel rotor integrated flywheels with almost the same capacity (~500 W-hr) weighted 615 kg, with a rotor weight of 150 kg [77, 142]. The real weight savings from composites occur when compared with similar designs (composite integrated flywheel vs. steel integrated flywheel, composite inside out- vs. steel inside out, etc.)

4.1.1.3 Pros and cons

This section highlights the main pros and cons associated with steel and composite rotor materials. This section when combined with the major misconceptions, as shown in the precious section, would give a good insight in selecting an appropriate rotor material for the flywheel. Every design has its own advantages and disadvantages and hence a compromise has to be made based on the potential flywheel application.

4.1.1.3.1 Steel rotors

Pros:

1. Isotropic material: easier to predict and has a long standing history of use.
2. Material cost is cheaper as compared to composites
3. Relatively simple design
4. Full vacuum chamber not required for operation- although partial vacuum is required (Note : attaining 0.0001 Pa vacuum is expensive)

Cons:

1. Lower power densities compared to composites
2. Higher rotor weight.
3. Substantial energy loss during idling due to high aerodynamic and mechanical bearing drag which means lower efficiency.
4. Rotational speeds are limited to avoid catastrophic burst failure modes.

4.1.1.3.2 Composite rotor

Pros :

1. High power density and lower rotor weight.
2. Compact design with low aerodynamic drag and losses.
3. More benign failure modes that can be contained.

Cons :

1. High cost of composites
2. Design phase is more complex due to the anisotropic nature of composites

3. Requires operation in a full vacuum chamber as composite rotors are thought to be more susceptible to heat induced rupture, caused by aerodynamic losses, than steel rotors.

4.1.1.4 Example: Comparing costs for a 1 kW-hr energy storage with steel and composite rotors.

Let us compare the material costs associated with a 1 kW-hr energy storage using steel and composite rotors. For the purposes of this example, we assume that the operational and maintenance (O&M) costs and other component costs (such as stator, housing, etc) are similar. The various parameters are shown in table 4-1.

Material	Density (kg/m^3)	Max. operating stress (MPa)	Material Cost ($/kg)	Capacity cost ($/kWh)
Steel – (median values of 1010, 4340 and carbon steel)	7850	700	1(raw)-3(fabricated)	1200
Composite (median values of IM7 and GFRE)	1560	1500	100	600

Table 4-1 Basic parameters of steel vs. composite rotor

Calculating based on the parameters above; we get the material cost of steel and composite which are summarized in Table 4-2.

	Steel	Composite
Volume (m^3)	0.01	0.0048
Weight (kg)	78.5	7.48
Material cost ($)	157	748
Total cost (Material + Capacity) ($)	**1357**	**1348**

Table 4-2 Material cost

The optimal choice of rotor material for a flywheel energy storage design depends entirely on the specific application. It is not appropriate to assume that steel rotors are ideal for low speed

applications and composites for high speed applications. Each application has to be analyzed, in terms of cost, time and design, prior to choosing the rotor material. While it may be simpler to design a steel rotor based flywheel system, this is not always the optimal choice. As with any design there are trade-offs and each option has to be individually evaluated against the other. Based on the advantages and application – the 1kW-hr ROMAC flywheel design will be made up of a composite rotor consisting of Carbon fiber.

4.1.2 Design of Composite rotor

The design of the composite rotor is a key part in building the FES system. Currently, there is no single methodology to design a composite rotor. Different researchers formulate different ways to approach this problem. For example, the work of Arvin and Bakis [113, 116, 143] optimizes the weight energy density while the works of Ha et al [120] and Krack et al [13, 118] target cost and total stored energy respectively. The basis used in this design is derived from the work of Giancarlo Genta [107-111]. Even though most of his work concentrates on isotropic rotors, the same techniques can be extended to designing a composite rotor. This thesis also uses standard theory Equations pertaining to plane stress elasticity solutions for polar orthotropic rings. The internal moments along with the rotational speed, pressure changes and temperature changes are considered. Due to the complexity of Equations, a linear elastic material assumption is made. The analytical model is used to calculate the initial dimensions after which a 3D non-linear FEA analysis will be conducted.

Consider a uniform cylinder made up of a unidirectional composite with inner and outer radii as r_i and r_o respectively. Let r be any point on the cylinder and u_r be the radial displacement at point r. If E_l , E_a and υ_{la} are the longitudinal modulus , traverse modulus and Poisson's ratio respectively with σ_r and σ_θ as the radial and tangential (hoop) stresses, the radial displacement at any point r can be given as

$$u_r = \frac{(\sigma_\theta - \sigma_r \vartheta_{la})r}{E_l} \qquad \textbf{(4-1)}$$

According to theory, [144, 145] the stress distribution in each ring can be written in cylindrical coordinates as ,

$$\frac{d\sigma_r}{dr} + \frac{\sigma_r - \sigma_\theta}{r} + \rho r\omega^2 = 0 \qquad \textbf{(4-2)}$$

The stress-strain relation can be written in cylindrical coordinates as

$$\sigma = Q(\epsilon - \beta\Delta T) \qquad \textbf{(4-3)}$$

Expressing this in matrix form, we have

$$\begin{bmatrix}\sigma_\theta \\ \sigma_z \\ \sigma_r\end{bmatrix} = \begin{bmatrix}Q_{11} & Q_{12} & Q_{13} \\ Q_{21} & Q_{22} & Q_{23} \\ Q_{31} & Q_{32} & Q_{33}\end{bmatrix}\begin{bmatrix}\epsilon_\theta \\ \epsilon_z \\ \epsilon_r\end{bmatrix} - \begin{bmatrix}\beta_\theta \\ \beta_z \\ \beta_r\end{bmatrix}\Delta T \qquad \textbf{(4-4)}$$

Where,

$\epsilon_\theta = \frac{u_r}{r}, \epsilon_r = \frac{d\sigma_r}{dr}$ and $\epsilon_z = \epsilon_0 + \epsilon_1 r$

The axial strain constants $\epsilon_0 and\ \epsilon_1$ can be computed from the force balance in the axial direction. As there is no external axial force, the summation of the axial forces of the rings should be zero. Hence,

$$u_r = -\rho\omega^2\varphi_0 r^3 + C_1\varphi_1 r^k + C_2\varphi_2 r^{-k} + \varphi_3\epsilon_1 r^2 + \varphi_4\epsilon_0 r + \varphi_{\beta_1}\Delta T r \qquad \textbf{(4-5)}$$

Where,

$$k = \sqrt{\frac{Q_{11}}{Q_{33}}}; \varphi_0 = \frac{1}{(9-k^2)Q_{33}}; \varphi_1 = \frac{1}{Q_{13}+kQ_{33}}; \varphi_2 = \frac{1}{Q_{13}-kQ_{33}} \qquad \textbf{(4-6)}$$

$$\varphi_3 = \frac{Q_{12}-2Q_{32}}{4Q_{33}-Q_{11}}; \varphi_4 = \frac{Q_{12}-Q_{23}}{Q_{33}-Q_{11}}\ ;\ \varphi_{\beta_1} = \frac{\beta_r - \beta_\theta}{Q_{33}-Q_{11}}$$

C_1 and C_2 are constants which can be determined from the boundary conditions [107](i.e zero radial stresses at the inner and outer surfaces of each ring).

The final Equations of radial stress and strain are given by Genta as

$$\epsilon_r = -3\rho\omega^2\varphi_0 r^2 + kC_1\varphi_1 r^{-(1+k)} + 2\varphi_3\epsilon_1 r + \varphi_4\epsilon_0 + \varphi_{\beta_1}\Delta T \qquad \textbf{(4-7)}$$

$$\sigma_r = -\rho\omega^2\varphi_5 r^2 + C_1 r^{k-1} + C_2 r^{-k-1} + \varphi_6\epsilon_1 r + \varphi_7\epsilon_0 + \varphi_{\beta_2}\Delta T \qquad \textbf{(4-8)}$$

Where,

$$\varphi_5 = (Q_{31} + 3Q_{33})\varphi_0; \varphi_6 = (Q_{31} + 2Q_{33})\varphi_3 + Q_{32};\ \varphi_7 = (Q_{31} + Q_{33})\varphi_4 + Q_{32}$$

$$\varphi_{\beta_2} = (Q_{31} + Q_{33})\varphi_{\beta_1} - \beta_r$$

For a carbon fiber ring, the stiffness matrix can be written, in simplified form as

$$\begin{bmatrix} Q_{11} & Q_{12} & Q_{13} \\ Q_{21} & Q_{22} & Q_{23} \\ Q_{31} & Q_{32} & Q_{33} \end{bmatrix} = \begin{bmatrix} \frac{E_1}{1-\upsilon_{12}\upsilon_{23}} & \frac{\upsilon_{12}E_1}{1-\upsilon_{12}\upsilon_{23}} & 0 \\ \frac{\upsilon_{21}E_1}{1-\upsilon_{12}\upsilon_{23}} & \frac{E_2}{1-\upsilon_{12}\upsilon_{23}} & 0 \\ 0 & 0 & G_{12} \end{bmatrix} \qquad \textbf{(4-9)}$$

Where

$E_1 = Longitudinal\ In-plane\ young's\ modulus, E_2 =$
$Transverse\ In-plane\ Young's\ Modulus, G_{12} = Inplane\ shear\ modulus, \upsilon_{12}, \upsilon_{23} =$
$Major\ in-plane\ poissons\ ratio.$

For simplicity purposes, the effect of temperature is neglected. The radial and tangential stresses in the cylinder due to the centrifugal loading is given by Genta as,

$$\sigma_r = \rho\omega^2 r_o^2 \left(\frac{3+\vartheta_{la}}{9-{\mu_x}^2}\right)\left[\Gamma\chi^{(\mu_x-1)} - (\Gamma-1)\chi^{(-\mu_x-1)} - \chi^2\right] \qquad \textbf{(4-10)}$$

$$\sigma_\theta = \rho\omega^2 r_o^2 \left(\frac{3+\vartheta_{la}}{9-{\mu_x}^2}\right)\left[\mu_x\Gamma\chi^{(\mu_x-1)} + \mu_x(\Gamma-1)\chi^{(-\mu_x-1)} - \chi^2\left(\frac{{\mu_x}^2+3\vartheta_{la}}{3+\vartheta_{la}}\right)\right] \qquad \textbf{(4-11)}$$

Where,

$$\chi = \frac{r}{r_i}, \beta = \frac{r_i}{r_o}, \mu_x = \sqrt{\frac{E_l}{E_a}} \text{ and } \Gamma = \left(\frac{\beta^{(-\mu_x-1)}-\beta^2}{\beta^{(-\mu_x-1)}-\beta^{(\mu_x-1)}}\right)$$

Equations (4-10) and (4-11) are applicable to orthotropic materials. The radial stress and displacement along with the tangential stress as a result of internal (P_{int}) and external (P_{out}) pressures are derived as

$$\sigma_\theta = \left(\frac{P_{int}\beta^{(\mu_x+1)} - P_{ext}}{1-\beta^{2\mu_x}}\right)\mu_x\chi^{(\mu_x-1)} + \left(\frac{P_{int} - P_{ext}\beta^{(\mu_x-1)}}{1-\beta^{2\mu_x}}\right)\mu_x\beta^{(\mu_x+1)}\chi^{(-\mu_x-1)} \quad \textbf{(4-12)}$$

$$\sigma_r = \left(\frac{P_{int}\beta^{(\mu_x+1)} - P_{ext}}{1-\beta^{2\mu_x}}\right)\chi^{(\mu_x-1)} - \left(\frac{P_{int} - P_{ext}\beta^{(\mu_x-1)}}{1-\beta^{2\mu_x}}\right)\beta^{(\mu_x+1)}\chi^{(-\mu_x-1)} \quad \textbf{(4-13)}$$

$$u_r = \left(\frac{r_o}{E_l 1-\beta^{2\mu_x}}\right)\left[\left(P_{int}\beta^{(\mu_x+1)} - P_{ext}\right)(\mu_x - \vartheta_{la})\chi^{\mu_x} + (P_{int} - P_{ext}\beta^{(\mu_x-1)})(\mu_x + \vartheta_{la})\beta^{(\mu_x+1)}\chi^{-\mu_x}\right] \quad \textbf{(4-14)}$$

In order to compute the tangential and radial stresses associated with the 1kW-hr flywheel, the following parameters of Graphite re-inforced carbon epoxy (GFRE) was used.

Property	Value
Youngs modulus X direction	$1.47 * 10^{11}$ Pa
Youngs modulus Y direction	$1.03 * 10^{10}$ Pa
Youngs modulus Z direction	$1.01 * 10^{10}$ Pa
Major Poisson's ratio (XY)	0.27
Major Poisson's ratio (YZ)	0.57
Major Poisson's ratio (XZ)	0.27
Shear modulus (XY)	$7 * 10^9$ Pa
Shear modulus (YZ)	$3.7 * 10^9$ Pa
Shear modulus (XZ)	$7 * 10^9$ Pa
Density	1605 Kg/m^3
Tensile Yield Strength	$2 * 10^8$ Pa
Tensile Ultimate Strength	$1.5 * 10^9$ Pa
Compressive Yield strength	$1.4 * 10^8$ Pa
Compressive Ultimate strength	$1.2 * 10^9$ Pa

Table 4-3 Parameters of carbon epoxy parameters

Using Table 4-3 and the mathematical model developed earlier, the stresses associated with the initial flywheel rotor dimensions of 230 mm (inner diameter) and 420 mm (outer diameter) were found. The angular velocity was taken as 40,000 rpm. The circumferential and radial stresses are given in Figure 4-1. It can be seen that the inertial stresses in the flywheel, when rotated at a very high speed, are highest in the circumferential direction. This is why composite rotors are usually filament wound with fiber reinforcements oriented in this direction. However, tensile stress is also developed in the radial direction due to mismatches in the growth of the rotor as well as Poisson effects. Because filament wound composite rotors lack reinforcement through the radial thickness, these rotors generally fail by radial delamination prior to fiber breakage in the circumferential direction. A good composite design would find a balance between tangential stresses and radial displacement.

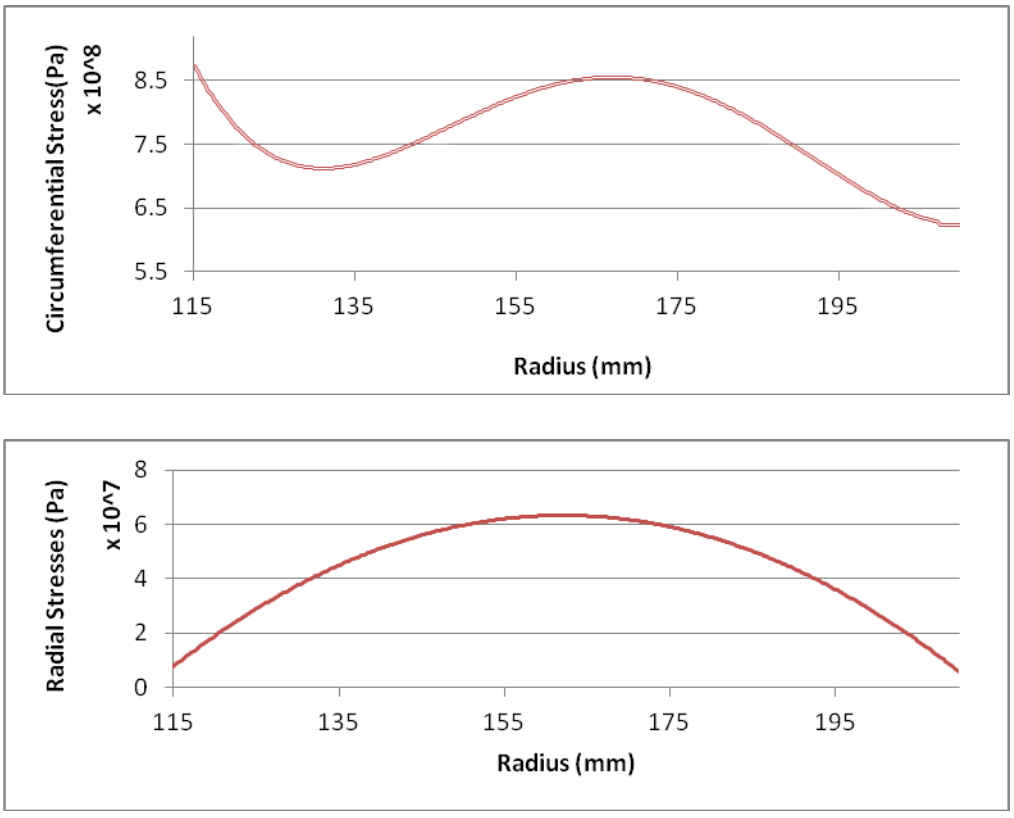

Figure 4-1 Computed Circumferential and radial stresses: 40,000 rpm

Another important factor to be considered is the radial displacement of the composite rotor during operation. For a 1kW-hr rotor, the radial displacement as a function of rotating speed is given in Figure 4-2. It was found that at the nominal rotating speed of 40,000 rpm, the predicted

radial displacement was about 1.12 mm. It should be noted that with time, the stress and strain profiles in a flywheel can change significantly. A study by Ha et al. suggests that the stresses (radial and tangential) would decrease by an average of 25% over 10-20 years of operation due to creep and stress relaxation of the composite [120]. To achieve high performance, the stresses in a composite rotor must be high during operation (but not more than the ultimate stress value after a safety factor of 2) while the radial displacement has to be very low.

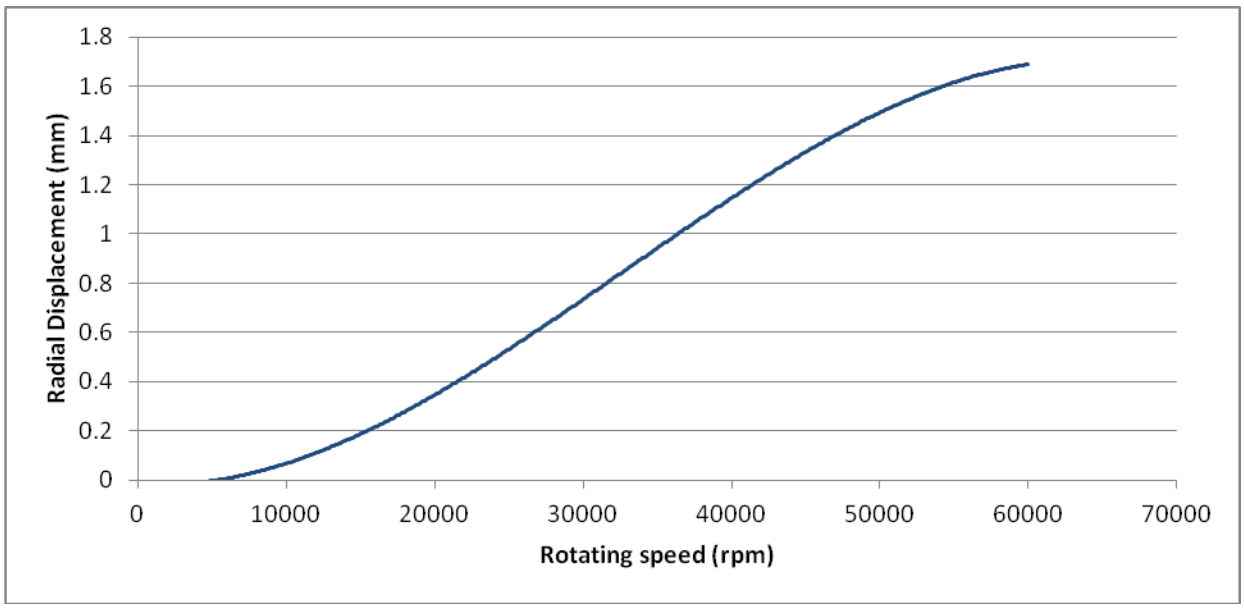

Figure 4-2 Radial Displacement vs. Rotating speed

The way chosen to reduce the very high tensile stresses and radial displacement is by adding a steel spline rotor to the inside of the composite part. Further, to prevent withdrawal of the flywheel rotor components (laminations, motor, etc) – an inner spline steel ring is also added. Figure 4-3 shows a model of the steel spline rings attached to the composite flywheel. Nylon adhesive will be used to wind the composite over the outer spline ring.

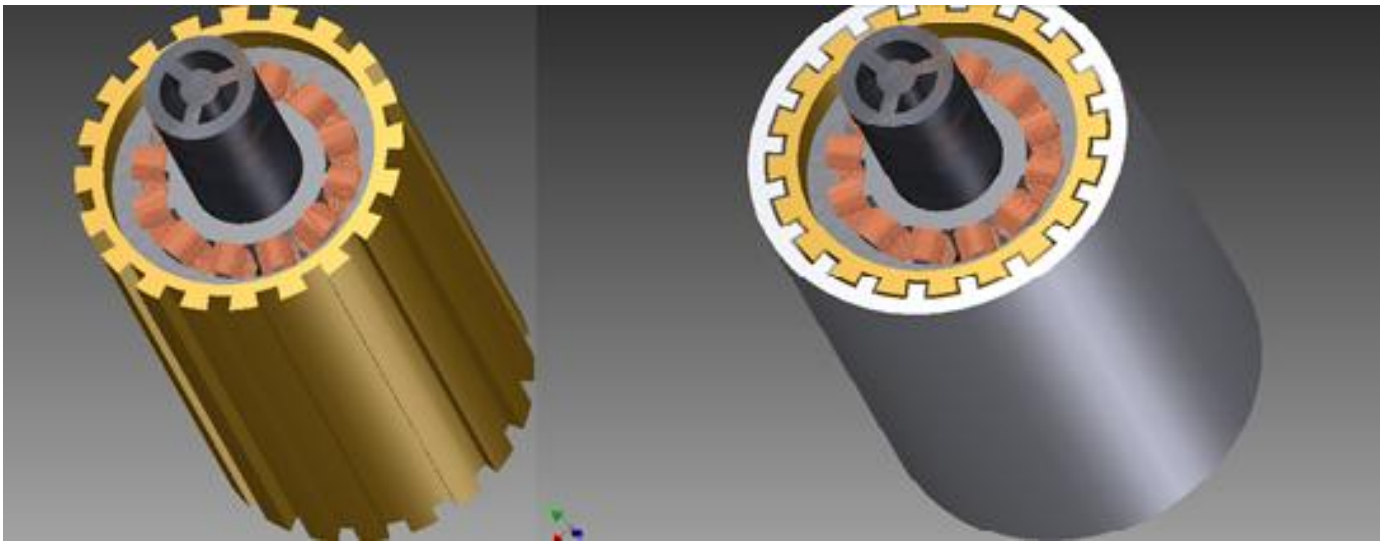

Figure 4-3 Inner (gold) and outer (silver) steel spline ring model

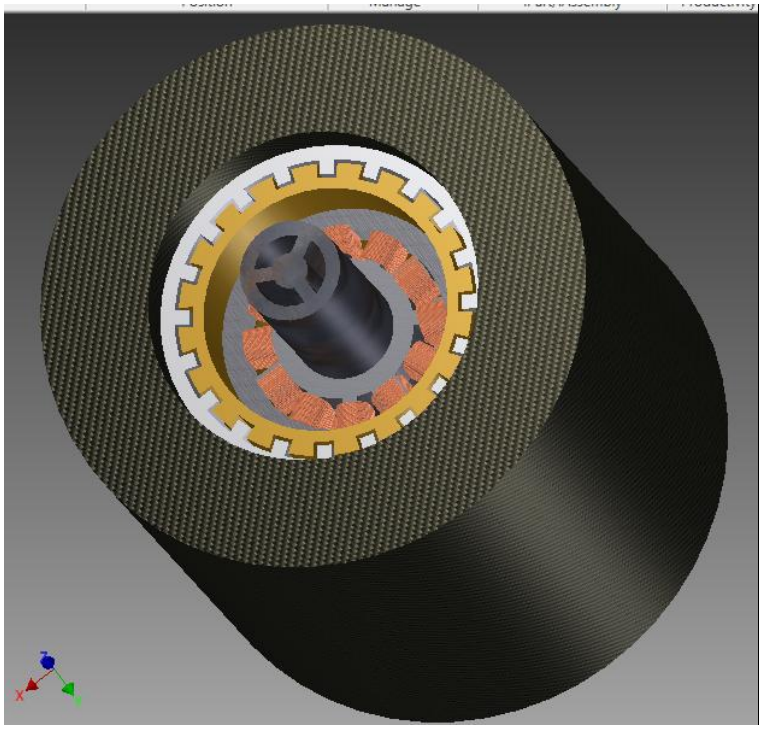

Figure 4-4 Model depicting attachment of composite rotor to the steel spline rings.

4.1.3 Stress Analysis on Composite rotor.

To verify the effects of the steel spline rings on the composite rotor, a three dimensional analysis was carried out in ANSYS. This study was also used to analyze the stresses associated when the steel ring is modeled together with the composite rotor. Using ANSYS PrepPost , the anisotropic carbon fiber properties were specified.

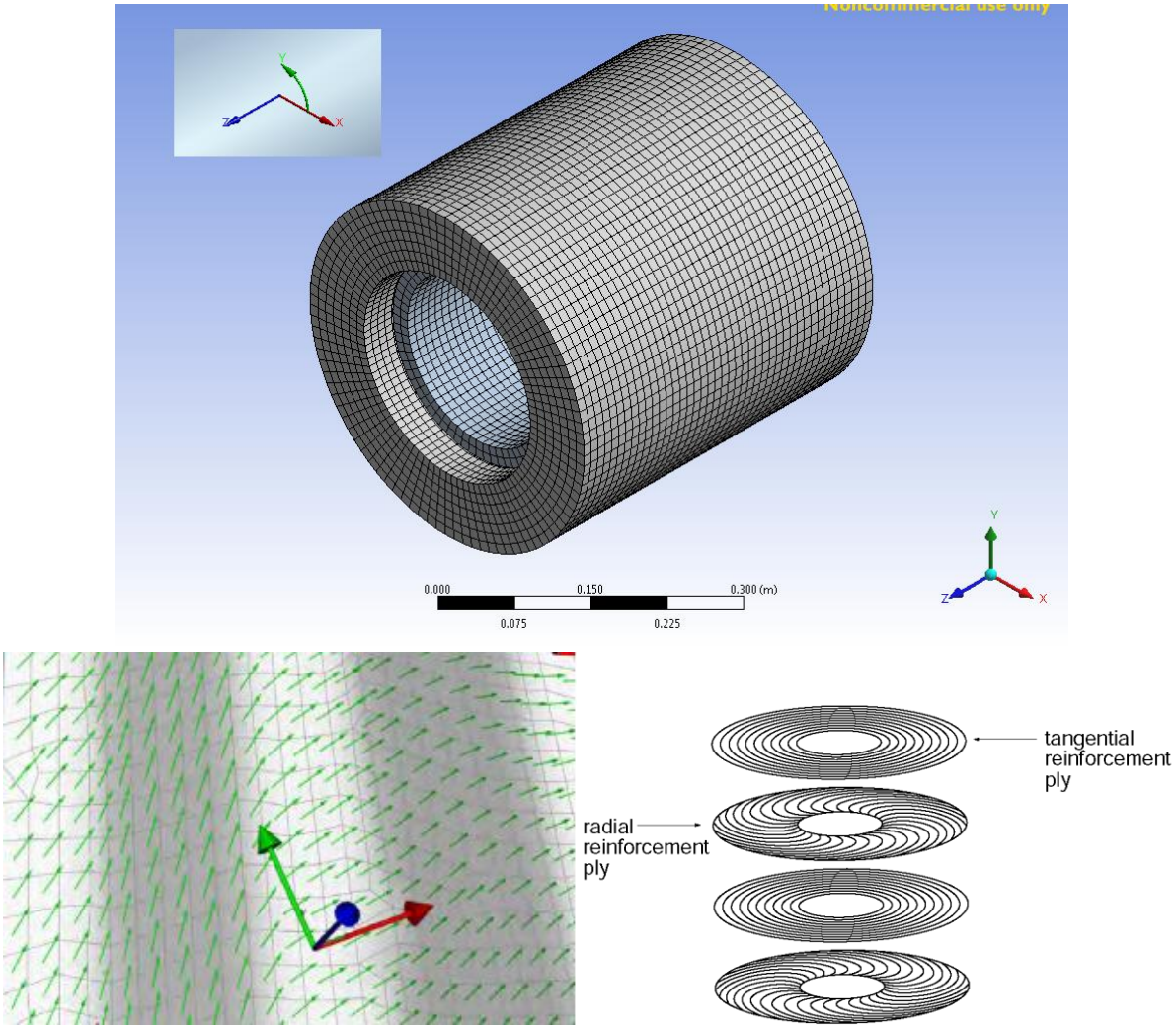

Figure 4-5 ANSYS prepost model of composite rotor

The model was set up as shown in Figure 4-5. The model shows the outer composite layer and the inner spine (steel). The outer composite disk was modeled as layers of 40 rings which were

wounded 45° to each other. This is done to simulate the actual filament winding process. The orthotropic properties of the composite were specified as shown in Table 4-3.

Parameter	Value
Young's Modulus	$2*10^{11}$ Pa
Poisson's Ratio	0.3
Density	7850 kg/m^3
Thermal expansion	$1.2*10^{-5}$ 1/°C
Tensile yield strength	$2.5*10^{8}$ Pa
Compressive yield strength	$2.5*10^{8}$ Pa
Tensile ultimate strength	$4.6*10^{8}$ Pa

Table 4-4 Properties of Steel

Further, a transformation from the global co-ordinates into cylindrical co-ordinates was done (X-Y-Z directions were transformed to Axial-Rotational – Torsional directions). A bonded contact region between the composite flywheel and inner spline ring was specified. A convergence mesh study was conducted and the results were found to be optimum at 225000 nodes. Having accurately modeled the problem- the boundary conditions were specified as follows:

1. The rotational speed was specified along the axial direction as 40,000 rpm
2. The entire structure was subject to frictionless support (due to magnetic bearings)
3. The entire model was constrained such that the displacement along the axial direction is zero.

Three separate cases were analyzed- the steel spline alone, the composite alone and the overall steel and composite structure. In order to simplify the analysis the outer steel spline was modeled as a uniform cylinder. The two major parameters of study were the tangential stresses and the radial deflection. The results are tabulated in Table 4-5

Parameter	Steel alone	Composite alone	Steel + Composite
Tangential stress (Pa)	1.5 *10^9 Pa	8.8*10^8 Pa	1.1*10^7 Pa
Radial Deflection (mm)	2 mm	1.2 mm	1.03mm

Table 4-5 Stress and radial deflection of three cases of flywheel analysis

From Table 4-5, the effect of the steel spline on the composite is evident. While the fibers of the composite try to grow inward- the steel spline rings tend to inhibit this growth. As a result the stresses observed on the overall case are much smaller – within the design range of the flywheel rotor (after a safety factor of 2). These results further prove a steel ring of this size alone cannot be rotated at a high speed of 40,000 rpm as the observed stresses are greater than the ultimate stress value. A combination of composite and steel is ideal for such high speed designs. The steel ring also accounts for a good bond between the spline and rotor components which will avoid withdrawal at such speeds.

Another study conducted was to analyze the tangential stresses (of the overall steel and composite structure) by changing the rotational speed. Using ANSYS, a safety factor of 2 was used as the maximum design allowable stress. It can be seen in Figure 4-6 that a design speed of 40,000-60,000 was found to be acceptable from a stress standpoint.

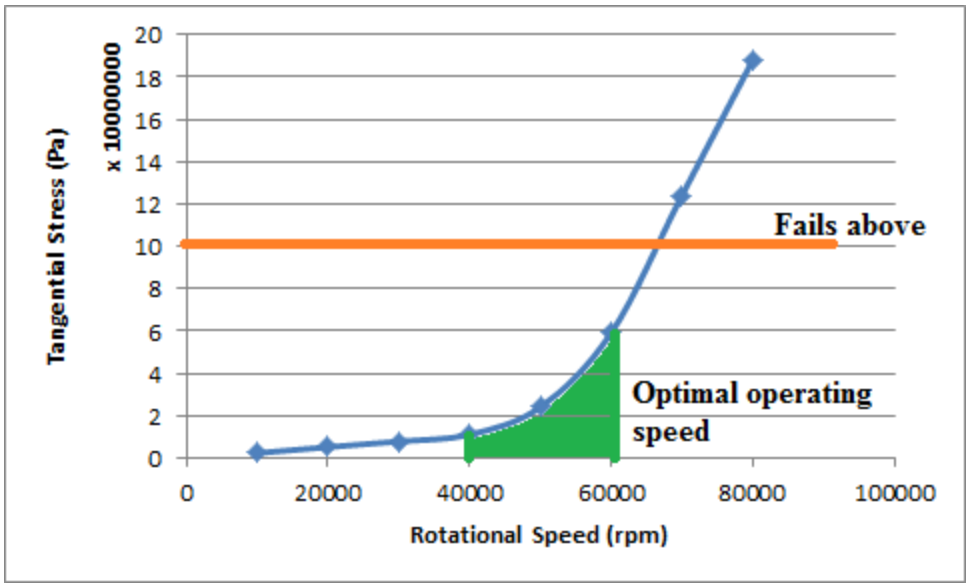

Figure 4-6 Tangential Stress vs Rotational speed

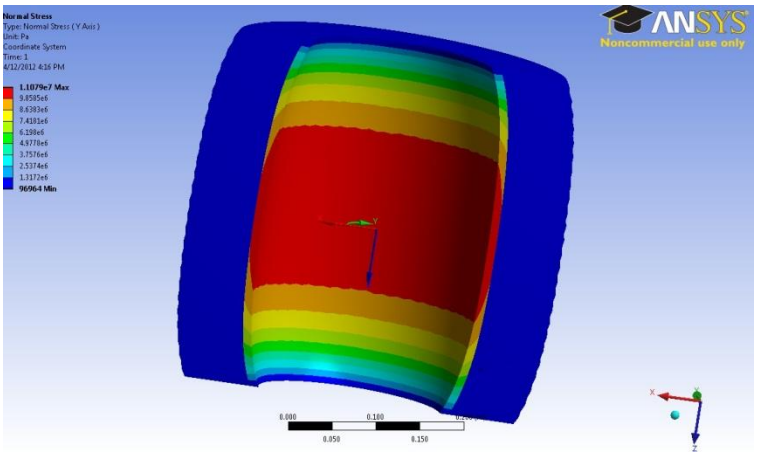

Figure 4-7 Tangential stresses of overall structure (steel +composite)

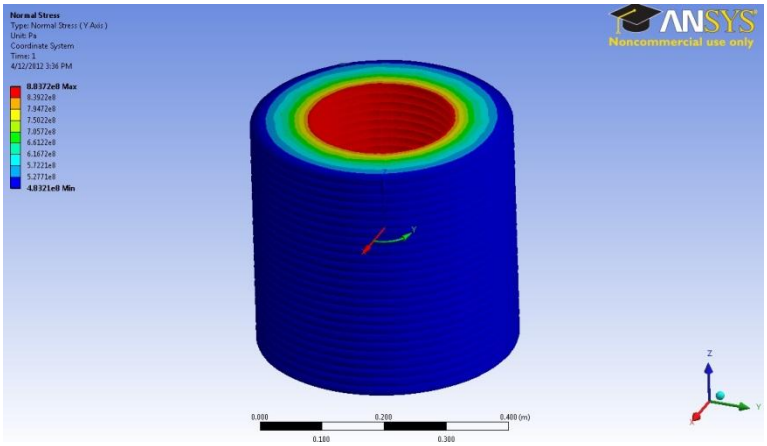

Figure 4-8 Tangential stress on composite alone

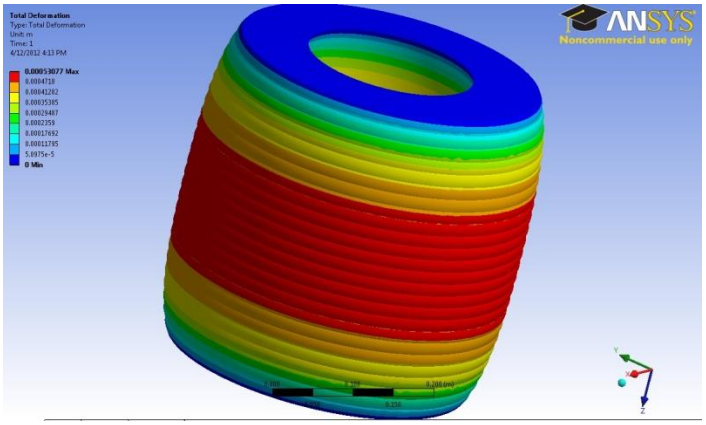

Figure 4-9 Radial deflection of overall structure (steel +composite)

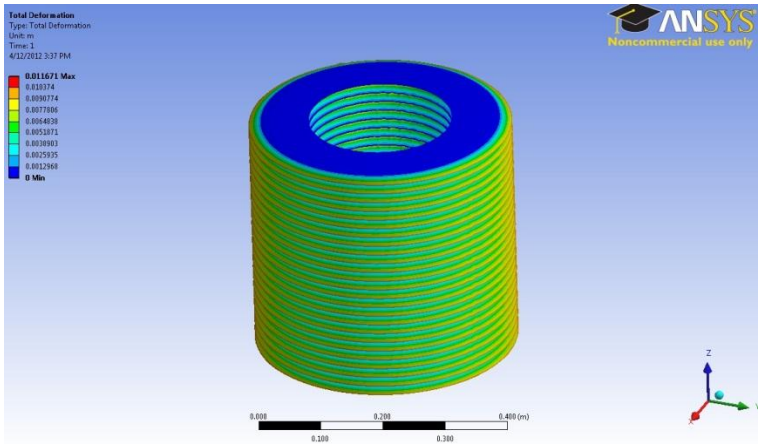

Figure 4-10Radial deflection of composite alone.

4.2 Housing

One of the greatest technical challenges in designing a safe and efficient flywheel is in designing the containment [146]. Specifically, the issue of flywheel burst containment has been a very important one. [147, 148]. To be successful at designing the containment, it is essential to be aware of the failure characteristics and potential hazards that exist for high speed flywheels. The failure characteristics for composite flywheel rotors are significantly different than for metal flywheel rotors, and the failure of a high speed composite rotor can create enormous loads due to the very high energy transfer occurring over a short period of time [114, 143]. When a carbon composite flywheel rotor fails and impacts a solid containment vessel above a threshold speed, the rotor is broken into fine particles as the result of the impact. The particles tend to move around the inside of the containment vessel, acting much like a fluid flowing on a curved surface. The fluid-like phenomenon can lead to significant axial loads impacting the ends of the containment structure, in addition to the expected radial and circumferential loads from impact [148]. There has been some experimental evidence showing this behavior. Particularly, the Demo IC failure conducted at the Oak Ridge National Laboratory [149], the intentional burst failure of the flywheel rotor at Munich [141]and the flywheel safety and containment program at the Defense advanced research projects agency (DARPA) [150] are good examples.

4.2.1 Design approach to reduce flywheel risk

With the significant amount of evidence showing the hazards involved with a high speed flywheel burst mode failure; it is not acceptable to downplay the issue of safety and containment. Flywheel rotors must be designed to operate with low risk, as has been successfully accomplished for rotors in gas turbine engines, which also run at very high speeds [151, 152]. In gas turbines, a containment shroud is provided to stop broken blades, thereby mitigating the consequence of a failed blade. However, the containment shroud is not designed to contain a hub failure.

The ROMAC flywheel uses the same concept for the housing. The housing is divided into two parts: the containment enclosing the flywheel and the housing for the overall system. A schematic of the containment is shown in Figure 4-11

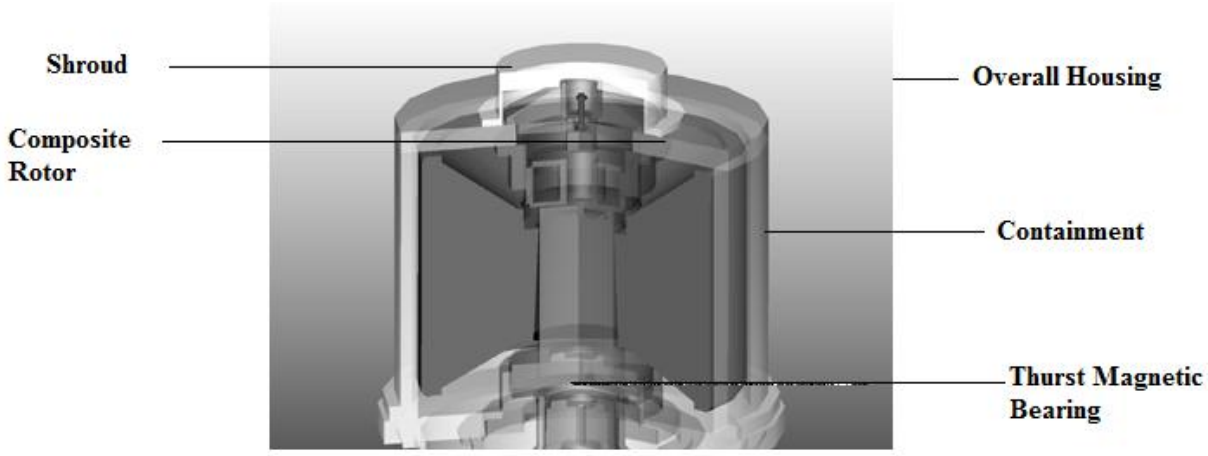

Figure 4-11 Schematic showing containment encasing the composite flywheel

The ANSI/AIAA standard developed by NASA and the US Air Force was used as the guideline in designing the containment and housing. [153] . A summary of the design guidelines used are presented below

1. Ultimate stress limit: The ANSI standard states that there should be a significant stress margin between the operating stress and ultimate stress. For high speed flywheels, the ultimate stress has to be at least 1.3 times the maximum operating stress although larger stress margins can result in a long rotor life. The radial and axial stresses must be considered in addition to the large hoop stresses.

2. Incorporate containment tailored to flywheel design: If the probability of a rotor burst cannot be set sufficiently low, containment is needed to reduce the consequence of the burst. If burst can be avoided through design, containment must still retain flywheels that could come loose and must contain fragments from partial flywheel failures.

3. Dual containment system: The AIAA standard states that for high speed flywheels, there should be a dual containment system- one to contain the rotor parts during burst failure and the other to prevent debris from flying out. Although this standard has been developed for space applications, the ROMAC flywheel will incorporate this technique as an added safety feature.

The ROMAC flywheel containment will have the properties as listed in Table 4-6

Parameter	Value
Material	Type 304 Stainless steel
Flywheel outer diameter	420 mm
Containment inner radius	425 mm
Containment thickness	100 mm
Youngs Modulus	185 GPa
Poissons Ratio	0.27
Yield Strength	210 MPa
Uniform elongation	25%
Ultimate Strength	620 MPa
Tangent Modulus	1.6 GPa

Table 4-6 Flywheel containment parameters

As indicated previously, the containment structure will comprise of three parts – 2 shrouds (1 at each end) and the rotor casing mid-section (burst liner wall). The main function of the shrouds is to reduce the rotor speed during failure.

An initial analysis was done to verify if the containment can withstand the failure of the flywheel. The first order calculation was deemed sufficient at the design stage since the impact assumptions will represent the worst case scenario for each of the failure mechanisms. Three failure modes of the composite flywheel were studied. The first was a tri-burst in which the composite flywheel breaks into three segments and each segment impacts the outer wall of the burst liner. The second was the fragmentation of the composite rotor that will produce a uniform pressure on the inner surface of the burst liner. The third mechanism was a tri burst failure in which the rotor components of the flywheel fail and deflect upward – impacting the shroud of the containment.

4.2.2 Failure mode 1 : Tri-burst Impact with burst liner wall.

The triburst impact assumes that the rotor breaks into three segments and that each segment impacts the burst liner intact. All of the energy in the segment is converted to the force of impact. No energy dissipation is assumed from the material deformation. The area of each impact is equal to the surface are of 1/3 of the rotor. Since each of the impact events is isolated the maximum stress will occur within the impact area and will be the same for each. The area of impact(A_i) is given by [154]

$$A_i = \frac{2}{3}\pi r_{c,h} h_c \qquad \textit{(4-15)}$$

The pressure exerted on this surface is due to the force of impact (F_i). This is given as

$$F_i = \frac{M_r V_{t.l}}{t_i} \qquad \textit{(4-16)}$$

The mass of the rotor segment is given by the volume of the segment and material density (ρ) and the translated linear velocity is given from the rotational energy in the flywheel rotor.

$$M_r = \frac{\pi}{3}(r_o^2 - r_i^2)h\rho \qquad \textit{(4-17)}$$

$$V_{t.l} = E_r^2 / M_r \qquad \textit{(4-18)}$$

The pressure exerted on the burst liner wall can be calculated by

$$P_{bc,i} = \frac{F_i}{A_i} \qquad \textit{(4-19)}$$

The input and output parameters are given in Table 4-7. It should be noted that the maximum stress obtained in less than the ultimate strength of the burst liner and hence should be contained.

Input parameters	
Rotational speed (ω)	60,000 rpm
Impact duration (t_i)	80 µ sec
Mass of rotor segment (M_r)	20 Kg

Output parameters	
Rotational energy (E_r)	3.2 MJ
Pressure exerted on burst liner wall ($P_{bc,i}$)	302.47 MPa
Maximum stress obtained on wall	512.21 MPa
Factor of Safety	2

Table 4-7 Input and output parameters of Tri-burst impact failure mode

4.2.3 Failure mode 2 : Flywheel disintegration and impact with Burst liner wall.

The outer ring disintegration assumes that the outer composite ring of the flywheel breaks apart and strikes with the containment wall. An assumption made is that the outer flywheel is evenly distributed and extends out uniformly. It was also assumed that no energy was dissipated due to heating or particle deformation. The area of impact is then given by

$$A_i = 2\pi r_{c,i} h_c \qquad \textit{(4-20)}$$

The force of impact and the pressure were computed in the similar fashion as (4-16) and (4-19). From these values the maximum stress can be calculated as below. The external pressure is taken to be zero since the burst liner is within a vacuum chamber.

$$\sigma_{max,burst} = P_{bc,i} \frac{((r_o^2 + r_i^2) - 2P_{ext,bc,i} r_o^2)}{r_o^2 - r_i^2} \qquad \textit{(4-21)}$$

The obtained values are tabulated in Table 4-8

Parameters	Value
Impact Force	5870 MN
Pressure exerted on burst liner wall ($P_{bc,i}$)	257.1 MPa
Maximum stress obtained on wall $\sigma_{max,burst}$	415.26 MPa

Table 4-8 Output parameters of failure mode 2

4.2.4 Failure mode 3: Containment shroud impact.

The impact of the flywheel rotor components onto the containment shroud was analyzed. The assumption made in this study was that the rotor components first hit the burst liner wall and

then deflected vertically (equal amounts upwards and downwards) along the wall and impacted the upper and lower containment shrouds uniformly. No energy was assumed to be lost during the impact with the burst liner wall. The determination of the maximum shear stress within the shroud is calculated by determining the force on the shroud. Since the shroud is a cantilevered surface, the maximum stress will occur at the base of the shroud nearest to the burst liner wall. The pressure exerted on the shroud can be calculated by dividing Equation (4-16) by the area of the shroud. If R_{ol} and R_{il} are the outer and inner radii of the shroud, the area can be computed as

$$A_{i,shroud} = \pi({r_{o,l}}^2 - {r_{i,l}}^2) \qquad \textbf{(4-22)}$$

The maximum stress will be due to the bending moment caused by the pressure on the shroud, In order to compute this value, the shroud was assumed to be a circular plate with a hole in the center. This plate is fixed along its edge to the burst liner walls. This assumption is very similar to the one presented by Baumeister [155]. Hence the maximum stress can be computed using

$$\sigma_{max,burst} = 0.259 * P_{bc,i} * \frac{{r_{o,l}}^2}{t_{o,l}^2} \qquad \textbf{(4-23)}$$

Using Equations ((4-22) and ((4-23), the maximum stress obtained in the shroud was calculated to be about 410.29 MPa. This value is lesser than the ultimate strength of the burst liner material with a factor of safety of 2.

4.2.5 Containment response to debris

The loading models developed to analyze containment response following flywheel failure are described by Pichot et al. [20, 83]. These models use fundamental energy and momentum principles to calculate the radial, axial and torsional loading on the containment wall and shroud. The ROMAC flywheel containment analysis uses the debris accumulation model to evaluate the design. This is because the debris accumulation model tends to produce longer duration loading and maximizes the torque on the containment. The assumption made in this model is that the debris is assumed to impact the inside wall of the containment and immediately deflected axially and eventually accumulating on the wall and shrouds.

4.2.5.1 Model :

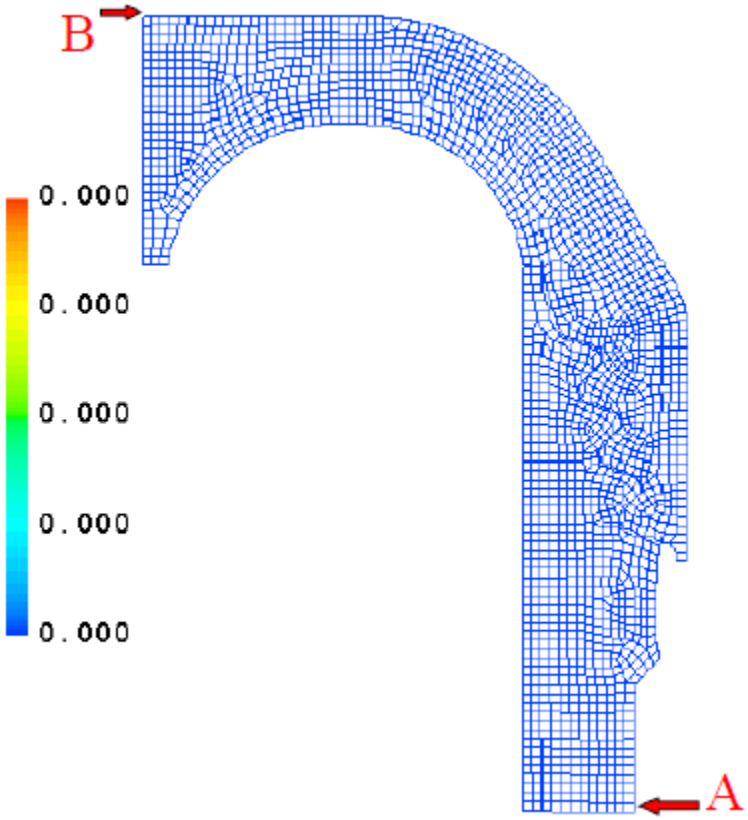

Figure 4-12 Model developed from STRAW

The model developed is based on the STRAW code developed by Argonne National Laboratory [156]. STRAW is a non-linear finite element code that uses explicit time integration. A computational time step of 0.15μs was used for all the simulations. An axi-symmetric finite element model composing of two disjoint meshes were created- one mesh represents the burst liner wall (marked A) and the other represents the shroud (marked B). Only one half of the containment was modeled to reduce computation time. The mesh is depicted in Figure 4-12. About 2500 nodes were used in the model.

The nodes along the horizontal symmetry plane of the casing were restricted to radial translational motion only. Thus, these boundary conditions represent a horizontal symmetry plane. For the end plate, the nodes were constrained from moving in the negative radial direction.

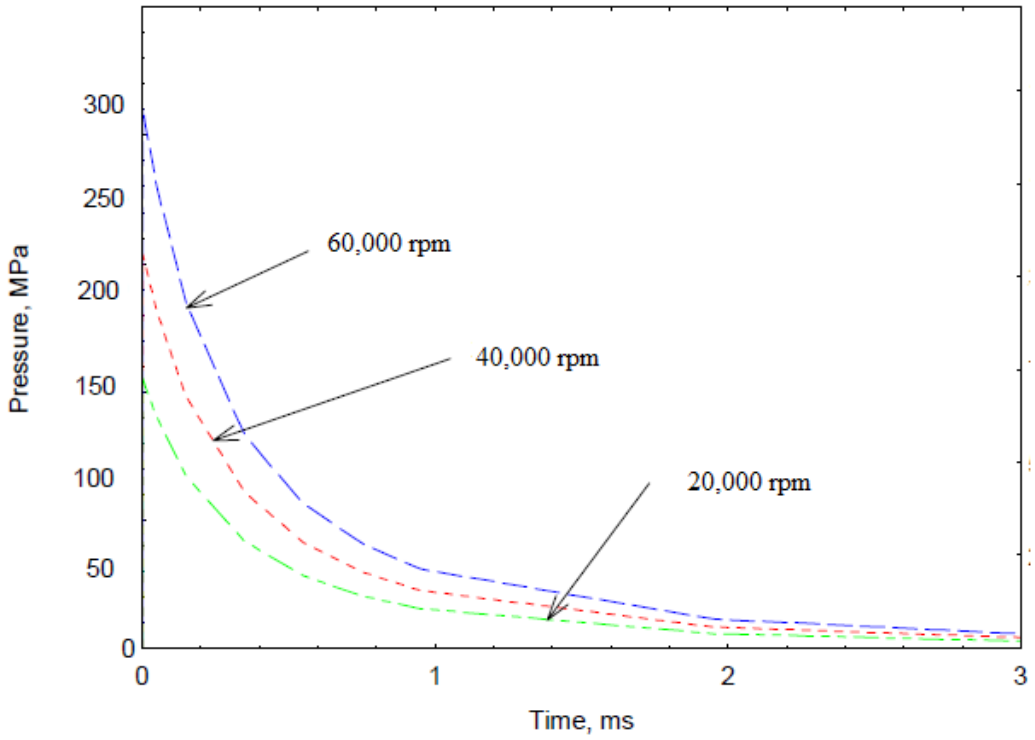

Figure 4-13 Pressure profile for different speed ranges

Using this model, the time dependent pressure histories were determined for 3 speeds: 20,000 rpm, 40,000 rpm and 60,000 rpm. These values are plotted in Figure 4-13. It can be seen that for the operating speed of 60,000 rpm, the pressure rises to a maximum value of about 300 MPa during the first 1.2μs and then gradually decays to about 10MPa at 3 ms. The obtained 2D analysis values were comparable with the calculated pressure values developed earlier.

Further, the radial displacement and the acceleration profiles of the burst liner wall and the shroud were studied. This is shown in Figure 4-14 and Figure 4-15. It can be noted that the maximum radial displacement obtained was only about 5μm which ensures that the containment will be able to withhold the debris in case of rotor failure. The simulated acceleration profiles show how the debris reduces its acceleration when it comes in contact with the burst liner wall and shroud walls.

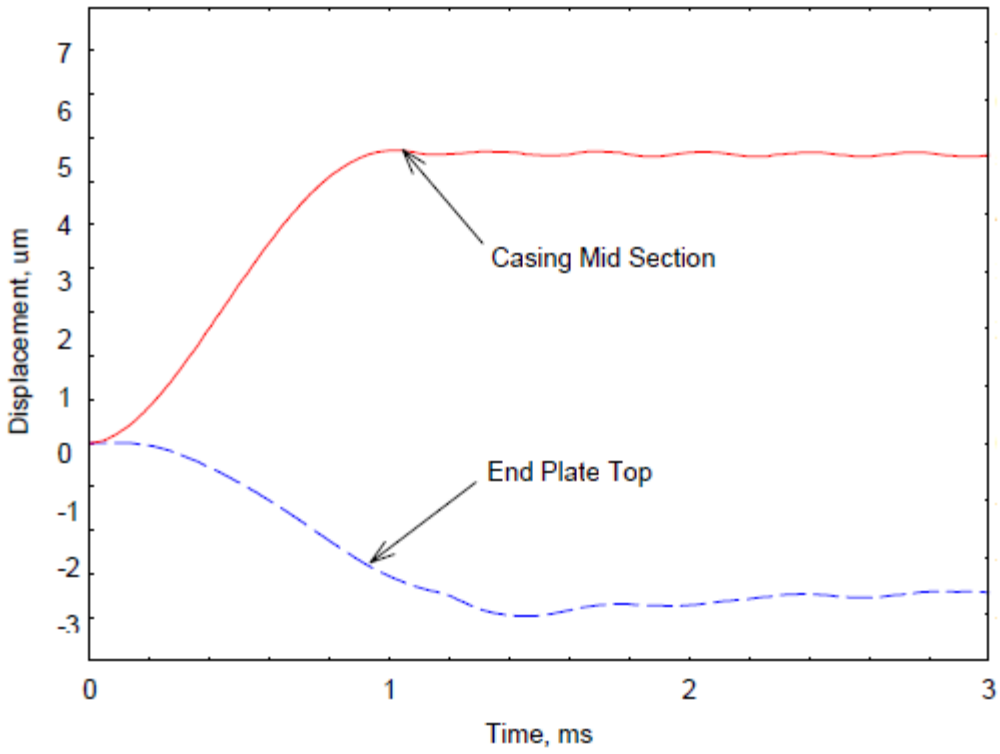

Figure 4-14 Radial Displacement profile of wall and shroud at 60,000 rpm

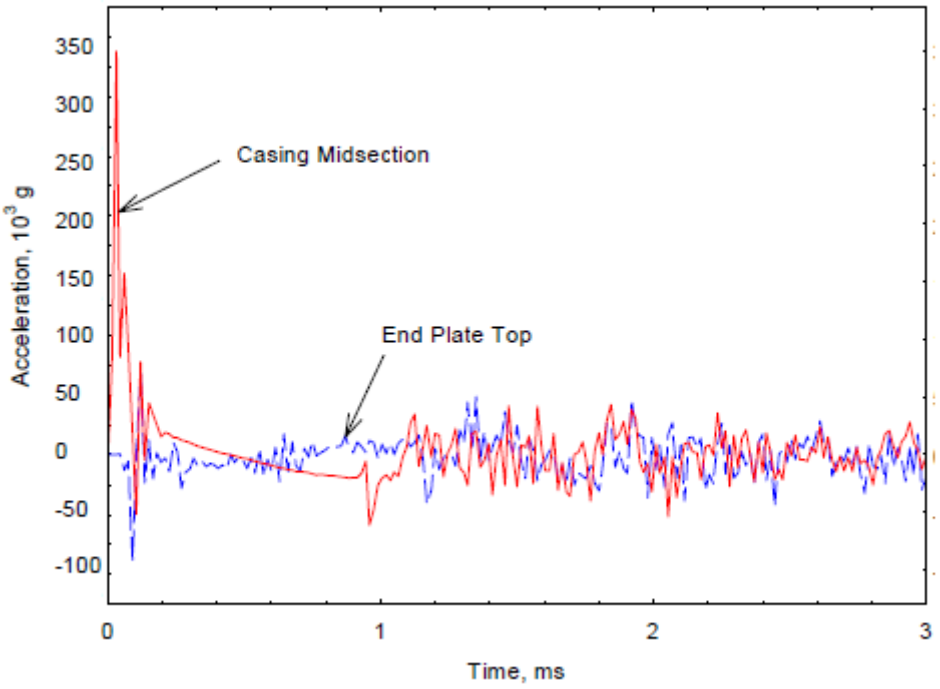

Figure 4-15 Acceleration Profile of wall and shroud at 60,000 rpm

The flywheel mechanical system components are presented in this chapter. A composite carbon fiber rotor is used in the ROMAC flywheel. The characterization of the composite behavior is studied by performing a stress analysis on the rotor. The housing was designed in such a way that it will be able to contain the rotor debris on failure. Three different modes of failure were studied. From a mechanical standpoint- it can be concluded that the composite flywheel is designed to be within the desired stress range and the housing will be able to withstand the damage created by the rotor on failure.

5 Bearing support system

The design of the magnetic bearing system is an integral part of having a good overall flywheel design. This chapter discusses the design and analysis of the magnetic suspension system of the ROMAC flywheel. This system is comprised of a double-acting thrust bearing and two radial magnetic bearings. Preliminary calculations are performed using linear circuit models to determine the various design parameters such as air gap; number of coil turns required, stator/rotor diameter and rotor lamination thickness. Finally, a 3-dimensional finite element analysis is conducted in ANSYS to verify the calculated design parameters from the linear circuit model. The magnetic flux path was calculated for both the thrust and radial magnetic bearings and important parameters such as load capacity, flux density, inductance, magnetic energy and slew rate were calculated.

5.1 Flywheel magnetic bearing design

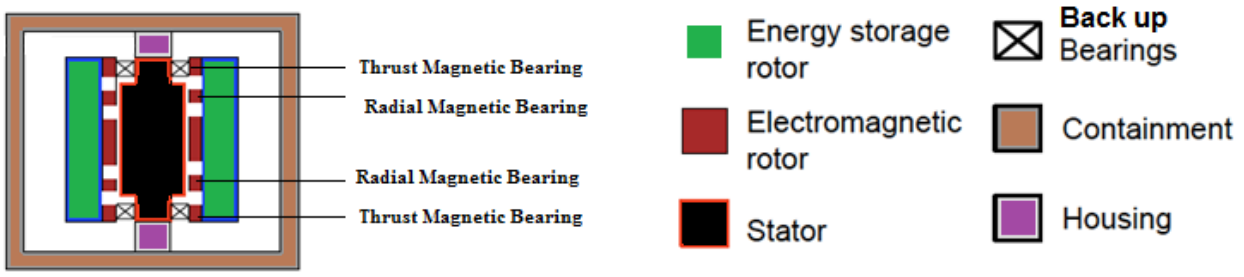

Figure 5-1 A schematic of the ROMAC flywheel design

As previously discussed in Chapter 3, the ROMAC flywheel rotor will be supported by a 5 axis AMB system comprising of 2 radial magnetic bearings and a double acting thrust magnetic bearing. The locations of these bearings are indicated in Figure 5-1. It can be seen that the double acting thrust bearing is located at the top and bottom of the rotor while the radial magnetic bearings are located equidistant on either sides from the PM alternator.

The dimensions of the composite rotor were computed previously. In order to have a storage capacity of 1 kW-hr, it was calculated that the composite flywheel should have a wall thickness of about 100 mm along with a height of about 400 mm and, assuming a carbon-fiber epoxy composite. The weight of the rotor was calculated to be around 60 kg. The polar mass moment inertia of the rotor was then 0.458 kg-m^2. At these dimensions, the flywheel should rotate at a maximum speed of 40,000 rpm and a minimum speed of 20,000 rpm to provide 1 kW-hr of energy storage. Silicon iron was chosen as the material for these bearings and the corresponding properties were considered in the calculations. These values are used as starting points for the magnetic bearing design.

5.2 Analysis

This section covers the linear circuit (LC) model and finite element analysis (FEA) for the thrust and radial magnetic bearing. Linear circuit models were used for the initial sizing of the double-acting thrust bearing and the radial bearings. These initial designs were then verified using a finite element analysis.

5.2.1 Thrust Magnetic bearing

A double-acting thrust magnetic bearing was designed for the flywheel. The sectional view of the thrust magnetic bearing is depicted in Figure 5-2. The main function of the bearing is to levitate the entire flywheel and to resist dynamic thrust loads while in operation. The bearing is comprised of three major parts: the thrust disk, which is the rotating part of the bearing and is attached to the flywheel, the thrust stator which is attached to the stator back iron and the coils inside the stator.

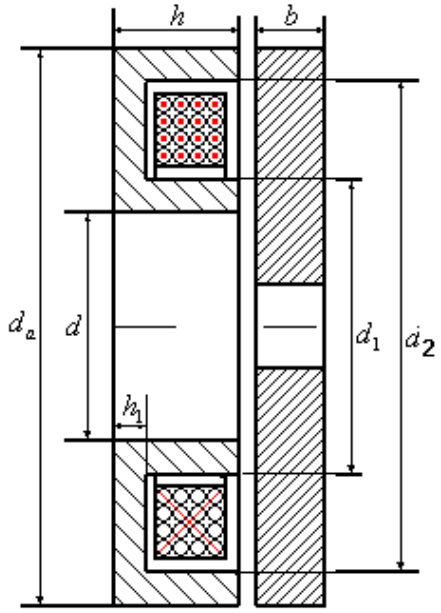

Figure 5-2 : Sectional view of the thrust magnetic bearing

The design load capacity *F* is computed using the total rotor weight and a safety factor. This is expressed as:

$$F = (SF) \times mg \qquad \textbf{(5-1)}$$

The design safety factor *SF* accounts for tolerances in the static load capacity, fringing and leaking effects, and unmodeled transient loads. Standard industrial practice is to select a safety factor of 3.

The magnetic force in a thrust bearing is given in terms of flux density *B* and pole cross sectional area *A* as:

$$F = \frac{B^2 A}{\mu_0} \qquad \textbf{(5-2)}$$

The flux density can further be written in terms of number of winding turns *N*, current in the coil *I* and air gap *g* as:

$$B = \frac{\mu_0 Ni}{2g} \tag{5-3}$$

Using Eqns. (5-1) - (5-3), the minimum pole cross-sectional area was calculated. The inner and outer diameters of the coil cavity were calculated by assuming equal flux going through the inner and outer poles. The constraint was enforced by forcing the pole face areas to be equal, or:

$$A_a = A_{gi} = A_{go} = \frac{\pi(d_1^2 - d^2)}{4} = \frac{\pi(d_a^2 - d_2{}^2)}{4} \tag{5-4}$$

Further, the number of turns was calculated based on the maximum current density J_{max}. The maximum current density is a limit commonly employed in industry for coil currents per area to avoid problems associated with coil overheating such as wire insulation break down. This value is usually about 7-9 A/mm^2. The required number of turns is also a function of the peak current I_{max}. The required number of turns is then:

$$N = \frac{A_a J_{\max}}{I_{\max}} \tag{5-5}$$

Using Eqs. (5-1) – (5-5), the initial sizing was done on the thrust bearing to determine the necessary parameters including pole widths, nominal air gap and number of coil turns. The coil inductance L_c can be approximated as:

$$L_c = \frac{\mu_o N^2 A_a}{2g} \tag{5-6}$$

And the maximum force slew rate can be calculated as [157, 158]:

$$\frac{dF_{tot}}{dt} = \frac{2I_b V_{\max}}{g_o} \tag{5-7}$$

Finally the current gain, K_i and the open loop stiffness K_x can be given by

$$k_i = \frac{2NB_{bias}A_a}{g} \qquad (5\text{-}8)$$

$$k_x = \frac{4B_{bias}{}^2 A_a}{\mu_0 g} \qquad (5\text{-}9)$$

5.2.1.1 Thrust Bearing Finite Element Analysis

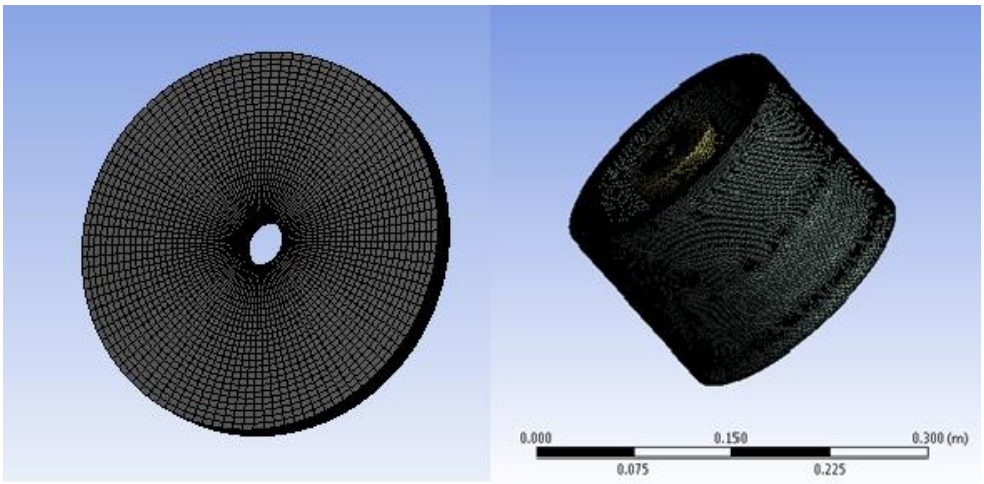

Figure 5-3: Thrust magnetic bearing model

A three dimensional FEA was conducted to verify the parameters obtained from the linear circuit model of the thrust bearing. ANSYS 11 was used to perform the analysis. A mesh density study was performed to ensure that the results had numerically converged. About 1 million elements were used in the analysis with a denser mesh in the air gap. Figure 5-3 shows the modeled thrust magnetic bearing

The flux path and the maximum load capacity were calculated when maximum current was applied to the coils. Other parameters of interest are the inductance, slew rate and magnetic energy. The circuit model developed earlier assumes that all the magnetic flux generated by the coils passes across the air gap. However, all actuators will have some flux which does not cross the gap, generally leaking directly from the sides of one pole to the sides of an adjacent pole. These effects are captured by the finite element model.

Inductance is not directly available from the finite element solution. However, the inductance can be found from the total magnetic field energy, *W*, produced by the maximum current. The inductance can then be calculated as [159]:

$$L_c = \frac{2W}{I^2} \qquad \textbf{(5-10)}$$

To compute the value of open loop stiffness, the rotor was centered in position corresponding to a zero net force. Subsequently, the rotor was moved in the x direction in increments of 0.05 mm and the corresponding force was noted down. This was repeated until sufficient points were obtained to plot a curve corresponding to force and displacement. The slope of this curve gives the open loop stiffness parameter

$$k_x = -\frac{d|f|}{dx}\bigg|_{x=x_0} \qquad \textbf{(5-11)}$$

Similarly, in order to obtain the current gain, k_i, the value of the perturbation current was changed incrementally and the corresponding force was noted. The slope of force vs. perturbation current gives the current gain.

$$k_i = -\frac{d|f|}{dx}\bigg|_{i=ip_0} \qquad \textbf{(5-12)}$$

5.2.2 Radial magnetic bearing

An inside out E-core type radial magnetic bearing is designed for the flywheel as depicted in Figure 5-4. This is one of the unique features of the ROMAC flywheel. In contrast to traditional magnetic bearing design, the bearing comprises of an inner stator component and an outer rotor lamination component. The stator poles are pointed outwards as can be seen in figure 5-4 (a). The stator component is attached to the back-iron while the laminations are attached to the inner steel spline rotor.

In this design, the rotating part of the bearing is the outer ring. The bearing poles, windings, and the back iron are inside of the rotating ring and are on the stator. The E-core arrangement has four quadrants. An example quadrant is shown in Figure 5-4(b). The main pole in the center has about twice the pole face area as the two auxiliary poles. The bearing has a total of 12 poles.

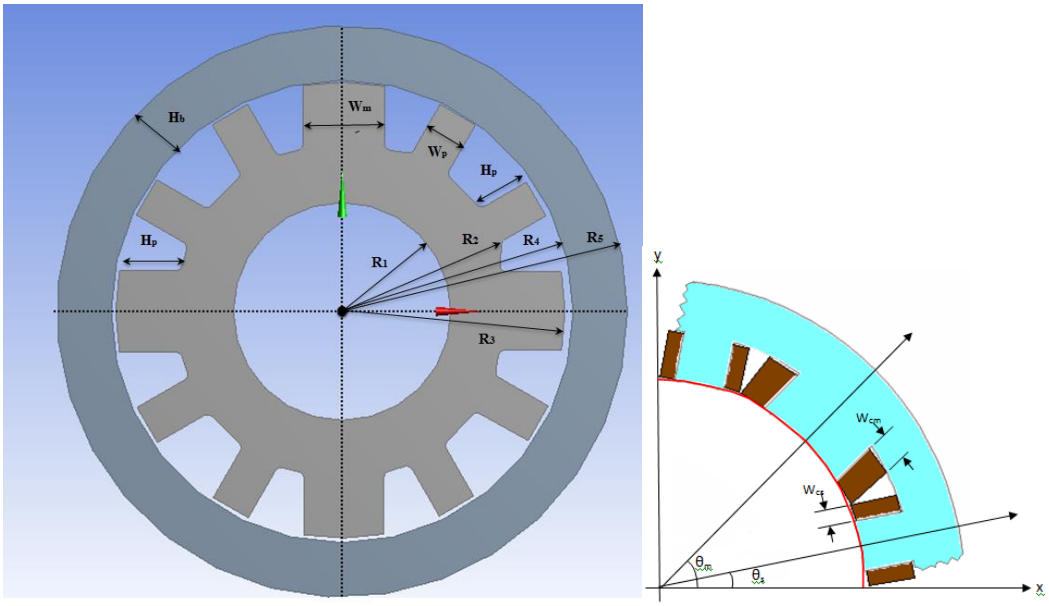

Figure 5-4 (a) Inside out E-core magnetic bearing (b) E-core magnetic bearing showing coil widths

The corresponding linear circuit for a single quadrant is shown in Figure 5-5 [29]. It is assumed that the magnetic flux is contained within each quadrant. Each quadrant has two magnetic flux loops.

5.2.2.1 Linear Circuit model

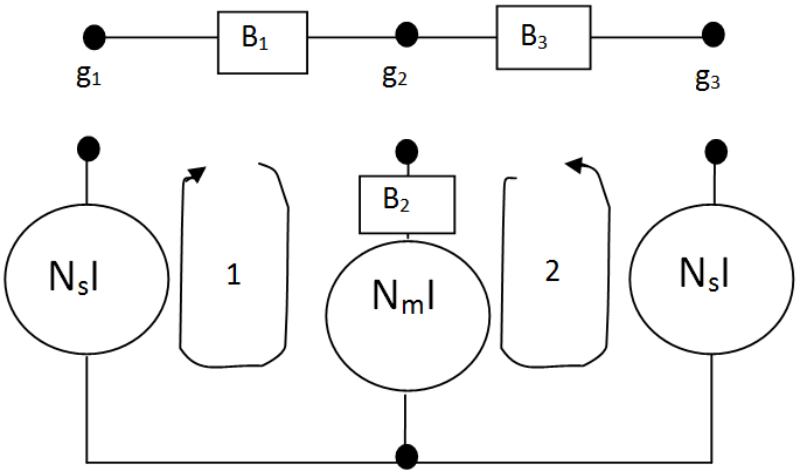

Figure 5-5 E-core Linear Magnetic Circuit Model [29]

The load capacity (F_{load}) of the radial bearing is calculated based on the rotor unbalance me_u. The unbalance level is based on residual unbalance levels recommended by API 617 [160].

$$me_u = 6350\frac{W}{N} \qquad \textbf{(5-13)}$$

In Eq. (5-9), the unbalance level me_u is expressed in g-mm. The weight of the rotor W is in kg, and the running speed N is in rpm. The units are not consistent, but the unbalance level is driven by specification. The resulting unbalance force amplitude is then given by:

$$F = \left(SF\right)me_u\Omega^2 \qquad \textbf{(5-14)}$$

The Eight Edition of API 617 will require a maximum safety factor of 12 for vibration limit checks.

The design radial force for one quadrants of the e-core bearing is found from [29]

$$F_{design} = \frac{A_{pm} B_{knee}{}^{2} [1 + \sin(45^{o} + \theta_{s})]}{2\mu_{o}} \quad \textbf{(5-15)}$$

Assuming equal flux density in all of the poles, the flux density can be found in terms of air gap g, number of main pole turns N_m, and side pole turns N_s-as:

$$B = \frac{\mu_{o}(N_{m} + N_{s})I}{2g} \quad \textbf{(5-16)}$$

Similar to the thrust bearing calculations performed in the previous section, the corresponding values of flux and current densities were taken. The three coils of each e-core are wound in series and the auxiliary poles have half the cross-sectional area of the main poles, the inductance for the circuit is given by [29]:

$$L = \frac{\mu_{0} A_{p} (N_{m} + N_{a})^{2}}{2g} \quad \textbf{(5-17)}$$

And the slew rate can be computed as

$$S = 2\frac{[1 + \sin(45^{\circ} + \theta_{s})]}{g} \sin(45^{\circ}) I_{b} V_{c} \quad \textbf{(5-18)}$$

Equations (5-9) to (5-14) were used to size the radial magnetic bearing.

Similar to the thrust bearing design, the values of K_i and K_x can be obtained from (5-8) and (5-9) respectively.

5.2.2.2 Finite Element analysis:

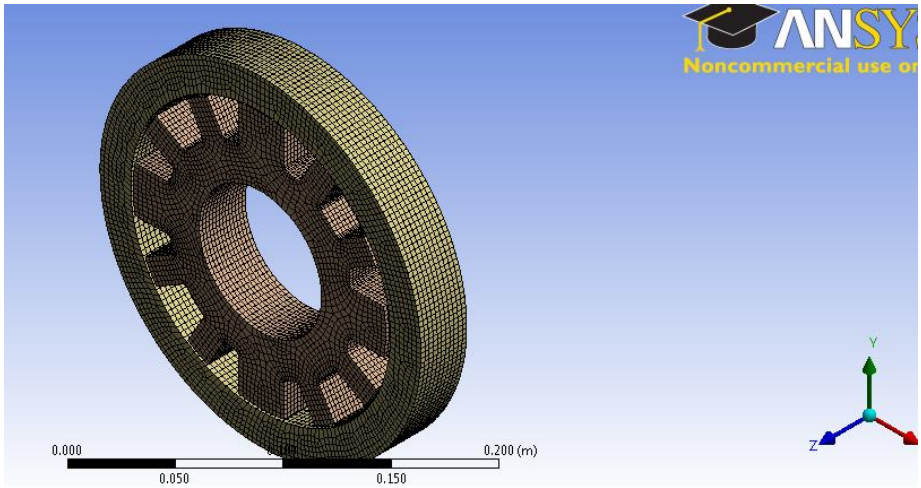

Figure 5-6 Radial magnetic bearing model

Because the circuit model assumes linear magnetic properties, the location and extent of saturation must be evaluated with finite element analysis (FEA). As with the case of the thrust bearing, an FEA was conducted to verify the load capacity, flux path and flux density while calculating parameters such as inductance, magnetic energy and slew rate. The E-core model is shown in Figure 5-6. The inductance was computed based on Eq. (5-10).

5.3 Results

5.3.1 Thrust magnetic bearing

The different parameters computed from the linear circuit model analysis are listed in Table 5-1. It should be noted that the design flux knee density was taken as 1.2T. This is a typical linear B-H flux limit for silicon iron alloys. Also, a packing factor of 0.7 was applied in computing the coil cavity dimensions. The packing factor accounts for unused space with round wire winding and wire insulation. The packing factor results in an increased volume when calculating the magnetic bearing size. A 14AWG wire was used for the analysis.

Notation	Parameter	Value
m	Mass of the flywheel	50 kg
SF	Safety Factor	3
F_{Design}	Minimum required Load capacity	1500N
B_{Knee}	Knee flux density	1.2 T
I_{max}	Maximum current in coil	10 A (based on amplifier)
I_b	Bias current in coil	5 A
g_0	Nominal air gap	1.5 mm
d	Stator inner diameter	70 mm
d_a	Stator outer diameter	300 mm
h	Stator thickness	50 mm
N	Number of turns	288 turns
x	Width of coil cavity	20 mm
l_c	Length of coil cavity	105 mm

Table 5-1: Thrust magnetic bearing parameters

5.3.1.1 Finite Element Analysis

A two-dimensional thrust bearing model was developed in ANSYS using the dimensions calculated with the linear circuit model. This was done to verify the model before performing a full 3 dimensional analysis. Figure 5-7 (a) shows the flux lines around the thrust bearing. It can be seen that at the highest flux density was observed at the air gap. The 2D model also shows there is some flux leakage associated with the model. Figure 5-7 (b) shows the amplitude of flux density distribution of the thrust bearing. The two peaks that can be seen correspond to the air gap of the thrust bearing. These are typical results which serve as a model check.

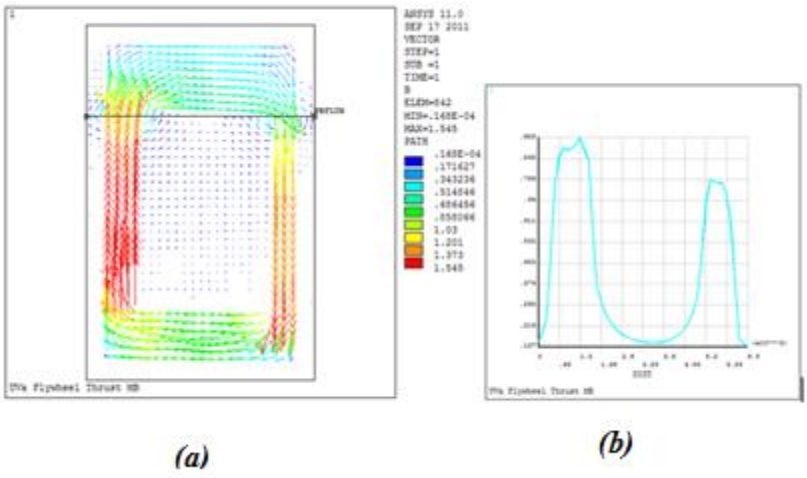

Figure 5-7: 2D Flux path and peaks for thrust bearing

The outputs studied in the 3D analysis were primarily the load capacity, flux density and the flux path. Figure 5-8 and Figure 5-10 show the results obtained from ANSYS. It should be noted that the flux density peaked at about 1.24 T with the obtained load capacity of 1800 N compared to the minimum required load of 1500 N. The force of the same magnitude (but opposite direction) was found on the thrust disk and well as the stator.

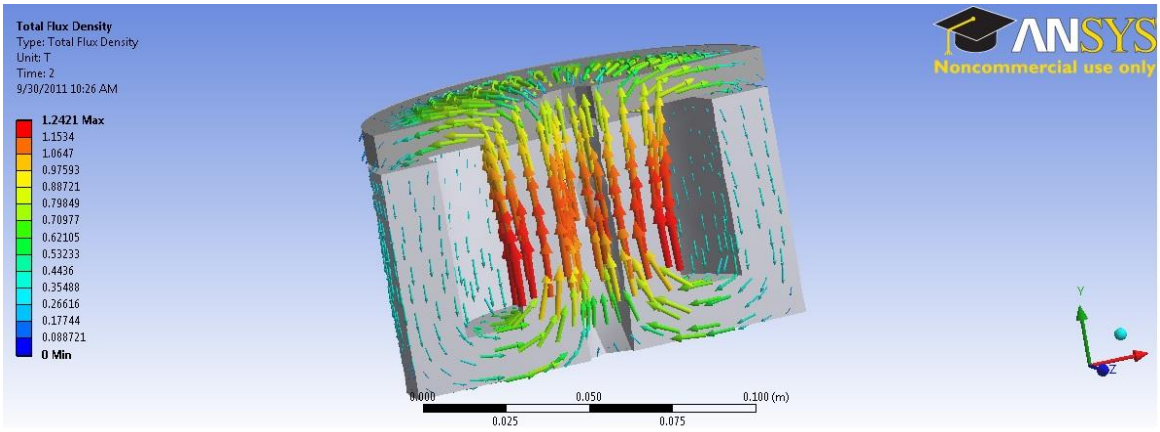

Figure 5-8: Flux path and total flux density of magnetic thrust bearing

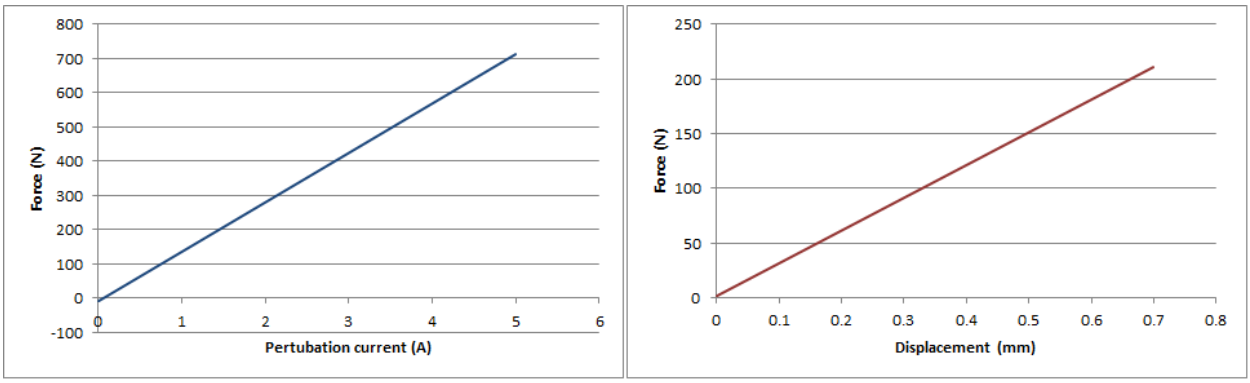

Figure 5-9 (a) Force vs. Displacement curve (b) Force vs. Current curve

The finite element model can also be used to estimate the leakage and improve the inductance calculation, which is a measure of the total magnetic field energy produced by a given current. The inductance value also gives us an idea of the frequency response of the bearing. Table 5-2 shows a comparison between the linear model and the FEA values obtained.

Analysis method	**Force (N)**	**Magnetic energy (J)**	**Inductance (mH)**	**Open loop stiffness (N/mm)**	**Current Gain (N/A)**	**Force Slew rate (N/s)**
Circuit Model	1500	-	68.1	172.1	286.6	$3.9 *10^6$
FEA	1812	3.82	74.5	143.92	299.05	$3.2 *10^6$

Table 5-2. Comparison of thrust bearing parameters

The inductance predicted by the finite element model was 9 percent higher than what was predicted by the linear circuit model. This led to a corresponding decrease in force slew rate predicted by the finite element model when compared to the linear circuit model. However, the load capacity prediction in the finite element model was significantly higher than the linear circuit model prediction.

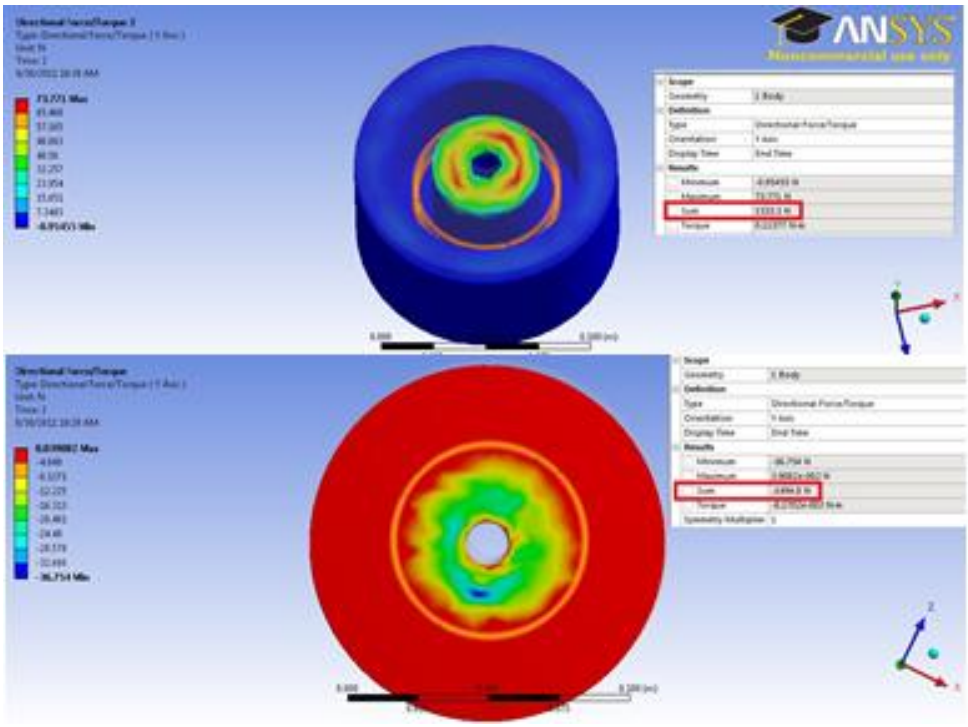

Figure 5-10: Force obtained from design on thrust stator and thrust disk

5.3.2 Radial magnetic bearing

The different parameters computed from the linear circuit model analysis of the e-core radial bearing are listed in Table 5-3. As with the thrust bearing, the design flux density was taken as 1.2T, and a packing factor of 0.7 was applied in computing the coil cavity dimensions. A 14AWG wire was used in the analysis.

Notation	Description	Value
F_{load}	Minimum required load capacity	850 N
W_m	Width of main pole	40 mm
W_s	Width of side pole	20 mm
W_{cm}	Core width on main pole	12.5mm
W_{cs}	Core width on side pole	6.25mm
L	Bearing axial length	92 mm
H_b	Height of back iron	33.5 mm
H_p	Height of radial pole	33.5 mm
H_c	Height of wounded coil	24 mm
H_l	Height of rotor lamination	30mm
R_1	Inner radius of Stator	35mm
R_2	Coil space radius	68.5mm
R_3	Outer radius of stator	101 mm
R_4	Inner radius of rotor laminations	102mm
R_5	Outer radius of rotor laminations	132mm
θ_m	Main pole centerline angle	45^o
θ_s	Side pole centerline angle	11^o
A_{pm}	Main pole cross sectional area	$3680mm^2$
A_{ps}	Side pole cross sectional area	$1840mm^2$
A_{cm}	Coil cross sectional area main	$418.75mm^2$
A_{cs}	Coil cross sectional area on side	$209.375mm^2$
N_m	Number of turns on main pole	134
N_s	Number of turns on side pole	67
g	Air gap	1 mm
I_{max}	Max current in coil	10A

Table 5-3 Calculated design parameters of radial magnetic bearing

5.3.2.1 Finite Element Analysis

A 3D finite element magnetic analysis was done to verify the load capacity, flux path, flux density, open loop stiffness and current gain as in the case of the thrust bearing. Having verified the model for errors a mesh convergence study was done to ensure that enough elements were selected for the analysis. About 1 million elements were used for the analysis. Figure 5-11 and Figure 5-12 show the results obtained from ANSYS. It should be noted that the flux density peaked at about 1.6 T at maximum current with the load capacity of 990 N. It should be noted that the minimum load capacity is 850 N.

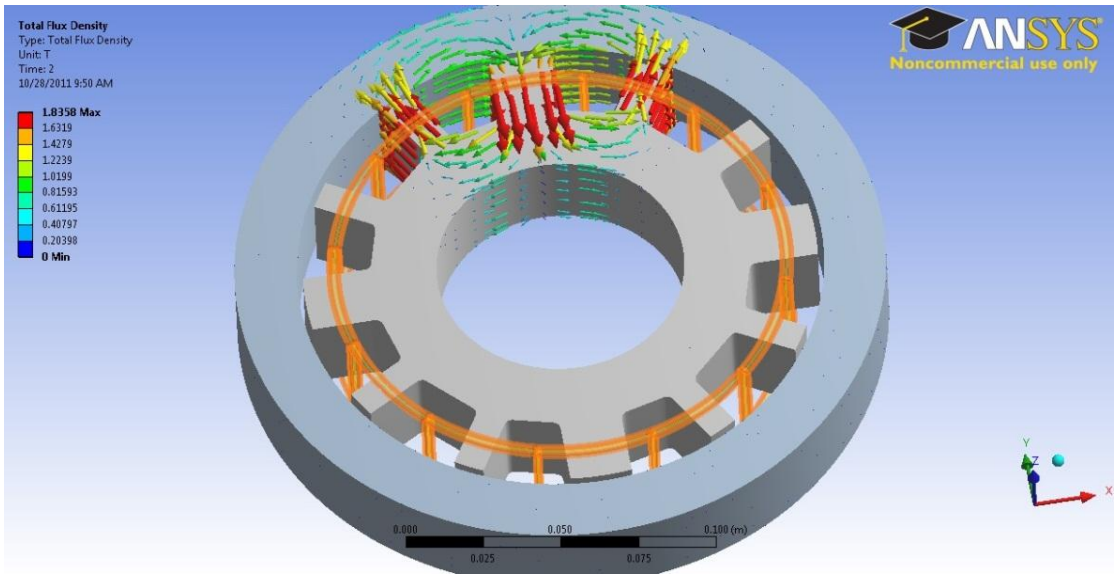

Figure 5-11: Flux path and total flux density of magnetic radial bearing

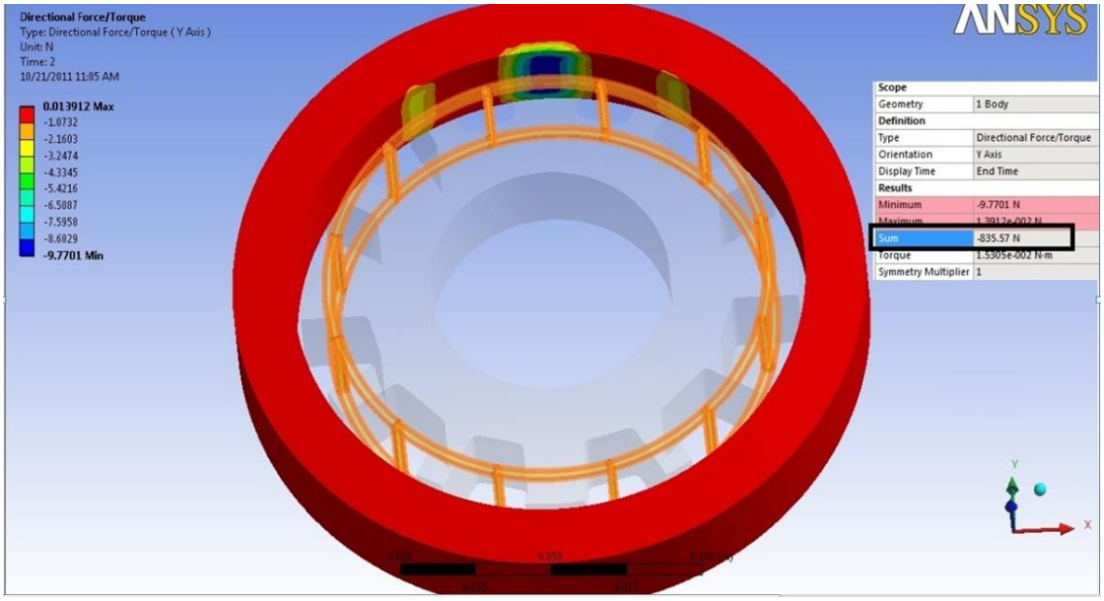

Figure 5-12 : Force obtained from 3D model on radial bearing laminations

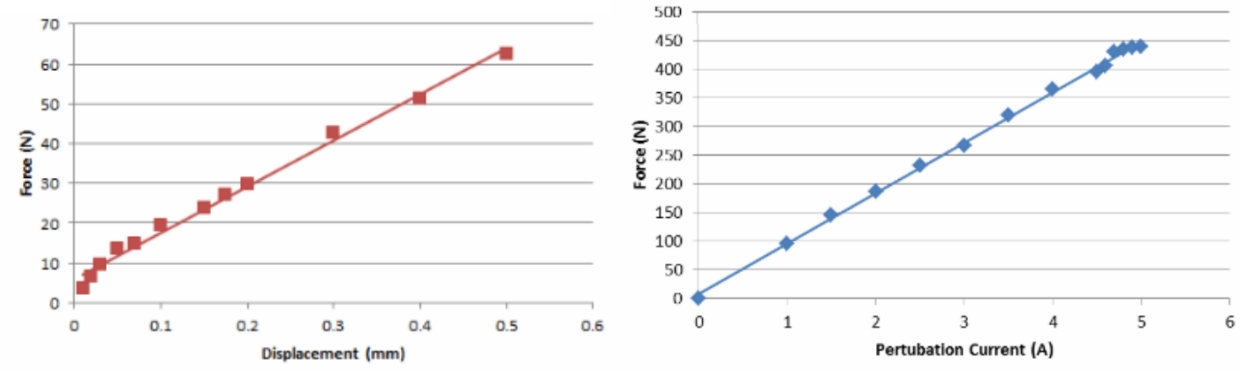

Figure 5-13 (a) Force vs displacement curve (b) Force vs. perturbation current curve

The corresponding curves are plotted in Figure 5-13. The slope of the curves gives the value of k_x and k_i respectively. From Figure 5-14, it is clear that the maximum flux density in the linear range is 1.36 T.

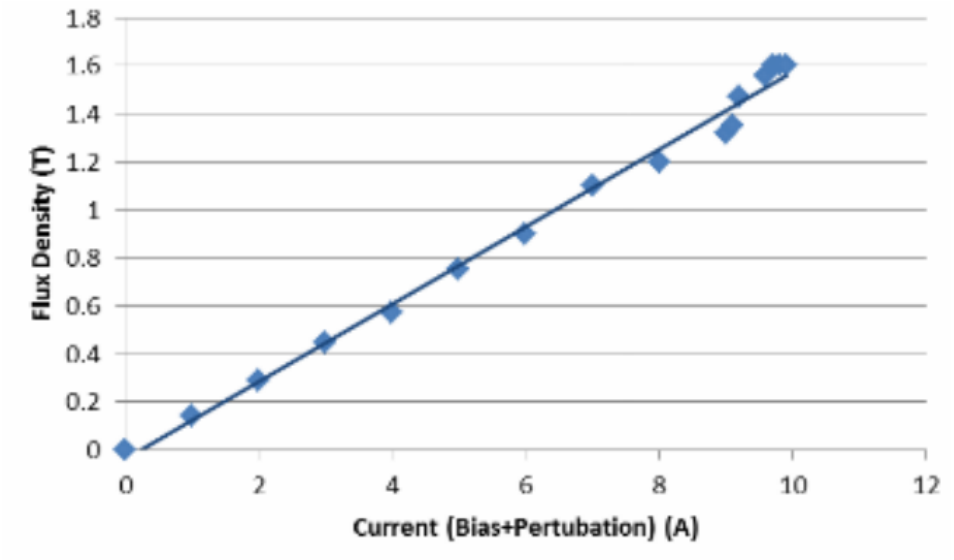

Figure 5-14 Flux density vs. Current

Table 5-4 shows a comparison between the linear model and the FEA values obtained in calculations of inductance slew rate and load capacity.

Analysis method	**Force (N)**	**Magnetic energy (J)**	**Inductance (mH)**	**Open Loop Stifness (N/mm)**	**Current gain (N/A)**	**Force Slew rate (N/s)**
Circuit Model	850	-	92.4	128.3	42.6	$7.1 * 10^6$
FEA	990	4.68	101.2	113.4	45.3	$6.4 * 10^6$

Table 5-4 Comparison of radial magnetic bearing parameters

As with the thrust bearing, the inductance predicted by the radial bearing finite element model was about 9 percent higher than that predicted by the linear circuit model. This resulted in a corresponding drop in force slew rate. The load capacity predicted by the finite element model was also higher than that predicted by the linear circuit model. However, the FEA predicted a peak flux of 1.36 T, which is entering the saturation flux region of silicon iron alloys.

This study discusses the design of a thrust and radial magnetic bearing for a flywheel energy storage system. This flywheel energy storage system comprises of two radial magnetic bearings and a double-acting thrust magnetic bearing.

The design procedure for both the thrust and radial magnetic bearings was similar. Firstly, the load capacity was calculated, from which the required pole surface area could be found. The air gaps, maximum current in the amplifier, inner and outer diameters of the stator along with their thickness were chosen based on which the number of coil turns, length and width of a pole and other parameters were calculated. Finally, these values were input in ANSYS and a 3 dimensional model was created. The flux path along with the load capacity was visualized to check if they match with the calculated values. It should be noted that both these techniques yielded similar results. The parameters such as flux path, flux leakage, saturation and non-linear effects were taken into account in the 3-D model making it a much more accurate technique.

The required load capacity of the thrust bearing was based on the weight of the flywheel while that of the radial bearing was calculated based on the rotor unbalance. Parameters such as slew rate, magnetic energy and inductance were compared between the linear and FEA models. When compared to the finite element models, the linear circuit models had lower predictions for load capacity, inductance, and a higher prediction of slew rate.

5.4 Back up bearings

The ROMAC flywheel backup bearing system consists of a duplex pair of 25 mm angular tapered roller SKF bearings at each end of the shaft. Four row tapered roller bearings are used to prevent excessive motion in both radial and axial directions. The lower backup bearing also acts as a backup thrust bearing due to the inclusion of thrust collars on the rotor. The dimensions of these bearings are provided in Table 5-5. The backup bearings have radial and axial clearances of 0.7 mm between the bearing inner races and the shaft. This clearance is less than one-half of the magnetic air gaps. The backup bearings are expected to carry load in the following cases:

1) When the system is at rest and the magnetic bearings are turned off,

2) In the event of a substantial shock transient that exceeds the capacity of the magnetic bearings

3) In the event of a component failure that causes the loss of one more axes of control for the magnetic bearing.

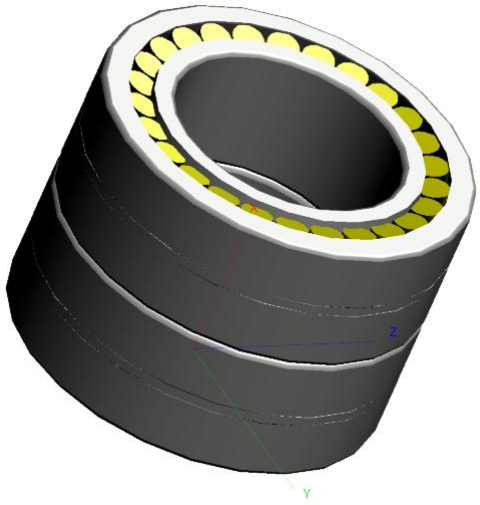

Figure 5-15 A schematic of a 4 row tapered roller bearings

The bearings are hybrid style with 52100 races and SiN_3 rollers and a light fill of vacuum compatible grease. Steel sleeves are used for the rotor contacting surfaces. Radial flexibility is provided by an elastomeric element between the mount and housing. The mount is free to slide in an axial clearance space of 0.025 mm. The net radial stiffness is $5.0 * 10^6$ N/m, resulting in a lowest radial natural frequency of 40 Hz. A hard stop limits radial deflection on the elastomer to 0.075 mm.

Inner diameter	**Outer diameter**	**Static load**	**Dynamic load**	**Fatigue load point**	**Mass supported**	**Designation**	
70 mm	300 mm	4680 KN	9300 KN	815 KN	300 kg	BT4B G/HA1	332441

Table 5-5 Parameters of Back up bearings

SKF produces an extensive range of four-row tapered roller bearings which covers not only the conventional designs with intermediate rings between the outer and/or inner rings, but also a new design with modified rings which integrate the intermediate rings. The particular advantages of these four-row tapered roller bearings without intermediate rings, which were developed by SKF, include

- simpler mounting because of fewer components
- improved load distribution over the four rows of rollers, leading to less wear and longer service life
- simpler axial location on the roll necks because of reduced inner ring width tolerances

6 Power Electronics

The power electronics (PE) is one of the most important components which determines the output and efficiency of the FES system [21]. The design and choice of power electronics depends on the input and output types of the system i.e DC or AC [161]. The objective of a PE design is to be capable of delivering the required power over a wide range of rotor speeds. A brushless permanent magnet generator (in a flywheel) produces variable frequency AC current. In most applications though, the load requires a constant frequency making it necessary to first rectify the current and then convert it back to AC. Power converters for energy storage systems are based on silicon controlled resistors (SCR), gate turn off thyristors (GTO) or insulated gate bipolar transistors (IGBT) switches. The most common kind of switches used in recent flywheel design is the IGBT [162]. This is because the IGBT is a solid-state switch device with the ability to handle voltages up to 6.7 kV, currents up to 1.2 kA and most importantly high switching frequencies.

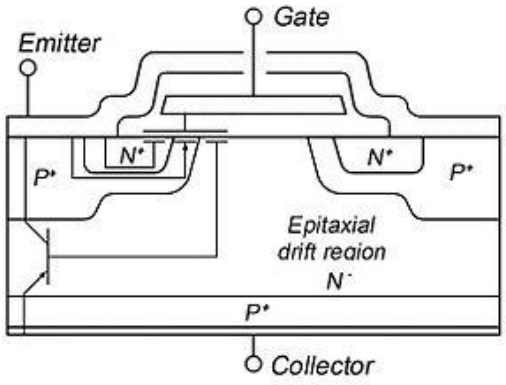

Figure 6-1 A schematic of an IGBT [163]

The technique used to produce AC current from DC is called Pulse-Width Modulation (PWM). Pulses of different length are applied to the IGBTs in the inverter, causing the DC current to be delayed by the inductive load and a sine wave is modulated [164]. A fast switching frequency in the power converter improves emulation of a sine wave mainly by eliminating some of the

higher order harmonics. To reduce the harmonic content even further a filter, consisting of capacitors and inductors, can be connected on the AC side of the output.

The 1KW-hr FES system will comprise of a three phase IGBT based inverter/rectifier system. A schematic of this system is shown in Figure 6-1. When the flywheel is operated in the motor mode (i.e being charged) the converter performs the function of the inverter. The external inductor is used in series when the FES system is in the motor mode to reduce total harmonic distortion which ultimately increases power losses and temperature. Similarly, when the flywheel is operated in the generator mode (i.e being discharged), the converter performs the function of the controlled rectifier. In this mode, the external inductor is bypassed which allows a large amount of current to be taken out of the system.The boost conveter will be a combination of the PM machine inductance, converter and DC link capacitor. The magnetic energy is stored in the PM machine winding inductances. This energy is then released through the machine-side converter and is boosted by the DC bus capacitor.

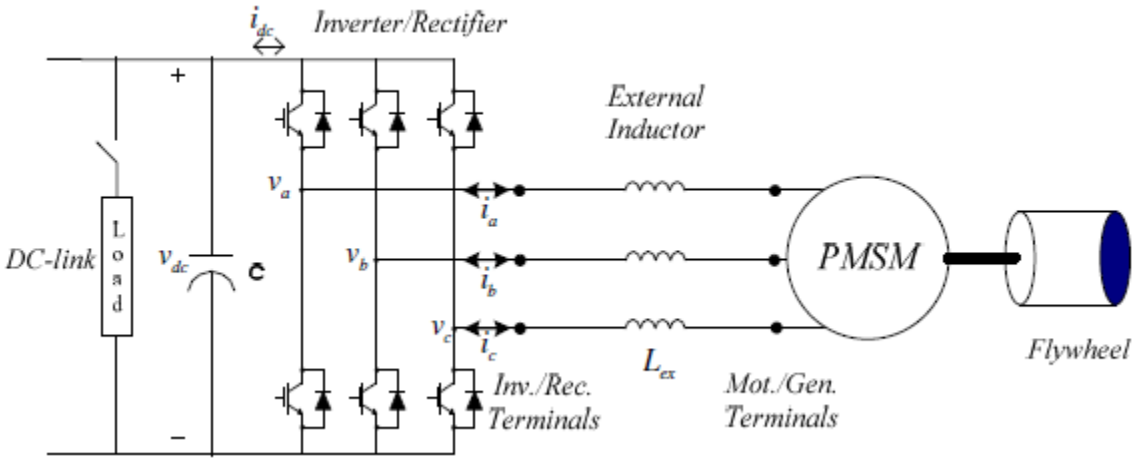

Figure 6-2 A schematic of the power electronics to be used in the 1KW-hr FES system[152]

Design of the PE system is a critical task as compromises have to be made between size, weight, volume, losses and cost. An analytical approach is used here based on [151, 152] to design the power electronics of the FES system.

6.1 Analytical model

The approach taken in this thesis is to model the power electronics using a detailed analytical model. This is done to gain a deeper insight into the model as opposed to using standard software codes (e.g.: Simulink, PSIM, etc.). By understanding the model, a good decision can be made on selecting a standard PWM/IGBT package. This study is based on the synchronous d-q reference frame (SDQRF) explained by Rafsanjan [152]. Figure 6-2 shows the schematic of the PE system. This includes a DC bus, a three phase PWM inverter/rectifier, and external inductor, a PMSM and the high speed flywheel. Each component is modeled individually and finally integrated to create an overall system model.

6.1.1 DC bus

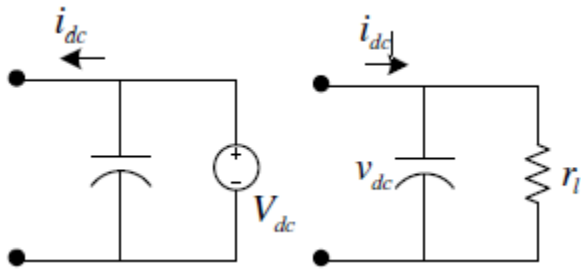

Figure 6-3 DC bus model (a) Motor mode (b) Generator mode[152]

When the flywheel is being charged, the DC bus is modeled in parallel with a capacitor as a DC power supply. During discharge, this power supply is replaced by a resistor and the current direction is reversed. This is shown in Figure 6-3. It is necessary to control the DC bus voltage (V_{dc}) during discharge as it varies widely otherwise. The bus current (i_{dc}) will vary with time during charge and discharge.

6.1.2 Permanent magnet synchronous machine (PMSM)

The 1 kW-hr flywheel uses a PMSM to act as the alternator. Figure 6-4 shows a cross section of a simplified three phase surface mounted slotless PMSM. The stator windings, *as-as′*, *bs-bs′*, and *cs-cs′* are shown as lumped windings for simplicity, but are actually distributed about the stator. It should be noted that rotational speed ω_r and rotor position θ_r can be defined as $N_p/2$ times the corresponding mechanical quantities where N_p is the number of poles (4 in this design).

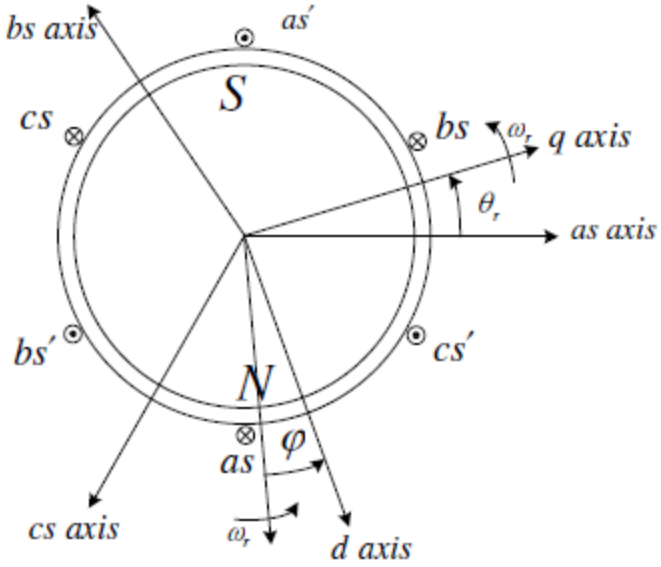

Figure 6-4 Cross section of a PMSM

The voltage Equation in the *abc* stationary reference frame can be given by

$$v_{abcs} = R_s i_{abcs} + N_p \lambda_{abcs} \qquad \textbf{(6-1)}$$

In the matrix form, the function f_{abcs} can be defined as

$$f_{abcs} = [f_{as} \quad f_{bs} \quad f_{cs}]^T \qquad \textbf{(6-2)}$$

Where f : v, I, λ

v, i and λ are the corresponding voltage , current and flux linkage. The stator resistance matrix can be given as

$$R_s = diag[r_s \quad r_s \quad r_s] \qquad \textbf{(6-3)}$$

The flux linkage can also be denoted in terms of the stator self-inductance matrix (L_s) as

$$\lambda_{abcs} = L_s i_{abc,s} + p\iota_m \qquad \textbf{(6-4)}$$

Where

$$L_s = \begin{bmatrix} L_{ls} + L_A & -\frac{1}{2}L_A & -\frac{1}{2}L_A \\ -\frac{1}{2}L_A & L_{ls} + L_A & -\frac{1}{2}L_A \\ -\frac{1}{2}L_A & -\frac{1}{2}L_A & L_{ls} + L_A \end{bmatrix} \quad \textit{(6-5)}$$

And

$$\iota_m = \sqrt{\frac{2}{3}}\,\lambda_m \begin{bmatrix} \sin(\theta_r + \varphi_1) \\ \sin(\theta_r + \varphi_1 - \frac{2\pi}{3}) \\ \sin(\theta_r + \varphi_1 + \frac{2\pi}{3}) \end{bmatrix} \quad \textit{(6-6)}$$

In (6-5) and (6-6) , L_{ls} and L_A are the stator phase leakage and magnetizing inductances respectively, ι_m is the PM flux linkages vector in which $\sqrt{2/3}\ \lambda_m$ denoted the amplitude of flux linkages as obtained from the stator phase windings. This is also called the back-EMF value associated with each stator phase winding. The arbitrary flux linkage phases is denoted by φ_1

The electromagnetic torque is then expressed as

$$T_e = \sqrt{\frac{2}{3}}\,\lambda_m \left[\left(i_{as} - \frac{1}{2} i_{bs} - \frac{1}{2} i_{cs} \right) \cos(\theta_r) - \frac{\sqrt{3}}{2} (i_{bs} - i_{cs}) \sin(\theta_r) \right] \quad \textit{(6-7)}$$

It should be noted that when the flywheel is operated in the motor mode, T_e in ((6-7) is positive. The expression relating speed and electromagnetic torque is given as

$$T_e = Jp\,\omega_m - f_m \omega_m \quad \textit{(6-8)}$$

Where, p is the derivative operator and f_m is the damping coefficient (N.m.s per radian) associated with the flywheel.

In the case of the 1kW-hr flywheel , the rotor is suspended magnetically and is operated in vacuum. Hence, the frictional and windage losses would be very small and hence f_m can be ignored. Chapter 7 shows the losses associated with each component. From theory, we can define the voltage and torque Equations in terms of the rotor reference frame. This is particularly

useful to transform the time varying variables into steady state constants. The transformation of the three phase variables in the stationary reference frame to the rotor reference frame is defined as

$$f_{qdos} = K_s - f_{abcs} \qquad \textbf{(6-9)}$$

Where

$$K_s = \sqrt{2/3}\begin{bmatrix} \cos(\theta_r + \varphi_1) & \cos(\theta_r + \varphi_1 - \frac{2\pi}{3}) & \cos(\theta_r + \varphi_1 + \frac{2\pi}{3}) \\ \sin(\theta_r + \varphi_1) & \sin(\theta_r + \varphi_1 - \frac{2\pi}{3}) & \sin(\theta_r + \varphi_1 + \frac{2\pi}{3}) \\ 1/\sqrt{2} & 1/\sqrt{2} & 1/\sqrt{2} \end{bmatrix} \qquad \textbf{(6-10)}$$

In the matrix form, f_{qdos} can be given as

$$f_{qdos} = [f_{qs} \quad f_{ds} \quad f_{os}]^T, f : v, i, \lambda \qquad \textbf{(6-11)}$$

To obtain the voltage Equation on the d-q axis, Equation ((6-1) is multiplied by K_s. After some differentiation, we obtain

$$v_{qdos} = r_s i_{qdos} + p\lambda_{qdos} - [pK_s]K_s^{-1}\lambda_{qdos} \qquad \textbf{(6-12)}$$

Where

$$[pK_s]K_s^{-1} = \begin{bmatrix} 0 & -\omega_r & 0 \\ \omega_r & 0 & 0 \\ 0 & 0 & 0 \end{bmatrix} \qquad \textbf{(6-13)}$$

Equation (6-12) can then be written as

$$v_{qdos} = r_s i_{qdos} + p\lambda_{qdos} - \omega_r X\lambda_{qdos} \qquad \textbf{(6-14)}$$

Where

$$X = \begin{bmatrix} 0 & 1 & 0 \\ -1 & 0 & 0 \\ 0 & 0 & 0 \end{bmatrix} \qquad \textbf{(6-15)}$$

Using the same technique, an expression for flux linkage can be given as

$$\lambda_{abcs} = K_s L_s K_s^{-1} i_{qdos} + K_s \iota_m = L_{qdos} i_{qdos} + \iota_{qdos} \quad \textbf{(6-16)}$$

Where

$$\iota_{qdos} = \lambda_m \begin{bmatrix} -\sin(\varphi - \varphi_1) \\ \cos(\varphi - \varphi_1) \\ 0 \end{bmatrix} \quad \textbf{(6-17)}$$

$$L_{qdos} = \begin{bmatrix} L_{ls} + \frac{3}{2} L_A & 0 & 0 \\ 0 & L_{ls} + \frac{3}{2} L_A & 0 \\ 0 & 0 & L_{ls} \end{bmatrix} \quad \textbf{(6-18)}$$

We also know that for the three stator windings,

$$i_a + i_b + i_c = 0 \quad \textbf{(6-19)}$$

Hence, the voltage in the d and q axis can be rewritten as

$$\begin{aligned} v_{qs} &= r_s i_{qs} + L p i_{qs} + \omega_r L i_{ds} + e_{qs} \\ v_{ds} &= r_s i_{qs} + L p i_{qs} - \omega_r L i_{qs} + e_{ds} \\ v_{os} &= 0 \end{aligned} \quad \textbf{(6-20)}$$

Where e_{qs} and e_{ds} are the back-Emf of the *q* and *d* axes respectively and are found from:

$$\begin{aligned} e_{qs} &= \omega_r \lambda_m \cos(\varphi - \varphi_1) \\ e_{qs} &= \omega_r \lambda_m \cos(\varphi - \varphi_1) \end{aligned} \quad \textbf{(6-21)}$$

The electromagnetic torque can then be expressed as

$$T_e = \frac{P}{2} \left[\lambda_{ds} i_{qs} - \lambda_{qs} i_{ds} \right] \quad \textbf{(6-22)}$$

Substituting λ_{ds} and λ_{qs} from Equation (6-18 we can deduce that

$$T_e = T_{qs} + T_{ds} \tag{6-23}$$

Where

$$T_{qs} = \frac{P}{2}\lambda_m \cos(\varphi - \varphi_1) i_{qs}$$
$$T_{ds} = \frac{P}{2}\lambda_m \sin(\varphi - \varphi_1) i_{ds} \tag{6-24}$$

Using Equations (6-1) to (6-24), the equivalent circuit of the PMSM can be determined. This is depicted in Figure 6-5. Using a similar technique, the equivalent model for the generating mode can also be found. This is given as

$$e_{qs} = r_s i_{qs} + Lpi_{qs} + \omega_r L i_{ds} + v_{qs}$$
$$e_{ds} = r_s i_{qs} + Lpi_{qs} - \omega_r L i_{ds} + v_{qs} \tag{6-25}$$

And

$$T_e = -\left(\frac{P}{2}\right)\lambda_m\left(\cos(\varphi - \varphi_1) i_{qs} + \sin(\varphi - \varphi_1) i_{ds}\right) \tag{6-26}$$

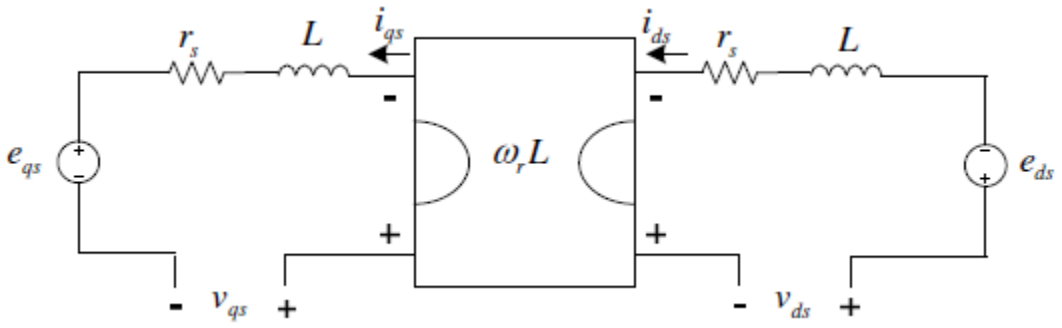

Figure 6-5 d-q model of PMSM in rotor reference frame.

6.1.3 PWM Inverter/Rectifier

It is also useful to transform the three phase controlled current PWM inverter into an equivalent stationary circuit using *d-q* theory as done above [152]. It should be noted that it is assumed that the switches operate in continuous conduction mode (CCM) and therefore the switch pattern can be used with any PWM control provided that the switching harmonics are not dominant. The

switching function is generally a continuous sinusoidal wave. If this function is denoted by *S* with an arbitrary phase φ_2 and an externally controlled modulation index *m*, the result of this transformation, based on theory, is given by

$$v_{abcs} = SV_{dc}\ ; S = \sqrt{\frac{2}{3}}\, m \begin{bmatrix} \sin(\theta_r + \varphi_2) \\ \sin(\theta_r + \varphi_2 - \frac{2\pi}{3}) \\ \sin(\theta_r + \varphi_2 + \frac{2\pi}{3}) \end{bmatrix} \qquad \textbf{(6-27)}$$

$$v_{qdos} = K_s V_{abcs} = K_s S V_{dc} = m V_{dc} \begin{bmatrix} -\sin(\varphi - \varphi_2) \\ \cos(\varphi - \varphi_2) \\ 0 \end{bmatrix} \qquad \textbf{(6-28)}$$

A major advantage of using this kind of transformation is that the switch set analysis becomes time-invariant. The equivalent circuit model of the PWM is shown in Figure 6-6.

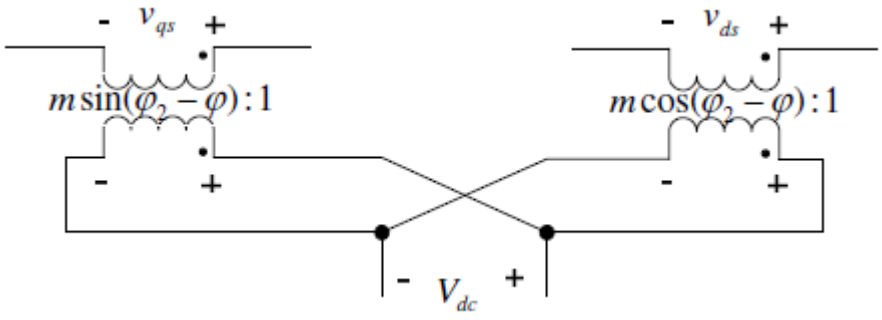

Figure 6-6 d-q model of the PWM inverter

Similarly the rectifier model can be summarized as

$$v_{abcs} = SV_{dc} \; ; \; S = \sqrt{\frac{2}{3}}\, m \begin{bmatrix} \sin(\theta_r + \varphi_2) \\ \sin(\theta_r + \varphi_2 - \frac{2\pi}{3}) \\ \sin(\theta_r + \varphi_2 + \frac{2\pi}{3}) \end{bmatrix} \qquad \textit{(6-29)}$$

$$v_{qdos} = K_s v_{abcs} = K_s S V_{dc} = m V_{dc} \begin{bmatrix} -\sin(\varphi - \varphi_2) \\ \cos(\varphi - \varphi_2) \\ 0 \end{bmatrix} \qquad \textit{(6-30)}$$

Even though Equations (6-29) and (6-30) seem similar to Equations (6-27) and (6-28) their behavior is completely different. The main difference between these two models is at the DC bus voltage. During the inverter mode, the DC bus voltage is a constant value (denoted by V_{dc}), while in the rectifier mode it is controlled externally (denoted by v_{dc}).

6.1.4 Flywheel

Having obtained the equivalent model for the PMSM and the PWM inverter/rectifier, the equivalent circuit of the flywheel can now be deduced. From theory, the differential Equation describing the flywheel system which relates torque, rotational speed and inertia is given as

$$T_e = Jp\omega_m + f_m\omega_m \qquad \textit{(6-31)}$$

Where p is the derivative operator. From Equation (6-31), it can be understood that the motor torque tends to accelerate the flywheel while the friction associated with the flywheel tends to slow it down. Considering that the flywheel is suspended on magnetic bearing, the effect of friction is assumed to be much smaller than the effect of torque. This Equation is very similar to the electrical representation of a voltage source moving the series combination of inertia and friction. This is shown in Equation ((6-32)

$$v = Lpi + ri \qquad \textit{(6-32)}$$

In the case of the flywheel, the sources of inertia and friction are the inductor and resistor respectively. Using electrical analogy theory, the mechanical side of the flywheel can be represented by an equivalent electric circuit as shown in Figure 6-7. The voltage across the terminals of each element represents the torque applied to it and the current through each element represents the speed of the shaft. This circuit clearly illustrates the power dissipated due

to frictional losses and the energy stored in the inertia and the mechanical power delivered by the motor. The voltage across the inertia represents J times the acceleration of the motor shaft.

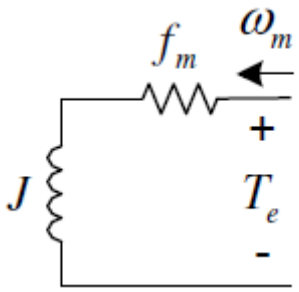

Figure 6-7 Equivalent electrical analogy of the flywheel

The current passing through each element represents the rotational speed of the rotor and voltage across the terminals of each element represents the torque applied to it. From Figure 6-7 it can be seen that power is dissipated due to frictional losses while the energy is stored due to the mechanical power supplied by the motor.

6.1.5 Inductor

At the design phase- it was assumed that a three phase inductor would be used. This was done in order to create a general model. However, if three single phase inductors are used, the model can be modified by removing the mutual inductances between the three phases (i.e setting them to zero). From electromagnetic theory, a coupled magnetic circuit is obtained [165]. This is shown in Figure 6-8. For an initial design, it was assumed that the magnetic path of the center of the leg is equal to the outer two legs. Using stationary reference frame theory, the corresponding voltage v_{abcs} can be obtained as

$$v_{abcs} = L_{ex} p i_{abcs} \qquad \textbf{(6-33)}$$

Where the inductance matrix L_{ex} is denoted as

$$L_{ex} = \begin{bmatrix} L_s^{ex} & -L_m & -L_m \\ -L_m & L_s^{ex} & -L_m \\ -L_m & -L_m & L_s^{ex} \end{bmatrix} \quad \textbf{(6-34)}$$

In Equation (6-34) L_s^{ex} and $-L_m$ stand for self and mutual inductance respectively. For the case of a single phase inductor $-L_m$ = 0.

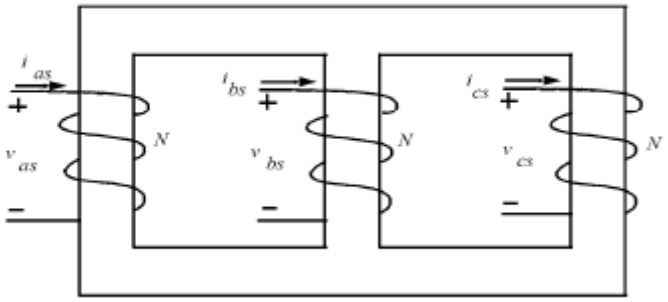

Figure 6-8 Model of a three phase external inductor

Using a similar technique as was done in modeling the PMSM, Equation (6-33) is multiplied by K_s as derived in Equation (6-10). This gives

$$v_{qdoex} = L_{qdoex} p i_{qdoex} + \omega_r X L_{qdoex} i_{qdoex} \quad \textbf{(6-35)}$$

Where,

$$L_{qdoex} = K_s L_{ex} K_s^{-1} \begin{bmatrix} L_s^{ex} + L_m & 0 & 0 \\ 0 & L_s^{ex} + L_m & 0 \\ 0 & 0 & L_s^{ex} - 2L_m \end{bmatrix} \quad \textbf{(6-36)}$$

It should be noted that the *d* and *q* axes inductances are equal (to L_{ex}). For the case of single phase inductors, $L_m = 0$

$$L_{ex} = L_s^{ex} + L_m \quad \textbf{(6-37)}$$

Hence, the *d*-*q* model of the inductor is obtained as

$$v_{qex} = L_{ex} p i_{qex} + \omega_r L_{ex} i_{dex}$$
$$v_{dex} = L_{ex} p i_{dex} - \omega_r L_{ex} i_{qex} \qquad \textit{(6-38)}$$
$$v_{oex} = 0$$

This model is depicted in an equivalent circuit as shown in Figure 6-9

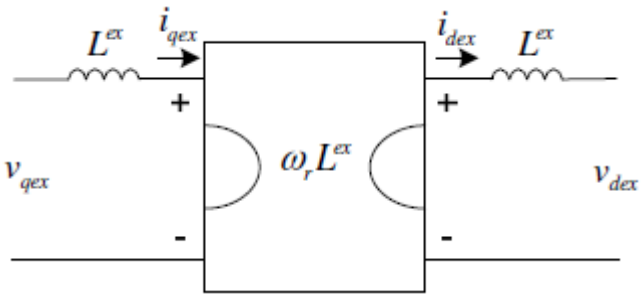

Figure 6-9 Equivalent circuit model of three phase inductor

6.1.6 Integrated *d-q* model

Having obtained models for the flywheel and the PMSM, an integrated *d-q* model can be formed. In order to do this, Equations from gyration theory are used [166]. While the flywheel by itself is stationary the electromechanical conversion in the PMSM involves a gyration since it links a flow variable on one side to an effort variable on the other side. From theory and the models obtained so far, this electromechanical conversion in the PMSM can be given as

$$T_{qs} = \left(\frac{P}{2}\right)\lambda_m(\cos(\varphi - \varphi_1)i_{qs}) \qquad (6\text{-}39)$$

$$e_{qs} = \left(\frac{P}{2}\right)\lambda_m\cos(\varphi - \varphi_1)$$

$$T_{ds} = \left(\frac{P}{2}\right)\lambda_m(\sin(\varphi - \varphi_1)i_{ds}) \qquad (6\text{-}40)$$

$$e_{ds} = \left(\frac{P}{2}\right)\lambda_m\sin(\varphi - \varphi_1)$$

$$T_e = T_{qs} + T_{ds} = Jp\omega_m + f_m\omega_m \qquad (6\text{-}41)$$

The gyration coefficients for the *d* and *q* axes are defined as

$$g_{qs} = \left(\frac{P}{2}\right)\lambda_m\cos(\varphi - \varphi_1) \qquad (6\text{-}42)$$

$$g_{ds} = \left(\frac{P}{2}\right)\lambda_m\sin(\varphi - \varphi_1)$$

The integrated model of the PMSM with the flywheel is shown in Figure 6-10

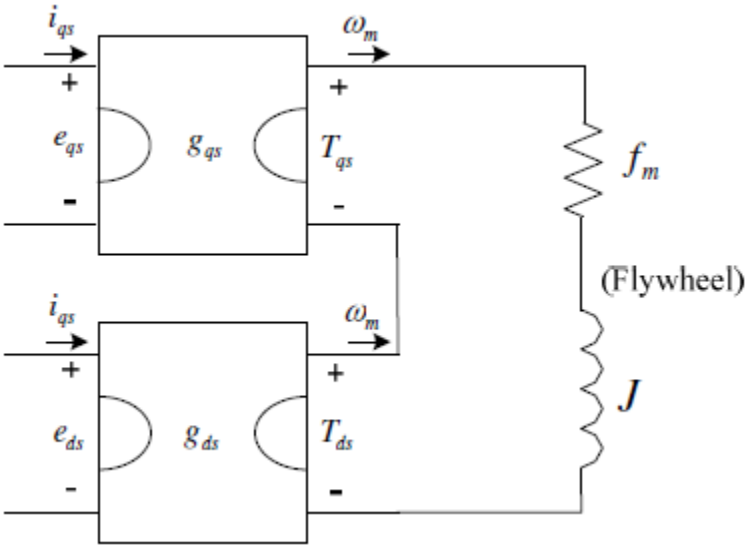

Figure 6-10 Circuit model showing integration of flywheel with PMSM

The next step is to model the integration of the PMSM with the inductor. From Equation (6-35), it can be seen that gyration takes place between the PMSM and the inductor. The Equation modeling this gyration coefficient for the PMSM (g) and the inductor (g_{ex}) is given by

$$g = \omega_r L \qquad (6\text{-}43)$$

$$g_{ex} = \omega_r L_{ex} \qquad (6\text{-}43)$$

$$g_{tot} = \omega_r L_{tot} = \omega_r (L + L_{ex}) \qquad (6\text{-}44)$$

The integrated model of the inductor with the PMSM is shown in Figure 6-11

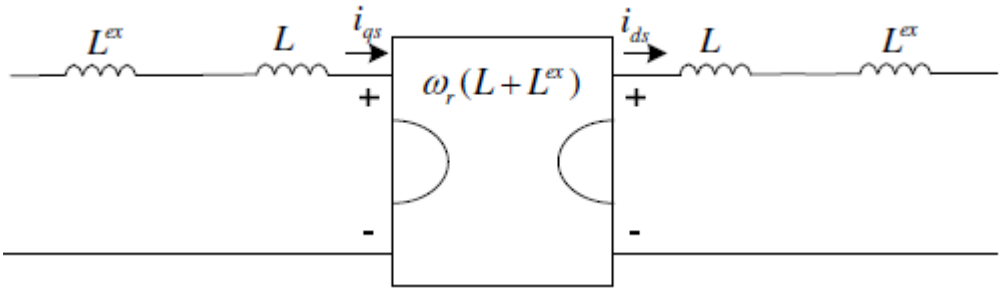

Figure 6-11 Circuit model showing integration of inductor with PMSM

The final integration is that of the inverter/rectifier output terminals with the PMSM and inductor terminals. This is obtained by substituting v_{qdos} given in Equation ((6-20) by the obtained term in Equation (6-28). Having completed the integration, the final model of the DC bus, PWM inverter/rectifier, the PMSM and the flywheel is shown in Figure 6-12. The FES system constantly changes between the charging and discharging mode where the PMSM behaves as a motor and generator respectively. Hence the equivalent circuit models of both these modes are shown in Figure 6-12

It is possible to simplify these stationary circuits by setting the phase of the *d-q* transform to an arbitrary value. Based on the models obtained as above, there are two possible choices, setting $\varphi=\varphi_1$ and $\varphi=\varphi_2$. It can be seen that by setting $\varphi=\varphi_1$ the original system is similar than what is obtained by setting $\varphi=\varphi_2$. This is because the first selection coincides with the standard *d-q* reference definition in literature where the d-axis is aligned with the Permanent magnetic field

axis. As shown in [152] it should be noted that there is no loss of generality by simplifying the model. The reduced model is shown in Figure 6-13 for the case of $\varphi=\varphi_1$ and in Figure 6-14 for the case of $\varphi=\varphi_2$.

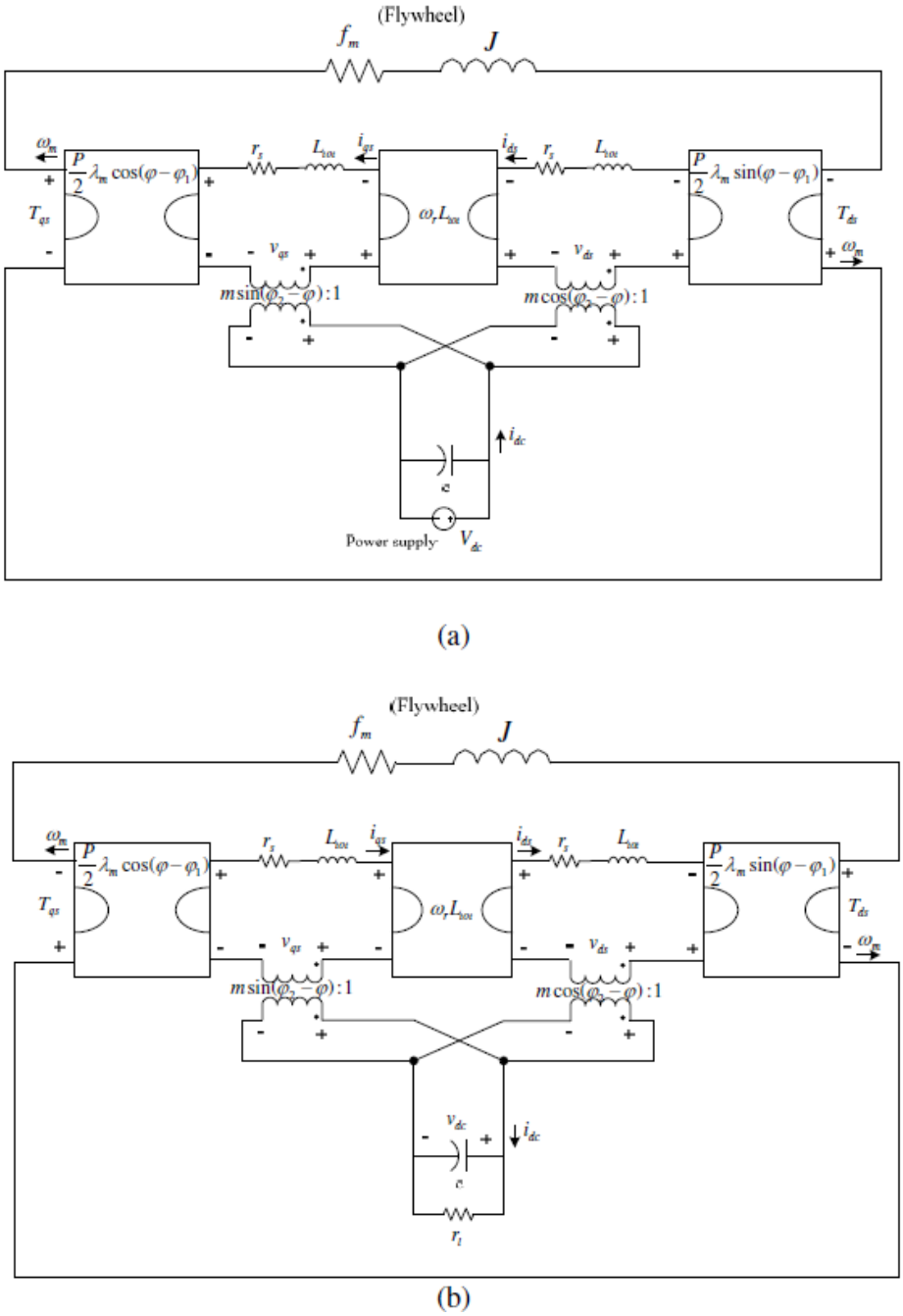

Figure 6-12 Integrated FESS model in (a) Charging mode (b) Discharging mode

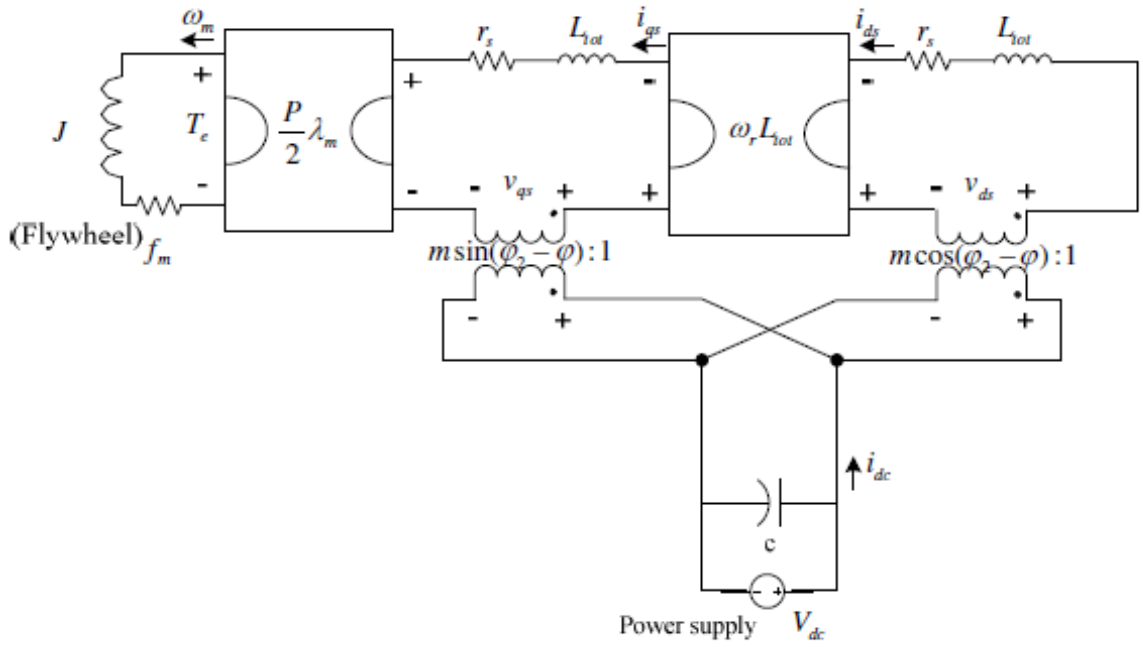

(a)

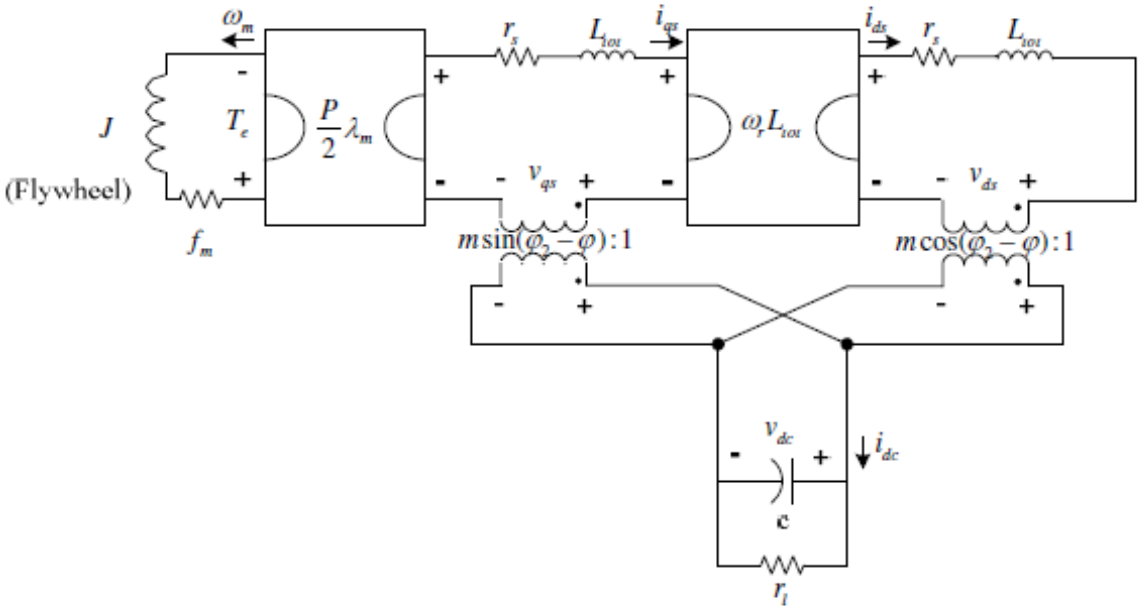

(b)

Figure 6-13 Reduced model of FES system integration using $\varphi=\varphi_1$ in (a) charging mode (b) discharging mode

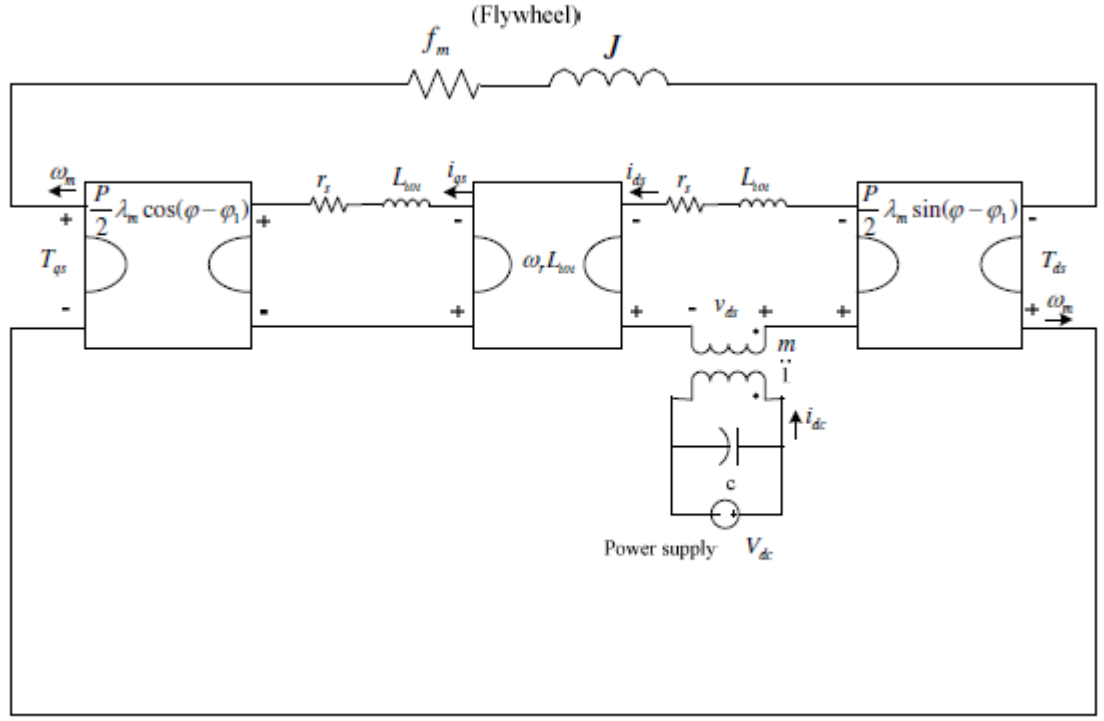

(a)

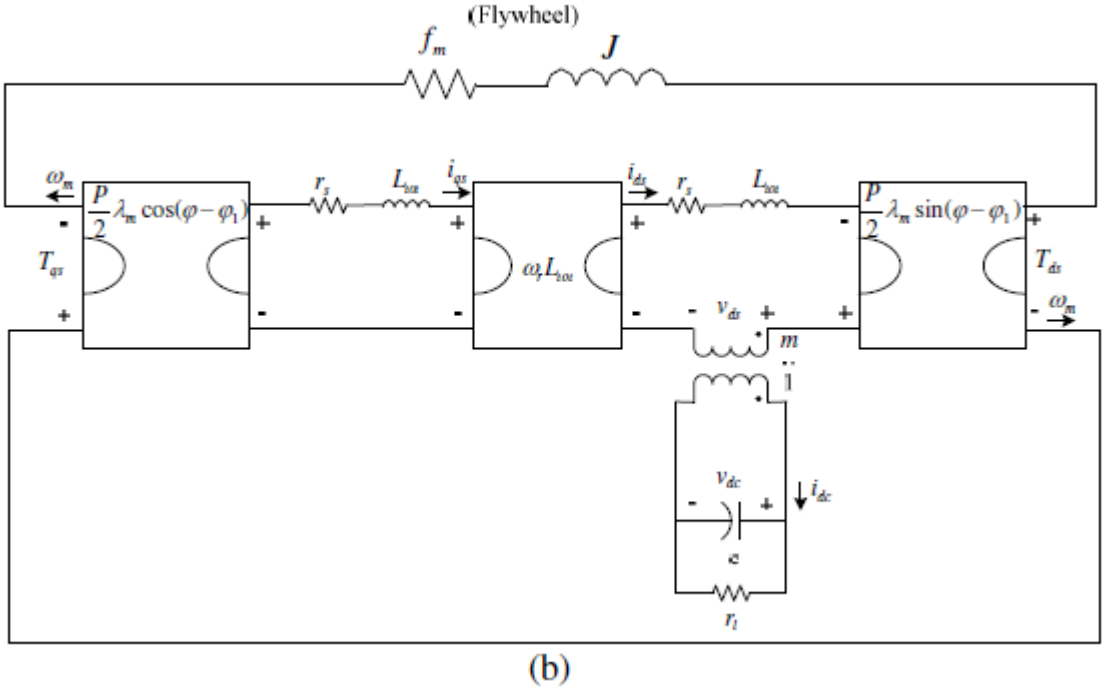

(b)

Figure 6-14 Reduced model of FES system integration using $\varphi=\varphi_2$ in (a) charging mode (b) discharging mode

6.2 Analytical Model Expressions

The expressions for the analytical model were expressed previously from Equations ((6-1) to ((6-44). Based on this the analytical models during charging and discharging was derived. This is presented in this section

6.2.1 Charging mode

The DC equivalent circuit of the FESS during charging mode is shown in Figure 6-12 while the reduced model is shown in Figure 6-13 and Figure 6-14. It should be noted here that this mode runs with a lower phase current and the time period is longer than the discharging mode. Hence the DC bus voltage is much higher than the voltage across the winding resistor r_s, which can be ignored for simplification. Using Kirchhoff's voltage loop Equations, the FESS behavior during charging mode is given as

$$\begin{aligned} -\omega_r L_{tot} I_{ds} &= -\lambda_m \omega_r = -V_{dc} M sin(\phi_0) \\ -\omega_r L_{tot} I_{qs} &= -V_{dc} M cos(\phi_0) \\ (P/2)^2 \lambda_m I_{qs} - Jp\omega_r &= 0 \end{aligned} \qquad \textbf{(6-45)}$$

Hence the expressions for I_{qs}, I_{ds} and ω_r can be written as

$$I_{qs} = -\left(\frac{2}{P}\right)^2 \frac{J}{\lambda_m} p\omega_r \qquad \textbf{(6-46)}$$

$$I_{ds} = -\left(\frac{2}{P}\right)^2 \frac{J}{\lambda_m} p\omega_r \tan(\phi_0) - \frac{\lambda_m}{L_{tot}} \qquad \textbf{(6-47)}$$

$$\omega_r = -\left(\frac{P}{2}\right)^2 \frac{\lambda_m V_{dc} M cos(\phi_0)}{L_{tot} Jp\omega_r} \qquad \textbf{(6-48)}$$

The PWM inverter output real power P_{inv}^{out} and reactive power Q_{inv}^{out} can be obtained as

$$\begin{aligned} P_{inv}^{out} &= V_{qs} I_{ds} + V_{ds} I_{ds} \\ Q_{inv}^{out} &= V_{qs} I_{ds} - V_{ds} I_{ds} \end{aligned} \qquad \textbf{(6-49)}$$

Where

$$V_{qs} = \lambda_m \omega_r + \omega_r L_{tot} I_{ds}$$

$$V_{ds} = -\omega_r L_{tot} I_{ds} \qquad \textit{(6-50)}$$

The power factor (PF) is given by

$$PF = \frac{P_{inv}^{out}}{\sqrt{P_{inv}^{out\,2} + Q_{inv}^{out\,2}}} \qquad \textit{(6-51)}$$

For the special case of when $I_{ds} = 0$, the PMSM is not run in a field weakening mode, ϕ_0 should be controlled in a way that the following Equation has to be satisfied

$$\tan(\phi_0) = -\left(\frac{P}{2}\right)^2 \frac{{\lambda_m}^2}{L_{tot} J p \omega_r} \qquad \textit{(6-52)}$$

Variable	**Case I : $I_{ds} \neq 0$**	**Case II : $I_{ds} = 0$**
I_{qs}	$-\left(\frac{2}{P}\right)^2 \frac{J}{\lambda_m} p\omega_r$	$-\left(\frac{2}{P}\right)^2 \frac{J}{\lambda_m} p\omega_r$
I_{ds}	$-\left(\frac{2}{P}\right)^2 \frac{J}{\lambda_m} p\omega_r \tan(\phi_0) - \frac{\lambda_m}{L_{tot}}$	0
ω_r	$-\left(\frac{P}{2}\right)^2 \frac{\lambda_m V_{dc} M \cos(\phi_0)}{L_{tot} J p \omega_r}$	$-\left(\frac{P}{2}\right)^2 \frac{\lambda_m V_{dc} M \cos(\phi_0)}{L_{tot} J p \omega_r}$
V_{qs}	$\lambda_m \omega_r + \omega_r L_{tot} I_{ds}$	$\lambda_m \omega_r$
V_{ds}	$-\omega_r L_{tot} I_{ds}$	$-\omega_r L_{tot} I_{ds}$
P_{inv}^{out}	$\lambda_m \omega_r I_{qs}$	$\lambda_m \omega_r I_{qs}$
Q_{inv}^{out}	$\lambda_m \omega_r I_{ds} + \omega_r L_{tot} I^2{}_{ds} + \omega_r L_{tot} I^2{}_{qs}$	$\omega_r L_{tot} I^2{}_{qs}$
PF	$\frac{P_{inv}^{out}}{\sqrt{P_{inv}^{out\,2} + Q_{inv}^{out\,2}}}$	$\frac{P_{inv}^{out}}{\sqrt{P_{inv}^{out\,2} + Q_{inv}^{out\,2}}}$
ϕ_0	-NA-	$-\left(\frac{P}{2}\right)^2 \frac{{\lambda_m}^2}{L_{tot} J p \omega_r}$

Table 6-1 Analytical model of FESS during charging mode

The analytical model of the FESS during charging mode is summarized in Table 6-1.

6.2.2 Discharging mode

Similar to the charging mode, the analytical model of the FES system during discharge can be derived. It should be noted that instead of the inverter, the rectifier mode is used during discharge. The Table 6-2 summarizes the results obtained.

Variable	**Case I : $I_{ds} \neq 0$**	**Case II : $I_{ds} = 0$**
I_{qs}	$-\left(\frac{2}{P}\right)^2 \frac{J}{\lambda_m} p\omega_r$	$-\left(\frac{2}{P}\right)^2 \frac{J}{\lambda_m} p\omega_r$
I_{ds}	$-\left(\frac{2}{P}\right)^2 \frac{Jp\omega_r}{2\lambda_m r_i M^2 cos(\phi_0)^2}(r_i M^2 sin(2\phi_0) - 2\omega_r L_{tot}$	0
V_{dc}/E	$-\left(\frac{2}{P}\right)^2 \frac{L_{tot} Jp\omega_r}{\lambda_m{}^2 M cos(\phi_0)}$	$\frac{L_{tot} I_{qs}}{\lambda_m M cos(\phi_0)}$
V_{qs}	$\lambda_m \omega_r - r_s I_{qs} - \omega_r L_{tot} I_{ds}$	$\lambda_m \omega_r - r_s I_{qs}$
V_{ds}	$-r_s I_{ds} + \omega_r L_{tot} I_{qs}$	$\omega_r L_{tot} I_{ds}$
P_{rec}^{in}	$\lambda_m \omega_r I_{qs} - r_s I_{qs}{}^2 - r_s I_{ds}{}^2$	$\lambda_m \omega_r I_{qs} - r_s I_{qs}{}^2$
Q_{rec}^{in}	$\lambda_m \omega_r I_{ds} - \omega_r L_{tot} I^2{}_{ds} - \omega_r L_{tot} I^2{}_{qs}$	$-\omega_r L_{tot} I^2{}_{qs}$
PF	$\frac{P_{rec}^{in}}{\sqrt{P_{rec}^{in}{}^2 + Q_{rec}^{in}{}^2}}$	$\frac{1}{\sqrt{1 + \left(\frac{L_{tot} I_{qs}}{\lambda_m}\right)^2}}$
ϕ_0	-NA-	$\frac{1}{2} sin^{-1}\left(\frac{2\omega_r L_{tot}}{r_i M^2}\right)$
M	-NA-	$\frac{\sqrt{V_{qs}^2 + V_{ds}^2}}{V_{dc}}$

Table 6-2 Analytical model of the FES system during discharge mode.

6.3 Output – Analytical model

Based on the above sections, the output of the analytical model was obtained. In order to do this – desired parameters of the flywheel, DC bus, inductor and FESS were first entered. This is summarized in Table 6-3

PMSM/Flywheel parameters	
Rated Power	10-20KW
No of Poles	4
Operating speed range	20,000-60,000 rpm
Back EMF constant	0.00712 Vrms/ rpm
Winding resistance (per phase)	10.32 mΩ
$L=L_{qs}=L_{ds}$	121.8 µH
Moment of inertia	0.92 Kgm^2
Torque	5 Nm
Current Density	5 A/mm^2
DC bus	
Voltage	500 V
Capacitor bank	34.2 mF
Resistive load	2.08 Ω
Inductor	
Charging Mode	200 µH
Discharging mode	0 µH (Ideally)
FES desired operation	
Rated output in Speed range	1 KW-hr
Duration of discharge	5 sec
Duration of charge	60 sec
Efficiency	90%

Table 6-3 FES system parameters and desired operation

Based on ((6-1) to ((6-52) , the various output parameters of the inverter and rectifier were obtained for different speed cases and are summarized in Table 6-4, Table 6-5 and Table 6-6

Speed (rpm)	**L_{ext} (µH)**	**I_{qs} (A)**	**I_{ds} (A)**	**I_{as} (Arms)**	**V_{qs} (V)**	**V_{ds} (V)**	**P_{inv}^{out} (kW)**	**Q_{inv}^{out} (KVar)**	**PF**	**M**	**ϕ_0 (deg)**
20,000	200	67.3	0	33.8	187.2	-25.2	13.2	1.01	0.99	0.41	42.5
40,000	200	67.3	0	33.8	204.1	-29.8	15.7	1.25	0.99	0.46	42.5
60,000	200	67.3	0	33.8	239.4	-31.3	18.3	1.43	0.99	0.49	42.5

Table 6-4 1KW-hr FESS charging in 60 seconds

Speed (rpm)	**L_{ext} (µH)**	**I_{qs} (A)**	**I_{ds} (A)**	**I_{as} (Arms)**	**V_{qs} (V)**	**V_{ds} (V)**	**P_{rec}^{in} (kW)**	**Q_{rec}^{in} (KVar)**	**PF**	**M**	**ϕ_0 (deg)**
20,000	0	910.4	0	512.0	177.1	193.6	270.1	-313.2	-0.61	0.51	31.3
40,000	0	910.4	0	512.0	191.2	215.7	283.7	-342.3	0.61	0.58	31.3
60,000	0	910.4	0	512.0	221.8	243.1	301.2	-365.7	-0.61	0.69	31.3

Table 6-5 1 KW-hr FESS discharging in 5 sec with constant I_{qs} (rectifier input)

Speed (rpm)	**L_{ext} (µH)**	**I_{qs} (A)**	**I_{ds} (A)**	**I_{as} (Arms)**	**V_{qs} (V)**	**V_{ds} (V)**	**P_{rec}^{in} (kW)**	**Q_{rec}^{in} (KVar)**	**PF**	**M**	**ϕ_0 (deg)**
20,000	0	865.8	0	434.1	176.2	210.2	240	-228.8	-0.56	0.50	39.1
40,000	0	843.2	0	417.9	190.4	209.5	240	-274.6	-0.61	0.54	41.6
60,000	0	811.0	0	398.2	219.3	208.7	240	-300.2	-0.66	0.57	42.5

Table 6-6 1KW-hr FES system discharging in 5 sec with constant power (rectifier input)

In order to verify the parameters as obtained from the analytical model, the commercial software package PSIM was used. The results comparing the analytical and the PSIM software are tabulated in Table 6-7

	Analytical Model				PSIM software			
Mode	Discharging		Charging		Discharging		Charging	
ω_r(rpm)	40,000	60,000	40,000	60,000	40,000	60,000	40,000	60,000
I_{qs} (A)	843.2	811.0	67.3	67.3	836.1	817.3	62	62
I_{ds}(A)	0	0	0	0	0	0	0	0
I_{as} (A)	417.9	398.2	33.8	33.8	421.2	400.7	31.2	31.2
Vs (V)	240	270	190	237	232	265	188	235
PF	-0.61	-0.66	0.99	0.99	-0.58	-0.62	0.91	0.88
P_{inv}^{out} **(KW)**	-NA	-NA-	15.7	18.3	-NA-	-NA-	12.3	16.2
Q_{inv}^{out} **(KVar)**	-NA-	-NA-	1.25	1.43	-NA-	-NA-	1.17	1.45
P_{rec}^{in} **(kW)**	240	240	-NA	-NA-	240	240	-NA	-NA
Q_{rec}^{in} **(KVar)**	-274.6	-300.2	-NA-	-NA-	-252.3	-281.7	-NA-	-NA-
M	0.58	0.69	0.46	0.49	0.55	0.67	0.48	0.52

Table 6-7 Comparison between PSIM and analytical model

In summary, a comprehensive analytical model of the high-speed FESS is created. For the chosen operating speed, the different electrical parameters such as current, voltage, resistance and power were calculated. It should be noted that at the nominal operating speed of 40,000 rpm, parameters for both charging and discharging were calculated. Based on these parameters, individual flywheel electronic components can be obtained standard from manufacturers or custom designed.

7 System level analysis of the flywheel

The individual mechanical components of the ROMAC flywheel were presented in Chapter 4 and Chapter 5. Figure 7-1 illustrates a schematic of the total flywheel system.

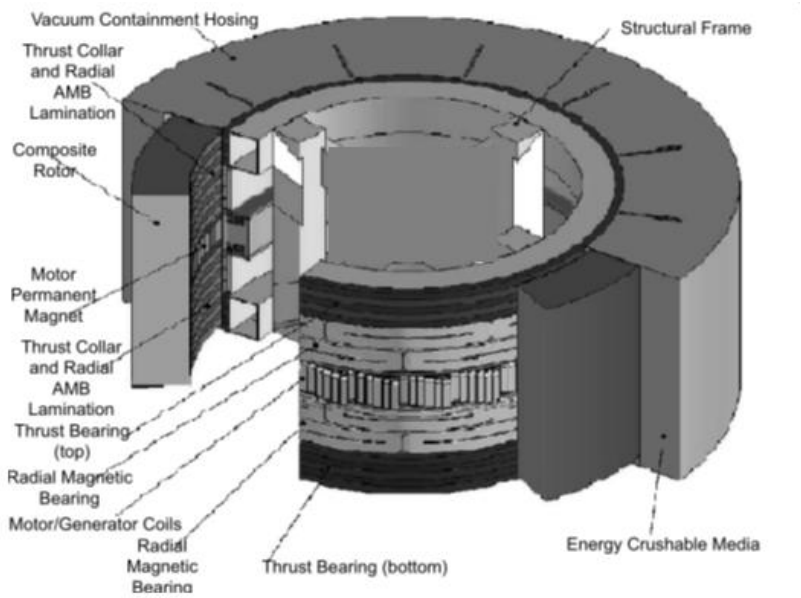

Figure 7-1 Schematic of ROMAC flywheel

In this chapter, a rotordynamic analysis will be presented. In addition, the design process of the magnetic bearing controls will also be shown.

7.1 Rotordynamic analysis

In order to perform a rotordynamic analysis, it is necessary to know the dimensions of each component. This is shown in Table 7-1.

Component	ID (mm)	OD (mm)	H (mm)	ρ (kg/m^3)	E GPa)	υ
Outer Spline	200	250	450	7850	200	0.27
Inner Spline	170	200	450	7850	200	0.27
Composite flywheel	250	410	400	1600	147	0.57
Radial bearing lamination	150	170	30	7400	120	0.23
Thrust Disk	200	300	30	7400	120	0.23
Radial Bearing Stator	70	138	30	7400	120	0.23
Thrust Bearing Stator	70	320	20	7400	120	0.23
Stator Back Iron	25	70	530	7400	120	0.23

Table 7-1 Component dimensions and material properties

As it can be seen, the rotor is about 450 mm in length and has a mass of about 60 kg. The overall polar and transverse moments of inertia are 0.228 kg-m^2 and 0.876 kg-m^2 respectively with a ratio of 0.26. The outer diameter and inner diameter of the rotor are 410 mm and 150 mm respectively. The cross section of the ROMAC flywheel rotor is shown in Figure 7-2.

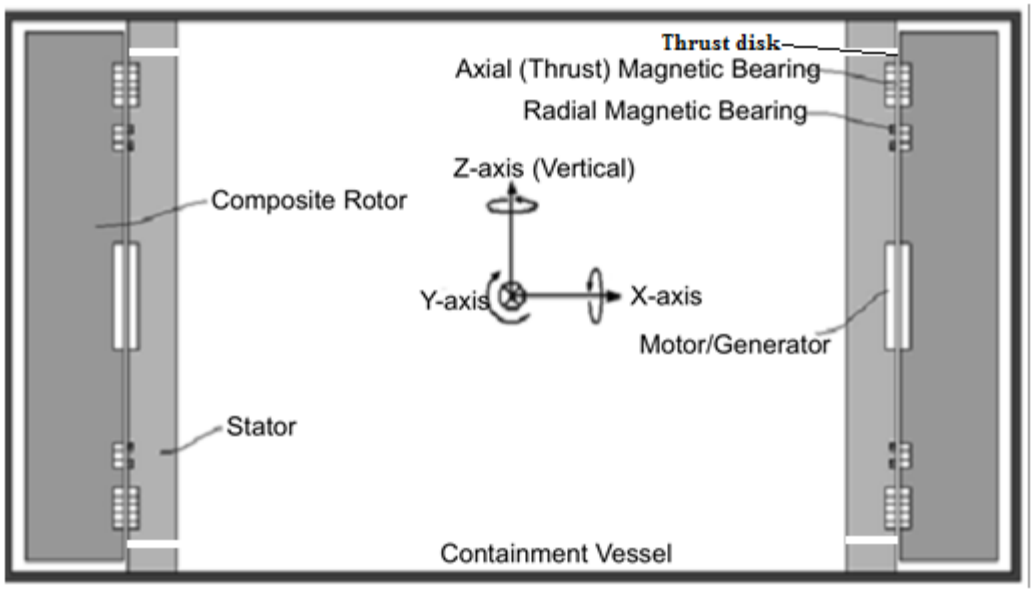

Figure 7-2 Cross section of the ROMAC flywheel

The general rotordynamic Equation of motion for a plant with conventional bearings is given by

$$[M]\{\ddot{q}\} + \{[C] + [G]\}\{\dot{q}\} + [K]\{q\} = \{f\} \qquad \textit{(7-1)}$$

Where q represents the physical coordinate degrees of freedom, f represents external forces and the mass matrix is denoted by M. The passive negative stiffness of the magnetic bearing is included in the bearing stiffness matrix K. The terms representing gyroscopic effects are combined with the damping matrix C. For the ROMAC flywheel, each rotor bending mode was given a static internal damping ratio of 0.25%. This is a conservative value for a rotor if no modal test data is available[167]. For system analysis with magnetic bearings, Equation (7-1) can be transformed to modal coordinates, μ, and converted to state space form as

$$\begin{aligned} [\dot{\mu}_p] &= [A_p]\{\mu_p\} + [B_p]\{f\} \\ \{q\} &= [C_p]\{\mu_p\} + [D_p]\{f\} \end{aligned} \qquad \textit{(7-2)}$$

Partitions of the characteristic matrix A_p contain the modal stiffness and the damping matrices. The input and output matrices B_p and C_p contain mass normalized eigenvenctors for modes selected for the system analysis. The feedforward matrix D_p includes the passive negative stiffness or the bearing stiffness [168].

7.1.1 Rotor model

A rotor model containing 21 nodes (20 stations) and 84 degree of freedoms was constructed within the ROMAC rotordynamics code Rotorlab+. The code determines the critical speeds of the rotor-bearing system and undamped mode shapes using the transfer matrix method [169]. The attached masses (laminations, collars, and permanent magnets) are treated as disks which include mass-inertia properties for the analysis. The stiffness contribution of the lamination stacks is accounted for by using an effective stiffness diameter. The input parameters of the rotor model are given in Table 7-2. The weight, polar moment of inertia I_P , and transverse moment of inertia I_T shown in the table are the properties of the added mass (collars, laminations, etc.) attached to the inner diameter of the composite rotor. Thrust bearings are located at nodes 2 and 20. Radial magnetic bearings are located at nodes 5 and 17.

Node	Weight (lbm)	Length (in)	OD (in)	ID (in)	I_P (lbm-in^2)	I_T (lbm-in^2)	E (PSI)	ρ (lbm/in^3)
1	0	0.1969	15.3543	5.90551	0	0	23.206	0.0580
2	4.0188	0.1969	16.8543	5.90551	42.031	126.7771	23.206	0.0580
3	0	0.9843	15.3543	5.90551	0	0	23.206	0.0580
4	0	0.5906	17.7165	5.90551	0	0	23.206	0.0580
5	5.3742	0.5906	19.2165	5.90551	75.861	231.6843	23.206	0.0580
6	0	0.9843	15.3543	5.90551	0	0	23.206	0.0580
7	0	0.9843	15.3543	5.90551	0	0	23.206	0.0580
8	0	0.9843	15.3543	5.90551	0	0	23.206	0.0580
9	0	0.9843	15.3543	5.90551	0	0	23.206	0.0580
10	0	0.9843	15.3543	5.90551	0	0	23.206	0.0580
11	19.729	0.9843	16.8543	5.90551	279.18	989.9547	23.206	0.0580
12	0	0.9843	15.3543	5.90551	0	0	23.206	0.0580
13	0	0.9843	15.3543	5.90551	0	0	23.206	0.0580
14	0	0.9843	15.3543	5.90551	0	0	23.206	0.0580
15	0	0.9843	15.3543	5.90551	0	0	23.206	0.0580
16	0	0.5906	17.7165	5.90551	0	0	23.206	0.0580
17	5.3742	0.5906	19.2165	5.90551	75.861	231.6843	23.206	0.0580
18	0	0.9843	15.3543	5.90551	0	0	23.206	0.0580
19	0	0.1969	15.3543	5.90551	0	0	23.206	0.0580
20	4.0188	0.1969	16.8543	5.90551	42.031	126.7771	23.206	0.0580
21	0	0	15.3543	5.90551	0	0	23.206	0.0580

Table 7-2 Input information for finite element model construction

Mode Shape	Free-Free Rotor	Rotor with support stiffness
First rigid body mode (Translation mode)	0 RPM	960.31 PRM
Second rigid body mode (Tilt mode)	0 RPM	1518.71 RPM
First bending mode	424,852 RPM	557,784 RPM
Second bending mode	482,119 RPM	1,051,543 RPM

Table 7-3 Predicted rotor critical speeds

It should be noted that the first bending mode occurs at a speed much higher than the operating speed. Hence, it is appropriate to assume a rigid rotor for analysis and controller design.

7.1.2 Natural Frequencies and Mode Shapes

The calculation of the natural frequencies and mode shapes is a very important step for the prediction of the rotor dynamic behavior. Here, a free-free system case (the case with no support stiffness and a rotational speed (Ω) of zero) is first analyzed. The natural frequencies of the first and the second rigid body are both 0 RPM. The first and second bending modes frequencies are calculated as 424,852 and 482,119 RPM, respectively. Due to the fact that the bearing stiffness changes due to the control currents, the stiffness parameter varies within a wide range. The relationship between the bearing stiffness and natural frequencies is depicted in the critical speed map in Figure 7-3. A bearing stiffness of k_x= 2069 lbf/in was chosen and the mode shapes were plotted (Figure 7-4). Increasing the bearing stiffness increases natural frequencies of each mode and changes the mode shapes.

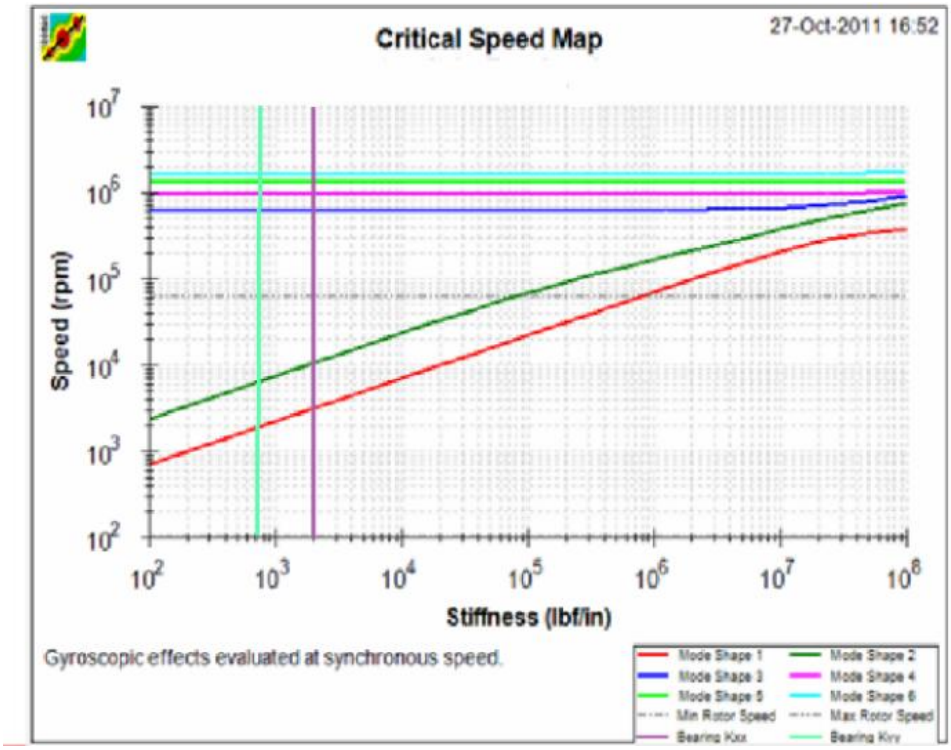

Figure 7-3 Critical Speed Map

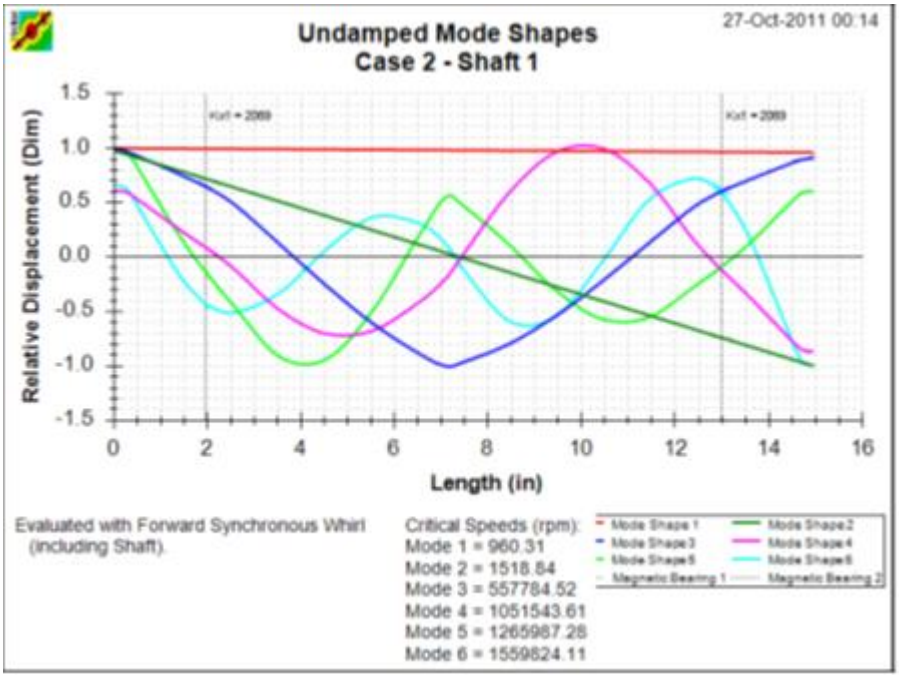

Figure 7-4 Mode Shapes

7.1.3 State space rotor model

From the critical speed map and mode shapes, it can be seen that the natural frequencies of the bending modes are significantly higher than the intended operational rotating speed range. Based on Equation (7-2, the ROMAC rotordynamics code called MODAL was used to generate a modally reduced state space model of a single free-free rotor [170]. It should be noted that only rigid body modes are being considered. The state space form of the free-free rotor model obtained from MODAL can be presented in terms of states z_x and z_y , inputs u_x and u_y, outputs r_x and r_y and gyroscopic matrix G as

$$\begin{bmatrix} \dot{z}_x \\ \dot{z}_y \end{bmatrix} = \begin{bmatrix} A & -\Omega G \\ \Omega G & A \end{bmatrix} \begin{bmatrix} z_x \\ z_y \end{bmatrix} + \begin{bmatrix} B & 0 \\ 0 & B \end{bmatrix} \begin{bmatrix} u_x \\ u_y \end{bmatrix} \qquad \textit{(7-3)}$$

$$\begin{bmatrix} r_x \\ r_y \end{bmatrix} = \begin{bmatrix} C & 0 \\ 0 & C \end{bmatrix} \begin{bmatrix} z_x \\ z_y \end{bmatrix}$$

In this particular transformation, we have ,

$$A = \begin{bmatrix} 0 & 0 & 1 & 0 \\ 0 & 0 & 0 & 1 \\ 0 & 0 & 0 & 0 \\ 0 & 0 & 0 & 0 \end{bmatrix}, B = \begin{bmatrix} 0 & 0 \\ 0 & 0 \\ 1.5634 & 1.5634 \\ -1.2722 & 1.2951 \end{bmatrix} \qquad \textit{(7-4)}$$

$$C = \begin{bmatrix} 1.5634 & -1.2722 & 0 & 0 \\ 1.5634 & 1.2951 & 0 & 0 \end{bmatrix}, G = \begin{bmatrix} 0 & 0 & 0 & 0 \\ 0 & 0 & 0 & 0 \\ 0 & 0 & 0 & 0.7304 \\ 0 & 0 & -0.7304 & 0 \end{bmatrix}$$

7.1.4 Campbell diagram:

Having analyzed the free-free case, the next step is to include the effect of the rotational speed. The translation mode will not be affected by the system gyroscopics and will yield a typical underdamped eigenvalue solution. The tilt mode is affected by gyroscopics which would yield complex expressions for the damped eigenvalues. All the forward and backward modes within the controller bandwidth can be excited by the AMBs and hence has to be considered in the

controller design. To understand the modes in detail, a plot of the natural frequencies ω_n and the rotational speed, called the Campbell diagram is plotted. It should be noted that the ratio (P) of J_p/J_t was taken to be 0.26 in the analysis.

The Campbell diagrams of both the free-free case and for the case where the support stiffness is included are shown in Figure 7-5 and Figure 7-6 respectively. As can be seen from <> as the rotational speed increases, the gyroscopic effect becomes more significant. Since the state space model of the rotor has already been derived, Equation (7-5 can be used to deduce the natural frequencies in terms of rotational speed.

$$\omega_{n,i} = eigenvalues\ of \begin{bmatrix} A & -\Omega G \\ \Omega G & A \end{bmatrix} \qquad \textbf{(7-5)}$$

Note that in the free-free rotor case, the backward mode for modes 1 is not visible because it is underneath the forward mode of mode 1. We can notice that, if we draw the line $\Omega=\omega_n$, this line intersects each mode as shown in Figure 7-6. The critical speeds occur when the 1X line intersects the ω_n line. This occurs at 701.09 rpm, 816.37 rpm, 960,41 rpm and 2241.77 rpm.

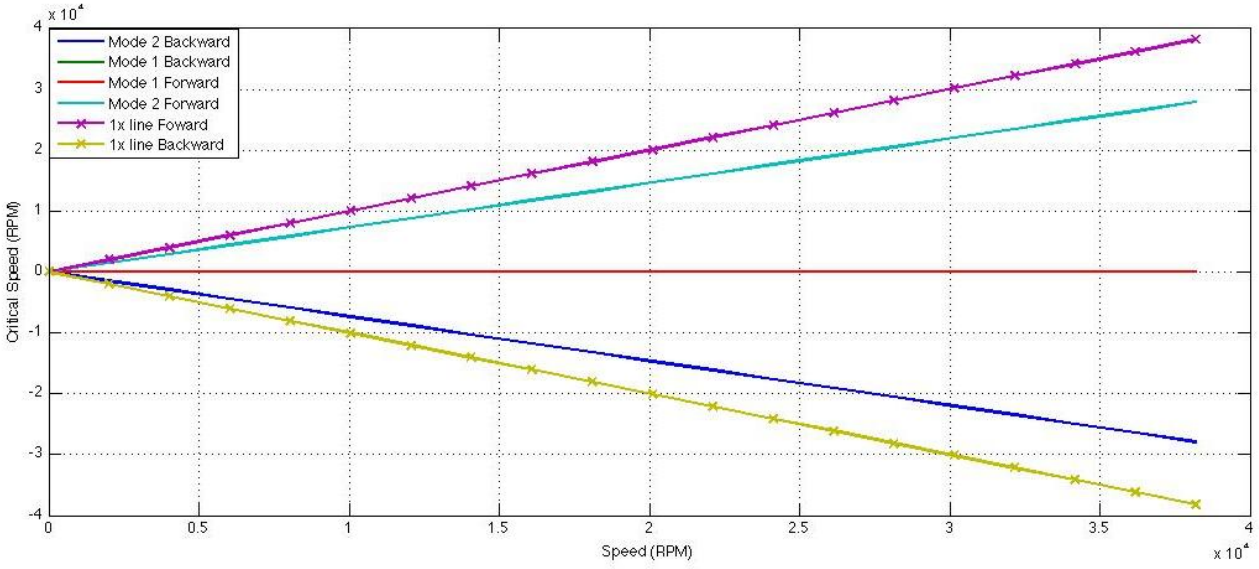

Figure 7-5 Campbell diagram of free-free rotor

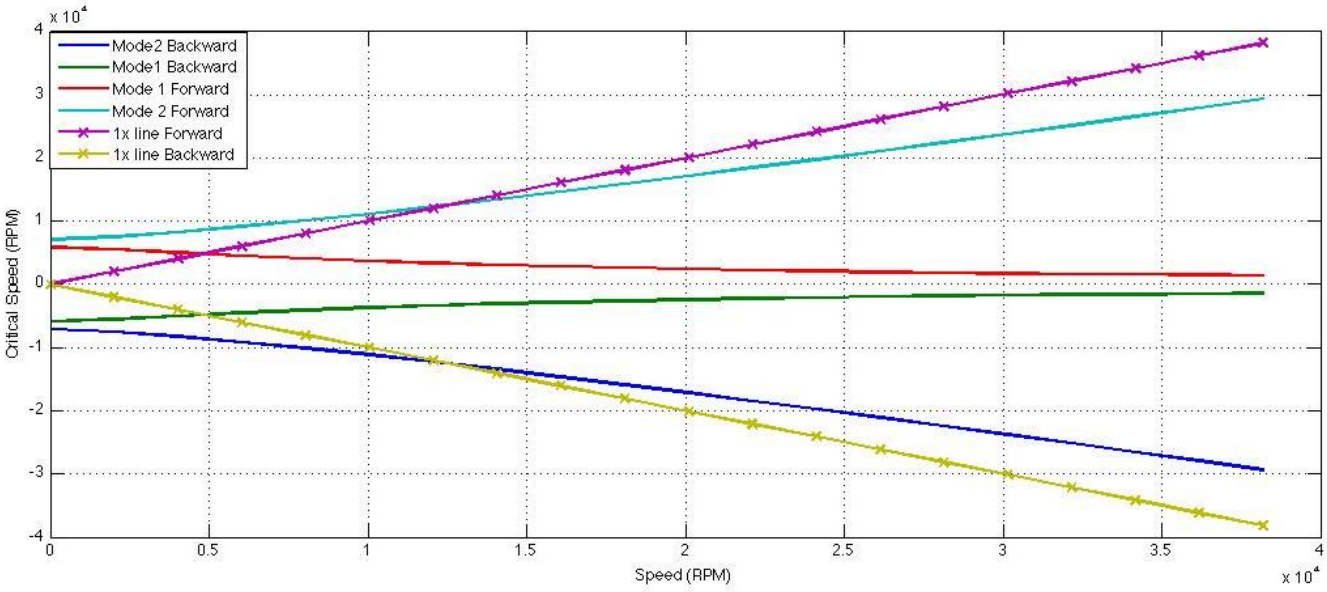

Figure 7-6 Campbell diagram of rotor with support stiffness

7.2 Unbalance Response:

The unbalance response of the flywheel rotor was also analyzed. A MATLAB code, originally developed by Dr. Wang of the Texas A&M University, was modified to perform the analysis. The rotor model presented in Table 7-2 was used. Inputs such as node, unbalance amplitude and phase were given. For the analysis, 3 nodes were chosen – the end of the rotor (node 20), the mid span of the rotor (node 11) and location of the unbalance (node 5). The speed range of 0 – 60,000 rpm was studied. The steady state unbalance response is given in Figure 7-7. It should be noted that the maximum unbalance amplitude obtained was about 0.06 mm. The transient unbalance response was also simulated over a time period of 0.2 seconds. This is shown in Figure 7-8. All steady state vibration amplitudes agree very well with the imbalance response analysis results.

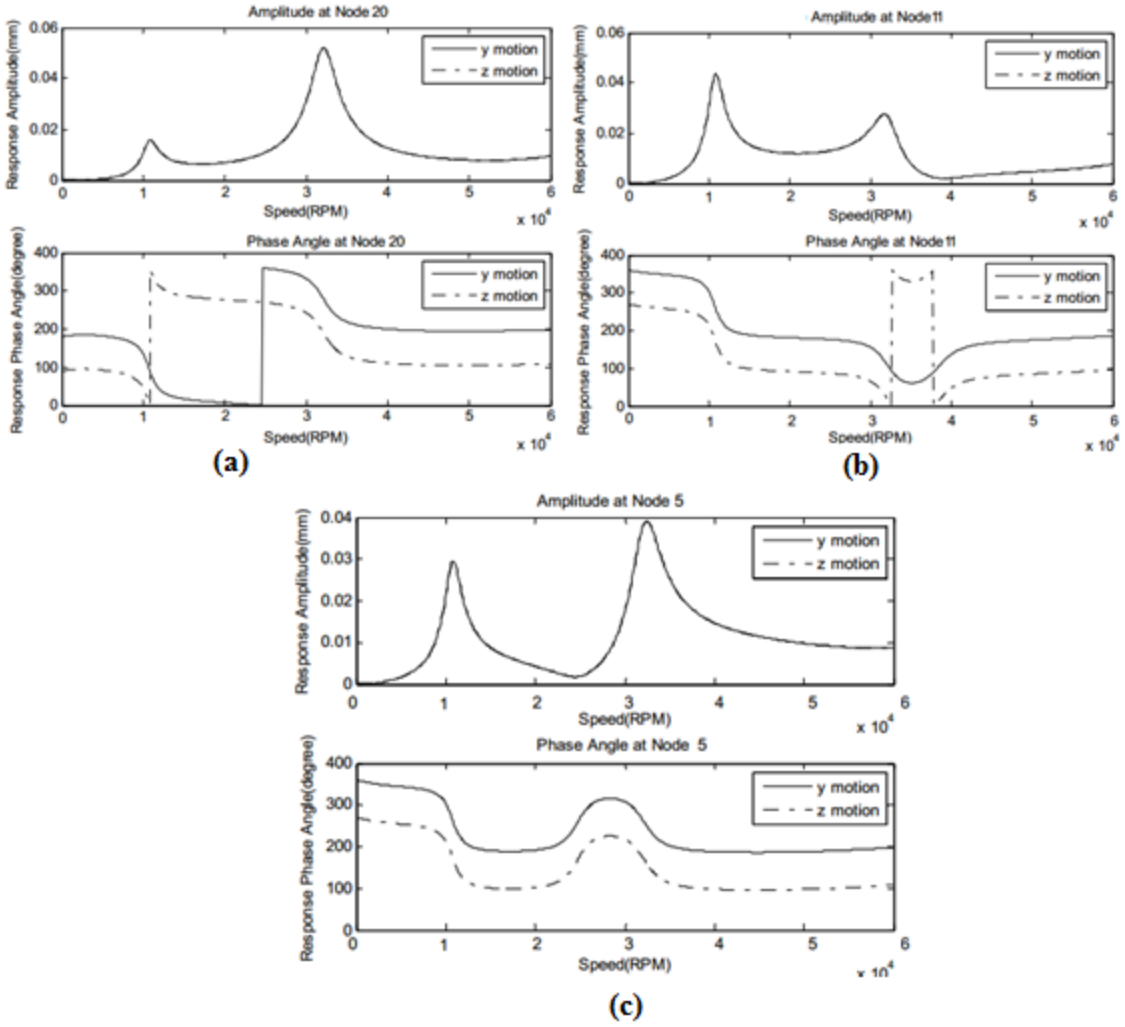

Figure 7-7 Unbalance response and phase angle for (a) Node 20- End point (b) Node 11- Mid span and (c) Node 5- Unbalance location

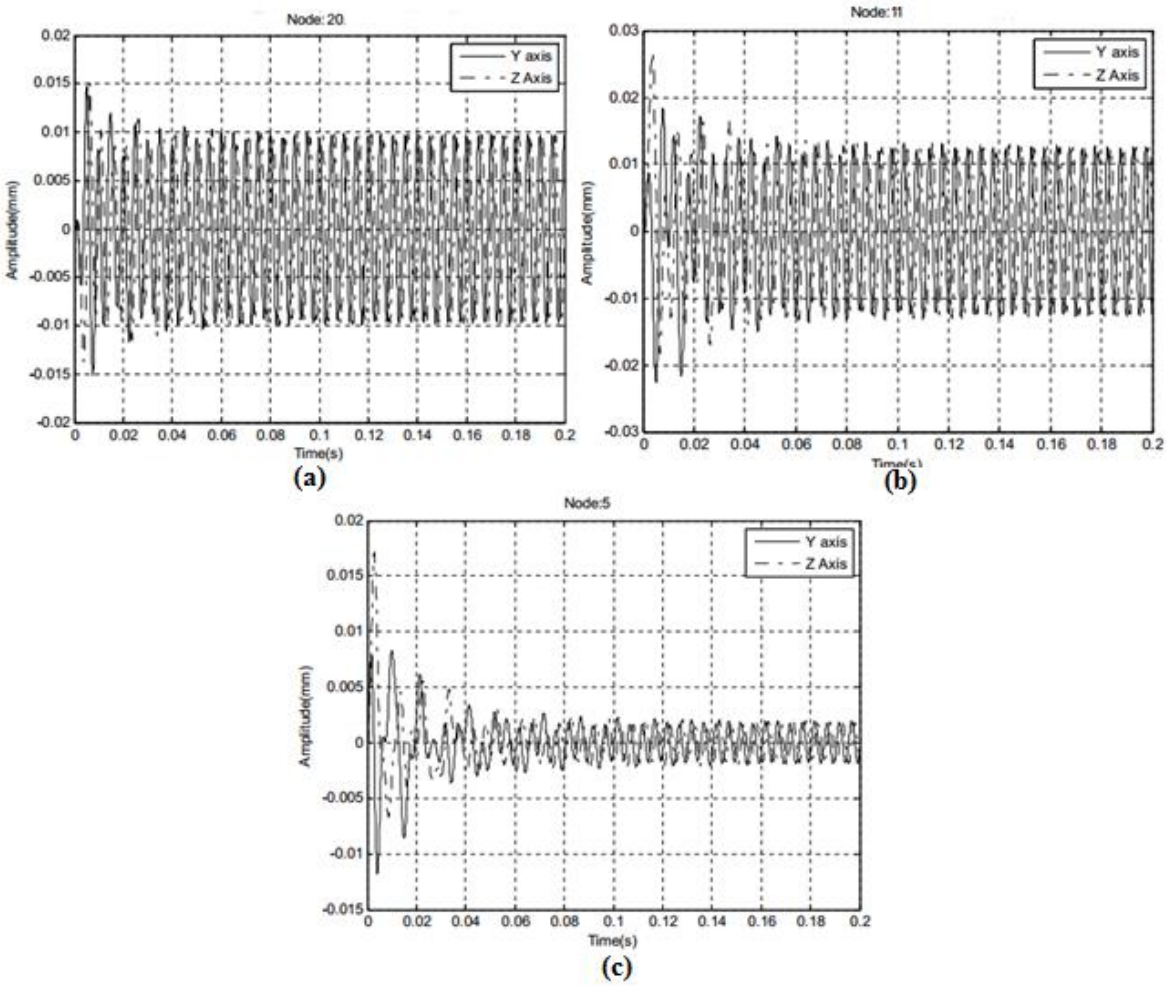

Figure 7-8 Unbalance Transient Response for (a) Node 20 (b) Node 11 (c) Node 5

7.3 Controller Design

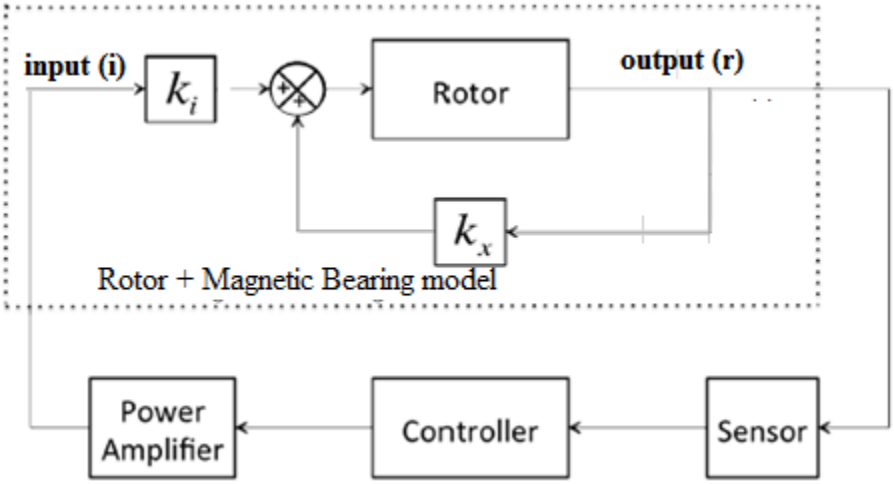

Figure 7-9 Closed-loop block diagram of the flywheel system

The design and analysis of the radial and thrust magnetic bearing is discussed in Chapter 5. The linearized force of the magnetic bearing in terms of the perturbation current (i) and the displacement (r) can be given by

$$f_{AMB} = k_x r + k_i i \qquad \textit{(7-6)}$$

Here k_x represents the negative stiffness with the rotor centered within the airgap and ki represents the current gain of the AMB at the same point. Based on equation (7-3) and (7-6), the rotor and magnetic bearing model in the state space model can be written as

$$\begin{bmatrix} \dot{z_x} \\ \dot{z_y} \end{bmatrix} = \begin{bmatrix} A + BCK_x & -\Omega G \\ \Omega G & A + BCK_x \end{bmatrix} \begin{bmatrix} z_x \\ z_y \end{bmatrix} + \begin{bmatrix} BK_i & 0 \\ 0 & BK_i \end{bmatrix} \begin{bmatrix} i_x \\ i_y \end{bmatrix} \qquad \textit{(7-7)}$$

$$\begin{bmatrix} r_x \\ r_y \end{bmatrix} = \begin{bmatrix} C & 0 \\ 0 & C \end{bmatrix} \begin{bmatrix} z_x \\ z_y \end{bmatrix}$$

Where the inputs to the model are the currents i_x and i_y that are obtained from the amplifier and the matrices

$$K_x = \begin{bmatrix} k_x & 0 \\ 0 & k_x \end{bmatrix}, K_i = \begin{bmatrix} k_i & 0 \\ 0 & k_i \end{bmatrix} \qquad \textit{(7-8)}$$

From finite element analysis techniques in ANSYS, the values of K_x and K_i were obtained as 113,400 N/m and 45.382 N/A respectively.

The closed loop model of the flywheel system is illustrated in Figure 7-9. The plant model shown inside the dashed-box part has already been derived. To complete the feedback control loop of the flywheel system, we need another three components which are: displacement sensors that will measure the rotor displacement and feed to the controller, power amplifiers that will generate currents for the bearing coils, and the controller that will compensate for the error of the rotor displacement from the desired position. In general, the controller for the active magnetic bearing system will be designed for initial levitation of the rotor, at zero rotational speed, and for the various rotational speeds. The PID controller is selected for the ROMAC flywheel because of its simplicity and reliability. The PID controller is appropriate for levitation because, at the initial levitation process, the difference between the initial rotor position and the desired rotor position (centerline) can be significant. This makes it difficult for other controllers such as H_∞, LQR and μ-synthesis design algorithms to estimate the system parameters.

This section describes the model of the displacement sensors and power amplifiers. The derived models are then combined with the rotor and magnetic bearing model to form the entire plant model. The design of the PID controllers based on the plant model is then presented using the root locus approach. Finally, the response of the flywheel system controlled by the designed PID controllers will be presented.

7.3.1 Modeling of Sensors and Power Amplifiers

The models of the sensors and amplifiers derived in this section will be based on a single axis since all axes are assumed to have the same type of sensors and amplifiers. Using the one-axis model of each component, a five axis model can be assembled. Modifying equation (7-2), we have

$$\dot{x_r} = \widetilde{A_r} x_r + B_r K_i i_a$$
$$y_r = C_r x_r \qquad \textit{(7-9)}$$

Where $\widetilde{A_r} = A_r + B_r K_x C_r$ and x_r are the 8 states of integration of the rotor and bearings and matrix i_a is the output from the power amplifiers.

7.3.1.1 Sensors

The displacement sensors used for this test rig are of the eddy current type, model 15N, manufactured by KAMAN instrumentation. The sensors operate in the 4-channel differential mode. Two eddy current sensors are installed for each axis of the magnetic bearing. Therefore, there are ten sensors mounted on the stator. The probe of each sensor is connected to the circuit board and produces differential output that is fed to the PID controller. This differential output signal is the displacement between the rotor surface and magnetic bearing. The differential output is used instead of the single-ended output because the differential output signal produces a smaller measurement range which is still in the linear range of measurement. On the other hand, if the single-ended output is used, some of the output measurement will lie in the nonlinear measuring range. The mathematical model of each sensor channel, with the assumption that the sensor is located at the magnetic bearing location, is given by

$$G_s(s) = \frac{K_s . \omega_s}{s + \omega_s} \qquad \textit{(7-10)}$$

In state space form, the sensor model can be written in terms of the rotor displacement output u_s and the sensor output y_s as

$$\dot{x_s} = A_s x_s + B_s u_s$$
$$y_s = C_s x_s \qquad \textit{(7-11)}$$

The parameters for equations (7-10 and (7-11) are listed in Table 7-4

Parameters	Value
K_s	6010 V/m
ω_s	73500 rad/s
A_s	-73500
B_s	16384
C_s	26961.365

Table 7-4 Parameter values of the sensor model

The combined model for the rotor, magnetic bearings and sensor can then be given as

$$\begin{bmatrix} \dot{x}_r \\ \dot{x}_s \end{bmatrix} = \begin{bmatrix} \widetilde{A_r} & 0 \\ B_s C_r & A_s \end{bmatrix} \begin{bmatrix} x_r \\ x_s \end{bmatrix} + \begin{bmatrix} BK_i \\ 0 \end{bmatrix} i_a \qquad \textit{(7-12)}$$

$$y_s = C_s x_s$$

7.3.1.2 Power Amplifiers

Power amplifiers are the components that convert the controller output signal to control current which is sent to the coils of magnetic bearing poles. Ten power amplifiers, model 422, manufactured by Copley Controls Corp., are chosen for the ROMAC flywheel. The input range of the power amplifier is $\pm$10 volts. The output range is $\pm$10 amperes. Here, the amplifier gain K_a was set to 3.6 A/V. The following equation represents the mathematical model of the power amplifier,

$$G_a(s) = \frac{K_a}{\left(\frac{s}{p}+1\right)\left(\frac{s^2}{\omega_n^2}+2\zeta_n\frac{s}{\omega_n}+1\right)} \qquad \textit{(7-13)}$$

The parameters of the power amplifier model are tabulated in Table 7-5

Parameters	Value
K_a	3.60 A/V
ω_n	9424.78 rad/s
ζ_n	0.66
p_1	10398.67 rad/s

Table 7-5 Parameter values of the power amplifier model

In state space form, the power amplifier model can we written in terms of the PID controller output u_a and the amplifier output i_a as

$$\dot{x_a} = A_a x_a + B_a u_a$$
$$i_a = C_a x_a \qquad \textit{(7-14)}$$

Where $A_a = \begin{bmatrix} -22900 & -13360 & -6923 \\ 16380 & 0 & 0 \\ 0 & 8192 & 0 \end{bmatrix}$, $B_a = \begin{bmatrix} 128 \\ 0 \\ 0 \end{bmatrix}$, $C_a = [0 \quad 0 \quad 194.70]$

The final plant model can then be derived as

$$\begin{bmatrix} \dot{x_r} \\ \dot{x_s} \\ \dot{x_a} \end{bmatrix} = \begin{bmatrix} \widetilde{A_r} & 0 & B_r C_a K_i \\ B_s C_r & A_s & 0 \\ 0 & 0 & A_a \end{bmatrix} \begin{bmatrix} x_r \\ x_s \\ x_a \end{bmatrix} + \begin{bmatrix} 0 \\ 0 \\ B_a \end{bmatrix} u_a \qquad \textit{(7-15)}$$

$$y_s = C_s x_s$$

7.3.2 Modeling of PID Controllers

The simplest type of controller that has been widely used in AMB systems is the PID controller. For the simplicity of the design process, the controllers for all axes are decoupled. This was achieved by the use of a compensation term in the equation. This approach has been proved and used due to its effectiveness with AMB systems [171]. Hence each controller is designed as a single-input single output (SISO) component. A SISO model of the plant can be extracted from Equation ((7-15) and placed in a closed loop system with a PID controller as illustrated in Figure 7-10.

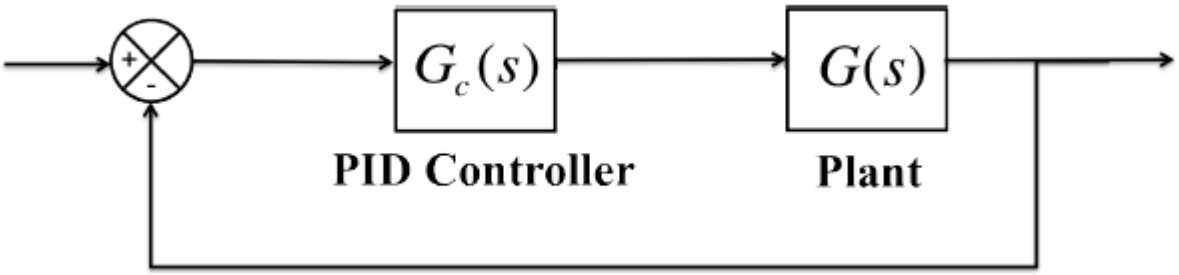

Figure 7-10 A closed-loop system with a PID controller

Assuming that the sensors are collated with the magnetic bearing, the transfer function of the AMB model (x-axis) is given by

$$G(s) = \frac{2.72\times10^{28}}{s^6+9.64\times10^4 s^5+1.90\times10^9 s^4+1.70\times10^{13} s^3+6.74\times10^{16} s^2-7.84\times10^{18} s-3.15\times10^{22}} \qquad \textbf{(7-16)}$$

To determine the parameters of the PID controller for the ROMAC flywheel, Equation (7-17) was used

$$G_c(s) = K_p \frac{(sT_i+1)(sT_d+1)}{sT_i(s\acute{T}_d+1)} \qquad \textbf{(7-17)}$$

Where K_p is the proportional gain, T_i is the integral time constant and T_d and $\acute{T}_d$ are the derivative time constants. These time constants are determined based on the rule-based procedure provided in [172]as

$$\acute{T}_d \ll T_d \leq \frac{1}{\omega} \ll T_i \qquad \textbf{(7-18)}$$

With $\omega = \frac{k_x}{m}$, k_x is the negative stiffness of the magnetic bearing and m is the rotor mass.

The approach used here in order to obtain the appropriate controller gains is based on the root locus method. Using this technique, additional zeros can be placed on the left side of the s-place in order to bring the poles to the left side – which makes the system stable. Further, the gain of

the system can be varied which directly affects the poles of the system. The structure of the PID controller is given in equation (7-17). Using the root locus method, the controller parameters to stabilize the system are obtained. The case of the system without the use of the controller is shown first. It should be noted that there is one pole on the right side of the s-place. This implies that the system is unstable. The corresponding eigenvalues of the plant are shown in Table 7-6.

Real part	**Imaginary part**
-73500	-
-10500	-
679	-
-679	-
-6210	7080
-6210	-7080

Table 7-6 Eigenvalues of the system without the controller

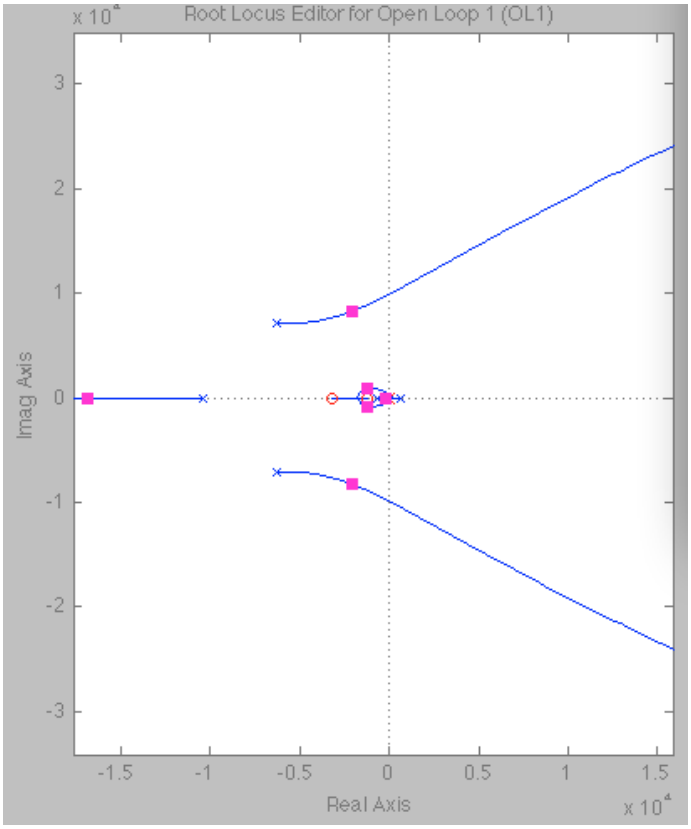

Figure 7-11 Root locus diagram of the plant with controller

In order to move the existing pole (in the right side of the s-plane) to the left, the root locus method allows for addition of zero(s) in the left side of the s-plane and varying the gain. For this system, two (negative) real zeros, one negative real pole (typically far away from the imaginary axis) and another pole (corresponding to the integral control term) on the imaginary axis are added. This was repeated using trial and error until the unstable pole moved to the left side of the s-plane. The stabilized closed loop system of the plant with the PID controller is shown in equation (7-19). The corresponding poles are shown in Table 7-7. It can be noted that all the real parts of the pole are negative (on the left side of the s-plane) which means that the system is stable.

$$G_c(s) = 0.49\frac{(6.25\times10^{-3}s+1)(6.25\times10^{-3}s+1)}{6.25\times10^{-3}s(7.11\times10^{-6}s+1)} \qquad \textit{(7-19)}$$

Real part	**Imaginary part**
-73500	-
-10500	-
-141000	-
-217	-
-8670	5700
-8670	-5700
-1910	2150
-1910	-2150

Table 7-7 Eigen values of the system with PID controller

The controller for the rest of the axes can be designed in the same manner to stabilize the system. After having all four controllers from the design step, they are combined to form a 4 input 4 output controller. To ensure that the AMB system will be stable, a simulation is run when all the controllers are in operation at the same time. To evaluate the controller performance, a step and response of 0.2 mm was simulated at the controller reference input. Figure 7-12 shows the stable responses of a single axis from the simulation. All the axes would have the same response as

shown in Figure 7-12. It can be seen that all system responses reach steady state within 0.016 seconds. The overshoot obtained was about 29.4% which is within the standard limits.

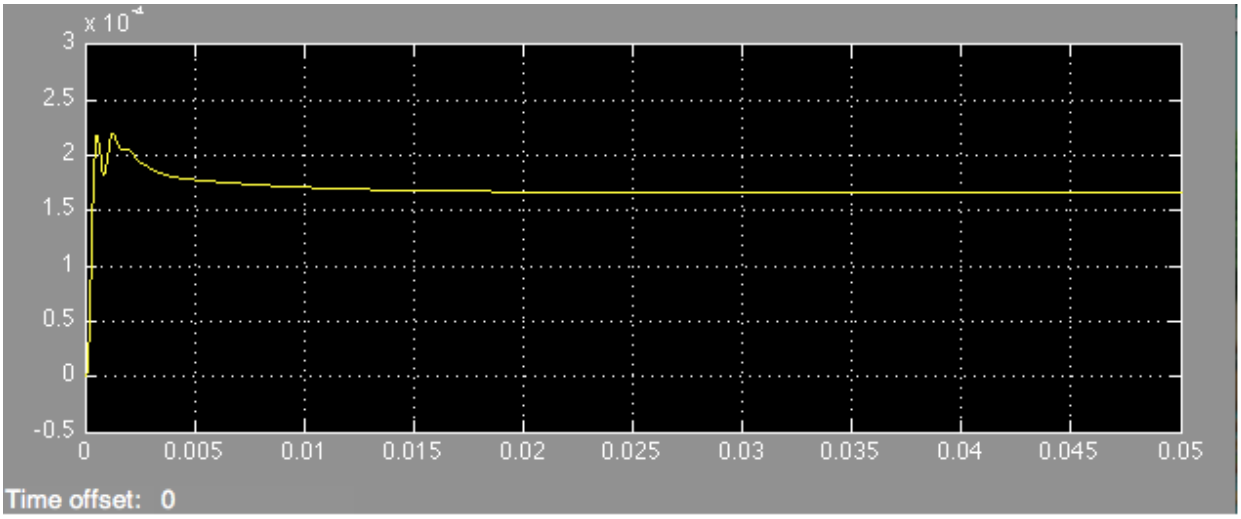

(a)

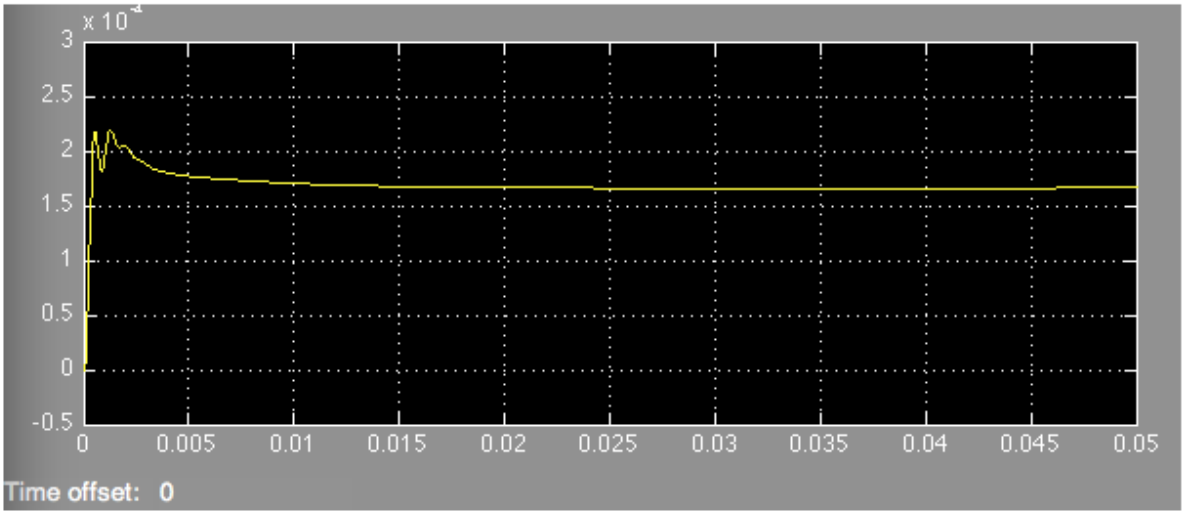

(b)

Figure 7-12 (a) Step and (b) Ramp response of radial bearing PID controller

In addition, the sensitivity function is plotted in Figure 7-13. It can be seen that the amplitude peaked at about 6.76 dB. The plot shows that the radial bearing's PID controller has high responsiveness to accommodate rapid changes in the input.

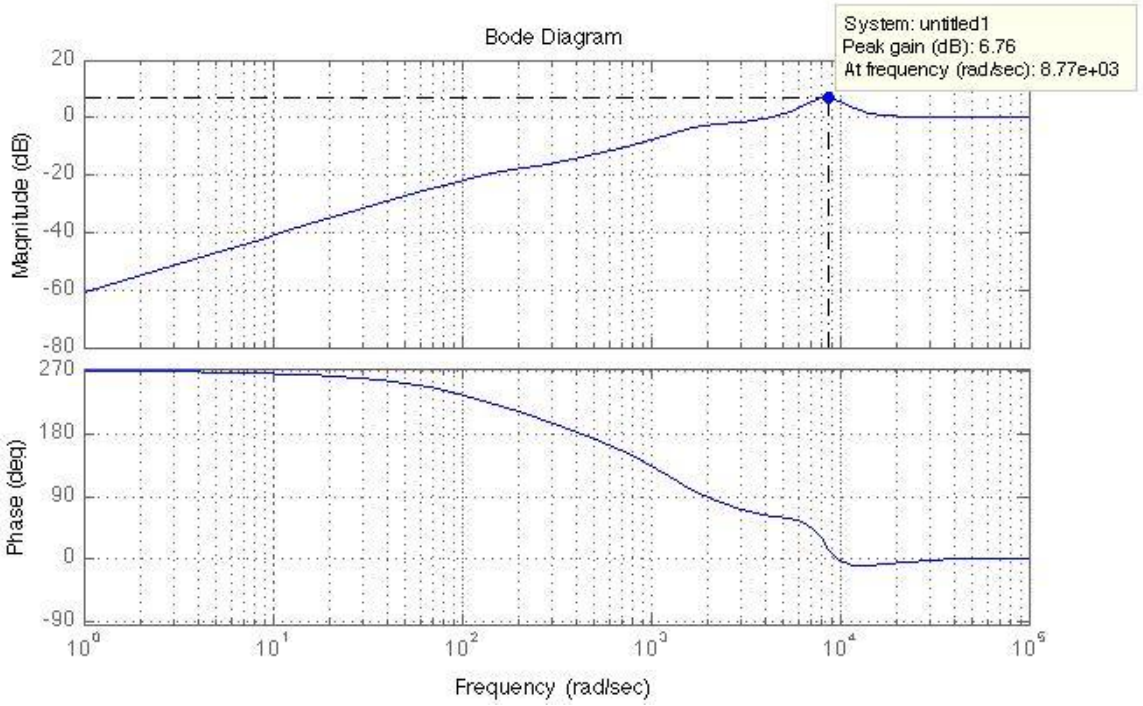

Figure 7-13 Sensitivity function of radial magnetic bearing PID controller

7.3.3 Thrust Bearing Controller

The controller for the thrust magnetic bearing was designed similar to the radial magnetic bearing. The same sensors and power amplifiers were used and hence their parameters remain unchanged. As with the case of the radial bearing, the eigenvalues of the system without and with the controller are shown in Table 7-8 and Table 7-9 respectively.

Real part	Imaginary part
-73500	-
-55556	-
-10399	-
-6210	7080
-6210	-7080
53.65	
-53.65	

Table 7-8 Eigen values of system without PID controller (unstable)

Real part	Imaginary part
-73500	-
-55626	-
-8923.4	5947.7
-8923.4	-5947.7
-2357.2	3097.5
-2357.2	-3097.5
-197.8	
-30.49	

Table 7-9 Eigen values of the system with PID controller (stable)

The stable root locus plot is shown in Figure 7-14 . Similar to the radial bearing, the step and ramp responses of the thrust bearing controller are obtained in addition to the sensitivity function plot. This is shown in Figure 7-15 and Figure 7-16 respectively.

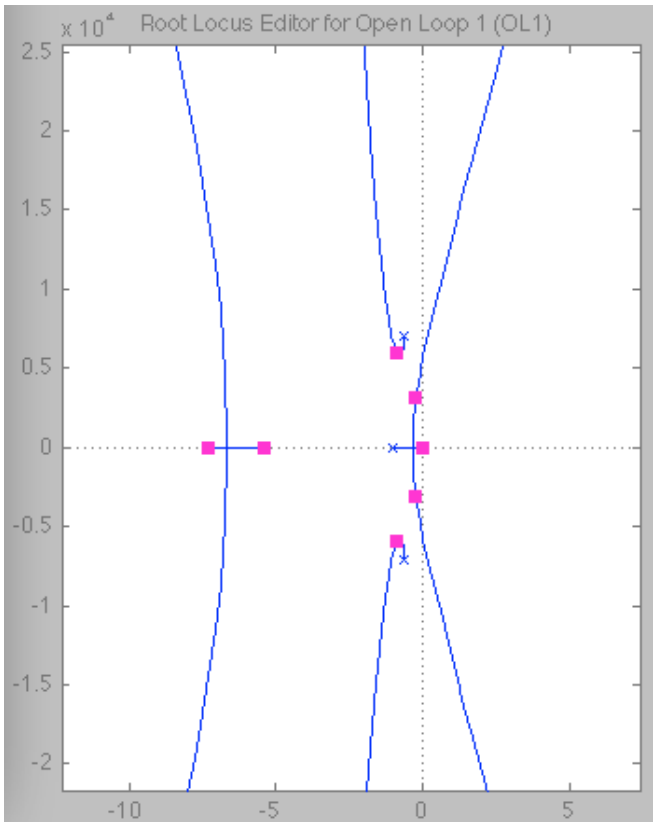

Figure 7-14 Root locus plot of system with thrust bearing controller

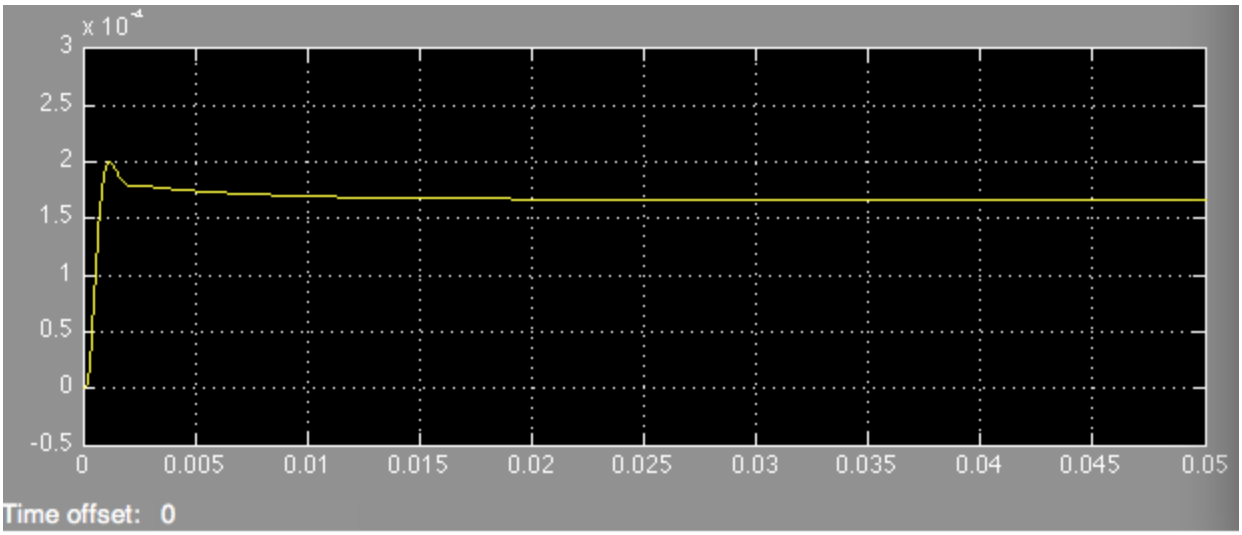

(a)

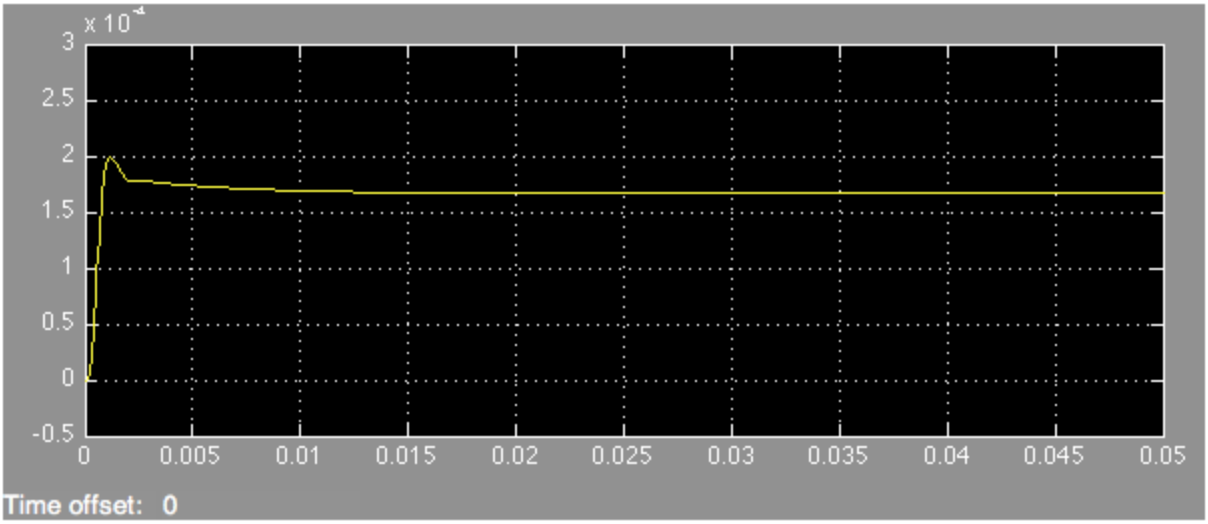

(b)

Figure 7-15(a) Step and (b) Ramp response of the thrust bearing PID controller

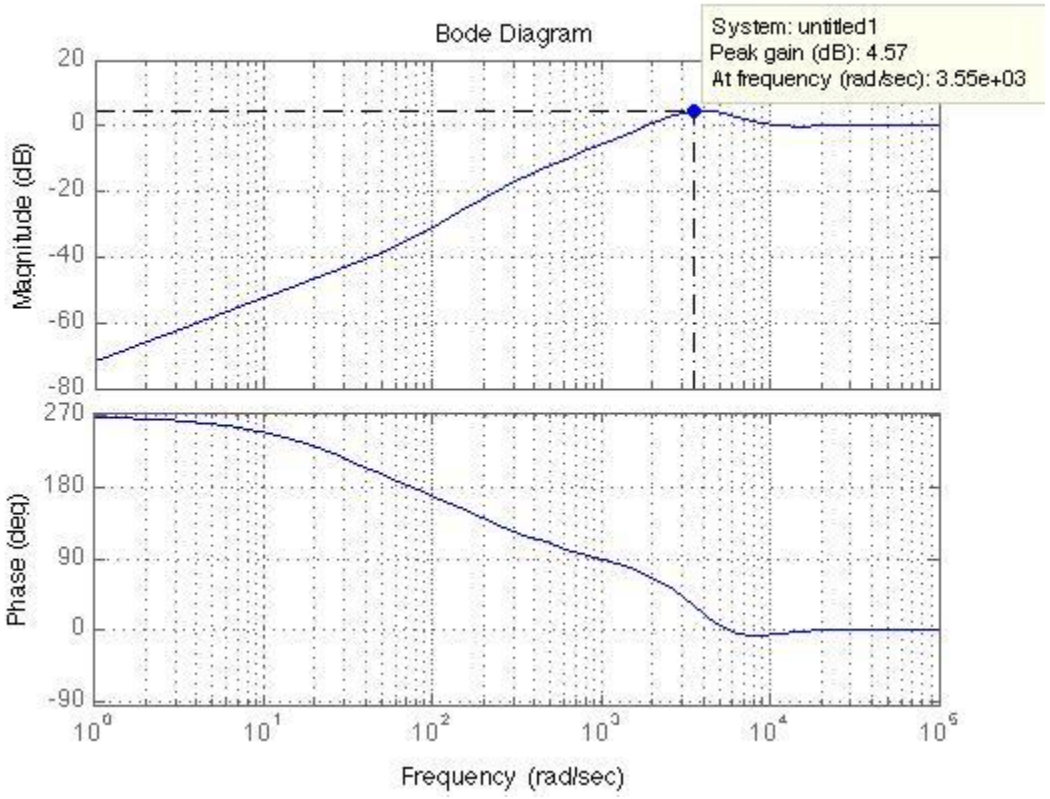

Figure 7-16 Sensitivity function of thrust magnetic bearing PID controller

The obtained overshoot value is 15%. As with the case of the radial bearing, the thrust bearing controller will also be able to handle the input changes in the magnetic bearing.

8 Losses Calculation and Thermal Modeling

The ROMAC flywheel is an electromechanical system which represents a very intricate complex system due to the various components and different materials used in its construction. Different components such as the PM alternator, magnetic thrust bearing and composite rotor contribute to losses which in turn transforms into heat. Hence, the safe operation of the FES system depends on the temperature tolerances of these components. While it is extremely difficult to accurately model the thermal behavior of the FES system, a good approximation can be made at the design stage with respect to estimating the losses and heat generated during operation. This section describes the various losses of the ROMAC FES system and the thermal model created to identify the heat sources.

8.1.1 Electrical and Mechanical Losses

The major form of electrical losses comes from the PM alternator and the magnetic bearings. The two major losses that fall under this category include the copper losses and iron losses. Copper losses are mostly incurred during load conditions and can be expressed as

$$P_{Cu} = 2{I_{DC}}^2 R_{sw} \qquad \textbf{(8-1)}$$

The temperature correction of the stator winding resistance is given by

$$R_T = R_{20}[1 + 0.00393(T_{win} - T_{20})] \qquad \textbf{(8-2)}$$

The iron losses can be calculated from the hysteresis loss, eddy current loss and excess loss. This is given by

$$P_{Iron} = P_{hyst} + P_{eddy} + P_{ex} \qquad \textbf{(8-3)}$$

A 1D model has been chosen for simplicity to give us a good initial understanding of the losses involved. It has been shown that a 1D model is sufficient to predict the losses with good accuracy [173]. A study suggests that the error obtained is within 10-15% [173]. The hysteresis loss for a one dimensional alternating field with flux densities between 0.2T and 1.5T is given by

$$P_{hyst} = k_{hys} f_{rm} V_{iron} B_m{}^{1.6} \qquad \textbf{(8-4)}$$

k_{hys} is the hysteresis loss constant which depends on the material [171].

The eddy current loss density of the alternator per cycle can be computed as [174]

$$P_{eddy} = \frac{\sigma_{mat} t_{th}{}^2}{12 f_f \rho} \times \frac{1}{T_{work}} \int_0^{T_{work}} \left|\frac{dB}{dt}\right|^2 dt \qquad \textbf{(8-5)}$$

In a finite element mode, the eddy current losses in the windings can be obtained from [175]

$$P_{eddy} = \frac{\pi^2 \sigma_{mat}}{4\rho} f_f{}^2 d_{cond}{}^2 m_{cond} \left[B_{mx}{}^2 + B_{my}{}^2\right] \eta_d{}^2 \qquad \textbf{(8-6)}$$

It is expected that the magnetic thrust bearing is the main source of eddy current losses [176]. The expression for eddy current loss in the magnetic thrust bearing in the frequency domain is [175]

$$P_{eddy,thrust} = |I(s)|^2 Re\left(\frac{N^2 s}{\mathcal{R}_r + \mathcal{R}_i \sqrt{s}}\right) \qquad \textbf{(8-7)}$$

The flux path division for the magnetic thrust bearing is given in Figure 8-1. The fringing flux in the air gap is calculated as

$$A_{eff} = \frac{1}{2}\left\{\pi\left[\left(r_1 + \frac{1}{2}g\right)^2 - \left(r_0 - \frac{1}{2}g\right)^2\right] + \pi\left[\left(r_3 + \frac{1}{2}g\right)^2 - \left(r_2 - \frac{1}{2}g\right)^2\right]\right\} \qquad \textbf{(8-8)}$$

The equivalent expression for each path is tabulated in Table 8-1.

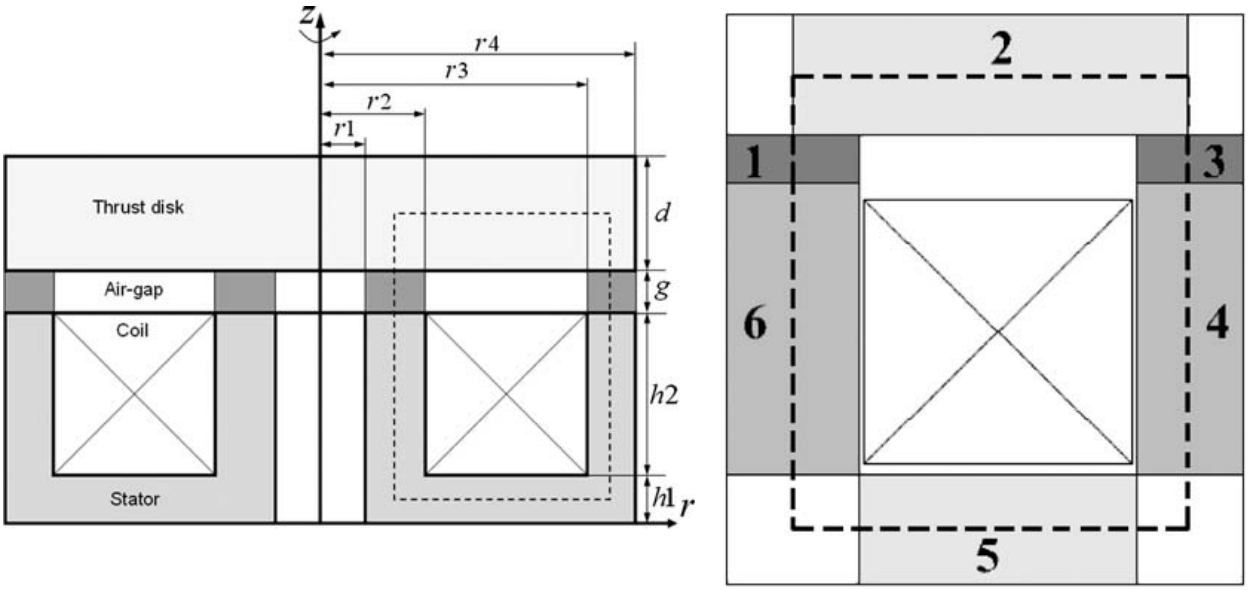

Figure 8-1 Flux path division of the magnetic thrust bearing.

Path no	Static Reluctance ($\mathcal{R}_r$)	Dynamic Reluctance ($\mathcal{R}_i$)
1	$g/\mu_0 A_{eff}$	0
2	$\ln((r_4+r_3)/(r_1+r_2))/(2\pi\mu_0\mu_r \mathrm{d})$	$\ln((r_4+r_3)/(r_1+r_2))/(2\pi\sqrt{\sigma/\mu_0\mu_r})$
3	$g/\mu_0 A_{eff}$	0
4	$h_1/[\pi\mu_0\mu_r({r_2}^2-{r_1}^2)]$	$h_1/[(2\pi r_2).\sqrt{\sigma/\mu_0\mu_r}]$
5	$\ln(r_3/r_2)/(2\pi\mu_0\mu_r h_2)$	$\ln(r_3/r_2)/(2\pi\sqrt{\sigma/\mu_0\mu_r})$
6	$h_1/[\pi\mu_0\mu_r({r_4}^2-{r_3}^2)]$	$h_1/[(2\pi r_3).\sqrt{\sigma/\mu_0\mu_r}]$

Table 8-1 Equivalent reluctance of the magnetic thrust bearing

The excess loss density per cycle is given by

$$P_{ex}=\frac{1}{f_f\rho}\sqrt{\sigma_{mat}k_{ex}}\times\frac{1}{T_{work}}\int_0^{T_{work}}\left|\frac{dB}{dt}\right|^2 dt \qquad \textbf{(8-9)}$$

For the ROMAC flywheel the hysteresis and excess constants are taken as $k_{hys} = 9.15 \times 10^{-3}$ and $k_{ex} = 2.2 \times 10^{-4}$ [174]. These values are based on material properties.

The mechanical losses comprise mainly of frictional losses or windage losses. Even though the ROMAC flywheel will be operated in vacuum, there will be air friction losses (as 100% vacuum is practically impossible). The air friction losses for a rotating flywheel can be given as

$$P_{air,rot} = C_f \pi \rho \omega^3 ({r_{out}}^4 - {r_{in}}^4) l_{fly} \qquad \textbf{(8-10)}$$

C_f is the frictional coefficient (taken as $3.26*10^{-3}$) [177]. A turbulent flow is assumed in these calculations.

The windage loss at the rotor ends can be computed using [178]

$$P_{air,rot} = \frac{1}{2} C_{f,end} \rho \omega^3 ({r_{out}}^5 - {r_{in}}^5) \qquad \textbf{(8-11)}$$

All the computed losses for the ROMAC FES system based on Equations (8-1 to (8-11) are tabulated in Table 8-2.

Losses	Value
Copper loss (Motor mode)	12 W
Copper loss (Generator mode)	9 W
Copper loss (Magnetic Bearings)	10 W
Eddy current loss (motor mode)	115 W
Eddy current loss (Generator mode)	115 W
Eddy current loss (Magnetic bearings)	102 W
Frictional loss (air gap)	175 W
Total Frictional loss	310 W
Total Windage loss	89 W
Total loss	638 W

Table 8-2 Electrical and Mechanical losses

It should be noted that properties of air were chosen for the above calculations. In reality, the ROMAC flywheel would be operated in vacuum which would greatly reduce the frictional and windage loss. This is because the continuous fluid model will not be valid at values close to 100% vacuum. A good estimation is that these losses would be reduced into half in vacuum [179]. The losses incurred from the power electronics cannot be predicted as it would depend on the specific component chosen. Generally these losses account for about 15%-20% of the total loss as indicated in Table 8-2 [162]

8.1.2 Heat Transfer

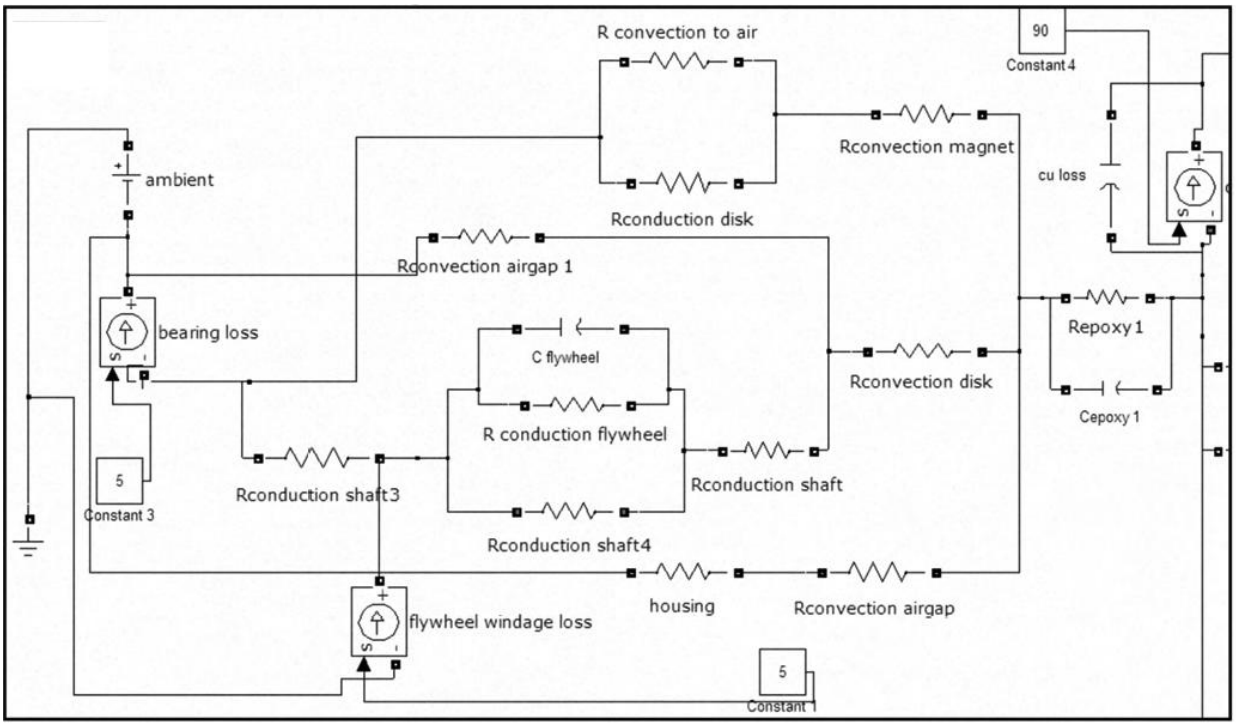

Figure 8-2 Lumped parameter thermal model for ROMAC FES system.

There are three methods by which heat is transferred or removed from the flywheel system: conduction, convection and radiation. The lumped parameter model showing these effects on the ROMAC FES system is depicted in Figure 8-2.

8.1.2.1 Conduction

In solids, heat is transferred from a high temperature region to a low temperature region with the thermal gradient taken into account. The heat transfer via conduction is given by Fourier's law as

$$Q_{cond} = -\kappa A_{fp} \frac{\partial T}{\partial x} \qquad \textbf{(8-12)}$$

A 1D model generally gives us a good approximation with an estimated error of about 20%. This is accounted for in the lumped model developed.

8.1.2.2 Convection

Heat transfer occurs from the surface of the fluid by either natural or forced convection. With natural convection, there is no artificial means of cooling and the process of heat dissipation is governed by Newton's law of cooling. This can be given as

$$Q_{conv} = h_{con} A_{fp} (T_1 - T_2) \qquad \textbf{(8-13)}$$

The heat transfer coefficient h_{con} is highly uncertain as it depends on many variables such as the temperature differences between the heated body and air, the geometry and properties of the surface. In many systems, heat is removed by means of a fan or a circulating liquid inside the machine. The approximation of the heat transfer coefficient in the case of forced convection is even more complicated as it depends on the fluid velocity and material properties of the medium and the flow direction. It is assumed that the ROMAC flywheel will have a turbulent flow with natural convection based on a similar study [180]. Since the flywheel will operate in vacuum, the heat transfer coefficient is dependent on the Reynolds number, Nusselt number and Prandtl number. The Reynolds number describes the characteristics of the velocity boundary layer, that is, laminar, transition or turbulent. The Nusselt number provides a measure of the convective heat transfer at the surface. The Prandtl number is the ratio of the rate at which momentum is transported to the rate at which thermal energy is transported in the laminar boundary layer. This number is an indication of relative rates of growth of the velocity and thermal boundary layers. It is assumed that the flow is turbulent with natural convection. The heat transfer coefficient is then obtained based on the thermal conductivity. Finally the Nusselt number is calculated. Equations (7-68) to (7-71) capture these relationships.

$$Re = \frac{U_m D_{in.cy}}{\vartheta_{vis}} \tag{8-14}$$

$$Turbuent\ Re \geq 10{,}000$$

$$h = \frac{\kappa}{R} N_u \tag{8-15}$$

$$N_u = 0.015 R_e^{\ 4/5} - 100\left(\frac{r_c}{R}\right)^2 \tag{8-16}$$

$$r_c = 2.5 \times 10^5 \frac{\vartheta}{\omega} \tag{8-17}$$

8.1.3 Radiation

In radiation, heat is transferred via electromagnetic waves. The transfer of radiant energy between surfaces is proportional to absolute temperature, emissivity and the geometry of each surface. Consider two surfaces at different temperatures T_1 and T_2 with surface areas A_1 and A_2. The transfer of heat can be found from

$$Q_{rad} = \left[\frac{\sigma_B (T_1^4 - T_2^4)}{\left(\frac{1-\varepsilon_1}{\varepsilon_1 A_1} + \frac{1}{A_1 F_{12}} + \frac{1-\varepsilon_2}{\varepsilon_2 A_2}\right)}\right] \tag{8-18}$$

8.1.4 Thermal equivalent circuit and analysis

A lumped parameter thermal model was created in Simulink in which the heat is represented by a current source and the temperature by a voltage source. All thermal resistances are expressed in °C/W and are represented as resistors and thermal capacitances. The elements in the system are described by nodes and all of these are connected by conduction, convection or radiation resistances. Figure 8-2 shows the equivalent lumped parameter model developed.

MotorCAD, a commercial thermal analysis software, was used for this analysis. A major advantage of this package is that the heat transfer network of the lumped circuit model was generated automatically by inputting parameters such as size, orientation, field, etc. This is shown in Figure 8-3.

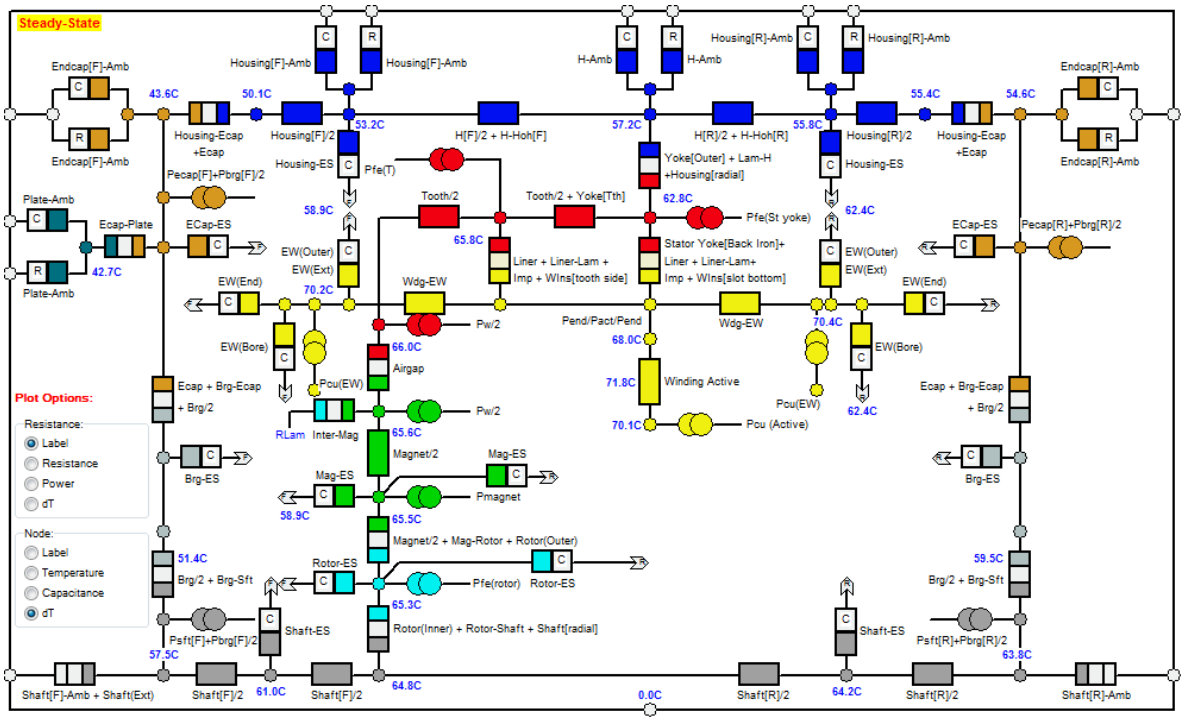

Figure 8-3 Heat transfer network of the lumped circuit model

Having created the model, a time transient analysis was done (in the motor mode) for about 300 seconds to calculate the temperature distribution at each part. This was sufficient for the system to reach steady state. A probe point was selected at each component to visualize the analysis. The results of the analysis are presented in Figure 8-4. It should be noted that the highest temperature was recorded at the alternator for the simulation. In general the rotor temperatures are higher than the stator counterparts. This is thought to be because of the higher rotor eddy current losses. As a result of the analysis, is shown that the ROMAC flywheel will operate within a safe temperature range and will not cause melting or demagnetization issues due to heat. However, it is necessary to actually measure these values in a prototype to have a clear understanding of the thermal system.

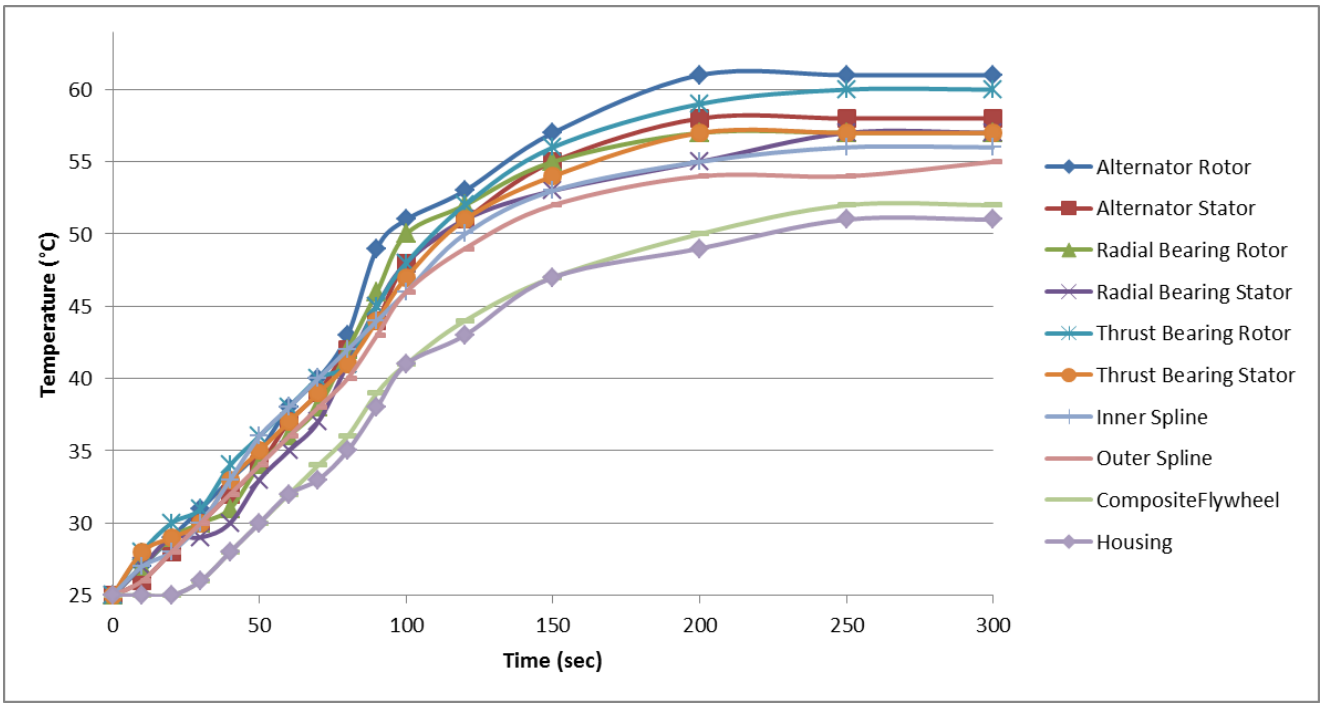

Figure 8-4 Time transient analysis of the ROMAC flywheel

In summary, the electrical and mechanical losses of the ROMAC flywheel were computed. The losses associated with different components such as the PM alternator, magnetic thrust bearing and composite rotor were calculated. Air was assumed to the fluid during calculations which resulted in a higher end losses estimate. The ROMAC flywheel will operate in near vacuum conditions. It should be noted that although an initial estimate is specified for the power electronics components, the losses cannot be predicted with accuracy as it varies widely with the selection of individual components. A thermal analysis was conducted to study the temperature effects of the flywheel during operation. This was done using a mathematical model and a lumped circuit model (MotorCAD). It was concluded that, there will be no temperature related effects to the ROMAC flywheel components under normal operating conditions.

9 Conclusions and Future work

9.1 Conclusion:

There is a recognized need to develop a clean, cost-effective and efficient means of energy storage solution to accommodate today's energy demands. Batteries are the most common method by which energy is being stored today mainly due to the low initial cost. However, over time, the costs of maintaining a battery based energy storage system can be substantial. This is mainly because of their low efficiency and the fact that they have to be replaced every 4 or 5 years. The environmental effects and production of harmful byproducts during operation are irrevocable. Their slow response time make them impractical to use with applications with rapid fluctuations. With the modern world's increasing awareness of the economic and environmental drawbacks associated with batteries, there is a huge demand to provide a viable solution.

Flywheels have been in existence for a very long time and their capabilities have been demonstrated. Flywheels are a promising solution in a number of energy storage applications due to their high efficiency, long cycle life, wide operating temperature range and high power and energy densities. In spite of all these advantages, the use of flywheels has not been fully exploited mainly due to their high initial cost and safety concerns. One of the main reasons for the high initial cost is that a heavy weight flywheel can be very expensive to manufacture and assemble. By reducing the weight of the flywheel, the manufacturing cost can go down. This thesis helps to acknowledge these issues by designing the ROMAC flywheel - a cost effective 1kW-hr energy storage flywheel for potential use in small scale applications. The ROMAC flywheel could be scaled up for use in large scale applications as well.

The main idea behind the design is that by increasing the operating speed, more energy can be stored in the flywheel. In order to keep the entire flywheel intact during operation, each component has to be designed and analyzed accordingly. The work done in the thesis is to design

the major components of the ROMAC flywheel and to analyze the entire system from an engineering perspective.

In Chapter 2, the different components of a flywheel along with a discussion on commercial flywheel systems and current research work were presented. We can conclude that while there is a proven need to develop flywheels, limited work is done on the design aspects of each key component. In a similar fashion, there have been a lot of proven state of the art technological advancements but very little work was done in putting them together. The work done in this chapter was to point out these key issues and address them by designing a 1kW-hr flywheel using the state of the art technology.

In Chapter 3, the design concept of the ROMAC flywheel was presented. Choices of different components such as composite rotor, magnetic bearings, IGBT based power electronics; PM alternator and housing were presented and discussed. It was concluded that the centrifugal stresses was one of the major limiting factors of the flywheel design which in turn depended on the choice of rotor material. Hence the rotor was designed first followed by the other components. Using plots of energy/weight, energy/volume, rotational speed and corresponding stresses, a preliminary initial sizing of the flywheel was obtained. The designed rotor had a weight of 60 kg and operated at 40,000 rpm. This was verified by a simplified stress analysis.

In Chapter 4, the design of the composite rotor was presented. The circumferential stress and radial stress were plotted against rotor radius to determine a more accurate rotor dimension. In order to prevent the rotor components from detaching, two steel spline rings were used. The spline rings ensure the structural integrity of the flywheel. A three dimensional analysis was done on the entire structure and it was concluded that the rotor would not fail structurally at the desired operating speed. This was followed by the design of the housing containment. Three different rotor failure modes were analyzed and discussed. A simple mathematical model proved that for each of the rotor failure mode, the housing will be able to contain the damaged rotor debris.

In Chapter 5, the bearing support system was presented. The designs of a thrust magnetic bearing and radial magnetic bearing were shown. The preliminary design was done using mathematical circuit models which was then analyzed using a three dimensional non-linear finite element

analysis. The different parameters of the magnetic bearing such as slew rate, magnetic energy and inductance were deduced. The choice of a 4 row tapered roller bearings to be used as a backup bearing was then justified and the different parameters of the backup bearings were presented. It was concluded that the designed magnetic bearings should be able to levitate and sustain the rotor during operation. In case of bearing failure, the backup bearing should be able to catch the rotor.

In Chapter 6, the chosen power electronic components were presented and discussed. Analytical models of the DC bus, PMSM, PWM invertor/rectifier and the flywheel were obtained. The integrated model combining all these components was then presented along with the specifications of each component. Both the charging and discharging characteristics were studied. Finally, PSIM was used to verify parameters such as current, power factor and voltage at different rotational speeds. It could be concluded that both these models prove that for an energy capacity of 1 kW-hr, the chosen power electronic parameters would suffice.

In Chapter 7, the system level analyses of the designed flywheel system are presented. A rotordynamic analysis was first performed and it was made sure that the ROMAC flywheel will not be operating near any critical speeds. This was followed by the design of a PID controller to control the magnetic bearings. The controller design and the various parameters of the sensor model were presented. The step response of the 4-input 4-output PID controller was plotted.

In Chapter 8, the losses associated with the electrical and mechanical components of the flywheel were deduced. Finally a heat transfer model was studied to identify heat sources and the temperature rise during nominal operation. It was deduced that under vacuum, the temperature rise during operation would not have any adverse effects on component performance.

In summary, the work done in this thesis is to perform a preliminary design of a cost effective 1 kW-hr flywheel for use in small or large scale applications. A unique barrel type design, which combines the state of the art technological advancements, was coined. The composite rotor, 2 thrust magnetic bearings, 2 radial bearings and power electronics were designed. System level analysis such as stress, thermal, electromagnetic, rotordynamic and failure analyses were performed to ensure design integrity. The primary form of cost saving comes from the material and manufacturing costs. The small size of the flywheel rotor is compensated by rotating it at a

higher speed to provide the desired energy capacity. The ROMAC flywheel will have estimated cost savings of about 40% over traditional flywheel designs.

9.2 Future Work

The work done in this thesis is to present a preliminary design of a 1 kW-hr energy storage flywheel. There exists a lot of scope and demand for continued research in this field. The ROMAC flywheel system prototype designed in this work lends itself to further modeling, analysis, and control studies. The ROMAC flywheel can be built based on the design principles presented in this thesis. Experimental validation of the presented simulation results could be done which can further prove the integrity of the flywheel. The energy losses of the flywheel system can be predicted with more accuracy which can be used to improve the design. Having verified and tested the design, several units could be connected in parallel to store a much larger energy capacity. A detailed drop analysis has to be done in order to verify the performance of the auxiliary bearings. A lot of scope exists in continued research in developing a more responsive magnetic bearing controller, conducting spin to failure tests, and accurately predict the thermal responsiveness of the system. Finally, practical applications of the designed flywheel can be tested.

References

[1] Asif, M., and Muneer, T., 2007, "Energy Supply, its Demand and Security Issues for Developed and Emerging Economies," Renewable and Sustainable Energy Reviews, **11**(7) pp. 1388-1413.

[2] Omer, A. M., 2008, "Energy, Environment and Sustainable Development," Renewable and Sustainable Energy Reviews, **12**(9) pp. 2265-2300.

[3] Lior, N., 2010, "Sustainable Energy Development: The Present (2009) Situation and Possible Paths to the Future," Energy, **35**(10) pp. 3976-3994.

[4] Ebrahim, T., and Zhang, B., 2008, "CleanTX Analysis on Energy Storage," Cleanenergy Incubator, University of Texas at Austin, .

[5] Chefurka, P., "Http://Www.Paulchefurka.Ca/WEAP2/WEAP2.Html," .

[6] Hall, P. J., and Bain, E. J., 2008, "Energy-Storage Technologies and Electricity Generation," Energy Policy, **36**(12) pp. 4352-4355.

[7] Dincer, I., 2000, "Renewable Energy and Sustainable Development: A Crucial Review," Renewable and Sustainable Energy Reviews, **4**(2) pp. 157-175.

[8] Narayan, R., and Viswanathan, B., 1998, "Chemical and electrochemical energy systems," Universities Press, .

[9] Nagorny, A. S., Jansen, R. H., and Kankam, M. D., 2007, "Experimental Performance Evaluation of a High Speed Permanent Magnet Synchronous Motor and Drive for a Flywheel Application at Different Frequencies," .

[10] Bitterly, J. G., 1998, "Flywheel Technology: Past, Present, and 21st Century Projections," Aerospace and Electronic Systems Magazine, IEEE, **13**(8) pp. 13-16.

[11] Hebner, R., Beno, J., and Walls, A., 2002, "Flywheel Batteries Come Around Again," Spectrum, IEEE, **39**(4) pp. 46-51.

[12] Hawkins, L., MCMULLEN, P., and LARSONNEUR, R., 2005, "Development of an AMB Energy Storage Flywheel for Commercial Application," International Symposium on Magnetic Suspension Technology, Dresden, Germany, Anonymous .

[13] Krack, M., Secanell, M., and Mertiny, P., "Rotor Design for High-Speed Flywheel Energy Storage Systems," .

[14] Arnold, S., Saleeb, A., and Al-Zoubi, N., 2002, "Deformation and Life Analysis of Composite Flywheel Disk Systems," Composites Part B: Engineering, **33**(6) pp. 433-459.

[15] Dell, R. M., and Rand, D. A. J., 2001, "Energy Storage—a Key Technology for Global Energy Sustainability," Journal of Power Sources, **100**(1) pp. 2-17.

[16] Lewis, D. W., 1995, Flywheel Storage System with Improved Magnetic Bearings, .

[17] Beltran San Segundo, H., 2011, "Energy Storage Systems Integration into PV Power Plants," Materia (s), **16**pp. 12-2011.

[18] Evliya, H., 2007, "ENERGY STORAGE FOR SUSTAINABLE FUTURE—A SOLUTION TO GLOBAL WARMING," Thermal Energy Storage for Sustainable Energy Consumption, pp. 87-99.

[19] Ricci, M., and Fiske, O. J., 2008, Third Generation Flywheels for Electric Storage, .

[20] Pichot, M., and Driga, M., 2005, "Loss reduction strategies in design of magnetic bearing actuators for vehicle applications," Electromagnetic Launch Technology, 2004. 2004 12th Symposium on, Anonymous IEEE, pp. 508-513.

[21] Bolund, B., Bernhoff, H., and Leijon, M., 2007, "Flywheel Energy and Power Storage Systems," Renewable and Sustainable Energy Reviews, **11**(2) pp. 235-258.

[22] Liu, H., and Jiang, J., 2007, "Flywheel Energy storage—An Upswing Technology for Energy Sustainability," Energy and Buildings, **39**(5) pp. 599-604.

[23] Kirk, J. A., and Studer, P. A., 1997, "Flywheel Energy Storage--II:: Magnetically Suspended Superflywheel," International Journal of Mechanical Sciences, **19**(4) pp. 233-245.

[24] Anonymous "Http://Www.Dg.History.Vt.Edu/Ch2/Storage.Html," .

[25] Hebner, R., Beno, J., and Walls, A., 2002, "Flywheel Batteries Come Around Again," Spectrum, IEEE, **39**(4) pp. 46-51.

[26] WOOD, W., 2011, "VYCON VDC," Broadcast Engineering, **53**(3) pp. 122-122.

[27] Andrews, J. A., Badger, D. A., Fuller, R. L., 2003, "Integrated Flywheel Uninterruptible Power Supply System." Integrated Flywheel Uninterruptible Power Supply System, .

[28] Babuska, V., Beatty, S., DeBlonk, B., 2004, "A review of technology developments in flywheel attitude control and energy transmission systems," Aerospace Conference, 2004. Proceedings. 2004 IEEE, Anonymous IEEE, **4,** pp. 2784-2800 Vol. 4.

[29] Tsao, P., Senesky, M., and Sanders, S. R., 2003, "An Integrated Flywheel Energy Storage System with Homopolar Inductor Motor/Generator and High-Frequency Drive," Industry Applications, IEEE Transactions On, **39**(6) pp. 1710-1725.

[30] Tarrant, C., 1999, "Revolutionary Flywheel Energy Storage System for Quality Power," Power Engineering Journal, **13**(3) pp. 159-163.

[31] Cimuca, G. O., Saudemont, C., Robyns, B., 2006, "Control and Performance Evaluation of a Flywheel Energy-Storage System Associated to a Variable-Speed Wind Generator," Industrial Electronics, IEEE Transactions On, **53**(4) pp. 1074-1085.

[32] Lazarewicz, M., 2002, "A description of the beacon power high energy and high power composite flywheel energy storage systems," Electrical Energy Storage Systems Applications and Technologies (EESAT) Conference Proceedings, Anonymous .

[33] Harlow, N., and Johnson, R. S., "INTEGRATING FLYWHEEL-BASED KINETIC ENERGY RECOVERY SYSTEMS IN HYBRID VEHICLES," .

[34] PIERCE, C., 2006, "Pentadyne's VSSDC," Broadcast Engineering, **48**(9) pp. 90-92.

[35] Parmley, D. W., 2008, Renewable Energy Power Systems, .

[36] Anonymous "Www.**kinetictraction**.Com/," .

[37] Active power, "Http://Www.Activepower.Com/Documents/Datasheets/CSMMS-US-W.Pdf," .

[38] Briat, O., Vinassa, J., Lajnef, W., 2007, "Principle, Design and Experimental Validation of a Flywheel-Battery Hybrid Source for Heavy-Duty Electric Vehicles," Electric Power Applications, IET, **1**(5) pp. 665-674.

[39] Hawkins, L., McMullen, P., and Larsonneur, R., 2005, "Development of an AMB Energy Storage Flywheel for Commercial Application," International Symposium on Magnetic Suspension Technology, Dresden, Germany, Anonymous .

[40] McMullen, P., Vuong, V., and Hawkins, L., 2006, "Flywheel Energy Storage System with AMB's and Hybrid Backup Bearings," Tenth International Symposium on Magnetic Bearings, Martigny, Switzerland, Anonymous .

[41] Darrelmann, H., 1999, "Comparison of high power short time flywheel storage systems," Telecommunication Energy Conference, 1999. INTELEC'99. The 21st International, Anonymous IEEE, .

[42] Anonymous "Www.**tribologysystems**.Com/Index_files/**TSI**_FESS_Overview.Pdf," .

[43] Bernard, N., Ahmed, H. B., Multon, B., 2003, "Flywheel Energy Storage Systems in Hybrid and Distributed Electricity Generation," Proceeding PCIM 2003, .

[44] Frank, A. A., and Beachley, N., 1979, Evaluation of the Flywheel Drive Concept for Passenger Vehicles, .

[45] Moosavi-Rad, H., and Ullman, D.G., 1990, "A band variable-inertia flywheel integrated-urban transit bus performance," Society of Automotive Engineers, .

[46] Luo, B., Wu, G., Wu, S., 1993, "Dynamic Modelling on Energy Storage System of High Speed Flywheel for Powertrain of Fuel Economy in City Bus," Society of Automotive Engineers, .

[47] Huang, Y., and Wang, K., 2007, "A Hybrid Power Driving System with an Energy Storage Flywheel for Vehicles," SAE Technical Paper, pp. 01-4114.

[48] Barr, A., and Veshagh, A., 2008, "Fuel Economy and Performance Comparison of Alternative Mechanical Hybrid Powertrain Configurations," SAE Technical Paper, pp. 01-0083.

[49] Zhang, H., Lin, Z., Huang, B., 2002, "A convex optimization approach to robust controller design for active magnetic bearing suspension systems," Proceedings of the Eighth International Symposium on Magnetic Bearings, Anonymous pp. 477-482.

[50] Li, G., Lin, Z., Allaire, P. E., 2001, "Stabilization of a high speed rotor with active magnetic bearings by a piecewise mu-synthesis controller," 6th Symposium on Magnetic Suspension Technology, Anonymous .

[51] Ahrens, M., Kucera, L., and Larsonneur, R., 1996, "Performance of a Magnetically Suspended Flywheel Energy Storage Device," Control Systems Technology, IEEE Transactions On, **4**(5) pp. 494-502.

[52] Hall, C. D., 1997, "High speed flywheels for integrated energy storage and attitude control," American Control Conference, 1997. Proceedings of the 1997, Anonymous IEEE, **3,** pp. 1894-1898.

[53] Ribeiro, P. F., Johnson, B. K., Crow, M. L., 2001, "Energy Storage Systems for Advanced Power Applications," Proceedings of the IEEE, **89**(12) pp. 1744-1756.

[54] Jiancheng, Z., Lipei, H., Zhiye, C., 2002, "Research on flywheel energy storage system for power quality," Power System Technology, 2002. Proceedings. PowerCon 2002. International Conference on, Anonymous IEEE, **1,** pp. 496-499.

[55] Barton, J. P., and Infield, D. G., 2004, "Energy Storage and its use with Intermittent Renewable Energy," Energy Conversion, IEEE Transactions On, **19**(2) pp. 441-448.

[56] Acarnley, P. P., Mecrow, B. C., Burdess, J. S., 1996, "Design Principles for a Flywheel Energy Store for Road Vehicles," Industry Applications, IEEE Transactions On, **32**(6) pp. 1402-1408.

[57] Brockbank, C., and Greenwood, C., 2010, "Fuel Economy Benefits of a Flywheel & CVT Based Mechanical Hybrid for City Bus and Commercial Vehicle Applications," SAE International Journal of Commercial Vehicles, **2**(2) pp. 115-122.

[58] Cross, D., and Brockbank, C., 2009, "Mechanical Hybrid System Comprising a Flywheel and CVT for Motorsport and Mainstream Automotive Applications," SAE Technical Paper, pp. 01-1312.

[59] Cross, D., 2008, "Optimization of Hybrid Kinetic Energy Recovery Systems (KERS) for Different Racing Circuits," SAE Technical Paper, pp. 01-2956.

[60] Flynn, M., Zierer, J., and Thompson, R., 2005, "Performance Testing of a Vehicular Flywheel Energy System," SAE Transactions, **114**(6) pp. 840-847.

[61] Burtt, D., 2007, "Fuel Economy Benefits of a High Torque Infinitely Variable Transmission for Commercial Vehicles," SAE Technical Paper, pp. 01-4206.

[62] Eby, D., Averill, R., Gelfand, B., 1997, "An injection island GA for flywheel design optimization," In: Fifth European Congress on Intelligent Techniques and Soft Computing EUFIT'97, Anonymous **1,** pp. 687-691.

[63] Hayes, R., Kajs, J., Thompson, R., 2000, "Design and Testing of a Flywheel Battery for a Transit Bus," SAE Transactions, **108**(6; PART 2) pp. 2199-2207.

[64] Anonymous "Www.Synchrony.Com," .

[65] Gabrys, C. W., and Bakis, C. E., 1997, "Design and Testing of Composite Flywheel Rotors," ASTM Special Technical Publication, **1242**pp. 1-22.

[66] Arvin, A. C., and Bakis, C. E., 2006, "Optimal Design of Press-Fitted Filament Wound Composite Flywheel Rotors," Composite Structures, **72**(1) pp. 47-57.

[67] Kascak, P. E., Kenny, B. H., Dever, T. P., 2001, "International Space Station Bus Regulation with NASA GLENN Research Center Flywheel Energy Storage System Development Unit," 2001., .

[68] Kenny, B. H., Mackin, M., Kascak, P. E., 2001, "Advanced motor control test facility for NASA GRC flywheel energy storage system technology development unit," IECEC- 36 th Intersociety Energy Conversion Engineering Conference, Anonymous pp. 91-96.

[69] Nelson, R. F., 2000, "Power Requirements for Batteries in Hybrid Electric Vehicles," Journal of Power Sources, **91**(1) pp. 2-26.

[70] Van Mierlo, J., Van den Bossche, P., and Maggetto, G., 2004, "Models of Energy Sources for EV and HEV: Fuel Cells, Batteries, Ultracapacitors, Flywheels and Engine-Generators," Journal of Power Sources, **128**(1) pp. 76-89.

[71] Thelen, R., Herbst, J., and Caprio, M., 2003, "A 2 MW flywheel for hybrid locomotive power," Vehicular Technology Conference, 2003. VTC 2003-Fall. 2003 IEEE 58th, Anonymous IEEE, **5,** pp. 3231-3235.

[72] Herbst, J., Thelen, R., and Walls, W., 2000, "Status of the Advanced Locomotive Propulsion System (ALPS) Project," HSGTA Conference, Anonymous pp. 10-13.

[73] Herbst, J. D., Caprio, M. T., and Thelen, R. F., 2003, "Advanced Locomotive Propulsion System (ALPS) Project Status 2003," Anonymous ASME, .

[74] Farges, J.P., 1994, "Organic conductors: fundamentals and applications," Marcel Dekker New York, .

[75] Mulcahy, T. M., Hull, J. R., Uherka, K. L., 2001, "Test Results of 2-kWh Flywheel using Passive PM and HTS Bearings," Applied Superconductivity, IEEE Transactions On, **11**(1) pp. 1729-1732.

[76] Fang, J., Lin, L., Yan, L., 2001, "A New Flywheel Energy Storage System using Hybrid Superconducting Magnetic Bearings," Applied Superconductivity, IEEE Transactions On, **11**(1) pp. 1657-1660.

[77] Post, R., Ryutov, D., Smith, J., 1997, "Research on Ambient-Temperature Passive Magnetic Bearings at the Lawrence Livermore National Laboratory," Proceedings of the MAG, **97**pp. 168-176.

[78] Post, R., and Ryutov, D., 1997, Ambient-Temperature Passive Magnetic Bearings: Theory and Design Equations, .

[79] Post, R., and Bender, D., 2000, "Ambient-temperature passive magnetic bearings for flywheel energy storage systems," Seventh International Symposium on Magnetic Bearings, Anonymous .

[80] Fiske, O., and Ricci, M., 2006, "Third generation flywheels for high power electricity storage," MAGLEV'2006: The 19th International Conference on Magnetically Levitated Systems and Linear Drives, Anonymous .

[81] Merritt, B. T., Dreifuerst, G. R., and Post, R. F., 1998, Halbach Array DC Motor/Generator, .

[82] Bowler, M., 1997, "Flywheel energy systems: current status and future prospects," Magnetic Material Producers Association Joint Users Conference, Anonymous pp. 22-23.

[83] Pichot, M., Kajs, J., Murphy, B., 2001, "Active Magnetic Bearings for Energy Storage Systems for Combat Vehicles," Magnetics, IEEE Transactions On, **37**(1) pp. 318-323.

[84] Ren, M., Shen, Y. D., Li, Z. Z., 2009, "Modeling and Control of a Flywheel Energy Storage System Using Active Magnetic Bearing for Vehicle," Information Engineering and Computer Science, 2009. ICIECS 2009. International Conference on, Anonymous IEEE, pp. 1-5.

[85] Carrasco, J. M., Franquelo, L. G., Bialasiewicz, J. T., 2006, "Power-Electronic Systems for the Grid Integration of Renewable Energy Sources: A Survey," Industrial Electronics, IEEE Transactions On, **53**(4) pp. 1002-1016.

[86] Rezeka, S., Awad, T., Saafan, A., 2004, "Fuzzy logic control of active magnetic bearing," Control Applications, 2004. Proceedings of the 2004 IEEE International Conference on, Anonymous IEEE, **1,** pp. 183-188.

[87] Agarwal, P. K., and Chand, S., 2010, "Fuzzy logic control of four-pole active magnetic bearing system," Modelling, Identification and Control (ICMIC), The 2010 International Conference on, Anonymous IEEE, pp. 533-538.

[88] Minihan, T., Lei, S., Sun, G., 2003, "Large Motion Tracking Control for Thrust Magnetic Bearings with Fuzzy Logic, Sliding Mode, and Direct Linearization," Journal of Sound and Vibration, **263**(3) pp. 549-567.

[89] Yin, L., and Zhao, L., "Nonlinear Control for a Large Air-Gap Magnetic Bearing System," Transactions, SMiRT, **19**.

[90] Cao, G., Fan, S., and Xu, G., 2004, "The characteristics analysis of magnetic bearing based on H-infinity controller," Intelligent Control and Automation, 2004. WCICA 2004. Fifth World Congress on, Anonymous IEEE, **1,** pp. 752-756.

[91] Nair, S., Vaidyan, M., and Joy, M., 2009, "Generalized design and disturbance analysis of robust H infinity control of active magnetic bearings," Advanced Intelligent Mechatronics, 2009. AIM 2009. IEEE/ASME International Conference on, Anonymous IEEE, pp. 1124-1129.

[92] Weiwei, Z., 2010, "A flywheel energy storage system suspended by active magnetic bearings with fuzzy PID controller," Computer Application and System Modeling (ICCASM), 2010 International Conference on, Anonymous IEEE, **5,** pp. V5-116-V5-119.

[93] Chen, H. C., 2008, "Adaptive Genetic Algorithm Based Optimal PID Controller Design of an Active Magnetic Bearing System," Innovative Computing Information and Control, 2008. ICICIC'08. 3rd International Conference on, Anonymous IEEE, pp. 603-603.

[94] Ritonj er, B., Dolinar, D., 2010, "Active magnetic bearings control," Control Conference (CCC), 2010 29th Chinese, Anonymous IEEE, pp. 5604-5609.

[95] Zhang, C., Tseng, K. J., Nguyen, T. D., 2011, "Stiffness Analysis and Levitation Force Control of Active Magnetic Bearing for a Partially-Self-Bearing Flywheel System," International Journal of Applied Electromagnetics and Mechanics, **36**(3) pp. 229-242.

[96] Lekhnitskii, S. G., 1977, "Elasticity Theory of an Anisotropic Body," M.:"Nauka, .

[97] Lekhnitskii, S.G., 1963, "Theory of elasticity of an anisotropic elastic body," Holden-Day, .

[98] Lekhnitskii, S., 1935, "Strength Calculation of Composite Beams," Vestnik Inzhen i Tekhnikov, **9**.

[99] Huang, Y., and Young, R., 1995, "Interfacial Behaviour in High Temperature Cured Carbon Fibre/Epoxy Resin Model Composite," Composites, **26**(8) pp. 541-550.

[100] Huang, J., and Fadel, G. M., 2000, "Heterogeneous Flywheel Modeling and Optimization," Materials & Design, **21**(2) pp. 111-125.

[101] Huang, Y., Frings, P., and Hennes, E., 2002, "Mechanical Properties of Zylon/Epoxy Composite," Composites Part B: Engineering, **33**(2) pp. 109-115.

[102] Pindera, M., Freed, A. D., and Arnold, S. M., 1993, "Effects of Fiber and Interfacial Layer Morphologies on the Thermoplastic Response of Metal Matrix Composites," International Journal of Solids and Structures, **30**(9) pp. 1213-1238.

[103] Schaff, J. R., and Davidson, B. D., 1997, "Life Prediction Methodology for Composite Structures. Part I—Constant Amplitude and Two-Stress Level Fatigue," Journal of Composite Materials, **31**(2) pp. 128-157.

[104] Poursartip, A., and Beaumont, P., 1986, "The Fatigue Damage Mechanics of a Carbon Fibre Composite Laminate: II—life Prediction," Composites Science and Technology, **25**(4) pp. 283-299.

[105] Fisher, C., and Lesieutre, G., 1999, "Health Monitoring of High Energy Density Rotor for use in Spacecraft Applications," Evolving and Revolutionary Technologies for the New Millennium, pp. 2145-2154.

[106] Shiue, F., Lesieutre, G. A., and Bakis, C. E., 2002, "A Virtual Containment Strategy for Filament-Wound Composite Flywheel Rotors with Damage Growth," Journal of Composite Materials, **36**(9) pp. 1103-1120.

[107] Genta, G., 1985, "Kinetic energy storage: theory and practice of advanced flywheel systems," Butterworths, .

[108] Genta, G., 2008, "Vibration dynamics and control," Springer, .

[109] Genta, G., 2005, "Anisotropy of Rotors Or Supports," Dynamics of Rotating Systems, pp. 227-263.

[110] Genta, G., 1999, "Vibration of structures and machines: practical aspects," Springer Verlag, .

[111] Genta, G., 1997, "Motor vehicle dynamics: modeling and simulation," World Scientific Publishing Company Incorporated, .

[112] Danfelt, E. L., Hewes, S. A., and Chou, T. W., 1977, "Optimization of Composite Flywheel Design," International Journal of Mechanical Sciences, **19**(2) pp. 69-78.

[113] Portnov, G., Bakis, C., and Emerson, R., 2004, "Some Aspects of Designing Multirim Composite Flywheels," Mechanics of Composite Materials, **40**(5) pp. 397-408.

[114] Fabien, B. C., 2007, "The Influence of Failure Criteria on the Design Optimization of Stacked-Ply Composite Flywheels," Structural and Multidisciplinary Optimization, **33**(6) pp. 507-517.

[115] Kyu Ha, S., Kim, D., and Sung, T., 2001, "Optimum Design of Multi-Ring Composite Flywheel Rotor using a Modified Generalized Plane Strain Assumption," International Journal of Mechanical Sciences, **43**(4) pp. 993-1007.

[116] Arvin, A. C., and Bakis, C. E., 2006, "Optimal Design of Press-Fitted Filament Wound Composite Flywheel Rotors," Composite Structures, **72**(1) pp. 47-57.

[117] Herakovich, C. T., and Tarnopol'skii, Y., 1989, "Handbook of Composites. Vol. 2. Structures and Design," Elsevier Science Publishers, P.O.Box 103, 1000 AC Amsterdam, the Netherlands, 1989., .

[118] Krack, M., Secanell, M., and Mertiny, P., 2010, "Cost Optimization of Hybrid Composite Flywheel Rotors for Energy Storage," Structural and Multidisciplinary Optimization, **41**(5) pp. 779-795.

[119] Ratner, J. K., Chang, J. B., and Christopher, D. A., 2003, "Composite Flywheel Rotor Technology-A Review," ASTM Special Technical Publication, **1436**pp. 3-28.

[120] Ha, S. K., Kim, J. H., and Han, Y. H., 2008, "Design of a Hybrid Composite Flywheel Multi-Rim Rotor System using Geometric Scaling Factors," Journal of Composite Materials, **42**(8) pp. 771-785.

[121] Pérez-Aparicio, J. L., and Ripoll, L., 2011, "Exact, Integrated and Complete Solutions for Composite Flywheels," Composite Structures, **93**(5) pp. 1404-1415.

[122] Nakken, T., Strand, L., Frantzen, E., 2006, "The Utsira wind-hydrogen system–operational experience," Proc. European Wind Energy Conf, Athens, Greece, Anonymous .

[123] Chen, H., Cong, T. N., Yang, W., 2009, "Progress in Electrical Energy Storage System: A Critical Review," Progress in Natural Science, **19**(3) pp. 291-312.

[124] Beaudin, M., Zareipour, H., Schellenberglabe, A., 2010, "Energy for Sustainable Development," .

[125] Yang, B., Makarov, Y., Desteese, J., 2008, "On the use of energy storage technologies for regulation services in electric power systems with significant penetration of wind energy," Electricity Market, 2008. EEM 2008. 5th International Conference on European, Anonymous IEEE, pp. 1-6.

[126] Abedini, A., Mandic, G., and Nasiri, A., 2008, "Wind Power Smoothing using Rotor Inertia Aimed at Reducing Grid Susceptibility," International Journal of Power Electronics, **1**(2) pp. 227-247.

[127] Hebner, R., Beno, J., and Walls, A., 2002, "Flywheel Batteries Come Around Again," Spectrum, IEEE, **39**(4) pp. 46-51.

[128] Brandenburg, L. R., and King, E. T., 1994, Hybrid Electric Vehicle Regenerative Braking Energy Recovery System, .

[129] Boretti, A., 2010, "Comparison of Fuel Economies of High Efficiency Diesel and Hydrogen Engines Powering a Compact Car with a Flywheel Based Kinetic Energy Recovery Systems," International Journal of Hydrogen Energy, **35**(16) pp. 8417-8424.

[130] Tarrant, C., 1999, "Revolutionary Flywheel Energy Storage System for Quality Power," Power Engineering Journal, **13**(3) pp. 159-163.

[131] Cross, D., and Brockbank, C., 2009, "Mechanical Hybrid System Comprising a Flywheel and CVT for Motorsport and Mainstream Automotive Applications," SAE Technical Paper, pp. 01-1312.

[132] Kilcullen, T., and Rittenhouse, J., "FLYWHEEL SYSTEMS: INCORPORTION IN HYBRID AUTOMOBILES," .

[133] dos Reis Covão, Luís André, 2008, "Master in Electrical and Computer Engineering," .

[134] Baggini, A.B., 2008, "Handbook of power quality," Wiley Online Library, .

[135] Ribeiro, P. F., Johnson, B. K., Crow, M. L., 2001, "Energy Storage Systems for Advanced Power Applications," Proceedings of the IEEE, **89**(12) pp. 1744-1756.

[136] Cross, D., and Hilton, J., 2008, "High speed flywheel based hybrid systems for low carbon vehicles," Hybrid and Eco-Friendly Vehicle Conference, 2008. IET HEVC 2008, Anonymous IET, pp. 1-5.

[137] Ibrahim, H., Ilinca, A., and Perron, J., 2008, "Energy Storage systems—Characteristics and Comparisons," Renewable and Sustainable Energy Reviews, **12**(5) pp. 1221-1250.

[138] Liu, H., and Jiang, J., 2007, "Flywheel Energy storage—An Upswing Technology for Energy Sustainability," Energy and Buildings, **39**(5) pp. 599-604.

[139] Dell, R. M., and Rand, D. A. J., 2001, "Energy Storage—a Key Technology for Global Energy Sustainability," Journal of Power Sources, **100**(1) pp. 2-17.

[140] Caprio, M. T., Murphy, B. T., and Herbst, J. D., 2004, "Spin Commissioning and Drop Tests of a 130 kW-hr Composite Flywheel," Proc. 9th Int. Symp. Magnetic Bearings, Paper, Anonymous **65,** .

[141] Ashley, S., 1996, "Designing Safer Flywheels," Mechanical Engineering, **11**pp. 88-91.

[142] Post, R., and Bender, D., 2000, "Ambient-temperature passive magnetic bearings for flywheel energy storage systems," Seventh International Symposium on Magnetic Bearings, Anonymous .

[143] Gabrys, C. W., and Bakis, C. E., 1997, "Design and testing of composite flywheel rotors," ASTM, Anonymous **3,** pp. 3-22.

[144] Kyu Ha, S., Kim, D., and Sung, T., 2001, "Optimum Design of Multi-Ring Composite Flywheel Rotor using a Modified Generalized Plane Strain Assumption," International Journal of Mechanical Sciences, **43**(4) pp. 993-1007.

[145] Ha, S. K., Jeong, H., and Cho, Y., 1998, "Optimum Design of Thick-Walled Composite Rings for an Energy Storage System," Journal of Composite Materials, **32**(9) pp. 851-873.

[146] Hansen, J. G., 2012, An Assessment of Flywheel High Power Energy Storage Technology for Hybrid Vehicles, .

[147] United States. Congress. House. Committee on Science. Subcommittee on Energy, 1996, "Partnership for a New Generation of Vehicles (PNGV): assessment of program goals, activities, and priorities: hearing before the Subcommittee on Energy and Environment of the Committee on Science, US House of Representatives, One Hundred Fourth Congress, second session, July 30, 1996," USGPO, .

[148] OKain, D., and Howell, D., 1993, Flywheel Energy Storage Technology Workshop, .

[149] Strubhar, J. L., Thompson, R. C., Pak, T. T., 2003, "Lightweight Containment for High-Energy Rotating Machines," Magnetics, IEEE Transactions On, **39**(1) pp. 378-383.

[150] Hsieh, B., Kulak, R., Price, J., 1998, Transient Analysis of a Flywheel Battery Containment during a Full Rotor Burst Event, .

[151] Toliyat, H. A., Talebi, S., McMullen, P., 2005, "Advanced high-speed flywheel energy storage systems for pulsed power applications," Electric Ship Technologies Symposium, 2005 IEEE, Anonymous IEEE, pp. 379-386.

[152] Talebi Rafsanjan, S., 2008, "Advanced High-Speed Flywheel Energy Storage Systems for Pulsed Power Application," .

[153] Chang, J., Christopher, D., and Ratner, J., "Flywheel Rotor Safe-Life Technology: Literature Search Summary," DIANE Publishing, .

[154] TEST, F. R. B., and DESIGN, C., 1998, "Orni," ORNL, **101**pp. 1.

[155] Marks, L.S., and Baumeister, T., 1922, "Mechanical engineers' handbook," McGraw-Hill, .

[156] Kennedy, J., and Belytschko, T., "Energy Source and Fluid Representation in a Structural Response code—STRAW. Argonne Natl Lab," .

[157] Maslen, E. H., and Meeker, D. C., 1995, "Fault Tolerance of Magnetic Bearings by Generalized Bias Current Linearization," Magnetics, IEEE Transactions On, **31**(3) pp. 2304-2314.

[158] Maslen, E.H., and Schweitzer, G., 2009, "Magnetic Bearings: Theory, Design, and Application to Rotating Machinery," Springer-Verlag Berlin Heidelberg, .

[159] Nehl, T., Fouad, F., and Demerdash, N., 1982, "Determination of Saturated Values of Rotating Machinery Incremental and Apparent Inductances by an Energy Perturbation Method," Power Apparatus and Systems, IEEE Transactions On, (12) pp. 4441-4451.

[160] Standard, A., 2004, "617, 2002,“," Axial and Centrifugal Compressors and Expander-Compressors for Petroleum, Chemical and Gas Industry Services,” Seventh Edition, American Petroleum Institute, Washington, DC, .

[161] Bose, B.K., 2006, "Power electronics and motor drives: advances and trends," Academic Press, .

[162] Rashid, M.H., 2001, "Power electronics handbook," Academic Pr, .

[163] Anonymous "Http://Upload.Wikimedia.Org/Wikipedia/Commons/Thumb/6/6c/IGBT_Cross_Section.Jpg/300px-IGBT_Cross_Section.Jpg)," .

[164] Akagi, H., and Sato, H., 2002, "Control and Performance of a Doubly-Fed Induction Machine Intended for a Flywheel Energy Storage System," Power Electronics, IEEE Transactions On, **17**(1) pp. 109-116.

[165] Stratton, J.A., 2007, "Electromagnetic theory," Wiley-IEEE Press, .

[166] Routex, J. Y., Gay-Desharnais, S., and Ehsani, M., 2000, "Modeling of hybrid electric vehicles using gyrator theory: application to design," Vehicular Technology Conference, 2000. IEEE VTS-Fall VTC 2000. 52nd, Anonymous IEEE, **5,** pp. 2090-2094.

[167] Hawkins, L., and McMullen, P., "An AMB Energy Storage Flywheel for Industrial Applications," .

[168] Antkowiak, B., and Nelson, F., 1998, "Rotodynamic Modeling of an Actively Controlled Magnetic Bearing Gas Turbine Engine," Journal of Engineering for Gas Turbines and Power, **120**(CONF-970604--) .

[169] Mushi, S. E., Lin, Z., and Allaire, P. E., 2012, "Design, Construction, and Modeling of a Flexible Rotor Active Magnetic Bearing Test Rig," Mechatronics, IEEE/ASME Transactions On, **17**(6) pp. 1170-1182.

[170] Swanson, E. E., Maslen, E. H., Li, G., 2008, "Rotordynamic Design Audits of AMB Supported Machinery," Proc. 37th Turbomachinery Symposium, Anonymous .

[171] Schweitzer, G., 2002, "Active magnetic bearings-chances and limitations," Proceedings of the 6th International Conference on Rotor Dynamics, Anonymous pp. 1-14.

[172] Polajžer, B., Ritonja, J., Štumberger, G., 2006, "Decentralized PI/PD Position Control for Active Magnetic Bearings," Electrical Engineering (Archiv Fur Elektrotechnik), **89**(1) pp. 53-59.

[173] Sullivan, C. R., 2001, "Computationally Efficient Winding Loss Calculation with Multiple Windings, Arbitrary Waveforms, and Two-Dimensional Or Three-Dimensional Field Geometry," Power Electronics, IEEE Transactions On, **16**(1) pp. 142-150.

[174] Zhao, N., Zhu, Z., and Liu, W., 2011, "Thermal analysis and comparison of permanent magnet motor and generator," Electrical Machines and Systems (ICEMS), 2011 International Conference on, Anonymous IEEE, pp. 1-5.

[175] Okou, R., Khan, M., Barendse, P., 2009, "Thermal model of electromechanical flywheel with brushless DC machine," Electrical Power & Energy Conference (EPEC), 2009 IEEE, Anonymous IEEE, pp. 1-5.

[176] Tian, Y., Sun, Y., and Yu, L., 2011, "Calculation of Eddy Current Loss for Magnetic Thrust Bearings," Proceedings of the Institution of Mechanical Engineers, Part J: Journal of Engineering Tribology, **225**(8) pp. 798-805.

[177] Suzuki, Y., Koyanagi, A., Kobayashi, M., 2005, "Novel Applications of the Flywheel Energy Storage System," Energy, **30**(11–12) pp. 2128-2143.

[178] Zeisberger, M., and Gawalek, W., 1998, "Losses in Magnetic Bearings," Materials Science and Engineering: B, **53**(1) pp. 193-197.

[179] Flynn, M.M., 2003, "A methodology for evaluating and reducing rotor losses, heating, and operational limitations of high-speed flywheel batteries," .

[180] Huynh, C., Zheng, L., and McMullen, P., 2007, "Thermal Performance Evaluation of a High-Speed Flywheel Energy Storage System," Industrial Electronics Society, 2007. IECON 2007. 33rd Annual Conference of the IEEE, Anonymous IEEE, pp. 163-168.

[181] Lukic, S. M., Cao, J., Bansal, R. C., 2008, "Energy Storage Systems for Automotive Applications," Industrial Electronics, IEEE Transactions On, **55**(6) pp. 2258-2267.

[182] Council, E. S., 2002, "Energy Storage, the Missing Link in the Electricity Value Chain," ESC (Energy Storage Council) White Paper, .

[183] Asif, M., and Muneer, T., 2007, "Energy Supply, its Demand and Security Issues for Developed and Emerging Economies," Renewable and Sustainable Energy Reviews, **11**(7) pp. 1388-1413.

[184] Hall, P. J., and Bain, E. J., 2008, "Energy-Storage Technologies and Electricity Generation," Energy Policy, **36**(12) pp. 4352-4355.

[185] Sims, R. E. H., Rogner, H. H., and Gregory, K., 2003, "Carbon Emission and Mitigation Cost Comparisons between Fossil Fuel, Nuclear and Renewable Energy Resources for Electricity Generation," Energy Policy, **31**(13) pp. 1315-1326.

[186] McCluer, S., and Christin, J. F., 2008, "Comparing Data Center Batteries, Flywheels, and Ultracapacitors," American Power Conversion, White Paper, **65**pp. 2008-2009.

[187] Schoenung, S. M., 2001, "Characteristics and Technologies for Long-Vs. Short-Term Energy Storage," Sandia Report SAND2001-0765, .

[188] Van der Linden, S., 2006, "Bulk Energy Storage Potential in the USA, Current Developments and Future Prospects," Energy, **31**(15) pp. 3446-3457.

[189] Hadjipaschalis, I., Poullikkas, A., and Efthimiou, V., 2009, "Overview of Current and Future Energy Storage Technologies for Electric Power Applications," Renewable and Sustainable Energy Reviews, **13**(6–7) pp. 1513-1522.

[190] Schoenung, S. M., and Hassenzahl, W. V., 2003, "Long-Vs. Short-Term Energy Storage Technologies Analysis A Life-Cycle Cost Study A Study for the DOE Energy Storage Systems Program," Sandia National Laboratories, .

[191] Baker, J., and Collinson, A., 1999, "Electrical Energy Storage at the Turn of the Millennium," Power Engineering Journal, **13**(3) pp. 107-112.

[192] Divya, K. C., and Østergaard, J., 2009, "Battery Energy Storage Technology for Power systems—An Overview," Electric Power Systems Research, **79**(4) pp. 511-520.

[193] McDowall, J., 2000, "Conventional battery technologies-present and future," Power Engineering Society Summer Meeting, 2000. IEEE, Anonymous **3,** pp. 1538-1540 vol. 3.

[194] Anderson, M. D., and Carr, D. S., 1993, "Battery Energy Storage Technologies," Proceedings of the IEEE, **81**(3) pp. 475-479.

[195] Divya, K., and Østergaard, J., 2009, "Battery Energy Storage Technology for Power systems—An Overview," Electric Power Systems Research, **79**(4) pp. 511-520.

[196] Bode, H., 1977, "Lead-Acid Batteries," .

[197] Dodson, V. H., 1961, "Some Important Factors that Influence the Composition of the Positive Plate Material in the Lead-Acid Battery," Journal of the Electrochemical Society, **108**pp. 401.

[198] Schoenung, S. M., and Hassenzahl, W., 2007, "Long Vs. Short-Term Energy Storage: Sensitivity Analysis," SAND2007-4253, .

[199] Singh, P., and Jonshagen, B., 1991, "Zinc□ Bromine Battery for Energy Storage," Journal of Power Sources, **35**(4) pp. 405-410.

[200] Cathro, K., Cedzynska, K., and Constable, D., 1985, "Some Properties of Zinc/Bromine Battery Electrolytes," Journal of Power Sources, **16**(1) pp. 53-63.

[201] Linden, D., and Reddy, T. B., 1995, "Handbook of Batteries," New York, .

[202] Oxley, J., 1980, "Zinc-bromine batteries for energy storage," Progress in Batteries and Solar Cells. Volume 3, Anonymous **1,** pp. 223-226.

[203] Hall, P. J., and Bain, E. J., 2008, "Energy-Storage Technologies and Electricity Generation," Energy Policy, **36**(12) pp. 4352-4355.

[204] McDowall, J., 1999, "Nickel-cadmium batteries for energy storage applications," Battery Conference on Applications and Advances, 1999. The Fourteenth Annual, Anonymous IEEE, pp. 303-308.

[205] Ogawa, H., Ikoma, M., Kawano, H., 1988, "Metal hydride electrode for high energy density sealed nickel-metal hydride battery," Power Sources 12: Research and Development in Non-Mechanical Electrical Power Sources, Anonymous **1,** pp. 393-409.

[206] Mantell, C. L., 1982, "Batteries and Energy Systems," .

[207] Tarascon, J., and Armand, M., 2001, "Issues and Challenges Facing Rechargeable Lithium Batteries," .

[208] Chalk, S. G., and Miller, J. F., 2006, "Key Challenges and Recent Progress in Batteries, Fuel Cells, and Hydrogen Storage for Clean Energy Systems," Journal of Power Sources, **159**(1) pp. 73-80.

[209] Anonymous "Http://Www.Power-Technology.Com/Uploads/Feature/feature1139/1-Caes-System.Jpg," .

[210] Lund, H., and Salgi, G., 2009, "The Role of Compressed Air Energy Storage (CAES) in Future Sustainable Energy Systems," Energy Conversion and Management, **50**(5) pp. 1172-1179.

[211] Succar, S., and Williams, R. H., 2008, "Compressed Air Energy Storage: Theory, Resources, and Applications for Wind Power," Princeton Environmental Institute Report, **8**.

[212] Koshizuka, N., Ishikawa, F., Nasu, H., 2002, "Present Status of R&D on Superconducting Magnetic Bearing Technologies for Flywheel Energy Storage System," Physica C: Superconductivity, **378**pp. 11-17.

[213] Buckles, W., and Hassenzahl, W. V., 2000, "Superconducting Magnetic Energy Storage," Power Engineering Review, IEEE, **20**(5) pp. 16-20.

[214] Hsu, C. S., and Lee, W. J., 1993, "Superconducting Magnetic Energy Storage for Power System Applications," Industry Applications, IEEE Transactions On, **29**(5) pp. 990-996.

[215] Chalk, S. G., and Miller, J. F., 2006, "Key Challenges and Recent Progress in Batteries, Fuel Cells, and Hydrogen Storage for Clean Energy Systems," Journal of Power Sources, **159**(1) pp. 73-80.

[216] Hoffmann, P., 2002, "Tomorrow's energy: hydrogen, fuel cells, and the prospects for a cleaner planet," The MIT Press, .

[217] Kong, V., Foulkes, F., Kirk, D., 1999, "Development of Hydrogen Storage for Fuel Cellgenerators. i: Hydrogen Generation using Hydrolysishydrides," International Journal of Hydrogen Energy, **24**(7) pp. 665-675.

[218] Smith, W., 2000, "The Role of Fuel Cells in Energy Storage," Journal of Power Sources, **86**(1) pp. 74-83.

[219] Hadjipaschalis, I., Poullikkas, A., and Efthimiou, V., 2009, "Overview of Current and Future Energy Storage Technologies for Electric Power Applications," Renewable and Sustainable Energy Reviews, **13**(6) pp. 1513-1522.

[220] Conway, B.E., 1999, "Electrochemical supercapacitors: scientific fundamentals and technological applications," Springer, .

[221] Shukla, A., Sampath, S., and Vijayamohanan, K., 2000, "Electrochemical Supercapacitors: Energy Storage Beyond Batteries," Current Science, **79**(12) pp. 1656-1661.

[222] Burke, A., 2000, "Ultracapacitors: Why, how, and Where is the Technology," Journal of Power Sources, **91**(1) pp. 37-50.

[223] Hasnain, S., 1998, "Review on Sustainable Thermal Energy Storage Technologies, Part I: Heat Storage Materials and Techniques," Energy Conversion and Management, **39**(11) pp. 1127-1138.

[224] , J. M., Cabeza, L. F., 2003, "Review on Thermal Energy Storage with Phase Change: Materials, Heat Transfer Analysis and Applications," Applied Thermal Engineering, **23**(3) pp. 251-283.

[225] Dincer, I., and Rosen, M., 2010, "Thermal energy storage: systems and applications," Wiley, .

[226] Farid, M. M., Khudhair, A. M., Razack, S. A. K., 2004, "A Review on Phase Change Energy Storage: Materials and Applications," Energy Conversion and Management, **45**(9) pp. 1597-1615.

[227] Anonymous "Http://Www.Scotland.Gov.Uk/Publications/2010/10/28091356/4," .

[228] Semadeni, M., 2003, "Energy Storage as an Essential Part of Sustainable Energy Systems," CEPE Working Paper Series, .

[229] Lindberg, M. R., 1985, "Engineering Economic Analysis," Mechanical Engineering Review Manual, 7th Edition, Professional Publications, San Carlos, California, .

[230] Schoenung, S. M., and Hassenzahl, W. V., 2003, "Long-Vs. Short-Term Energy Storage Technologies Analysis. A Life-Cycle Cost Study. A Study for the DOE Energy Storage Systems Program," Sandia National Laboratories, .

APPENDIX

A. Short Term Energy Storage

A.1. Introduction to Energy Storage technologies

Energy storage technologies are rapidly emerging as a potential research area primarily due to their contribution in stabilizing electric grids and assuring a steady source of power in case of power outages. Without energy storage, a delivery network capable of withstanding the highest load must be developed which should cater to variable end-user demands. Development of such a system is impractical in terms of cost, safety, reliability and energy utilization [139]. The current demand in the electricity market facilitates the use of these technologies for power storage during low usage times or in combination with renewable energy generation sources. Another potential demand for these technologies is to store "wasted" energy and supply it back to the grid as a means of energy regeneration [181] .

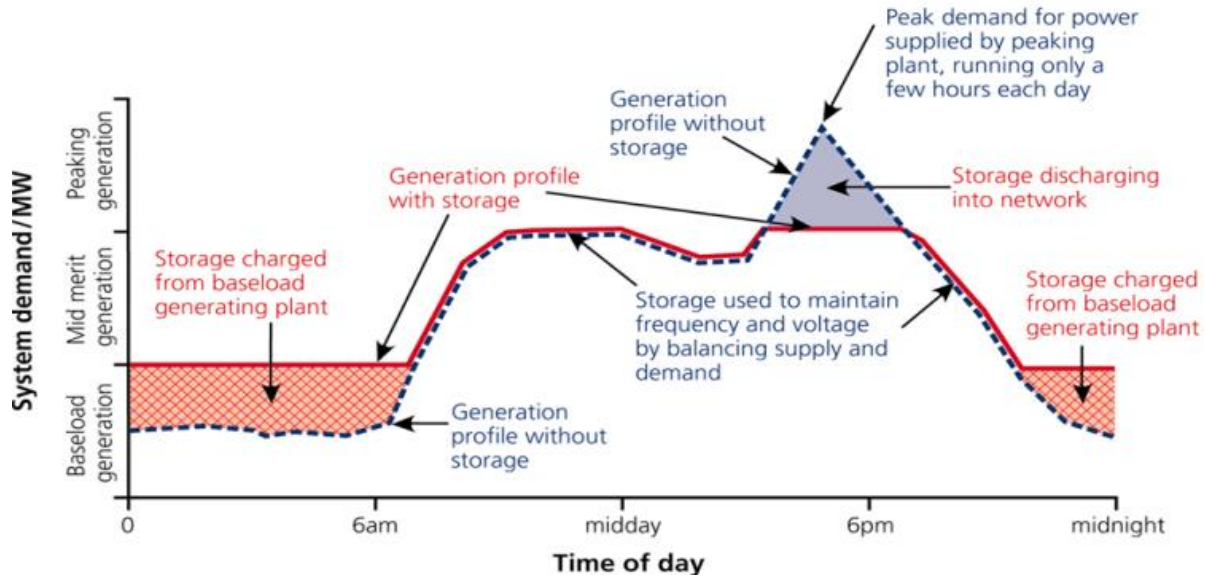

Figure A-1 Load profile of a large scale energy storage facility with and without storage[182]

The demand for electric power is increasing exponentially and is projected to grow globally by 36% from 2010 to 2035[183]. However, the generation and transmission facilities have not been able to satisfy these demands due to various economic, technical and environmental constraints [139, 182]. In advanced power applications, generators will not be able to respond quickly in case of frequent power disturbances to the load. These are just some of the areas where energy storage technologies can be used to ensure power quality and reliability. An ideal energy storage solution will have the means to rapidly damp oscillations, respond to sudden changes in load, supply load during transmission or distribution interruptions and correct load voltage profiles with rapid reactive power control[184].

From a market role standpoint, energy storage technologies will help to supply power as and when needed. The primary benefits of these technologies are:

1) Lower the need for additional transmission resources.
2) Provide better integration of renewables into the system.
3) Drastically reduce the investment required for new facilities.
4) Improve the reliability of electricity supply.
5) Support more efficient use of existing assets, and
6) Increase the overall efficiency of existing power plant and transmission facilities[182]

A.1.1. Energy Storage vs. Energy Generation

Energy storage must not be confused with energy generation. Energy generation refers to the process of extracting electrical energy from other forms of energy such as burning fossil fuels, splitting of atoms or tapping water from a dam. The raw energy is converted to “shaft horsepower” which is utilized as the prime mover to rotate a generator thus converting mechanical, chemical, thermal, or nuclear energy into electricity [185]. The utility then distributes the electricity to business and home consumers across a network of power lines and transformers.

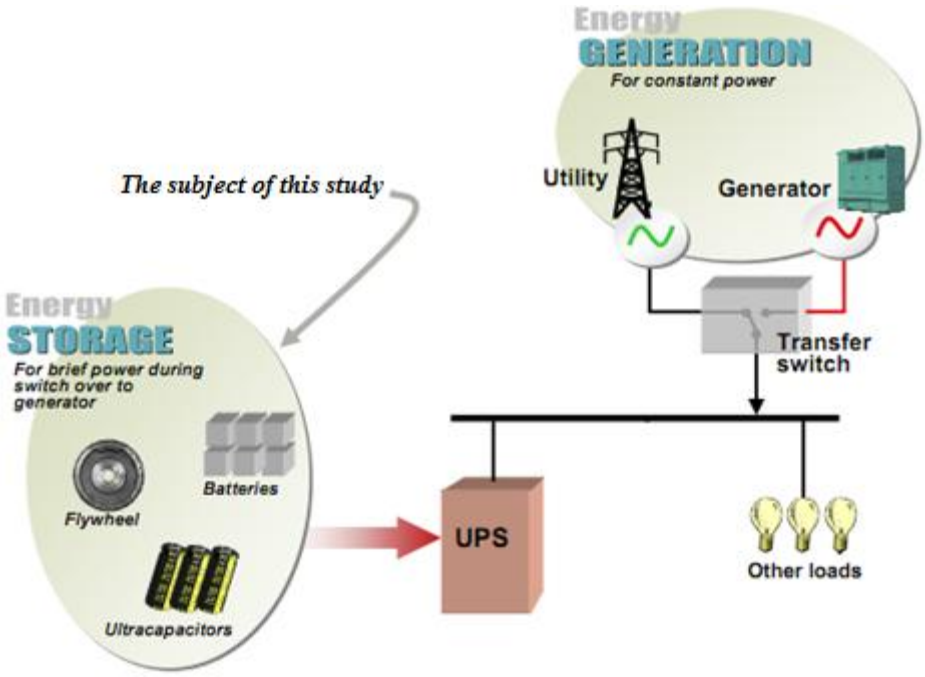

Figure A-2. Energy storage Vs Energy generation [186]

Energy storage, on the other hand, supplements overall energy availability by providing a stored source of energy in the event of interruption to the normal electrical flow. Energy storage addresses the challenges of a rapid switchover to an alternative power source when a power disturbance occurs, and the stable delivery of power to the load until the disturbance is resolved[137, 184]. By reducing peak demands for power generation and offering greater flexibility among power supply options (including renewables), energy storage systems not only help utilities by improving their cost-effectiveness, reliability, power quality and efficiency, they also reduce the environmental impact of electricity generation, transmission, and distribution[135].

A.2. Energy Storage Technologies

Energy storage technologies can be broadly classified into two divisions: long term energy storage and short term energy storage [187]. As the name indicates- long term energy storage technologies store energy for a period of days or weeks. A good example of this would be hydro-reservoirs. The topic of interest in this chapter is to compare different short term energy storage technologies. Short term energy storage technologies falls under three categories depending upon their applications. They are: bulk energy storage, distributed generation and power quality [135, 188, 189]. Bulk energy storage is primarily used for load leveling or load management while distributed generation and power quality are used for peak shaving (i.e shifting demand from peak times to times with lower demand) and end user reliability respectively. Bulk energy storage technologies store energy for a longer period of time ranging from hours to days or months while the latter two applications require short-term energy storage. Table A-1 provides a brief description of the characteristics of the various categories of short term energy storage.

Application Category	**Discharge Time Range**	**Discharge Power Range**	**Stored Energy Range**	**Applications**
Bulk energy storage	1-10 hours	10-1000 MW	10-8000 MWh	Spinning reserve, load management
Distributed generation	0.5 – 4 hours	100-2000 KW	50-8000 KWh	Transmission deferral, peak shaving
Power quality	1-30 seconds	0.1 – 2 MW	0.1 – 20 KWh	End use power quality & reliability

Table A-1 Short term energy storage applications category [190]

Depending on the application category, different energy storage technologies are considered. Due to the limitations in storage or power output, not all technologies are suitable for all

applications. Table A-2 provides a list of technologies in use (or being considered) in each application category.

Application Category	Technologies Used / Considered
Bulk Energy Storage	Lead-Acid Batteries Ni/Cd Batteries Zn/Br Batteries Pumped hydro Na/S batteries (Considered)
Distributed Generation	Lead-Acid Batteries Ni/Cd Batteries Na/S Batteries Li-ion Batteries Zn/Br Batteries V-redox batteries Compressed Air energy storage (CAES) Hydrogen Fuel Cell High Speed Flywheels (Considered)
Power Quality	Lead-Acid Batteries Li-ion Batteries (Considered) Superconducting magnet energy storage (SMES) (Considered) Ultra-Capacitors (Considered) Low Speed Flywheels High Speed Flywheels (Considered)

Table A-2. Energy storage technologies for various applications[189, 191, 192]

From Table A-2 it can be easily deduced that batteries are by far the most common kind of short-term energy storage used today. Other technologies being considered, especially for distributed generation and power quality applications include compressed air energy storage, hydrogen fuel cells, superconducting magnet energy storage, ultra-capacitors and flywheels. This study is aimed at comparing all the alternatives currently under consideration by the power generation industry to chemical batteries. Special attention will be given to ultra-capacitors, flywheels and SMES as they are all deemed as viable alternatives to batteries.

A.2.1. Description of Energy Storage Technologies

This section briefly describes the various energy storage technologies used today. Specifically, descriptions of battery systems, ultra-capacitors, flywheels and SMES are given followed by a side by side comparison between them.

9.2.1.1 A.2.1.1 Batteries

Batteries are one of the oldest and the most popular means of energy storage used today primarily because of their low initial cost. Batteries are devices which store energy electrochemically and are composed of two electrodes separated by an electrolyte. A typical battery system comprises of low-power/voltage modules that are connected in series or in parallel to achieve a desired electrical characteristic [193]. When a voltage is applied to the terminals, a chemical reaction occurs and this forms the charge-cycle for the battery. In a similar fashion, reversal of the reaction cause energy to flow out of the batteries and this forms the discharge-cycle.

There are different kinds of batteries available for different applications [194]. Choosing the right kind of battery requires knowledge of the advantages and disadvantages associated with each type. The most suitable batteries for distributed energy and power quality applications are discussed in brief below.

A.2.1.2 Lead-Acid batteries

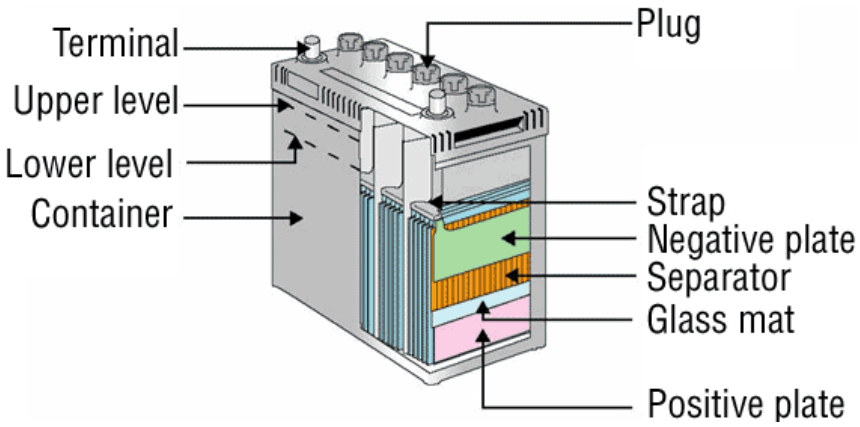

Figure A-3. Schematic of a typical lead-acid battery[195]

Lead-acid batteries are electrochemical energy storage devices that may be reversibly charged and discharged many times. Each cell of a charged lead-acid battery comprises a positive electrode of lead dioxide (PbO_2) and a negative electrode of sponge lead (Pb), separated by a microporous material. When these electrodes are immersed in an aqueous sulfuric acid electrolyte, a nominal open-circuit potential of 2 V is created [196]. When the circuit between the two electrodes is closed, the battery discharges its stored energy; The lead dioxide on the positive electrode is reduced to lead oxide, which reacts with sulfuric acid to form lead sulfate; the sponge lead on the negative electrode is oxidized to form lead ions that react with sulfuric acid to form lead sulfate. In this way, the chemical energy stored in the battery is converted to electrical energy. Then, by means of an external source of direct current, the battery can be recharged by reversing the oxidation-reduction reactions to convert electrical energy into stored chemical energy. Several thousand charge-discharge cycles are possible with properly designed lead-acid batteries.

In general, there are two types of lead-acid battery designs for distributed generation/power quality applications: flooded electrolyte and valve regulated lead acid battery (VRLA)[197] . In the flooded electrolyte batteries, an aqueous solution of sulfuric acid is used. The lead dioxide and sponge lead in flooded cells are supported on lead alloy grids, containing alloy additions of antimony and arsenic for increased strength and extended cycle life. For deep cells (say, 1 m

tall), air-lift pumps are employed to overcome acid stratification and periodic additions of water are required (for example, every six months)[193]. Ventilation is provided from the cover to allow the escape of gases formed during the battery charging process. The VRLA uses the same basic electrochemical technology as flooded lead-acid batteries, except that these batteries are closed with a pressure regulating valve, so that they are sealed. In addition, the acid electrolyte is immobilized [194].

Lead-acid batteries have been used for energy storage in several large installations. The estimated energy storage cost of the batteries is about $150/kWh [198]. The average cost of the power conversion system (PCS) for systems in the 0.5- to 2-MW range is expected to be about $175/kW for continuous rating. The batteries are typically replaced every 2-3 years for flooded cells and every 2-4 years for a VRLA. Efficiency of the system is about 75-80%. Maintenance costs for a 2-MW plant are based on a service contract of about $30K per year (or $15/kW) for flooded cells and $10K for VRLA batteries[190]. In addition to this, the recycling costs are estimated to be about $2K per year. The above cost is based on a typical lead –acid battery system and these values can fluctuate widely depending upon the specific application. [190]

A.2.1.3 Zinc-Bromine batteries

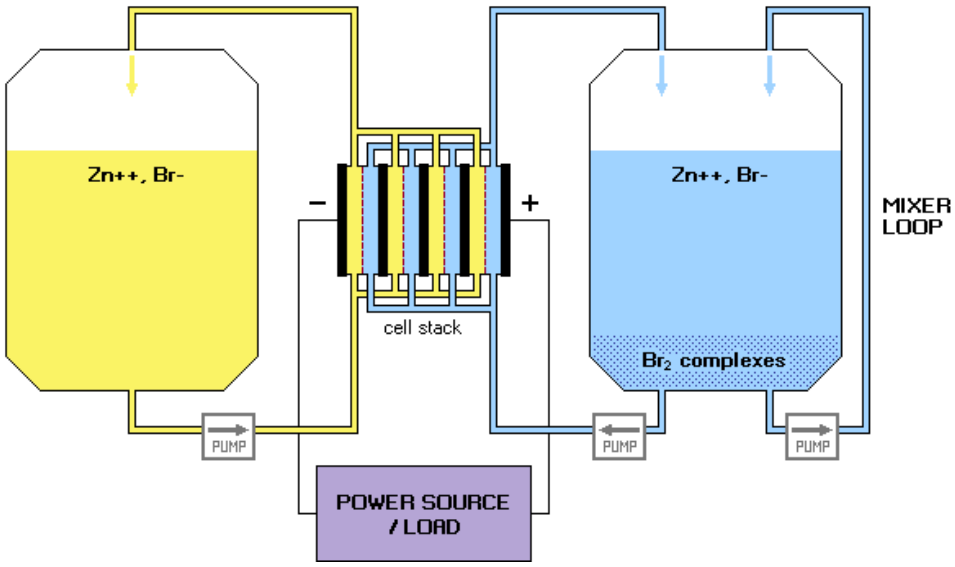

Figure A-4. Working principle of a Zn-Br battery[199]

The zinc–bromine (ZnBr) flow battery is a type of hybrid flow battery. A solution of zinc bromide is stored in two tanks- one for storing the positive electrode reactions and the other for the negative reactions. In each cell of a ZnBr battery, two different electrolytes flow past carbon plastic composite electrodes in two compartments separated by a micro-porous poly olefin membrane[200]. During discharge, Zn and Br combine into zinc bromide, generating 1.8 V across each cell. During charge, metallic zinc will be deposited (plated) as a thin film on one side of the carbon plastic composite electrode. Zinc bromine batteries from different manufacturers have energy densities ranging from 34.4–54 W-h/kg [200, 201].

The standard, container-enclosed units that are being built today have 250-kW capacity and can deliver 500 kWh with an efficiency of about 65%. These units consist of a single converter and ten modular, 50-kWh battery units [200, 202]. The cost of installing the battery portion (DC) of the unit is $400/kWh which implies that a 500-kWh unit will cost $200K. The power conversion portion of the system costs an additional $250/kW. The latter cost is higher for smaller units and

will decrease for units of 1 MW or greater. A converter cost of $175/kW was used as for other batteries[201]. The expected life of the battery depends on the operational mode. It is expected to survive about 2000 cycles with limited degradation, which would be manifested by a decrease in efficiency to about 60%. Expressed differently, the battery would exhibit a decrease in total stored energy from 500 kWh to about 450 kWh[193, 194]. An eight-year replacement cost for the Zn/Br battery, which is $100/kWh was used. The estimate of operation and maintenance costs is based on the use of service contracts of $5/KW- year for 250-kW units, or $20/kW[187, 190, 198]. The service cost is expected to decrease for larger installations.

A.2.1.4 Nickel-Cadmium batteries

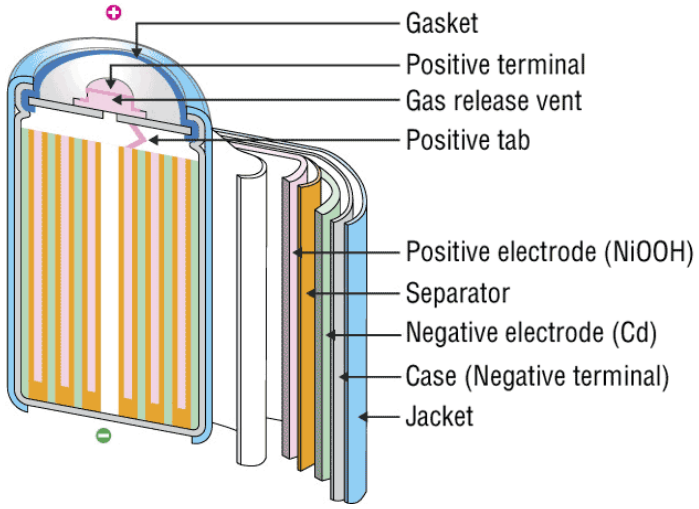

Figure A-5. Schematic of a typical Ni-Cd battery[203]

Nickel-cadmium (Ni-Cd) batteries provide very long lives in stationary applications, and are typically quite resistant to wear and tear. Unfortunately, they are typically expensive, and this limits their application to the most demanding duties [204]. For stationary applications, almost all Ni-Cd batteries are flooded types. The traditional construction is with pocket plates, in which the active materials are encased in a series of perforated steel pockets, linked together to form a plate [205]. Newer types for stationary applications include sintered plates, fiber plates and plastic-bonded plates. Cells may also employ hybrid construction with, for example, sintered positives and plastic-bonded negatives. In more recent years, low-maintenance Ni-Cd types have appeared, using flooded construction, but with enhanced recombination of charge gas to reduce

water consumption. One of the main drawbacks of these kinds of batteries is that cadmium is highly toxic[204, 206].

A typical cost of installation of Ni-Cd batteries ranges from $600 -$900/kWh. The battery life ranges from 2 – 5 years depending upon the number of charge/discharge cycles per day. Maintenance charges are about the same as the VRLA which is about $5/kW-year. Recycling costs are a little higher compared to other batteries due to the highly toxic nature of cadmium. [190, 201, 202]

A.2.1.5 Lithium-ion batteries

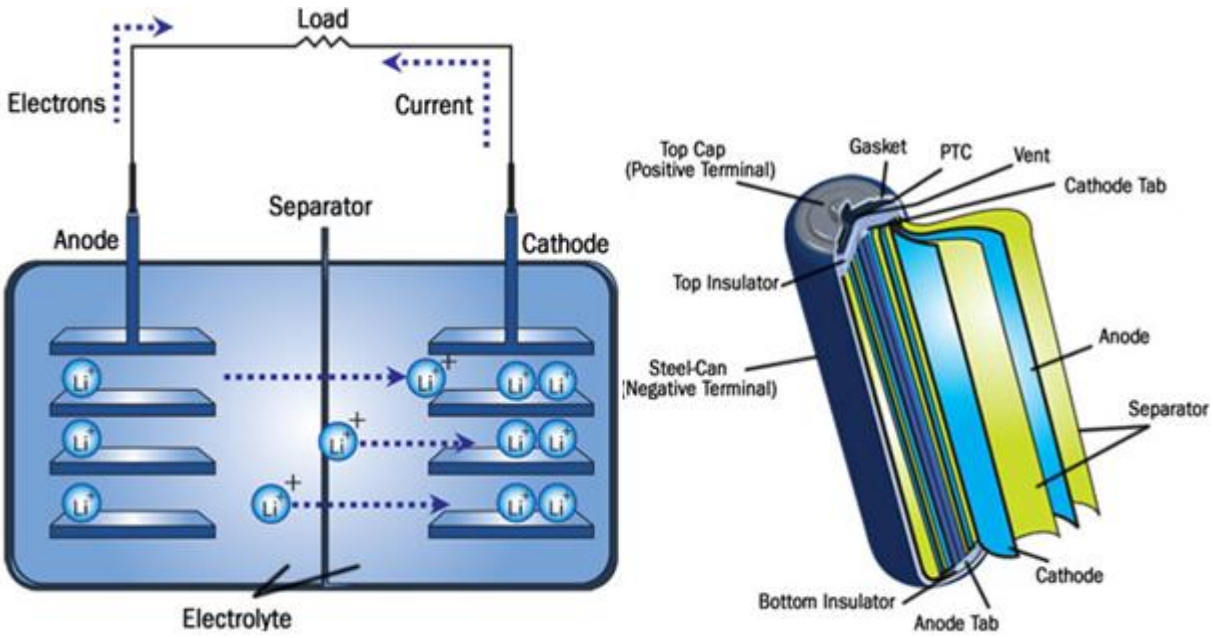

Figure A-6. Schematic and working principle of a typical Li-ion battery[195, 203]

Lithium ion batteries are gaining recognition in recent years due to their higher storage capacity and relatively lower toxic discharge. The cathode in these batteries is a lithiated metal oxide and the anode is made of graphitic carbon with a layered structure. The electrolyte is made up of lithium salts dissolved in organic carbonates [193, 194]. When the battery is being charged, the lithium atoms in the cathode are ionized and migrate through the electrolyte toward the carbon anode where they combine with external electrons and are deposited between carbon layers as lithium atoms. This process is reversed during discharge. A drawback of these batteries are that while they have been considered for huge amounts of energy storage- there has not been any large and successful Li-ion based systems yet[207].

They are of interest because they have power densities (kW/m^3), energy densities (J/m^3), specific powers (kW/kg) and specific energies(kW/kg) that are significantly greater than the batteries discussed above. Interim numbers suggest that costs are about $500/kWh of installed storage with converter costs slightly higher than those for lead-acid batteries, which are around

$175/kW[187, 198]. A Li-ion system's lifetime should be on the order of 2000 cycles, or 3 to 7 years. Efficiency is expected to be relatively high (about 80-85%) for this technology [208] .

Table A-3 summarizes the different characteristics of each of the above discussed battery technologies.

	Flooded/Valve regulated Lead Acid	**Zn-Br**	**Ni-Cd**	**Li-Ion**
Environmental Impact	Harmful – lead and acid must be disposed of safely and electrolyte must be contained	Harmful- acid must be disposed of safely.	Very Harmful- Highly contained disposal system required	Less harmful (comparatively) but adequate methods of safe disposal must be followed
Relative cost	Low	Low	High	High
Cost trend (projected in next five years)	Increase -mainly due to increase in lead prices	Increase	Decrease	Decrease
Discharge/Recharge Characteristics	Slow discharge/Slower recharge	Slow discharge/Slower recharge	A little faster discharge /slow recharge	Faster discharge/slow recharge
Maintenance Cost (Rough Estimate)	$5-$15/KW-year	$5-$10/KW-year	$5-$7/KW-year	A little lower than others
Gravimetric Energy density (Wh/Kg)	30-40	30-50	35-55	90-200
Volumetric energy density (Wh/L)	60-80	55-80	30-150	230-500
Gravimetric Power density (W/kg)	180-200	75-415	50-150	750-1250
Technology Performance history	Used for over 100 years	20 years	15-20 years	Less than 5 years

Life expectancy range	2000 cycles (3- 5 years)	2000 cycles (3- 5 years)	2000 cycles (3- 5 years)	2000 cycles (3- 7 years at most)
Operating temperature range	15°C-25°C	15°C-25°C	-40°C-60°C	-20°-60°C

Table A-3. A comparison between different battery systems[137, 192-194]

A.2.1.6 Compressed Air Energy Storage (CAES)

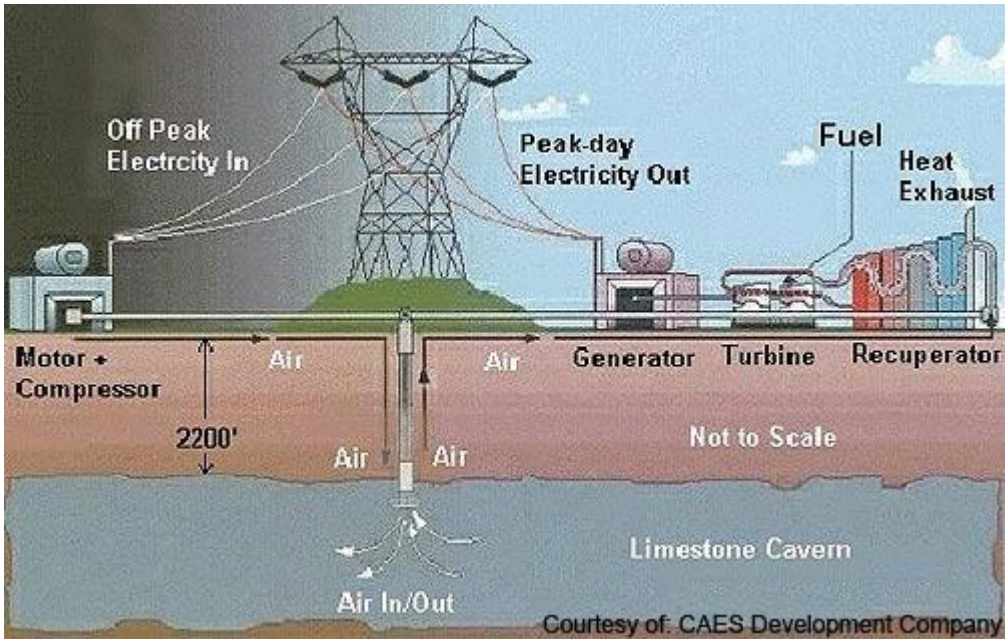

Figure A-7. Schematic of a typical CAES system[209]

Compressed air energy storage (CAES) is an extension to the basic gas turbine technology which uses off-peak electricity supply to store compressed air underground. Since the cost of electricity during off-peak hours is relatively low (with higher supply than demand), energy is used to store compressed air at that time. There are three ways in which storage of gas can be achieved. They are adiabatic, diabatic or isothermic. To return electricity to the consumers, air is extracted from the reservoir [210]. It is first preheated in the recuperator. The recuperator reuses the energy extracted by the compressor coolers. The heated air is then mixed with small quantities of oil or gas, which is burnt in the combustor. The hot gas from the combustor is expanded in the turbine to generate electricity. One of the main advantages of this technology is that since the compressed gas is stored at very high pressures (usually 3-8 MPa), the storage reservoir could be relatively smaller as compared to batteries due to the reduced volume of the gas [211]. An ideal place to store this compressed gas would be in ancient salt mines or underground natural gas storage caves although recent studies suggest that storage underground in high pressure piping can be done easily[137, 184].

CAES systems are used today on very large scales for storage times of up to a year and are proposed as an alternative for batteries in small/medium scale short term power applications[135]. The methodology would remain the same for small scale systems. The only difference is that compressed air would be stored under high pressure (around 10MPa) in cylinders and an electrical compressor can be used as a generator during retrieval. It is estimated that units of storage between 50kW and 50 MW are possible [184]. Because there are no commercially available CAES systems for short-term energy storage, a lot of research has to be done in this field. One of the major drawbacks of this technology is the efficiency. Large Scale bulk storage has an efficiency of 50-60% and it is projected that the efficiency for small scale applications would be a little higher – in par with batteries. Another disadvantage of using CAES systems is the startup time [210]. A typical CAES plant takes about 9 – 12 minutes to start under normal operating conditions. This time is too long when we consider short-term energy storage. While, the environmental effects are much lesser using CAES than batteries, the former tends to be more expensive to maintain. It is projected that the operational and maintenance cost of a typical system would be around $10/KW-year with an installation cost of about $50/KWh. [190, 210]

A.2.1.7 Superconducting Magnetic Energy Storage System (SMES)

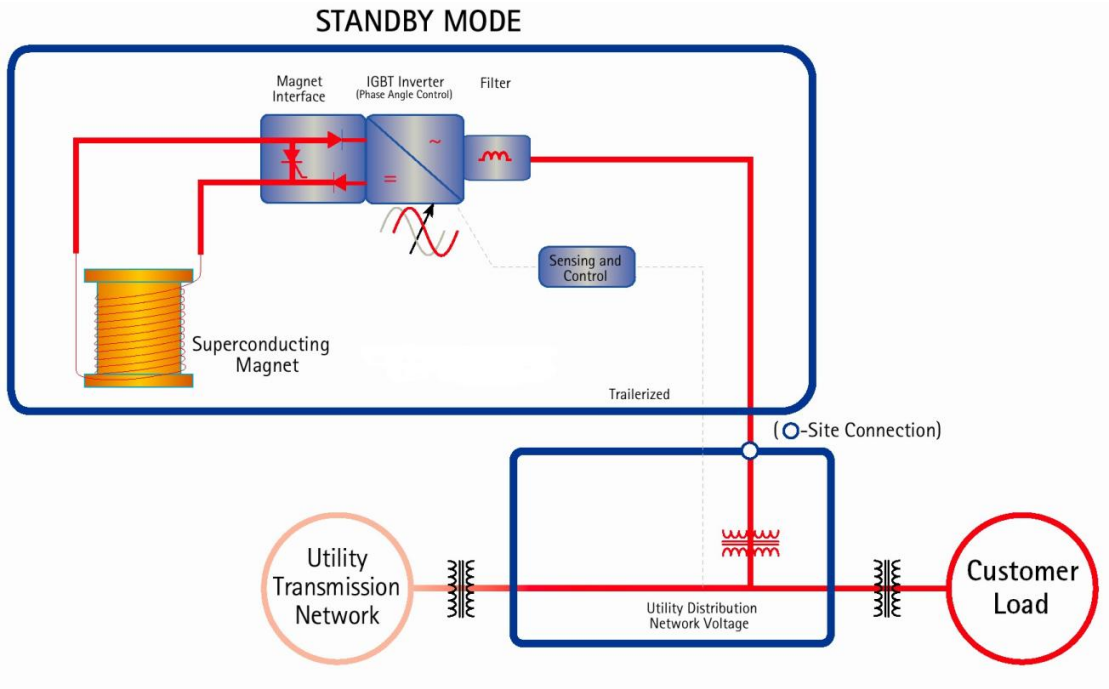

Figure A-8. Working principle of a SMES system[212]

Superconducting Magnetic Energy Storage (SMES) is an emerging technology in which systems store energy in the magnetic field created by the flow of direct current in a coil of cryogenically cooled, superconducting material[213]. A SMES system includes a superconducting coil, a power conditioning system, a cryogenic refrigerator, and a cryostat/vacuum vessel to keep the coil at the low temperature required to maintain the coil in a superconducting state [214]. The inductively stored energy (E) and the rated power (P) are the common specifications of a SMES device and can be expressed as

$$E = \frac{1}{2}LI^2 ; P = \frac{dE}{dt} = LI\frac{dI}{dt} = VI \qquad \textit{(A-1)}$$

where L is the inductance of the coil, V is the voltage across the coil and I is the dc current flowing through the coi(No Reference Selected)l[135]. Although research is being conducted on larger SMES systems in the range of 10 to 100 MW, recent focus has been on the smaller micro-SMES devices in the range of 1 to 10 MW. Micro-SMES devices are available commercially for power quality applications. SMES are highly efficient at storing electricity (greater than 95%), and provide both real and reactive power. Moreover, these systems are capable of discharging the near totality of the stored energy, as opposed to batteries. Power is available almost instantaneously, and very high power output is provided for a brief period of time [213, 214]. They are very useful for applications requiring continuous operation with a great number of complete charge−discharge cycles. The fast response time of less than 100 ms of these systems makes them ideal for regulating load leveling. Due to their construction, they have a high operating cost and are therefore best suited to provide constant, deep discharges and constant activity. Their major shortcoming is the refrigeration system which is quite costly and makes operation more complicated [135]. These facilities currently range in size up to 3 MW units, and are generally used to provide grid stability in a distribution system and power quality at manufacturing facilities requiring ultra-clean power such a chip fabrication facility.

For a SMES design a compromise is made between each factor considering the parameters of energy/mass ratio, Lorentz forces, stray magnetic field, and minimizing the losses for a reliable, stable, and economic SMES system. The cost of an SMES system can be separated into two independent components where one is the cost of the energy storage capacity and the other one is the cost of the power handling capability. Storage related cost includes the capital and

construction costs of conductor, coil structure components, cryogenic vessel, refrigeration, protection, and control equipment [213]. Power related cost has the capital and construction costs of the power conditioning system. While the power related cost is lower than energy related cost for large-scale applications, it is more dominant for small-scale applications. The costs associated with a typical SMES system are: $50,000/kWh-delivered and $200/kW for the power conversion system. The efficiency is very high at 0.95, but the energy requirement to operate the refrigerator is relatively high at 0.01-kW/kW-delivered [190, 198].

A.2.1.8 Hydrogen energy storage

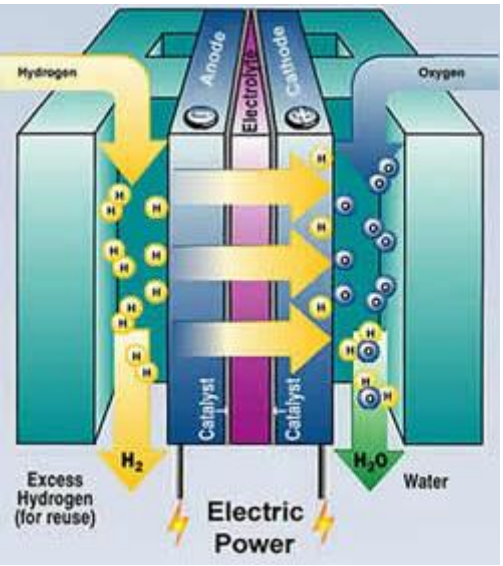

Figure A-9. A hydrogen fuel cell[215]

Hydrogen energy storage is a relatively new technology which has been on the market for less than 5 years. It should be noted that systems such as fuel cells in which hydrogen is actually stored post production forms a part of an energy storage method[216]. Systems in which hydrogen is merely produced are classified as generators and do not constitute an energy storage technique. The main idea behind a fuel cell is to restore energy already spent to produce hydrogen using water electrolysis[217]. Just like a battery, the storage system proposed includes three key components: electrolysis which consumes off-peak electricity to produce hydrogen, the fuel cell which uses that hydrogen and oxygen from air to generate peak-hour electricity, and a hydrogen buffer tank to ensure adequate resources in periods of need. The most common kind of hydrogen fuel cells used for distributed generation and power quality applications is the proton exchange membrane (PEM) type fuel cells [218]. The efficiency is a little higher than batteries (about 85%) and they have a comparatively higher response time (generally 5 – 10 minutes) [216-218]

It should be noted than hydrogen energy storage is still in its developmental stages and current research systems developed have an energy storage capacity of about 10kW-hr. A decent cost estimate of this technology is as follows: A PEM fuel cell costs about $1500/kW and storage tanks cost about $15/kWh[137, 184]. While the storage costs are relatively low, the set up and

operational costs are projected to be atleast 5 – 10 times higher than batteries. In addition, hydrogen energy storage techniques require a lot of maintenance which makes them unsuitable for short term energy storage today. The risks associated with such a system are yet to be analyzed carefully. Different materials are still under investigation as to their storage potential depending on the temperature and pressure of the hydrogen.

An alternative to the fuel cell used today is to burn the hydrogen in a combustion engine [139, 194]. Diesel engines have been modified for this task and produce electricity at a relatively high efficiency for an engine but overall low efficiency (about 45%). The overall system operates the same as the fuel cell system. The advantage of the engine is the relatively inexpensive power generation, at about $300/kW [187, 190].

A.2.1.9 Ultra-capacitors

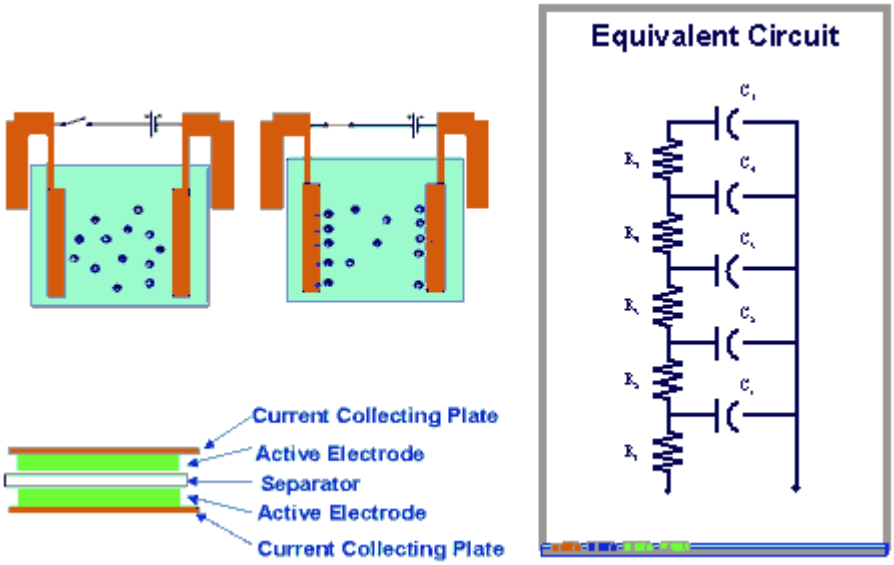

Figure A-10. A schematic of an ultra-capacitor[219]

Ultra-capacitors (also known as super-capacitors) are in the earliest stages of development as an energy storage technology for electric utility applications. Capacitors store electric energy by accumulating positive and negative charges (often on parallel plates) separated by an insulating dielectric [220]. The super-capacitor resembles a regular capacitor except that it offers very high capacitance in a small package. They rely on the separation of charge at an electric interface that is measured in fractions of a nanometer, compared with micrometers for most polymer film

capacitors. Energy storage is by means of static charge rather than of an electro-chemical process inherent to the battery. The capacitance, C, represents the relationship between the stored charge (q) and the voltage (V) between the plates. The capacitance depends on the permittivity of the dielectric the area of the plates (A) and the distance between the plates (d). The energy stored on the capacitor depends on the capacitance and on the square of the voltage[221]. Mathematically, this can be expressed as

$$Q = CV; C = \frac{\epsilon A}{d}; and\ E = \frac{1}{2}CV^2 \qquad \textbf{(A-2)}$$

Energy storage in ultra-capacitors is done in the form of an electric field between two electrodes. This is the same principle as capacitors except that the insulating material is replaced by an electrolyte ionic conductor in which ion movement is made along a conducting electrode with a very large specific surface (carbon percolate grains or polymer conductors) [221, 222]. Ultra-capacitors are ideal devices for power quality and short-term energy storage. A typical charge/discharge time for an ultra-capacitor is about 1- 10 seconds which makes this technology stand well above all others [137]. Ultra-capacitors are however still very expensive to produce and may suffer from lower voltage potential due to the need for aqueous electrolytes. A typical cost of an ultra-capacitor is about $45K/kWh [187, 190]. They can reach even higher energy and power densities than the other technologies without sacrifices in affordability or cyclic stability but a major drawback is that the current designs facilitate storage of about 1-10kWh. A super-capacitor is highly durable- lasting about 8-10 years, and has an efficiency of 95%. [190]Service life is decreased when they are discharged more rapidly than their design rating. They also have a self-discharge rate of 5% which means that the energy stored must be utilized quickly. They are however still a new and unproven technology and still require more research to better understand and realize their full potential [135, 137, 221].

A.2.1.10 Thermal Energy Storage

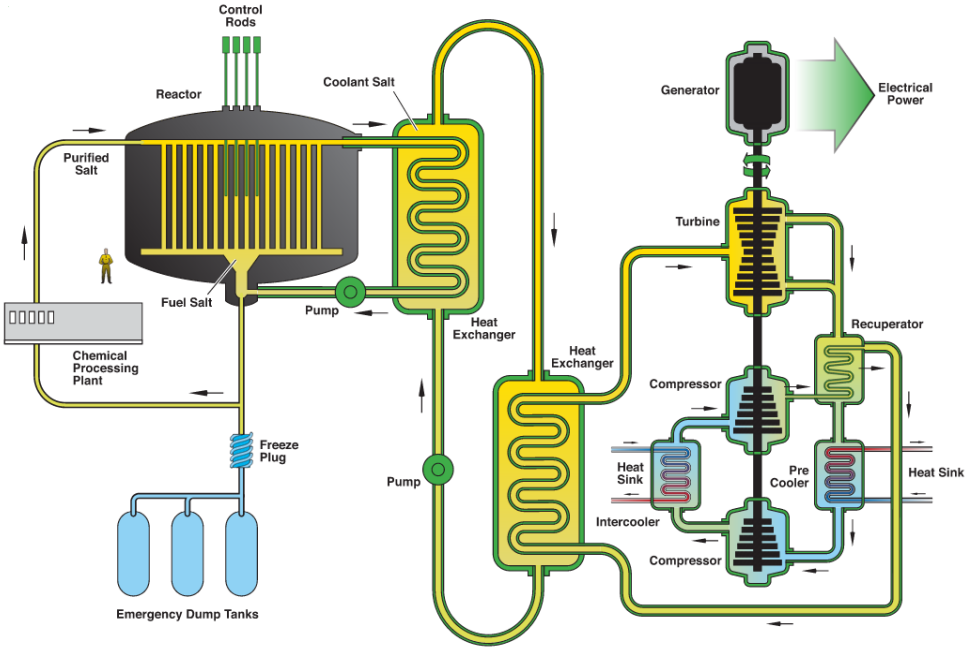

Figure A-11. A schematic of a molten salt reactor [219]

Thermal energy storage comprises a number of technologies that store thermal energy in energy storage reservoirs for later use. Thermal energy is often accumulated from active solar collector or more often combined heat and power plants, and transferred to insulated repositories for use later in various applications, such as space heating, domestic or process water heating. [223]

The energy is stored at a given temperature, The higher the heat the higher the concentration, The fusion enthalpy grows with the fusion temperature of the bulk material used. The most common kinds of thermal energy storage include solar energy storage (i.e. solar cells), molten salt and water-based technology [224]. Using water as the storage fluid involves high temperatures, above 200 $^{\circ}$ C, making it impossible to store the water in a confined groundwater basin because irreparable damage to the ground would occur. Very large volume watertight cisterns set in rock are needed. [225, 226]

One of the major drawbacks of using thermal energy storage techniques is the highly corrosive nature of the fluid (or salt) involved [137]. For example, sodium hydroxide ,a fluid which is used extensively today for thermal energy storage , is highly toxic and should be disposed safely.

While, research is going on in this field to use this technology for short term energy storage- the relatively overall bulky system size along with the high maintenance costs and a low efficiency of about 50% discourages use of this technology[187, 225].

A.2.1.11 Flywheels

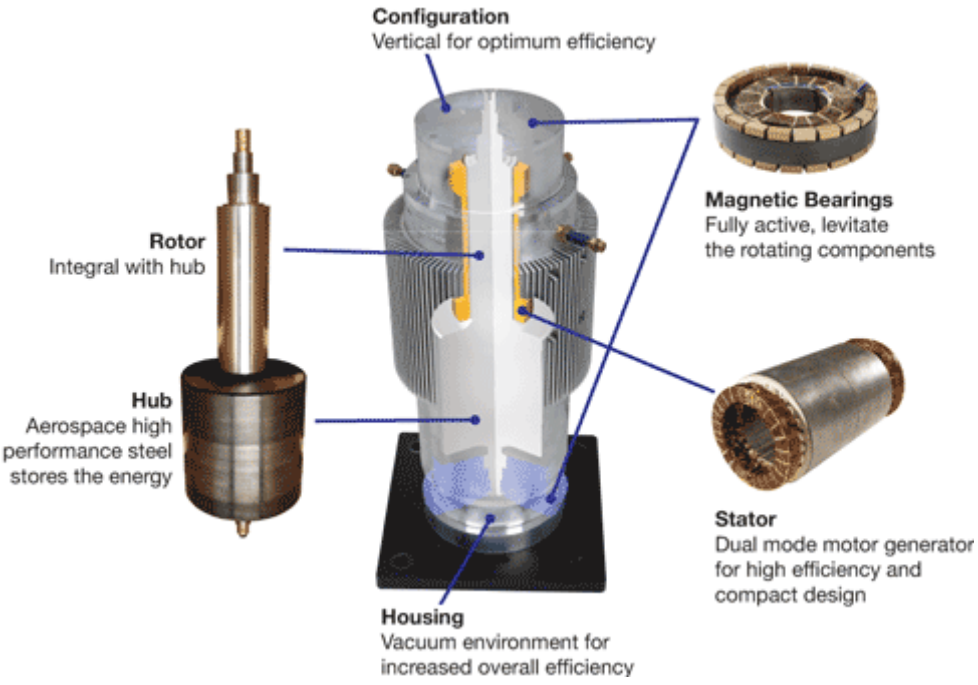

Figure A-12. Different components of a flywheel energy storage system[26]

An emerging alternative to batteries is the high-speed flywheel. Since there are no chemical reactions to reverse and little friction since flywheels are typically levitated by magnets in a vacuum chamber, flywheels have the technical strengths of high efficiency (~95%), high power, and long life[21]. Dubbed “electromechanical batteries” , flywheels store kinetic energy in a cylindrical or ringed mass, spinning at very high speeds (~10,000-200,000 rpm), for a high energy density (0.1-1kWh/L). A flywheel is a mass rotating about an axis, which can store energy mechanically in the form of kinetic energy [11, 100]. Apart from the rotating flywheel, the other main components of a flywheel storage system are the motor/generator, rotor bearings (usually magnetic) and the power interface. Once the flywheel starts to rotate (as a result of the motor), it is in effect a mechanical battery that has a certain amount of energy that can be stored depending on its rotational velocity and its moment of inertia. The faster a flywheel rotates the

more energy it stores [22]. This stored energy can be retrieved by slowing down the flywheel via a decelerating torque and returning the kinetic energy to the electrical motor, which is used as a generator.

The flywheel can be either low speed, with operating speeds less than 20,000 rpm, or high-speed with operating speeds up to 50,000 rpm[135, 137] .Low speed flywheels are usually made of steel rotors and conventional bearings. Typical specific energy achieved is around 5 W-hr/kg. High-speed flywheels use advanced composite materials for the rotor with ultra-low friction bearing assemblies. These light-weight and high-strength composite rotors can achieve specific energy of 100 W-hr/kg. Also, such flywheels come up to speed in a matter of seconds or minutes, rather than the hours needed to recharge a battery. The container for high-speed flywheels is either evacuated or helium filled to reduce aerodynamic losses and rotor stresses.

The main advantages of a flywheel include reduced maintenance requirements, a long service life of about 25-30 years, unlimited charge/discharge cycles, very high efficiency of about 95% and sustainability (i.e. no harmful byproducts). Unlike ultra-capacitors, flywheels are an older technology which are in use today and can support a higher power capacity range (1kW-150MW)[139]. The main focus for development of this technology has been the power quality control and distributed generation applications. The major disadvantage of using flywheels is associated with the high initial set up cost[187, 190]. The cost of the energy generation for a flywheel is based on the cost of the motor/generator system and the converter from variable frequency output to DC. These costs are assumed to be about $200-$300/kW. The initial set up cost of a flywheel ranges widely depending upon the application, but a median value is estimated to be around $50K/kWh. However, the high initial set up cost can be justified over the 25-30 year service life period of the flywheel as the operation and maintenance costs are very low compared to other technologies. The fact that they do not have to be replaced periodically along with no harmful environmental effects makes them an ideal candidate to replace batteries. [10, 21, 190]

A.3. Comparison between short term energy storage technologies

This section presents an in depth comparison of all the energy storage techniques discussed above. Various categories such as performance, storage capacity, discharge/recharge time, history, operational costs, installation and maintenance costs, etc. are analyzed.

A.3.1. Performance Characteristics

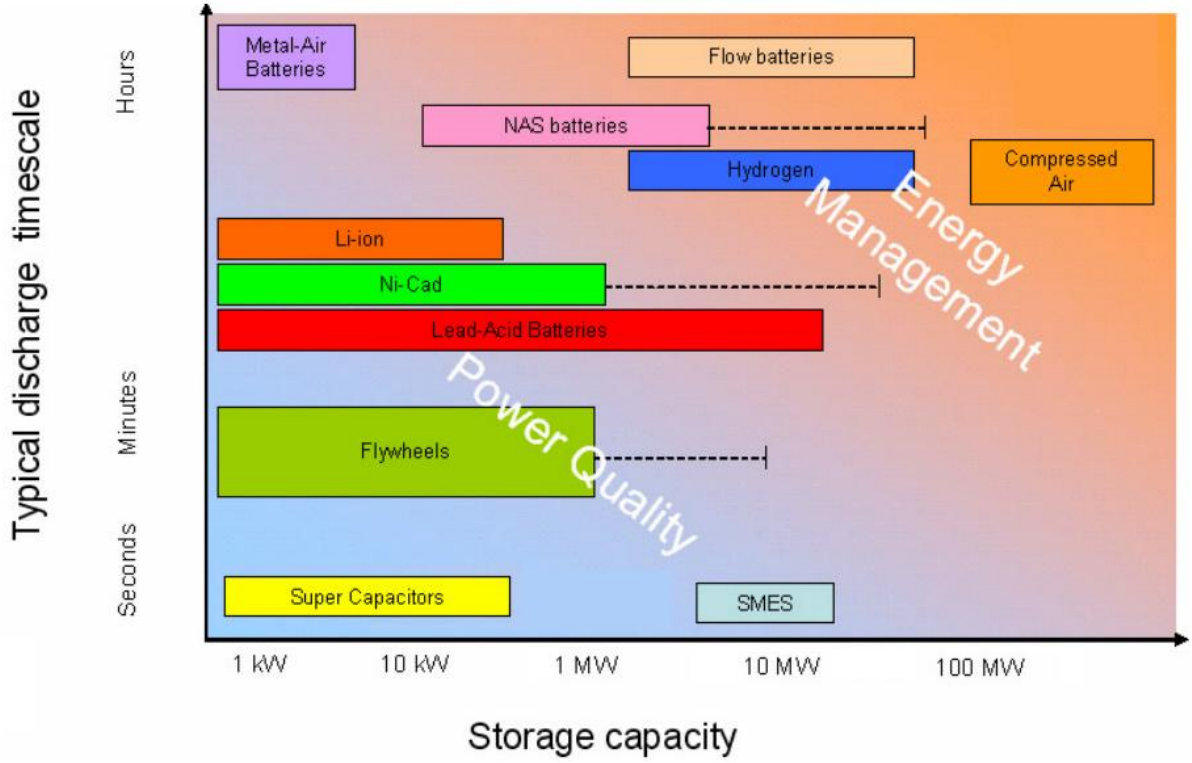

Figure A-13. Discharge time vs. Storage capacity chart [227]

The main performance characteristics that differentiate between technologies are the storage capacity, discharge time and recharge time. Figure A-13 depicts a typical comparison between the common technologies of energy storage used today [137, 227]. As it is evident from the figure, batteries, super-capacitors, SMES and flywheels are amongst the choices worth considering for short term energy storage for the purposes of power quality control and distributed generation. Since the discharge time of hydrogen fuel cells and CAES are in the range of hours, they are more suitable for energy management. This study focuses on power quality and distributed energy and hence will not consider these alternatives.

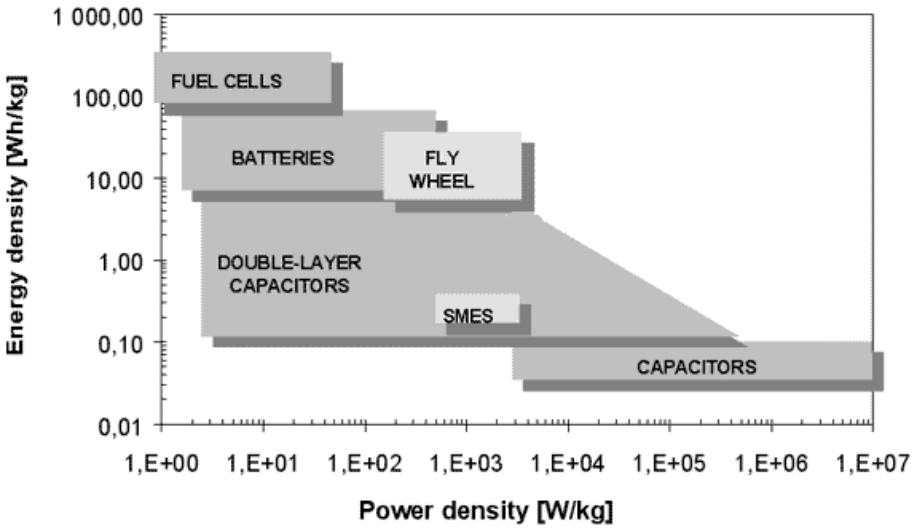

Figure A-14. Energy density vs. Power density[137]

Figure A-14 shows the energy density vs. power density for the various technologies. It can be seen that flywheels have a higher power density than comparable batteries. Figure A-15 analyzes the 4 major technologies for their discharge time vs. recharge times[186]. Batteries have very long recharge times- typically 10 – 20 times of their discharge times. Flywheels, SMES and ultra-capacitors have much lower recharge/discharge ratios giving them greater advantage over traditional batteries. A recharge time of a few seconds to a few minutes is ideal when it comes to short-term energy storage especially in applications with constant fluctuations in voltage or frequency.

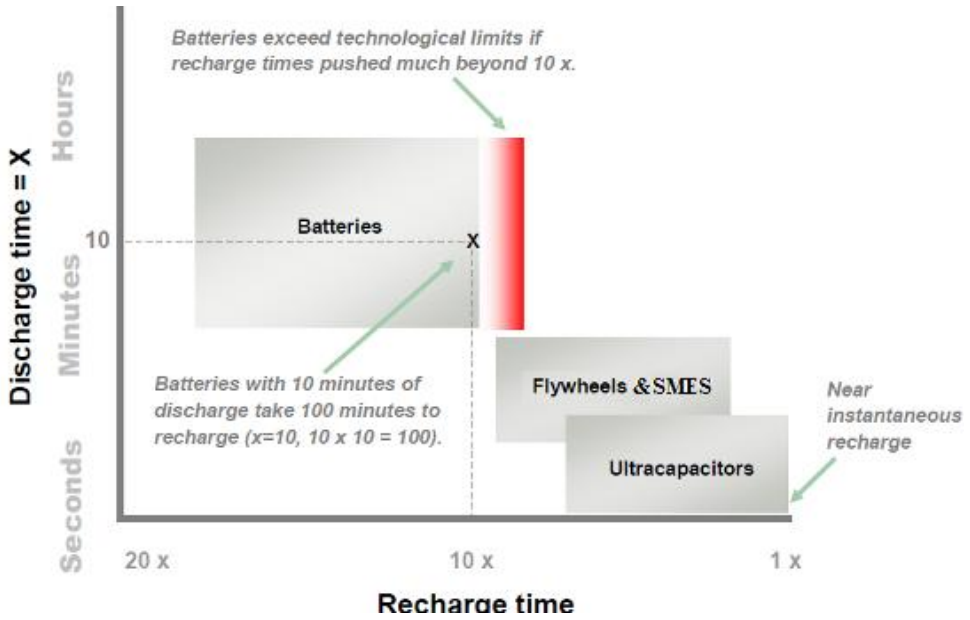

Figure A-15. Discharge time vs. Recharge time for batteries, flywheels, SMES and ultra-capacitors.[186]

A.3.2. Commercial Maturity and Cost estimate availability

One of the major deciding factors in selecting a mature system is the market history of that particular technology along with their advancements throughout the years. A product that has been made commercially available with a proven performance history would be an ideal selection rather than technologies which are in the beginning stage. ***Table A-4*** gives a comparison between commercial maturity and cost certainty for short term energy storage technologies [189]. Note that this comparison is specifically for power quality and distributed generation applications.

Technology	Commercial maturity	Cost certainty
Lead acid batteries	Mature – many products in use today	Specific price lists are readily available
Zn-Br batteries	Fairly immature – prototypes available but unproven yet	Cost determined based on specific project (varies)
Ni-Cd batteries	Mature – products are commercially available	Cost determined based on specific project (varies)

Li-Ion batteries	Immature – ongoing research topic ; not available on a commercial basis	Uncertain.
CAES	Fairly immature – prototypes available but unproven yet	Price quote available
SMES	Fairly mature- several products are commercially available	Price quote available
Hydrogen fuel cells	Immature – ongoing research topic ; not available on a commercial basis	Uncertain.
Hydrogen combustion engine	Fairly mature- several products are commercially available	Specific price lists are readily available
Ultra-capacitor	Immature – prototypes available but no large scale use yet	Cost determined based on specific project (varies)
Low speed flywheel	Fairly mature- several products are commercially available	Specific price lists are readily available
High speed flywheel	A little less mature than low speed flywheels – a few products are commercially available	Cost determined based on specific project (varies)

Table A-4. Commercial maturity and cost certainty of various energy storage technologies.

From Table A-4 it can be inferred that batteries (particularly lead-acid) have been available for a very long time which makes them a low-risk technology to use in terms of reliability. Further, the initial set up costs for batteries are quite low as compared to flywheels, super-capacitors and SMES which is mainly why they are the most popular kind of short term energy storage. Ultra-capacitors and hydrogen fuel cells are relatively very new technologies and hence will not

constitute a suitable choice for application today. Hence, SMES and flywheels can be considered as the best alternatives to batteries from a commercial maturity point of view.

A.3.3. Short term energy storage technology profiles

From the above sections it can be deduced that flywheels, ultra-capacitors and SMES can be considered as potential alternatives to batteries. It is worthwhile to understand the profiles surrounding each technology. For the purposes of this comparison, all forms of chemical batteries (i.e Li-ion, Lead-acid, Zn-Br, Ni-Cd, etc) are categorized generally under batteries while flywheels include both high speed and low speed ones. Table A-5 compares the technology profiles of batteries against ultra-capacitors, SMES and flywheels. [187]

	Batteries	**Ultra-capacitors**	**SMES**	**Flywheels**
Operating Conditions	Narrow temperature range	Wide temperature range	Narrow temperature range	Wide temperature range
Environmental Impact	Very Harmful due to chemicals	Harmful if burnt	Less harmful (refrigeration system produces harmful gases)	Less harmful (recycling of power electronics and composites)
Recycling/Safety	Significant government and local regulations for management of lead ,acid and other chemicals	Requires high voltages to operate	Comparatively safer	Encasements are required for higher rpm flywheels (in case of breakage while spinning)
Power Range	Up to multiple megawatts	A few kilowatts	A few kilowatts	Up to multiple megawatts
Reliability	Moderate	Very High	High	Very High
No of deep charge/discharge	Up to 3000	Up to a million	Up to a million	Up to 10 million

cycles				
Recharge time	10 times discharge time	Seconds	A few minutes (application dependent)	Seconds or minutes
Typical run time	5 minutes – 8 hours	1 second to 1 minute	A few seconds to 10 minutes	1 second to 10 minutes
Facilities installed in the US	More than 70 MW installed by utilities in 10 states	Several test units, 1 defense unit , non-commercial	5 facilities with approximately 1 MW (total) installed in 5 states	6 facilities installed in 4 states- several tests units, semi-commercial
Potential/Actual Applications	Electricity- power quality , DG , spinning reserve, transmission and distribution, UPS systems, peak shaving, frequency/voltage regulator, Transportation, Integration with renewables.	Consumer electronics, power quality, transportation, defense.	Electricity- transmission and distribution, power quality.	Electricity- power quality, DG, transmission and distribution, UPS systems, peak shaving, spinning reserve, frequency/voltage regulator, Transportation, Integration with renewables, space and defense.

Table A-5. Short term energy storage technology profiles

It can be understood that ultra-capacitors and SMES are relatively new technologies which have potential to be developed on a large scale through research. Based on the applications, reliability and charging capabilities – flywheels are a viable alternative to batteries. It should also be mentioned that while the initial cost of batteries is significantly lower than the initial cost of

flywheels- the environmental impacts and maintenance costs are significantly lower for the latter.

A.4. Cost Characteristics

It is worthwhile to compare the cost characteristics of each technology. Costs such as operational, energy related, maintenance and several others are compared. Since the costs of technologies vary according to their specific applications, two tables are provided – one for distributed generation applications (Table A-6) and the other for power quality (Table A-7).[190]

Technology	Energy-Related Cost ($/kW-hr)	Power Related cost ($/kW)	Balance of plant ($/kW)	Efficiency (AC to AC)	Replacement cost ($/kW-hr)	Replacement frequency (years)	Parasitic Loss	Fixed O& M ($/kW-yr)
Lead Acid Batteries (flooded cell)	150	175	50	0.75	150	6	0.1%/day	15
Lead Acid batteries (VRLA)	200	175	50	0.75	200	5	0.1%/day	5
Ni/Cd	600	175	50	0.65	600	10	Not known	25
Zn/Br	400	175	0	0.60	100	8	0.01%/hr	20
Li-Ion	500	175	0	0.85	500	10	0.01%/hr	25
CAES	120	550	50	0.79	0	None	None	10
Flywheels	1000	300	0	0.95	0	None	0.05%/day	$1000/yr
Hydrogen Fuel Cell	15	1500	0	0.59	$100/KW	6	None	3.8
Electrolyzer (to	NA	300	NA	0.9	$50/KW	6	None	Not Known

accompany fuel cell of engine)								
Hydrogen engine	15	300	0	0.44	$100/KW	10	None	2.5

Table A-6. Cost characteristics of energy storage technologies for distributed generation [190]

Technology	**Energy-Related Cost ($/kW-hr)**	**Power Related cost ($/kW)**	**Efficiency (AC to AC)**	**Replacement cost ($/kW-hr)**	**Replacement frequency (years)**	**Parasitic loss storage (kW/kW)**	**Fixed O& M ($/kW-yr)**
Lead Acid Batteries (flooded cell)	300	250	0.75	300	6	0.00001	10
Li-Ion	500	200	0.85	500	10	0.0001	10
Micro-SMES	50,000	200	0.95	0	None	0.01	10
Flywheels (high speed)	1000-24,000	300	0.95	0	None	0.0005	5
Flywheels (Low speed)	25,000-50,000	300	0.95	0	None	0.002	5
Super-capacitor	30,000-70,000	300	0.95	0	None	0.0001	5

Table A-7. Cost characteristics of energy storage technologies for power quality applications

A.5. Discussion and Conclusion

The potential alternatives to batteries that were compared were SMES, super-capacitors, CAES, hydrogen fuel cells and flywheels. Different factors such as cost, technical specifications and performance were compared in determining a good alternative to batteries. It is determined that batteries have the lowest initial cost for power quality and distributed generation applications, but do not always have the lowest life-cycle cost. When considering a 10-year service life, the replacement and maintenance costs can add up substantially. Batteries have to be replaced every 2 or 3 years depending on the application, since they have a very limited number of charge/discharge cycles. Furthermore, the environmental effects created by battery byproducts such as lead or acid are irreversible. The response times are substantially longer and efficiencies are substantially lower for batteries compared to other technologies, which add to their disadvantages. Due to these factors, alternatives to batteries are being considered today.

CAES and hydrogen fuel cells cannot currently be considered as suitable alternatives due to the fact that a lot of changes have to be made to current systems in order for them to produce efficient results. For example, to use CAES, an underground site has to be developed which is impractical in terms of operations and cost. Hydrogen fuel cells are relatively very new and a lot of research as to be done to understand their potential completely. In addition, a lot of byproducts are produced during manufacture and operation which are harmful to the environment. With low efficiencies of about 60-70%, high initial setup costs and very high maintenance costs, these two technologies are not good alternatives to batteries today.

SMES seems to have high potential as a battery replacement considering the efficiency reached, but there are certain limitations which prevent it from being a good competitor to batteries. For instance, installation of an SMES requires a refrigerator system which can be quite complicated. In current designs, the refrigeration system is very expensive and requires regular maintenance. While the amount of harmful emissions from this system is significantly lower compared to the above technologies, there is still a dangerous amount released to the atmosphere. Further, SMES cannot be used at very high temperatures. It is very probable that such a system has good potential to replace batteries in the future with improvements in design, but they cannot be implemented today effectively without a few tradeoffs.

Super-capacitors are considered to have immense potential as a good alternative to batteries especially in short term energy applications [228]. However, the history of these devices is very short and the cost of installing such a system can be very expensive. Moreover, the maximum power storage in super-capacitors is on the order of kilowatts as opposed to the megawatt range required by many applications. The risks associated with this technology are not very well known. Although they are a promising technology, they are still expensive, have an unproven lifetime, and have a more limited temperature range. Super-capacitors also tend to have a large series resistance and require high voltages to operate which imposes a large time constant and thus slower response time. Of all the above technologies discussed above, super capacitors can be considered the closest alternative to batteries. However- they are still in their infant stage and require a lot of research to tap their entire potential.

Flywheels have immense potential and are a strong candidate to replace batteries. They have been proven to have many advantages over their counterparts. The high efficiency, fast response time, unlimited charge/discharge cycles and minimal required maintenance all add to their attractive features. One of the major disadvantages of flywheels is the high initial cost. Considering the fact that flywheels have a service life of 10-20 years, the high initial cost can be justified, primarily due to the reduced maintenance costs. Typically, no regular replacement is needed, unlike batteries, which can result in a reduced life-cycle cost. Another major argument for flywheels is safety. Flywheels operate by spinning a rotor at very high speeds, which poses a safety hazard during a failure event. However, newer flywheels use composite materials instead of steel. Fatigue or other failure modes for composites are more benign than steel failure modes and safety measures can be designed. Many advancements have been made in composite rotors over the years that enhance safety. For example, it is now easier to predict failure modes of composites [119].

It is clear from this study that batteries are the dominant technology and cannot be replaced in every application in which they are used today. This is primarily due to the low initial cost and market availability. However, in the field of power quality and distributed generation, flywheels, super-capacitors and SMES can be considered good alternatives as their unique advantages stand out when compared to traditional batteries. Each technology has its own advantages and disadvantages and hence the choice of one single alternative can be quite complicated. SMES

and super-capacitors can be used in low power applications but flywheels are the best choice today as they can be used in both low and high power applications. The current initial cost of flywheels, which can be justified long term with reduced life-cycle costs, generally pertains to large scale applications such as energy and transportation today. There are significant opportunities for research in developing a cost-effective flywheel which can be used in small to medium scale applications. Development of such a flywheel could prove beneficial as the design would then be a viable alternative to batteries in many applications.

B. Cost Analysis of flywheels

This appendix shows an initial cost analysis comparing flywheels to other traditional means of energy storage including lead acid batteries, Na/S batteries, Zn/Br batteries. The aim of this study is to show that over a considerable period of time, the cost of flywheels are comparable to that of batteries and that the high initial cost can be justified.

B.1. Associated Costs

The main costs taken into account in this study are the Capital costs, Installation costs, Operational costs, Maintenance costs and replacement costs. A description of these costs is shown below.

B.1.1. Capital Cost

There are two major costs attributed with capital costs for storing electricity - the energy cost and the power cost. The energy cost is taken to be the cost of the storage elements which includes manufacturing and assembly costs. Note that assembly costs described here merely refers to the cost of putting together the entire system and does not coincide with the installation costs. The power cost is the cost of the power electronics involved in the storage element. Depending on the type of energy storage the power cost would combine costs of rectifiers, inverters and printed circuit boards (PCB).

B.1.2. Installation costs

The installation cost is the cost of installing the unit at the desired location. This would include labor and any ground work (for ex: underground systems) required to perform the installation.

B.1.3. Operational costs

The operational cost covers all costs occurring after the initial installment. Depending on the type of energy storage, these costs include annual operational costs, fuel costs, cost due to CO_2 emissions and electric losses.

B.1.4. Maintenance and Replacement costs

The maintenance and replacement costs are the costs associated with predicted system failure, general maintenance costs, recycling costs, periodic reinvestment and replacement costs.

B.2. Model

The economics of techniques such as Compressed air energy storage and pump hydro can be analyzed easily using production costing techniques. However, this cannot be used for estimating accurate costs for batteries and flywheels since there might be an overlap of costs involved. A simplified model is hence created to analyze the cost economics of these systems. In this model, all the above described costs are combined into the cost of storing a unit of electricity. This cost is then combined with the conventional electricity price to determine the total price of stored electricity. Hence the feasibility of the energy storage technique per unit of electricity stored can be deduced from this number.

The annual energy cost (EC_{year}) is the total energy discharged annually by an energy storage system which can be given by

$$EC_{year} = P_{rated} * n_{c/d} * t_{c/d} * N_{oper} \qquad \textbf{(B-1)}$$

The annual operational and maintenance cost ($O\&M_{year}$) can be combined together and calculated as

$$O\&M_{year} = P_{rated} * OM_{KW} \qquad \textbf{(B-2)}$$

Similarly , The total cost of power electronics (PE_{cost}) is given by

$$PE_{cost} = P_{rated} * PE_{KW} \quad \textbf{(B-3)}$$

The total cost for the storage units can be given as

$$TS_{cost} = \frac{P_{rated} * t_{c/d} * TS_{cost,KW}}{\eta_{eff}} \quad \textbf{(B-4)}$$

$$\eta_{eff} = \frac{E_{out,discharge}}{E_{in,charge}}$$

The manufacturing and assembly costs of the entire system (AM_{cost}) is given as

$$AM_{cost} = P_{rated} * t_{c/d} * AM_{KW} \quad \textbf{(B-5)}$$

Hence, the annualized capital costs can be given as

$$CC_{year} = (AM_{cost} + TS_{cost} + PE_{cost}) * CRF \quad \textbf{(B-6)}$$

$$CRF = \frac{i_r(1+i_r)^y}{(1+i_r)^y - 1}$$

The Capital recovery factor was obtained from Lindberg's analysis on Engineering economic analysis [229].

The cost of replacement (R_{cost}) depends on the frequency of replacement over the life of the plant and the market value of the product at that time. The replacement cost also covers the recycling costs of the older component. This can be given as

$$R_{cost} = P_{rated} * t_r * R_{KW} \quad \textbf{(B-7)}$$

Finally, the cost per unit of electricity stored can be given as

$$TC_{kW-hr} = \frac{CC_{year} + R_{cost} + O\&M_{year}}{P_{rated} * n_{c/d} * t_{c/d} * N_{oper}} \quad \textit{(B-8)}$$

B.3. Results

The total cost per unit of electricity stored can be given using equation (B-8). This cost was compared between Lead-Acid batteries, Na/S batteries, Zn/Br batteries Compressed Energy storage and flywheels. It should be noted that the systems for each energy storage type were chosen based on distributed generation and power quality applications. All the input parameters chosen are the average values of 3 or 4 different systems. For example, the input parameters of flywheels are average values of Beacon, Vycon, TSi Tribology and Active Power systems. These input parameters are obtained from a study at Sandia National Laboratory [230]. The various cost output along with the total cost per unit of electricity is summarized in Table B-1

Parameters	**Lead Acid**	**Na/S**	**Zn-Br**	**Flywheels**
Rated output (kW)	2500	2500	2500	2500
No of cycles	2200	2500	5000	200,000
Replacement frequency (years)	5	10	8	20
η_{eff}	0.75	0.60	0.65	0.95
PE_{cost} **($/kW)**	200	175	200	250
EC_{year} **($/kW)**	300	500	275	600
TS_{cost} **($/kW)**	385	575	325	650
AM_{cost}	200	250	225	12000

($/kW)				
CC_{year} **($/kW)**	785	1000	750	9050
Installation costs ($/kW)	325	450	400	8000
$O\&M_{year}$ ***($/kW-hr)***	15	25	20	15
R_{cost} **($/kW-hr)**	150	230	100	70
Total Initial cost ($/KW)	1110	1450	1150	20900
Total operational cost ($/kW-hr)	165	255	120	85

Table B-1 Cost Parameters of various energy storage systems

From table B1, it should be noted that the total initial cost of a flywheel is roughly 20 times more than that of comparable batteries. However, this is compensated by the low per kW-hr cost of operation throughout the lifetime of the flywheel. This operational cost includes cost of periodic maintenance, replacement, recycling and regular operation. It can be deduced that in an operational period of 20 years, the cost of flywheels are substantially lesser than comparable batteries. Figure B-1 captures the projected cost of flywheels and batteries over 20 years.

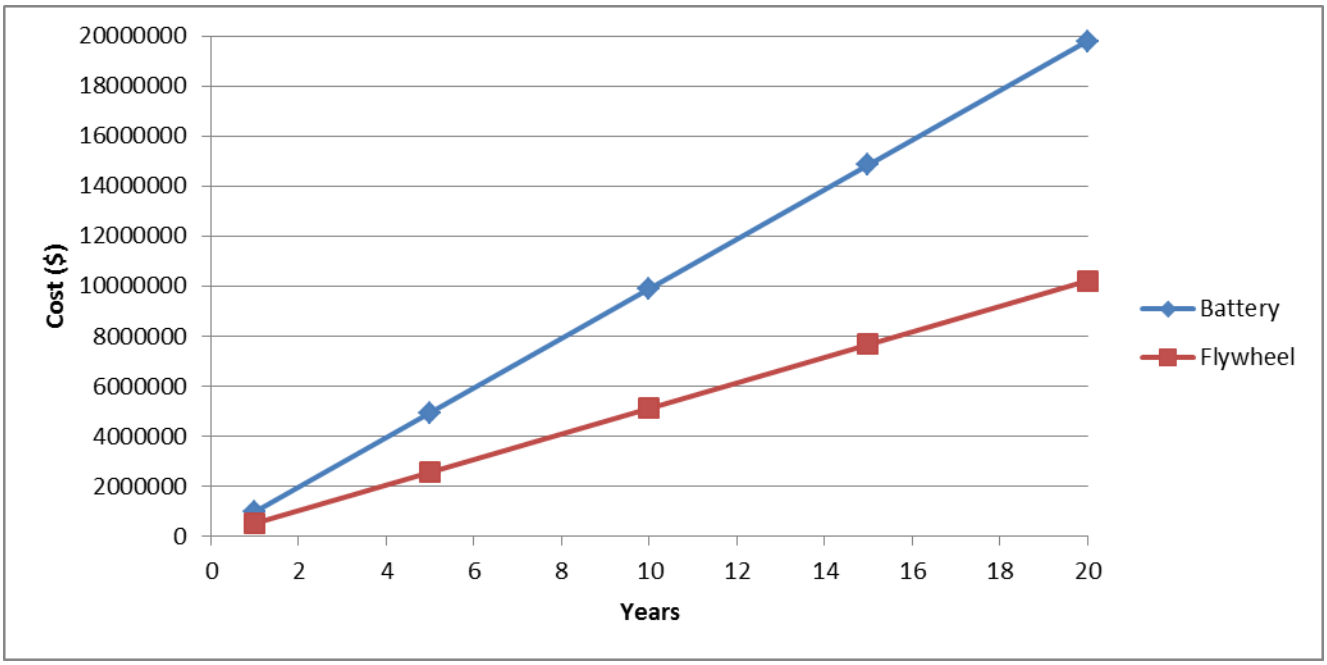

Figure B-1 Projected cost of flywheels vs. batteries

An important note here is that the cost of batteries and flywheels has been normalized to per kW-hr which includes the maintenance and replacement costs. Batteries show a higher cost per kW-hr as they have to be replaced every 4 or 5 years and require more maintenance. Further, the above cost estimates assume steady and normal operation as the variable costs (in case of failure, for example) cannot be predicted with certainty. In addition, cost of carbon offset is not taken into account. This cost, if taken into account, would further prove than flywheels are advantageous over batteries as there are no harmful emissions during operation.

As it is evident from table B-2, the initial average cost of the flywheel is very high and impractical in small scale applications. The major factors that drive up the high initial costs are the assembly, manufacturing and installation costs. One way to keep these costs down is by designing a flywheel which uses less material. This can be achieved by increasing the operating speed of the flywheel. The ROMAC flywheel is designed in this way to be a cost effective flywheel.

Parameter	Average value	ROMAC flywheel
Material cost	100	100
Average Volume of rotor (m^3/kW-hr)	0.065	0.033
Average Weight of flywheel rotor (kg/kW-hr)	113 kg	60 kg
Manufacturing cost ($/kW-hr)	12000	6360
Installation cost ($/kW-hr)	8000	6000
Capacity cost ($/kW-hr)	600	600
Total cost ($/kW-hr)	26000	12960

Table B-2 Cost comparison between ROMAC flywheel and average flywheel cost

Assuming all the other costs are the same, the manufacturing and installation costs of the ROMAC flywheel are almost 40% lesser than the average commercial flywheel available today. These cost savings can make it a viable candidate for use in small scale energy storage solutions.